NASA/TP—2001–210770

Effects of Gas-Phase Radiation and Detailed Kinetics on the Burning and Extinction of a Solid Fuel

Jennifer L. Rhatigan
Lyndon B. Johnson Space Center

National Aeronautics and
Space Administration

Johnson Space Center
Houston, Texas 77058-3696

June 2001

Acknowledgments

This document constitutes the dissertation I submitted in partial fulfillment of the requirements for the degree of Doctor of Philosophy at Case Western Reserve University. As such, I would like to express my gratitude to the following individuals and organizations that have shared in this undertaking, making it both possible and enjoyable. While I carried the fire, others sustained it:

Dr. Jackie Sung, who served as thesis advisor.

Dr. James T'ien, who served as thesis co-advisor

The NASA Glenn Research Center management, who sponsored the fellowship and discretionary funding which enabled me to pursue this research; in particular, Dr. Thomas L. Labus, who sponsored, advised, and encouraged me throughout this effort.

The Johnson Space Center and International Space Station Program management, who continued to support this effort upon my transfer to Houston; in particular, Mr. Rick Nygren and Mr. Bill Stephenson provided invaluable support.

My friends and colleagues at NASA, both at the Glenn Research Center and the Johnson Space Center—for all their help and encouragement.

Kathy Weisskopf, for her editorial assistance and support.

My husband, Stephen Frick. This work is for you, in the hope that it might keep you safe when you journey into space.

Available from:

NASA Center for AeroSpace Information
7121 Standard
Hanover, MD 21076-1320

National Technical Information Service
5285 Port Royal Road
Springfield, VA 22161

This report is also available in electronic form at http://techreports.larc.nasa.gov/cgi-bin/NTRS

Contents

Section **Page**

List of Tables

List of Figures

Abstract

This is the first attempt to analyze both radiation *and* detailed kinetics on the burning and extinction of a solid fuel in a stagnation-point diffusion flame. We present a detailed and comparatively accurate computational model of a solid fuel flame along with a quantitative study of the kinetics mechanism, radiation interactions, and the extinction limits of the flame.

A detailed kinetics model for the burning of solid trioxane (a trimer of formaldehyde) is coupled with a narrowband radiation model, with carbon dioxide, carbon monoxide, and water vapor as the gas-phase participating media. The solution of the solid trioxane diffusion flame over the flammable regime is presented in some detail, as this is the first solution of a heterogeneous trioxane flame. We identify high-temperature and low-temperature reaction paths for the heterogeneous trioxane flame.

We then compare the adiabatic solution to solutions that include surface radiation only and gas-phase and surface radiation using a black surface model. The analysis includes discussion of detailed flame chemistry over the flammable regime and, in particular, at the low stretch extinction limit. We emphasize the low stretch regime of the radiatively participating flame, since this is the region representative of microgravity flames. When only surface radiation is included, two extinction limits exist (the blow-off limit, and the low stretch radiative limit), and the burning rate and maximum flame temperatures are lower, as expected. With the inclusion of surface and gas-phase radiation, results show that, while flame temperatures are lower, the burning rate of the trioxane diffusion flame may actually increase at low stretch rate due to radiative feedback from the flame to the surface.

The trioxane diffusion flame model is then extended to include surface absorption of radicals from the gas phase. We compare the results to the inert surface case and also include surface radiation both with and without surface radical interactions. Results indicate that, for the model studied, surface absorption of radicals from the gas phase is unimportant.

1.0 Introduction

This section introduces the scientific and engineering motivations for this study of solid fuel diffusion flames. It also provides an orientation to the organization of the text, and gives the reader a 'roadmap' to the major topics addressed in the study.

1.1 Motivation

This research has been prompted by several considerations. The immediate consideration in this pursuit is spacecraft fire safety. An understanding of burning and extinction of solid fuel diffusion flames, particularly at the low stretch rates characteristic of the microgravity environment endemic in spacecraft, is necessary to design and build safer spacecraft. A more fundamental—but certainly related—consideration is the exploration of the physics that lead to extinction of solid fuel diffusion flames. Evidence indicates that thermal radiation within a flame is an important low stretch rate extinction mechanism. Moreover, radiative interactions with a solid fuel surface are important as well. A final consideration is accuracy of the flame model. By contemporary standards, this includes detailed kinetics analyses. This is the first attempt to analyze both radiation and detailed kinetics on the burning and extinction of a solid fuel stagnation-point diffusion flame.

1.2 Organization of the Report

The focus of this thesis, beginning with Section 2 and concluding with Appendix 3, is a study of the effects of radiation and detailed kinetics on the burning and extinction of a solid fuel in a stagnation-point diffusion flame. Section 2 provides a background to orient the reader to the current state of the research in this area. Section 3 addresses the problem formulation of the solid trioxane stagnation-point diffusion flame to include accurate gas-phase radiation and detailed kinetics. The narrowband radiation model of Bedir [1998] is used along with surface radiation and emission, coupled with the detailed kinetics model of the fuel. Section 4 addresses the physical properties and kinetics of trioxane, and how the kinetics mechanism is validated. Section 5 covers the numerical methods used for the solutions.

Section 6 contains the results of the study of the solid trioxane burning in the opposed jet diffusion flame configuration with radiation and detailed kinetics. We examine global flame response of trioxane burning in air, including flame temperature, fuel burning rate, and flammability, and detailed flame structure for cases including surface radiation and a combination of gas-phase and surface radiation. We also examine detailed chemistry, reaction pathways, and sensitivity, with emphasis on the low stretch extinction limit.

Section 7 contains a study of the effects of surface radical interactions on the heat balance at the surface, since this has potential to affect the kinetics and heat balance of the solid diffusion flame.

Section 8 summarizes our findings from the foregoing sections and suggests potential future research directions with this problem.

During our early attempts to understand the interactions between gas-phase radiation and surface radiation in the burning of a solid fuel, we developed a relatively simple model and adapted it to facilitate parametric comparisons. Appendix 4 contains the parametric study of the effects of both gas-phase and surface radiation on the burning and extinction of a solid fuel in a stagnation-point diffusion flame. This early study helped establish the understanding of the radiative interactions in the solid flame and sparked our interest in pursuing the research that is the focus of the body of this work. Therefore, we refer the interested reader to Appendix 4 first, to obtain a fundamental understanding of the interactions between gas-phase and surface radiation in a solid fuel. In Appendix 4, we use a two-flux radiation solution with carbon dioxide and water vapor as gray participating media. The fuel modeled is PMMA (polymethylmethacrylate). The model assumes a one-step finite rate overall gas-phase chemical reaction. The results demonstrate that both gas-phase and solid surface radiation become increasingly important as flame stretch rate decreases. This early work was followed by a publication [Rhatigan et al. 1998] wherein a comparison is made between the results discussed in Appendix 4 and a model that includes a non-gray gas analysis.

2.0 Background

In this section, we introduce the concepts important to this study, review recent progress in the area, and establish relevance to the field of study.

Diffusion Flames: Flames are distinguished by the means with which the fuel and oxidizer come in contact for reaction. Diffusion flames are flames in which the course of the reaction is influenced or controlled by the flow field of the flame. That is, the reactants and oxidizer come into contact and burn by means of fluid transport mechanisms. The flame seeks the stochiometric zone of the mixture brought about by the flow field. Burning in a diffusion flame has a rate associated with it—the stretch (or strain) rate. Stretch rate is characterized by flow nonuniformity, flame curvature, and flame unsteadiness. Burning will cease at either too high a stretch rate (blow-off extinction) caused by insufficient residence time for reaction, or too low a stretch rate (radiative extinction), caused by insufficient temperature to maintain reaction due to radiative losses.

Flame configuration: Diffusion flame configurations are distinguished by the orientation of the fuel to the oxidizer flow. Counterflow diffusion flames are those in which the fuel and oxidizer flows are geometrically opposed to each other and meet at a stagnation-point. This configuration—also known as the opposed jet diffusion flame—is well studied because the similarity solution for the flow field is known, the geometry is simple and quasi-one-dimensional, and comparison between computational models and experiments are relatively straightforward. Oxidizer and fuel velocities control flame location. Moreover, the flame in this case is typically planar and purely strained.

We used a special case of the counterflow configuration to study burning of solid and liquid surfaces by directly impinging the oxidizer stream on a burning surface. Where the oxidizer stream impinges directly on a burning surface, it is commonly called the opposed-jet configuration. The flow field is characterized by the same counterflow similarity solution, with only a change in boundary condition (on the fuel side). The fuel flow is created from solid fuel vaporization from the surface and, in this case, the flow rate of fuel from the surface is an eigen-value solution for the given oxidizer velocity.

Flow Parameter: The counterflow diffusion flame is further distinguished by a constant radial velocity gradient (constant stretch rate). For the free stream velocity of the oxidizer jet flowing in direction r (radial direction parallel to the surface), U_e, the stretch rate, a, is defined by $U_e=ar$. The stretch rate has the units of inverse time, so that it also gives the characteristic time for the problem. It is a convenient term in modeling diffusion flames because a number of parametric quantities can be related to the stretch rate [Liñán 1974] and thus many modeling studies are posed using the stretch rate, rather than the velocity, as the flow parameter.

Extinction Limits: The flammable regime of the stagnation-point diffusion flame is bounded by two extinction limits—a high stretch (blow-off) limit and a low stretch (quench) limit. Much of the research emphasis has been on extinction at the blow-off limit, caused by insufficient gas residence time at high stretch rates. The emphasis on the blow-off limit is well deserved—it has both fundamental and practical significance. It is also easily observed in a laboratory. The low stretch extinction limit has only been postulated until recently because the buoyant flows characteristic of earth's gravity limit the observation of very low stretch diffusion flames.

Importance of Flame and Surface Radiation: T'ien has led an effort to elucidate low stretch extinction due to radiative heat loss, beginning with his 1986 paper [T'ien 1986], in which he established the possibility that surface radiation can be a significant factor in the physics of low stretch diffusion flames and can indeed lead to extinction. He incorporated solid surface emission in the opposed jet diffusion flame model, showing that radiative losses at low stretch can be the predominant heat loss from the surface and cause flame quenching.

Radiative emission from a hot flame is partly a heat loss and partly a heat feedback mechanism to the burning solid. Emission from the burning solid surface can be partially absorbed by the gaseous flame and the rest escapes to the ambient as a heat loss. Gas-phase absorption and emission are functions of the radiative (optical) thickness of the gas. The optical thickness of the gas varies with stretch rate, typically thickening in the low stretch regime due to a thicker flame, and resulting in increased global concentrations of the participating media. Radiation can become a predominant heat transfer mechanism at low stretch rate and thus become the controlling mechanism for flame extinction (quenching).

Progress in Understanding the Radiative Extinction Limit: T'ien and his co-workers and students have contributed to a growing body of work on the radiative extinction of diffusion flames, with emphasis on the low stretch regime found in a microgravity environment. The group has established how radiation originating from the hot fuel surface, the gaseous flame, or a combination of the two, affects the extinction limits of diffusion flames. Starting with inclusion of surface radiation only, Foutch and T'ien [1987] studied mixed convection (buoyant and forced) in the stagnation region of a solid cylinder. They demonstrated the low stretch extinction limit due to surface radiation loss. Lee and T'ien [1989] studied vertical burning of a solid surface PMMA fire, and included surface and gas-phase radiation. They used a two-flux model for the gas-phase radiation, and included CO_2 and H_2O, and soot in the radiative treatment. Chao et al. [1990] analytically demonstrated the existence of the low stretch extinction limit in droplet combustion, considering radiative emission only from the gas phase (i.e., optically-thin treatment). Grayson et al. [1994] examined flame spread over a thin solid in a low-speed concurrent flow and included solid surface radiation loss. Jiang [1995] also examined flame spread over a thin solid and included gas-phase radiation in the model (two-dimensional gray gas model, with a discrete ordinates solution). The low stretch extinction mechanism was validated by experiment [Olson 1997] in the lower stagnation region of a large radius solid cylinder. Bedir [1998] improved the gas-phase radiation treatment by adapting the narrowband radiation model with discrete ordinate solution to the stagnation-point diffusion flame. The importance of optical thickness in flames was recently demonstrated by Shih et al. [1999], who studied a very low pressure opposed jet $H_2/O_2/CO_2$ diffusion flame using detailed kinetics and the narrowband radiation model. They found that the flame is unusually thick due to the combined effects of low pressure (slow chemistry), radiation, and low stretch rate. The effect of flame radiation was studied directly by varying the amount of CO_2, which is a strongly participating gas. Frate et al. [2000] examined the opposed jet gaseous diffusion flame of dry CO and oxygen, using both the narrowband radiation model and detailed kinetics. The effect of suppressant addition on the flammability limits was examined and compared using CO_2 and Ar, with the former as a radiatively participating species. A reversal in the trend of suppressant effectiveness was found at low stretch rates as compared to higher stretch rates.

Building on this body of work, this study takes up the problem of including both accurate radiation and flame chemistry models in the burning and extinction of a solid fuel in a stagnation-point diffusion flame. The study of the low-stretch solid fuel diffusion flame bears relevance to both the typical materials and ventilation-induced flow regime important in spacecraft fire safety.

Detailed Kinetics: In this study, we seek to establish the importance of accuracy in the kinetics portion of the model of stagnation-point diffusion flames that is similar to that of the radiation model. The solution of accurate, detailed kinetics of even the simplest fuel-oxidizer combinations has been an intractable problem until very recently. Comprehensive kinetic mechanisms of fuel oxidation are very difficult to obtain. Individual reactions cannot be measured but must be surmised from observation of constituent overall reactions. Determining rate constants associated with detailed reaction steps presents an additional challenge. The computational power (speed and memory) to perform the quantum theory analysis is still quite limited. Detailed mechanisms estimated from experimental data for the most simple fuels have only recently become available but are still under debate as to their rigor under extension to variation of flame phenomena, flow field, pressure, temperature, etc. In addition, solving the detailed kinetics problem is computationally complex due to numerical stiffness associated with the varying timescales of the flow field and detailed reactions.

Initial attempts to solve the counterflow diffusion flame problem used single step, finite rate, global reactions to model reaction mechanisms. As these lacked any information on the formation and consumption of intermediate species, they were limited. During the 1980s and early 1990s, pursuit of 'reduced' kinetics mechanisms gained popularity as both computer capabilities and understanding of some of the important intermediate reactions increased (e.g. [Dixon-Lewis et al. 1984, Bui-Pham and Seshardri 1990, Chen 1990, Maas and Pope 1992]). 'Reduced' or simplified mechanisms were developed from a set of detailed kinetics, with emphasis on only the most important intermediate species (i.e. those that control either the rate of the reaction or the formation of other significant species). The problems are solved numerically with the set of 'reduced' reactions, using the steady state assumption for those species deemed less important.

These studies mentioned above focused on gas-phase fuel and oxidizer combinations. Solid fuels, however, are more relevant to practical fire safety, as compared to gaseous and liquid fuels. The problem of the burning solid poses some kinetically unique considerations. Most studies have assumed one-step kinetics for the burning of a solid for several reasons. First, detailed oxidation mechanisms for only the most structurally simple fuels are available (e.g., H_2, CO, CH_2O, CH_4) over a range of temperatures that typically does not include the condensed phase. Secondly, the phase change mechanism of the fuel must be understood (i.e., does the fuel liquefy and then burn as a liquid, or does it sublimate and burn from the gas phase?). Lastly, the kinetics mechanism of the solid burning must be known for an accurate estimate of the solid surface temperature.

We have found a fuel uniquely suited to this study. Trioxane is a solid fuel that sublimates readily and depolymerizes in the gas phase directly to formaldehyde. Detailed oxidation mechanisms for formaldehyde are available. Moreover, it is structurally similar to other polymers used in spaceflight hardware, such as Delrin and Celcon. All aspects of this fuel can be modeled in detail, so that experimental verification is feasible. Study of trioxane serves as both a first step toward understanding other more complex solid fuels, and a detailed validation of all the models associated with the solid burning modeling through the comparison with future experimental results.

3.0 Formulation for a Computational Study of Solid Trioxane Combustion in Stagnation-Point Flows

3.1 Background

In this section and in Sections 4 through 7, we again examine a solid fuel burning in a stagnation-point configuration, but with a somewhat different emphasis. While initial studies in Appendix 4 used a parametric variation of radiative properties, here we use the most accurate and comprehensive models available for both the radiative heat transfer and detailed kinetics to examine the flammable regime of a solid fuel burning in a stagnation-point configuration.

The recent emphasis on modeling of diffusion flames with detailed kinetics is the result of the concurrent availability of convenient computational capabilities and detailed kinetics mechanisms for a variety of simple fuels. The study of detailed kinetics mechanisms for the combustion of fuels has focused primarily on simple gaseous fuels, such as H, CO, and CH_4 (e.g. [Dixon-Lewis et al. 1984]), since the combustion of these fuels forms the mechanisms for the combustion of more complex fuels. Combustion of solids in diffusion flames with detailed kinetics has not received the same amount of attention, primarily due to the lack of detailed kinetics data for simple solid fuels.

While it has been shown the solid fuels are potentially complex in a radiative sense, comprehensive radiation modeling tools are now available that can model both the gas phase and surface radiative interactions. Excellent and contemporary reviews of gas-phase radiation studies in diffusion flames can be found in Bedir et al. [1996], T'ien and Bedir [1997], and Bedir [1998].

Opposed jet gaseous diffusion flames have been studied in models that include both radiation and detailed kinetics (e.g. [Daguse et al. 1996, Frate et al. 2000]). Previous models of the burning of a solid fuel have not included both gas-phase radiation and detailed kinetics. This is the first attempt to include accurate modeling of both phenomena in the same analysis for a solid fuel. While both simple and sophisticated gas-phase radiation models have been studied for solid combustion, they have relied on simplified, one-step overall reaction kinetics. We are interested in observing the detailed kinetics at the low stretch radiative extinction limit and also the effects that a more accurate kinetics model may have on the outcome of the radiation predictions. The two phenomena are indirectly coupled in the gas phase because changes in concentration of radiatively participating species (e.g. H_20, CO_2, CO) brought about by the kinetics affect the optical thickness of the gas, and thus the gas-phase radiative heat transfer.

Insight into the detailed kinetics serves several purposes. First, it allows us to judge the necessary accuracy required for future models. Is a single step or reduced model sufficient, or is a detailed kinetics analysis necessary for an accurate estimate of the importance of radiation in this type of study? Second, it allows us to study in detail the evolution of each participating species. We can know with accuracy the concentration of radiatively participating species throughout the flame, and thus better understand the gas-phase radiation interaction with a solid fuel. Third, it allows us to evaluate the potential effects of radical interactions with the solid surface. Finally, the inclusion of detailed kinetics in this study establishes a benchmark for the study of the combustion of solids (or for that matter, liquids) where radiative interactions with a surface are potentially important, such as in a microgravity environment.

3.2 Nomenclature

The nomenclature listed below was developed to remain consistent with as much of the notation as possible used in the primary references [Kee et al. 1980, Lutz et al. 1996, and Bedir 1998], while maintaining some continuity with the earlier work in Appendix 4. This necessitated the use of more subscripting than might be desirable, but ensures the continuity of the development.

a	radial velocity gradient of stagnation-point flow, $U_e = ar$, 1/s
c_p	constant pressure specific heat of the gas mixture, J/mol-K
$c_{p,f}$	constant pressure specific heat of the gas phase fuel, J/mol-K
$c_{p,s}$	constant pressure specific heat of the solid fuel, J/mol-K
D_{kj}	diffusion coefficient between species k and j, cm^2/s
D^{T}_{kr}	thermal diffusion coefficient, g/cm-s
F	similarity variable related to mass flux, g/cm^2-s (equation 3-1b)
G	similarity variable related to radial component of velocity, g/cm^3-s (eqn 3-1a)
E	similarity variable related to radial pressure gradient, J/cm^4 or g/cm^3-s^2 (Eqn 3-1c)
h	enthalpy, J/mol
I	total radiation intensity: radiation energy flux per unit solid angle, per unit area normal to the path, J/cm^3-s
K	total number of species
k_{fi}, k_{ri}	forward/reverse rate constant of the ith reaction, units depend on reaction
L	total latent heat of the fuel at vaporization temperature, J/g
l	length of domain, cm
L^o	latent heat of the fuel at the reference temperature, J/g
$\dot{m}$	mass flux (total), g/cm^2-s
p	pressure, atm
Q_i	heat release rate of reaction i, J/cm^3-s
Q_T	total heat release rate due to reaction, J/cm^3-s
q	radiation heat flux, J/cm^2-s
q_a	radiation heat flux absorbed by the surface, J/cm^2-s
q_e	radiation heat flux emitted from the surface, J/cm^2-s
q_i	radiation heat flux incident at the surface, J/cm^2-s
q_{net}	net radiation heat flux into the surface, J/cm^2-s
q_r	radiation flux reflected from the solid surface, J/cm^2-s
r	radial coordinate or radius, cm
r_i	rate of progress of the ith reaction, mol/cm^3-s
S	direction of travel of radiation flux
T	temperature, degrees Kelvin
T_{max}	maximum flame temperature, degrees Kelvin
u	axial velocity, cm/s or pressure pathlength, atm-cm (depending on context)
U_e	axial velocity at edge of boundary layer, cm/s
V_k	diffusion velocity of species k, cm/s
v	radial velocity, cm/s
W_k	molecular weight of species k, g/mol
x	axial coordinate, cm
Y_k	mass fraction of species k
X_k	mole fraction of species k

Z_{rot}	rotational relaxation collision parameter (number of collisions needed to establish rotational equilibrium of a molecule)
α_p	polarizability
α	total hemispherical absorptivity of the surface
γ	spectral line half-width for narrowband model, cm
δ_ν	mean line spacing parameter for narrowband model, cm
ε	total hemispherical emissivity of the surface
κ	gray gas absorption coefficient, path length^{-1}
κ_ν	spectrally dependent absorption coefficient, path length^{-1}
κ_p	Planck-mean absorption coefficient, (atm-cm)$^{-1}$
λ	thermal conductivity, J/cm-s-K
μ	viscosity, kg/m-s, or direction cosine
ν	spectral frequency, cm^{-1}
ν_{ki}'	stochiometric coefficient of the *k*th reactant species in the *i*th reaction
ν_{ki}''	stochiometric coefficient of the *k*th product species in the *i*th reaction
ρ	mass density, g/cm^3
σ	Stefan-Boltzman constant, $5.6696\mathrm{x}10^{-8}$ W/m^2-K^4
τ	transmittance
Ω	solid angle
$\dot{\omega}$	reaction rate, mol/cm^3-s

Subscripts:

b	black-body value
e	equivalent band parameter, or edge of the flame
F	gas-phase mixture at fuel-side of domain (x=0)
g	gas-phase of mixture
f	gas-phase fuel species (trioxane)
i	reaction index
k	species index
o	oxidizer side of domain (x=l)
s	solid surface or solid phase of fuel (trioxane)
w	mean wall quantity
ν	spectral quantity
$-\infty$	reference to a distance within the surface such that the temperature decays exponentially to $T_{-\infty}$
∞	quantity at outer limit or edge of domain

Superscripts:

o	reference point at which a property is evaluated, such as latent heat
+	reference to positive x side of surface
-	reference to negative x side of surface

3.3 Governing Equations and Boundary Conditions

Governing Equations: The governing equations are taken from Kee et al. [1988] and Lutz et al. [1996] for an opposed jet diffusion flame. These are expressed in terms of a fixed jet velocity, fixed jet separation distance formulation. The momentum and species governing equations from Kee et al. [1988] and Lutz et al. [1996] are repeated here for convenience. Figure 3-1 shows the flow configuration.

Conservation of mass in cylindrical coordinates is given by:

$$\frac{\partial}{\partial x}(\rho u)+\frac{1}{r}\frac{\partial}{\partial r}(\rho v r)=0$$

Adapting the von Karman similarity analysis, and recognizing that the similarity variables *F(x)* and *G(x)* are functions of x only, the similarity functions are given by:

$$G(x)=-\frac{\rho v}{r}=\frac{dF(x)}{dx} \qquad \textbf{(3-1a)}$$

The above equation is the continuity equation expressed by the similarity functions. *F* is defined by:

$$F(x)=\frac{\rho u}{2} \qquad \textbf{(3-1b)}$$

and the radial momentum equation is satisfied by the eigen-value

$$E=\frac{1}{r}\frac{\partial p}{\partial r}=const. \qquad \textbf{(3-1c)}$$

In the limit of potential flow, the eigen-value is related to the stretch rate by [Kee et al. 1988, Dixon-Lewis 1990, Sung et al. 1996]

$$E=-\rho_O a^2$$

The axial momentum equation, expressed in terms of the similarity variables, is:

$$E-2\frac{d}{dx}\left(\frac{FG}{\rho}\right)+\frac{3G^2}{\rho}+\frac{d}{dx}\left[\mu\frac{d}{dx}\left(\frac{G}{\rho}\right)\right]=0 \qquad \textbf{(3-1d)}$$

The species conservation equation for species $k=1,2\ldots K$ is given by:

$$\rho u\frac{dY_k}{dx}-\frac{d}{dx}(\rho Y_k V_k)-\dot{\omega}W_k=0 \qquad \textbf{(3-1e)}$$

Since we are interested in the effects of flame radiation, the energy equation is modified to include the radiation from participating media in the flame. Adapting Bedir's formulation [1998] for the energy equation to include gas-phase radiation, the energy equation is:

$$\rho u c_p\frac{dT}{dx}-\frac{d}{dx}\left(\lambda\frac{dT}{dx}\right)+\left(\sum_{k=1}^{K}\rho Y_k V_k c_{pk}\right)\frac{dT}{dx}+\sum_{k=1}^{K}\dot{\omega}_k h_k+\frac{dq_{net}}{dx}=0 \qquad \textbf{(3-1f)}$$

The first and third terms represent the convection; the second term represents the conduction; the fourth term is the combustion heat release; and the fifth term is the radiative source term. The radiative source term can be found by solving the radiative transfer equation [Bedir 1998], described in detail in Section 3.4.

The formulation is modified using the technique of Sung et al. [1996] to allow potential flow on the oxidizer side, and plug flow on the fuel side, to be consistent with the flow formulation of Appendix 4. As such, the stretch rate ahead of the flame on the oxidizer side is chosen as the single parameter to characterize the strained flow.

Boundary Conditions for the Solid Fuel Case: The boundary conditions in Kee et al. [1980] and Lutz et al. [1996] are formulated for an opposed jet configuration (Figure 3-1(a)). In this work, the boundary conditions are written for a jet impinging on a solid fuel surface, also called a stagnation-point configuration (Figure 3-1(b)). The fuel surface is modeled as impermeable to all species except fuel vapor. Radical interactions at the surface are neglected here, but are considered in Section 7.

Heat Balance: Figure 3-1(c) shows the heat balance at the solid surface . The surface is modeled as a solid heated to a gas (by the flame), so that liquid formation (melting of the solid) and any resulting liquid motion is neglected. Performing the energy balance at the fuel surface (x=0), we use the no slip condition, such that v=0 at x=0, and

Conduction from gas to solid +net radiation into solid = Latent heat for phase change of solid to gas + Conduction into solid, or

$$\lambda_g \frac{dT}{dx^+}\Big|_{x=0+} + q_{net} = \dot{m}L + \lambda_s \frac{dT}{dx^-}\Big|_{x=o-}$$

The total latent heat is given by (see Appendix 3):

$$L = L^o + \int_{T^o}^{T_s} c_{p,f}\,dT - \int_{T^o}^{Ts} c_{p,s}\,dT$$

where L^o is the latent heat at the reference temperature, T^o, at 298K. The specific heat of the solid is assumed approximately constant, and the latent heat, L, is evaluated at the surface temperature. The fuel is assumed to be thick enough such that the temperature profile into the solid is an exponential decay from T_s to $T_{-\infty}$ (infinite slab assumption). The heat flux at the surface on the fuel side is:

$$\lambda_s \frac{dT}{dx}\Big|_{x=0-} = \dot{m}c_{p,s}\left(T_s - T_{-\infty}\right)$$

The total mass flux at x=0 is expressed by:

$$\dot{m} = \rho_F u_F = 2F$$

where the subscript F refers to the fuel side *location* of the mass balance. Combining the expressions above, we have the following boundary condition on axial velocity at x=0:

$$2F = \rho_F u_F = \frac{\lambda_g \left(\frac{dT}{dx}\right)_{x=0+} + q_{net}}{\left(L^o + \int_{T^o}^{Ts} c_{p,f}\,dT + c_{p,s}\left(T^o - T_{-\infty}\right)\right)} \qquad \textbf{(3-2a)}$$

Now the equation is somewhat simplified if the ambient temperature is the reference temperature, such that $T^o = T_{-\infty}$.

$$2F = \rho_F u_F = \frac{\lambda_g \left(\frac{dT}{dx}\right)_{x=0+} + q_{net}}{\left(L^o + \int_{T^o}^{T_s} c_{p,f}\, dT\right)} \qquad \textbf{(3-2b)}$$

The term in the denominator can be evaluated once for a particular fuel and surface temperature. These are addressed for trioxane in Appendix 3.

The net radiation flux into the surface is the difference between the flux the surface absorbs (incident less reflected) and the flux the surface emits:

$$q_{net} = q_a - q_e$$

The absorbed radiation flux into the surface is expressed as the difference between the incident flux and the reflected flux, and related to the surface absorptivity by the following expression:

$$q_a = q_i - q_r = q_i - (1-\alpha)q_i = \alpha q_i$$

Assuming a gray surface, the emitted flux is given by:

$$q_e = \varepsilon\sigma T_s^4$$

Then the net radiative flux to the solid surface is expressed as:

$$q_{net} = \alpha q_i - \varepsilon\sigma T_s^4 \qquad \textbf{(3-2c)}$$

where radiation is incident from the flame. In this case, the incident radiation flux, q_i, is composed of the flame radiation flux as well as flux from the background radiation. The incident radiative flux at the surface from the flame is found by solving the radiation transfer equation (Section 3.4). If the flame radiation is excluded and the gas is assumed to be transparent, the net radiative flux to the solid surface is given by the expression for radiation transfer between two infinite parallel planes at temperatures T_s and T_∞, where the background is at T_∞:

$$q_{net} = -\varepsilon_s\sigma T_s^4 + \varepsilon_\infty\sigma T_\infty^4 \qquad \textbf{(3-2d)}$$

This development is general, so that other surface properties can be modeled in the future. For our purposes specific to the trioxane flame model, the surface and background are modeled as perfect (black-body) radiators, with absorptivity and emissivity equal to 1.0. This is not intended to be a physical representation of the trioxane fuel surface, but an example case for modeling purposes. As pointed out in Appendix 4, this case is the most radiatively complex surface condition. The computational results reflect a physically realistic, albeit extreme, contribution of radiative heat transfer to this physical situation and therefore give an indication of the importance radiation can have. Appendix 4 focused on the full range of possible solid surface radiative conditions. The surface radiative condition here is identical to that of Case 1 in Appendix 4; however, since the surface temperature is relatively low in comparison to all cases in Appendix 4 (thus reducing emission), behaviors of Case 2 (no emission) from Appendix 4 can be evident as well. Hence, comparison of the adiabatic and radiative trioxane flames can illustrate whether the trioxane surface exhibits the characteristics of Case 1 or Case 2. This will be demonstrated in Section 6. Furthermore, transmission of radiation through the solid surface is neglected.

Mass Balance. Now turning to the mass balance at the surface, we start with the general expression for the mass balance:

$$\dot{m} = \rho_F u_F = \rho_f u_f + \sum_k \rho_k u_k$$

The boundary condition at the surface on the fuel species equation is derived from the fact that at the surface (x=0), the u_k=0 so that:

$$\dot{m} = \rho_f u_f = \rho_F u_F = 2F$$

Also,

$$u_f = u_F + V_f$$

$$\rho_f = Y_f \rho_F$$

where V_f is the diffusion velocity of the fuel species. Combining,

$$\dot{m} = \rho_f u_f = \rho_F Y_f \left(u_F + V_f\right) = \rho_F u_F$$

then solving for Y_f:

$$Y_f = \frac{u_F}{\left(u_F + V_f\right)} \qquad \textbf{(3-3)}$$

Now for all other species at x=0:

$$\rho_k u_k = 0$$

since $u_k = 0$. Then from the velocity definition

$$u_k = u_F + V_k = 0$$

so that the boundary condition on non-fuel species at the surface is:

$$u_F = -V_k \qquad \textbf{(3-4a)}$$

The diffusion velocity is dependent upon the mass fraction, so the diffusion velocity expression can be discretized (using the mixture averaged formulation) and solved implicitly for Y_k.

Alternatively:

$$Y_k u_F = -Y_k V_k \qquad \textbf{(3-4b)}$$

Equation 3-4(b) is a convenient form to solve Y_k in the OPPDIF program (discussed in Section 5), since the "diffusion velocity" is calculated as a product $Y_k V_k$. It is the form of the equation used in this work. The formulation of equation 3-4(b) is more general because it can be used with either the mixture-averaged diffusion velocity calculation, or the multicomponent diffusion velocity calculation.

Table 3.1 contains a comparison between the boundary conditions of the opposed flow formulation (OPPDIF) and the solid fuel stagnation-point flow formulation (OPPDIFSOLID) at x=0. Note that the stagnation-point boundary conditions can be implemented with or without flame and/or surface radiation effects.

At x=l, the oxidizer side, the boundary conditions are unchanged from those of Kee et al. [1988] except the potential flow approximation for G. This is summarized in Table 3.2.

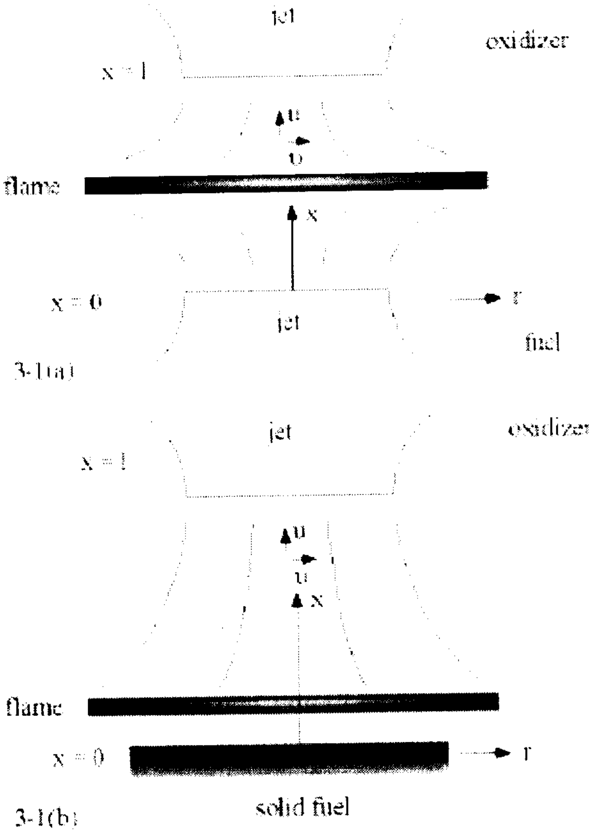

3-1(a)

3-1(b)

Figure 3-1(a & b): Illustration of changes to geometry of problem.

(a) Two gas jets impinging; (b) gas-jet impinging on solid surface.

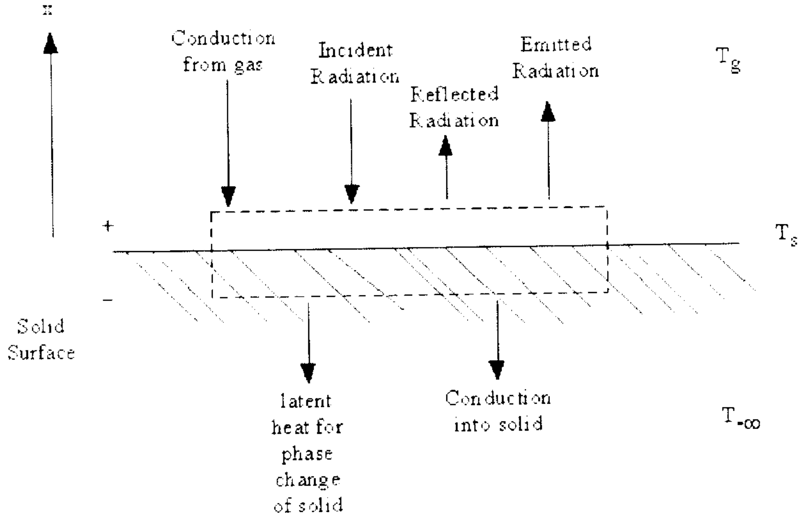

$T_g > T_s > T_{-\infty}$

Figure 3-1(c): Control volume for energy balance on solid surface.

Table 3-1: Boundary Condition Comparison at x=0 Between the Opposed Jet Formulation and the Stagnation-Point Formulation

Dependent Variable	Opposed Flow Boundary Condition at x=0	Stagnation-Point Boundary Condition at x=0
F	$\frac{\rho_F u_F}{2}$	$\frac{\lambda_g \left(\frac{dT}{dx}\right)_{x=0+} + q_{net}}{2\left(L^o + \int_{T^o}^{Ts} c_{p,f}\, dT\right)}$
G	0	0
T	T_s	T_s
Y_k	$\rho_F u_F Y_k + \rho_F V_k Y_k = (\rho_F u_F Y_k)_{-\infty}$	$fuel: Y_f = \frac{u_F}{(u_F + V_f)}$ $other: u_F = -V_k$

(Note that -∞ in the species equation refers to the upstream value on the fuel jet side)

Table 3-2: Boundary Condition Comparison at x=l Between the Opposed Jet Formulation and the Stagnation-Point Formulation

Dependent Variable	Opposed Flow boundary condition at x=l:	Stagnation-Point boundary condition at x=l:
F	$\frac{\rho_l u_l}{2}$	$\frac{\rho_l u_l}{2}$
G	0	$-\delta\sqrt{-\rho_l E}$ $\delta = 1$: potential flow $\delta = 0$: plug flow
T	T_s	T_s
Y_k	$Y_{k,l}$	$Y_{k,l}$

3.4 Flame Radiation Model

Radiation contributes to the heat balance in two places in the model of the solid stagnation-point flame. The solid surface both emits radiation and absorbs incident radiation from the flame (and background). This effect is modeled in the surface heat balance boundary condition. Radiation also constitutes a heat loss from the flame, reducing flame temperature. This effect is modeled in the energy equation as the derivative of the radiation flux term. The topic of this section is the formulation of the radiative heat transfer equation for solution of the derivative of the radiation flux term in the flame energy balance.

The physics of radiative participation of gases in a flame are complex in that the radiative properties of real gases vary with direction, wavelength, temperature, and pressure. The modeling challenge is to retain the important dependencies, while simplifying enough to allow for numerical tractability.

Radiation heat transfer models are primarily distinguished by the rigor with which the spectral dependence of the radiative properties is treated. Another distinction is the treatment of the directional dependence. The radiation heat transfer equation is typically posed in a form to express most conveniently and accurately the spectral dependencies. The following discussion addresses the treatment methods used in this study, as well as the methods of Appendix 4, in contrast to refinements used here. Bedir et al. [1996] and Bedir [1998] provide thorough discussions and comparisons of these models, as well as other types of radiation models as applied to diffusion flames.

Spectral Dependence: The simplest models use the gray gas assumption [Seigel and Howell 1981] wherein the radiative properties of the gas are spectrally independent. In these models, the radiation intensity, I, is attenuated from the black-body radiation intensity over direction, s, by a spectrally independent absorption coefficient, κ:

$$\frac{dI}{ds} = \kappa(I_b - I)$$

and the derivative of the net radiative heat flux is given by:

$$\frac{dq}{dx} = \frac{d}{dx}\int_{4\pi} \mu I d\Omega$$

where μ is the direction cosine, and Ω is the solid angle.

The selection of the gray gas absorption coefficient κ for gases that are inherently spectrally dependent is a difficult task. In many flame analyses, Planck mean absorption coefficient, κ_p, is used. The Planck mean absorption coefficient is given as a continuous function of the temperature and partial pressure of the gas. In Appendix 4, we use the Planck mean absorption coefficients for CO_2 and H_2O. Using the Planck mean absorption coefficient, solving the radiative transfer equation is relatively simple. But, as pointed out earlier, in the cases where flame radiation is important, the flame is normally not optically thin, thus using the Planck mean absorption coefficient introduces quantitative inaccuracy.

In the following work, we have chosen to use the most accurate radiation model that is now computationally tractable in a problem of this type. The narrowband model is used to replicate the spectral properties of the participating gases. Indeed, the narrowband model is typically used as the benchmark with which to compare the accuracy of other radiation transfer equation approximations.

Real gases absorb and emit in discrete intervals and quantities across the radiation spectra. These irregular patterns are a result of transitions in energy states of the gas molecules in the presence of radiative energy, or photons. Emission represents a release of photons, while absorption represents the capture of a photon. Since this process occurs in discrete energy transitions, or quanta, at fixed frequencies, the emissive and absorptive properties of a gas appear as lines at discrete intervals across a frequency spectra. Several phenomena contribute to the 'broadening' of these lines into 'bands,' so that photons are absorbed or emitted over ranges of frequencies. If the bands are sufficiently narrow, the black-body radiation intensity, I_{bv}, can be taken out of the integral, because it does not vary much over the bandwidth, Δv_i:

$$\int_{\Delta v_i} \kappa_v I_{vb}(T) dv = I_{bi}(T) \int_{\Delta v_i} \kappa_v dv$$

where i is the band index, in this instance. If the bandwidth is broad, a number of sufficiently narrow bands can be used. The narrowband model is thus a numerically convenient representation of the spectral absorption and emission bands of the molecular gas.

This model is described in detail in Bedir [1998] and is summarized here. We include collision broadening here as the primary broadening effect of significance at atmospheric pressure and the temperature range of interest (infrared) [Seigel and Howell 1981]. Collision broadening is the result of changes of energy state of the molecules because of increased collisions as the density or pressure of the gas increases. Collisions can occur with molecules of the same gas (self-broadening) or with other constituent gas molecules. Doppler broadening is also included in the model [Shih et al. 1999], since it can also be significant in the infrared region [Ozisik 1973]. Doppler broadening is a result of the thermal motion of the radiating gas molecules, and contributes to the broadening of the line at high temperatures and/or low pressures.

The statistical narrowband model is used for the assumed band spacing of the spectra. The statistical model allows for nonuniform spacing and height of the spectral absorption coefficient bands through assumption of probability distributions of line strengths and positions.

Here we choose to use CO_2, H_2O, and CO as the radiatively participating species. These gases are well known to be the dominant radiative contributors in hydrocarbon flames. No narrowband radiation data is available on the gas-phase trioxane fuel vapor, or its decomposition product, formaldehyde. We have assumed these gases to be negligible absorbers, but this should be evaluated in the future. A number of studies have included the radiative effects of fuel vapor, including Kashiwagi [1979] and Bedir [1998]. The hydrocarbon fuels examined have not been found to be dominant contributors to radiative loss, but they do have an effect.

The narrowband model requires a database composed of the reciprocal mean line spacing parameter ($1/\delta_\nu$) and the mean absorption coefficient, κ_ν, for each spectral band over the spectrum at different temperatures. While line-by-line data are available for the gases of interest here, it is not yet numerically tractable in a solution of this type. The narrowband data used here for CO, CO_2 and H_2O are correlated with the line-by-line HITRAN'92 database [Rothman et al. 1992]. The temperature and spectral ranges are 300-2900 K and 150-9300 cm^{-1}, with a spectral bandwidth of 25 cm^{-1}. It has been demonstrated [Soufiani et al. 1985, Soufiani and Taine 1989] that the statistical narrowband model with an exponential tailed inverse line strength distribution used here [Malkmus 1967] is in excellent agreement with the line-by-line calculations of Soufiani and Taine [1997] for CO_2 and H_2O.

The model is posed in terms of transmittance, rather than absorptance. This yields the most accurate representation for the data because the translation to intensity involves several assumptions that can lead to inaccuracies [Bedir 1998]. The transmittance of a gas volume is defined as the fraction of the incident energy that passes through the gas volume. In the absence of reflection and scattering, then the transmitted energy along a path is the incident energy minus the absorbed energy. The average transmittance of an isothermal and homogeneous gas over path length $(s'-s)$ of a molar fraction X_k and total pressure p is given as [Bedir 1998]:

$$\tau_{\nu,k}(s' \to s) = \exp\left[-\frac{\beta_\nu}{\pi}\left(\sqrt{1+\frac{2\pi u \kappa_\nu}{\beta_\nu}}-1\right)\right]$$

where $\beta_\nu = 2\pi\gamma_\nu / \delta_\nu$ is the mean line width to spacing ratio inside the spectral range (band), $\Delta\nu$, γ_ν is the line half-width, and the pressure path length is $u = X_k p|s' \to s|$. The Curtis Godson approximation [Godson 1953] is used to extend the above to non-isothermal, nonhomogeneous media. This approximation assumes the transmittance of a non-isothermal, nonhomogeneous medium is that of an equivalent isothermal and homogeneous medium. Here the subscript e refers to the equivalent band parameters, and the following quantities are used in the transmittance equation:

$$u(s' \to s) = \int_{s'}^{s} pX_k \, ds''$$

$$\kappa_{\nu,e}(s' \to s) = \frac{1}{u} \int_{s'}^{s} pX_k \kappa_\nu \, ds''$$

$$\beta_{\nu,e}(s' \to s) = \frac{1}{u\kappa_{\nu,e}} \int_{s'}^{s} pX_k \kappa_\nu \beta_\nu \, ds''$$

The transmittance of a mixture of gases is the product of the individual gas transmittances:

$$\prod_k \tau_k$$

Then the radiative transfer equation, written in terms of transmittance over a narrowband, for an absorbing, emitting, non-gray medium is [Bedir 1998]:

$$\begin{aligned} \frac{\partial I_\nu(s,\Omega)}{ds} &= \left(\frac{\partial \tau_\nu (s' \to s)}{\partial s'} \right)_{s'=s} I_{b\nu}(s) + I_{w\nu}(s_w, \Omega) \frac{\partial \tau_\nu (s_w \to s)}{\partial s} \\ &+ \int_{s_w}^{s} \frac{\partial}{\partial s} \left(\frac{\partial \tau_\nu (s' \to s)}{\partial s} \right) I_{b\nu}(s') ds' \end{aligned} \qquad \textbf{(3-5)}$$

where the subscript w refers to the mean wall quantity, and Ω refers to the solid angle. The first term on the right side represents the local emission. The second and third terms represent the local absorption of surface emission and absorption of emission from the participating media along the line of sight. These two terms are neglected in the optically thin limit, where there is no appreciable absorption by the gas.

From the spectral intensity in equation (3-5), the derivative of the net radiative heat flux is found by integration over the solid angle and frequency:

$$\frac{dq}{dx} = \frac{d}{dx} \sum_{\Delta\nu} \left[\int_{4\pi} \mu I_\nu \, d\Omega \right] \Delta\nu \qquad \textbf{(3-6)}$$

Equation (3-6) is used in equation (3-1(e)) to solve the energy equation. Here $q = q_{net}$.

Scattering has been neglected in the formulation development. The only potential source of a scattering medium in a problem of this type would be soot formation. Trioxane burns with a clear or blue flame in standard air, indicating soot is not generated in significant quantities to affect the radiation heat transfer. Moreover, our focus is at the extinction limits, where the temperatures are below the threshold for soot formation and soot is not observed [Grayson et al. 1994, Olson 1997]. For these reasons, the effects of soot radiation have been neglected in this analysis.

Directional Dependence: The two-flux model used in Appendix 4 is among the simplest of the radiation models because the radiation intensity is isotropic (independent of position and direction) in the two flux directions. That is, the intensity is isotropic in the positive direction and the negative direction, but not the same value. Directional dependence can be improved by using the discrete ordinates method, wherein the angular variation of radiation intensity is modeled over discrete intervals, or ordinates. The two-flux model in essence uses two ordinates. Increasing the number of ordinates gives increased accuracy; however, selecting the appropriate ordinates and applying weighting (by Gaussian distribution or other means) are important features of the discrete ordinates method. Since the radiative transfer equation is solved for each ordinate, increasing the number of ordinates also increases computational complexity (solution time and storage requirements). Specifics of the numerical process for the discrete ordinates method are described in Section 5.

4.0 Kinetics and Properties of the Solid Fuel

4.1 The Solid Fuel

Criteria for Selection of Fuel: The criteria for fuel selection included the following: the fuel is solid at room temperature; the decomposition kinetics are known; the thermodynamic properties are known; and the combustion of the fuel has practical application. For these reasons, we have selected 1,3,5-trioxane as the fuel to be modeled.

Characteristics of Trioxane: Trioxane is classified as a cyclic trimer of formaldehyde [Kirk-Othmer Encyclopedia, Handbook of Thermoplastics 1997]. It is also known as s-trioxane, 1,3,5-trioxane, 1,3,5-trioxacyclohexane or trioxymethylene [Handbook of Thermoplastics 1997]. Trioxane is a colorless, crystalline, flammable solid that sublimes readily. It decomposes directly and exclusively to formaldehyde [Kirk-Othmer Encyclopedia, Handbook of Thermoplastics 1997, Melia et al. 1967, Hochgreb and Dryer[1] 1992]. The kinetics of trioxane decomposition to formaldehyde are known [Hochgreb and Dryer[1] 1992, Irdam and Kiefer 1990], as are the kinetics of the subsequent formaldehyde oxidation [Hochgreb and Dryer[2] 1992, Hochgreb et al. 1990, Hochgreb 1991]. The thermodynamic properties of trioxane have been reported by Melia et al. [1967], among others. Trioxane is a very stable solid fuel and has an almost infinite shelf life. It burns steadily with a hot, smokeless blue flame. The military uses it in bar form as a meal warmer and campers and hikers use it as a fuel source, particularly in cold and wet weather. It is advertised for use to warm hands and food, and to start a fire in windy conditions or with rain-wet wood. Industrially, it is used to form acetyl resins, which are polymers of formaldehyde [Kirk-Othmer Encyclopedia]. The physical properties of trioxane are listed in Table 4-1 and the molecular structure is sketched below.

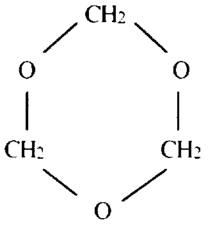

Since the kinetics of formaldehyde oxidation are fairly well understood, any of the acetyl resins that are polymers of formaldehyde and that decompose from the solid, such as Delrin or Celcon, could be analyzed in a similar manner, given the Arrhenius law for the decomposition of these solids and their thermodynamic properties.

Table 4-1: Physical Properties of Trioxane

Quantity*	Value
Molecular formula	$C_3H_6O_3$
Molecular weight	90.08 g/mole
Melting point	336 K
Boiling point	388 K
Heat of formation	-465 kJ/mol
Heat of fusion	15.1 kJ/mol
Heat of sublimation	55.6 kJ/mol (6.17E09 erg/g)
Specific gravity at 65°C (molten)	1.17
Specific heat (solid) @298 K Specific heat (gas) @298 K	113.1 J/mol-K (1.255E07 erg/g-K) 81.88+/-3.50 J/mol-K

* [Melia et al. 1967, NIST Chemistry Web book]

4.2 Kinetics of Trioxane

Trioxane decomposition to formaldehyde is homogeneous and first order. It boils (at 115°C) without decomposition. Pure trioxane shows no appreciable depolymerization below 250°C (523 K) in the absence of a decomposition catalyst [Kirk-Othmer Encyclopedia]. Formaldehyde is the sole product of the decomposition of trioxane and this dissociation is well separated from that of its product [Hochgreb and Dryer[1] 1992, Irdam and Kiefer 1990]. The overall reaction for the decomposition is:

$$C_3H_6O_3 \rightarrow 3CH_2O \qquad (1)$$

Hochgreb and Dryer[1] [1992] give the reaction rate for the unimolecular decomposition of trioxane between 700 and 800 K (step 1 of Table 4-2). This reaction rate was validated against data gathered from a larger temperature range (545 to 1270 K) and found to be most accurate in the low to mid range of the temperature distribution. Here, the model is constructed such that the solid trioxane vaporizes upon heating and then decomposes directly to gaseous formaldehyde. Since the dissociation of trioxane is well separated from that of formaldehyde, the solutions to follow are not sensitive to reaction 1. The formaldehyde burns in air at atmospheric pressure via the decomposition kinetics described below.

4.3 Kinetics Model and Validation

We evaluated three models for the decomposition of formaldehyde against available data over a range from fuel-rich to fuel-lean in order to determine the most appropriate model for use with the diffusion flame. Hochgreb and Dryer[2] [1992] provide a mechanism in a 1992 publication as well as a set of data on formaldehyde oxidation. The GRI database [Smith et al.] contains a more recent mechanism (releases 1.2 and 3.0) optimized for comprehensive description of natural gas combustion. Both of the GRI mechanisms are modified to include trioxane decomposition, and exclude the nitrogen chemistry. Nitrogen is modeled as a nonreacting third body. Since experimental data are provided in Hochgreb and Dryer[2] [1992], the three mechanisms are evaluated against these data. The following section contains a description of the validation process and a discussion of the important reactions in the selected model.

Hochgreb et al. [Hochgreb and Dryer[2] 1992, Hochgreb et al. 1990, Hochgreb 1991] studied the oxidation of formaldehyde and published the complete reaction mechanism (steps 2 through 38 in Table 4-2). Their mechanism is based on a complete review of previously published experimental data, as well as the addition of original experimental data to complete the range of temperatures tested. The experiments used trioxane as the source of formaldehyde. Trioxane was melted, vaporized, and decomposed directly to formaldehyde and forced through a flow reactor at atmospheric pressure, with N as the diluent. In the kinetics analysis, the $CO/H_2/O_2$ set was extracted from Yetter and Dryer's comprehensive reaction mechanism [1991], and the HCO reactions come from the review by Tsang and Hampson [1986] and work by Timonen et al. [Timonen et al.[1] 1987, Timonen et al.[2] 1987, Timonen et al. 1988]. The CH_2O reactions are a combination of previous work [Tsang and Hampson 1986, Roth and Just 1984] and new mechanisms supported by the experiments. Hippler et al. [1990] give a reaction mechanism for HO_2+HO_2 based on a high and low temperature range, which is used here. The original paper gives uncertainty factors for each reaction, which range from 1.5 to 4. Appendix 1 contains the CHEMKIN input file (rate constants) for the complete reaction mechanism, along with complete notations of data sources and uncertainty factors.

Model Validation: Hochgreb's kinetic mechanism is compared to the formaldehyde subset of the 1.2 release of the GRI oxidation kinetics in a perfectly stirred reactor model (PSR) [Glarborg et al. 1986]. PSR is a program that predicts temperature and species composition for a given system residence time in a perfectly stirred reactor. It is useful in comparing kinetic mechanisms, because flow field effects are eliminated by the 'perfectly stirred' supposition, where mixing rates are infinitely fast.

The GRI mechanism and Hochgreb's mechanism compare poorly [Sung et al. 1999], especially the critical residence time and temperature leading to extinction. We communicated with Ms. Hochgreb [Hochgreb 1999], who noted that the original paper contained a typographical error in the crucial $H+O_2 \rightarrow OH+O$ reaction of three orders of magnitude in the pre-exponential term. The correction appears here in Table 4-2 (and Appendix 1).

We validated the corrected formaldehyde reaction mechanism against the data in Hochgreb [1991] in order to demonstrate reproducibility. We used the data from Hochgreb's thesis as opposed to the data in the paper [Hochgreb and Dryer[2] 1992] because the paper contains numerous typographical errors. We then compared these to the modified GRI 1.2 model for the formaldehyde subset of reactions (using the constituents of formaldehyde oxidation given by Hochgreb [1991]) with the SENKIN code [Lutz et al. 1988] to select the most appropriate model for the diffusion flame study. Figures 4-1 through 4-8 show the comparison of Hochgreb's mechanism, the GRI 1.2 mechanism, and the flow reactor data for the oxidation of formaldehyde from Hochgreb [1991] over a range of equivalence ratios and temperatures. In each of the figures, Hochgreb's mechanism is shown by dotted lines, the GRI mechanism by solid lines, and the data from Hochgreb [1991] as data points. Adapting Hochgreb's approach, all three plotted data sets have been matched via time-offset calculation at 50% formaldehyde consumption. The reader may note that this matching appears to work better 'upstream' rather than 'downstream.' We believe this is due to the authors' emphasis on fuel decomposition, rather than product formation.

The data in Figures 4-1 through 4-8 show that the GRI 1.2 and Hochgreb's mechanisms compare relatively well to the experimental data for fuel-lean flames. For the fuel-rich condition (Figures 4-3, 4-6, and 4-8), Hochgreb's mechanism is a better predictor of the kinetics. Only for the high-temperature, very fuel-lean case (Figure 4-7) could a case be made that the GRI mechanism is slightly more accurate. Since the diffusion flame contains both fuel-rich and fuel-lean regions, Hochgreb's mechanism is the better model for our study.

The GRI mechanism has been recently updated with the 3.0 release. We compared the formaldehyde portion of the GRI 3.0 release to Hochgreb's mechanism to see if the predictions in the fuel-rich region had been improved over the GRI 1.2 release. Figure 4-9 shows these results. The Hochgreb mechanism remains a better predictor than the GRI 3.0 mechanism in the fuel-rich region. For these reasons, Hochgreb's mechanism [Hochgreb and Dryer[2] 1992, Hochgreb 1991] is used in this study.

Important Reactions: The original paper [Hochgreb and Dryer[2] 1992] gives a discussion of the important reactions, which is summarized below. The important reactions are described in terms of a high temperature path and a low temperature path. There is an additional distinction between fuel-lean and fuel-rich mechanisms.

It is important to note that Hochgreb's model and experiments were conducted using a homogeneous system, evaluated at constant temperature and fuel equivalence ratio. The following summary applies to this system. It is compared to the heterogeneous diffusion flame system of interest in this work, in later sections.

Below 1100 K, the formaldehyde is attacked primarily by OH and H. While the reaction rate of HO_2 with the formaldehyde is relatively slow, this reaction indirectly controls the reaction progress because it produces HCO, which in turn is responsible for production of H and OH. HO_2 is the main chain carrier in this temperature range. Thus the most important reactions in the low temperature range are:

$CH_2O+H \text{ (or } OH) \rightarrow HCO+H_2 \text{ (or } H_2O)$ (5) or (7)
$HCO+O_2 \rightarrow CO+HO_2$ (10)
$CH_2O+HO_2 \rightarrow HCO+H_2O_2$ (8)
$H_2O_2+M \rightarrow OH+OH+M$ (35)

Note that the equation numbers are consistent with Table 4-2. As the temperature increases beyond 1100 K, less HO_2 is produced, and the thermal decomposition of formyl, $HCO+M \rightarrow H+CO+M$ (reaction 9) becomes faster than that of (10). Thus, the rate of production of H is determined from the competition between (9) and (10) in lean flames. At the higher temperatures, the branching route, $H+O_2 \rightarrow O+OH$, reaction (20), surpasses reaction (35) as the main branching path. So that the important reactions for the high temperature range are:

CH_2O+H (or OH)$\rightarrow HCO+H_2$ (or H_2O) (5) or (7)
$HCO+M \rightarrow CO+H+M$ (9)
$H+O_2 \rightarrow OH+O$ (20)

Hochgreb found the rate of formaldehyde consumption below 1100 K for fuel-rich cases to be particularly sensitive to the concentration of O_2. In the presence of oxygen, the formaldehyde is consumed in a branching mechanism, rather than a straight chain, allowing multiple pathways for radical attack of the formaldehyde. The controlling reactions governing the straight-chain and branching mechanisms are outlined as follows:

Straight-chain:

$CH_2O+H \rightarrow HCO+H_2$ (5)
$HCO+M \rightarrow H+CO+M$ (9)

Branching:

$CH_2O+H \rightarrow HCO+H_2$ (5)
$HCO+M \rightarrow H+CO+M$ (9)
$HCO+O_2 \rightarrow CO+HO_2$ (10)
$CH_2O+HO_2 \rightarrow HCO+H_2O_2$ (8)
$H_2O_2+M \rightarrow OH+OH+M$ (36)

Since we are interested here in a diffusion flame burning in standard air, we expect to observe this effect in the fuel-rich, lower-temperature regions of the flame; that is, between the flame and the solid surface. The region between the flame and the surface contains less oxygen, and is therefore a fuel-rich region, while the outer edge of the flame, while low in temperature, is lean.

In Appendix 4, we demonstrated that the maximum flame temperature has a non-monotonic variation with stretch rate, and that the maximum flame temperature near the radiative extinction limit is much lower than that of the blow-off limit. Hence, we anticipate that, for the radiative flame here, the dominant reactions over the low and high stretch rates follow Hochgreb and Dryer's[2] [1992] low- and high-temperature mechanisms, respectively.

We further note that the sensitivity to O_2 concentrations limits the experimental accuracy in Hochgreb and Dryer[2] [1992] because background concentrations were present from air leaks into the experimental apparatus. There is also a large discrepancy between observed and predicted results in the very fuel-rich region. The paper does not recommend any mechanism changes to alleviate the discrepancy because of the many possible explanations for the differences.

Other Considerations: For the purposes of this study, we assume trioxane burns in air and include the N molecule as a nonreacting third body. In reality, small quantities of intermediate NO_x species would be formed in the combustion. This study is not focused on the formation of NO_x species, nor is the formation of these species expected to change the results, especially the global burning rate and extinction limits. Therefore, the N chemistry is neglected in the kinetics.

Table 4-2: Reaction Mechanism for Solid Trioxane Combustion

Rxn #	Reactions Considered; $k=AT^{b}\exp(-E/RT)$	A	b	E
1	C3H6O3=>3CH2O	1.90E+15	0.0	47,500
2	CH2O+M=HCO+H+M	4.21E+23	-1.7	92,170
3	CH2O+M=H2+CO+M	8.25E+15	0.0	69,540
4	CH2O+O2=HCO+HO2	2.05E+13	0.0	38,920
5	CH2O+H=HCO+H2	5.18E+07	1.7	1,834
6	CH2O+O=HCO+OH	1.81E+13	0.0	3,078
7	CH2O+OH=HCO+H2O	3.43E+09	1.2	-447
8	CH2O+HO2=HCO+H2O2	1.47E+13	0.0	15,200
9	HCO+M=H+CO+M (1)	1.85E+17	-1.0	17,000
10	HCO+O2=CO+HO2	4.22E+12	0.0	0
11	HCO+H=CO+H2	7.23E+13	0.0	0
12	HCO+O=CO+OH	3.00E+13	0.0	0
13	HCO+O=CO2+H	3.00E+13	0.0	0
14	HCO+OH=CO+H2O	3.00E+13	0.0	0
15	HCO+HO2=CO2+OH+H	3.00E+13	0.0	0
16	CO+OH=CO2+H	9.29E+03	2.2	-2,625
17	CO+HO2=CO2+OH	6.63E+13	0.0	22,950
18	CO+O+M=CO2+M (2)	4.00E+13	0.0	-4,540
19	CO+O2=CO2+O	2.53E+12	0.0	47,690
20	H+O2=OH+O	3.52E+16	-0.7	17,070
21	H2+O=OH+H	5.08E+04	2.7	6,292
22	OH+OH=H2O+O	2.88E+00	3.7	-4,313
23	OH+H2=H2O+H	2.16E+08	1.5	3,430
24	H2O2+OH=H2O+HO2	7.00E+12	0.0	1,430
25	H2O2+H=H2O+OH	1.00E+13	0.0	3,590
26	HO2+HO2=H2O2+O2 (3)	4.20E+14	0.0	11,980
27	HO2+HO2=H2O2+O2 (3)	1.30E+11	0.0	-1,629
28	H+HO2=OH+OH	1.69E+14	0.0	874
29	H+HO2=H2+O2	6.63E+13	0.0	2,126
30	HO2+OH=H2O+O2	1.45E+16	-1.0	0
31	HO2+O=O2+OH	1.81E+13	0.0	-397
32	H2O2+H=H2+HO2	4.82E+13	0.0	7,948
33	O+O+M=O2+M (2)	6.17E+15	-0.5	0
34	H2+M=H+H+M (2)	4.58E+19	-1.4	104,400
35	H+OH+M=H2O+M (2)	2.25E+22	-2.0	0
36	H2O2+M=OH+OH+M (2)	1.20E+17	0.0	45,500
37	O+H+M=OH+M (2)	4.72E+18	-1.0	0
38	H+O2+M=HO2+M (2)	2.00E+15	0.0	-1,000

Rate constants listed are for the forward reaction. Units: mole, cm^3, s, cal.

(1) CO enhanced by 1.9, CO$_2$ enhanced by 1.9, H$_2$O enhanced by 16, and H$_2$ enhanced by 1.89.

(2) CO enhanced by 1.9, CO$_2$ enhanced by 1.9, H$_2$O enhanced by 16, and H$_2$ enhanced by 2.5.

(3) duplicate reaction.

Reaction (1) from [Hochgreb and Dryer[1] 1992]; Reactions 2-38 from [Hochgreb and Dryer[2] 1992]

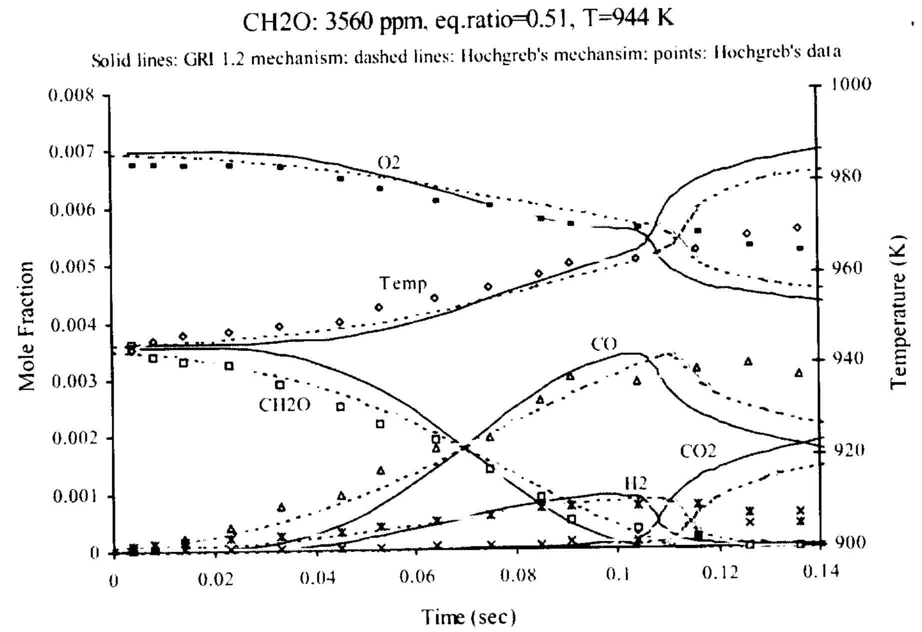

CH2O: 3560 ppm, eq.ratio=0.51, T=944 K

Solid lines: GRI 1.2 mechanism; dashed lines: Hochgreb's mechansim; points: Hochgreb's data

Figure 4-1: Comparison of kinetics mechanisms (Hochgreb vs. GRI 1.2) with experiments for 3560 ppm CH_2O, equivalence ratio=0.51, and flow reactor temperature T_{FR}=944 K.

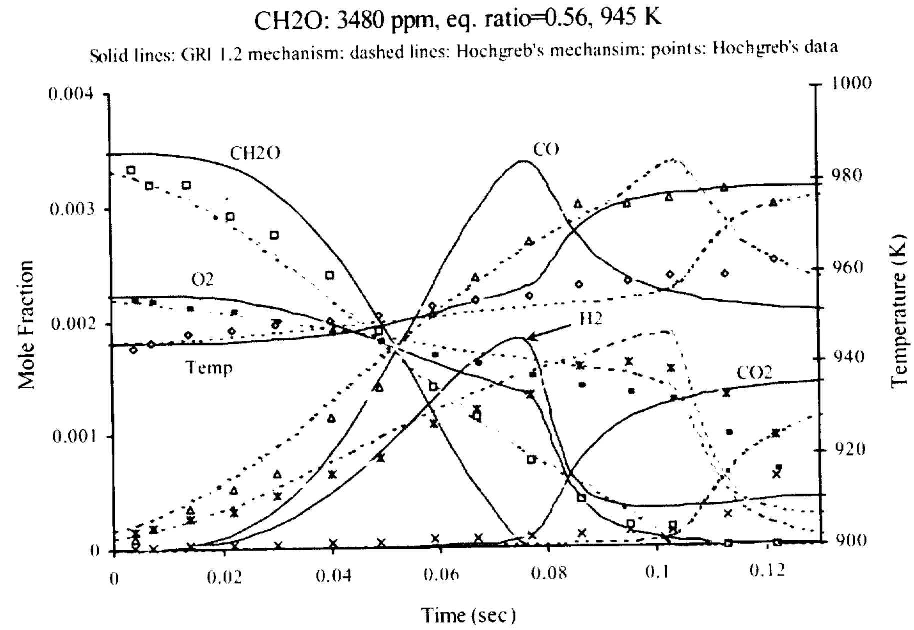

CH2O: 3480 ppm, eq. ratio=0.56, 945 K

Solid lines: GRI 1.2 mechanism; dashed lines: Hochgreb's mechansim; points: Hochgreb's data

Figure 4-2: Comparison of kinetics mechanisms (Hochgreb vs. GRI 1.2) with Experiments for 3480 ppm CH_2O, equivalence ratio=0.56, and flow reactor temperature T_{FR}=945 K.

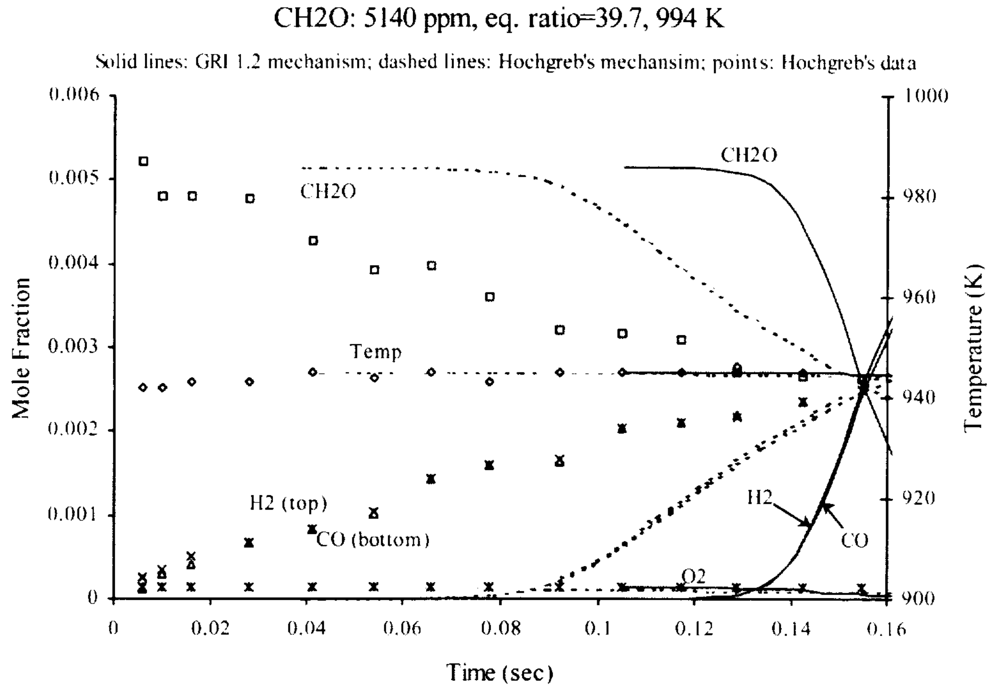
CH2O: 5140 ppm, eq. ratio=39.7, 994 K

Solid lines: GRI 1.2 mechanism; dashed lines: Hochgreb's mechansim; points: Hochgreb's data

Figure 4-3: Comparison of kinetics mechanisms (Hochgreb vs. GRI 1.2) with experiments for 5140 ppm CH_2O, equivalence ratio=39.7, and flow reactor temperature T_{FR}=994 K.

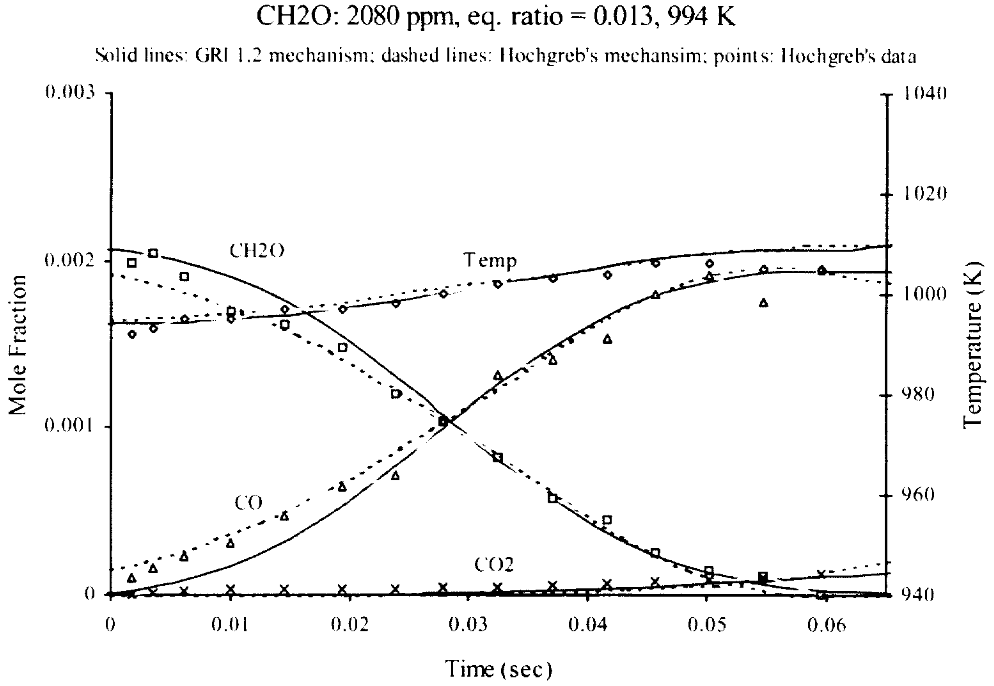
CH2O: 2080 ppm, eq. ratio = 0.013, 994 K

Solid lines: GRI 1.2 mechanism; dashed lines: Hochgreb's mechansim; points: Hochgreb's data

Figure 4-4: Comparison of kinetics mechanisms (Hochgreb vs. GRI 1.2) with experiments for 2080 ppm CH_2O, equivalence ratio=0.013, and flow reactor temperature T_{FR}=994 K.

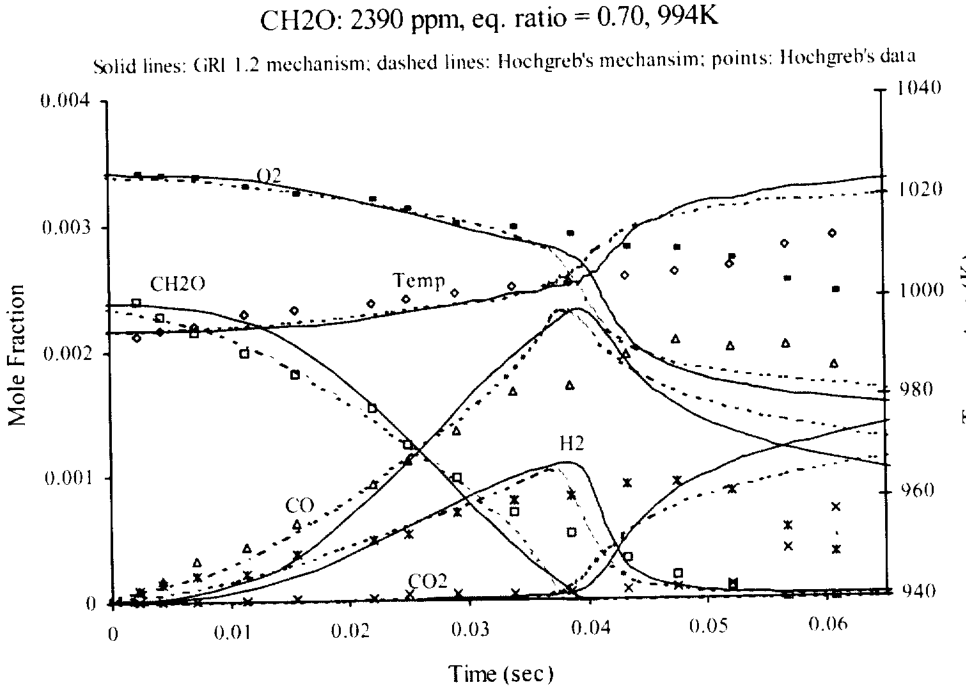

Figure 4-5: Comparison of kinetics mechanisms (Hochgreb vs. GRI 1.2) with experiments for 2390 ppm CH_2O, equivalence ratio=0.70, and flow reactor temperature T_{FR}=994 K.

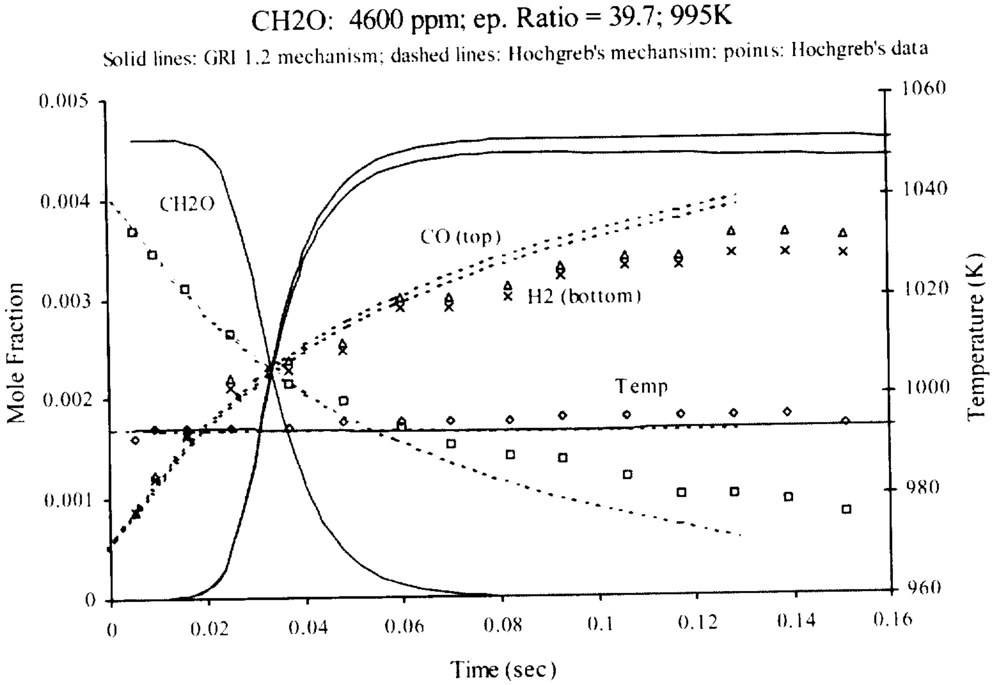

Figure 4-6: Comparison of kinetics mechanisms (Hochgreb vs. GRI 1.2) with experiments for 4600 ppm CH_2O, equivalence ratio=39.7, and flow reactor temperature T_{FR}=995 K.

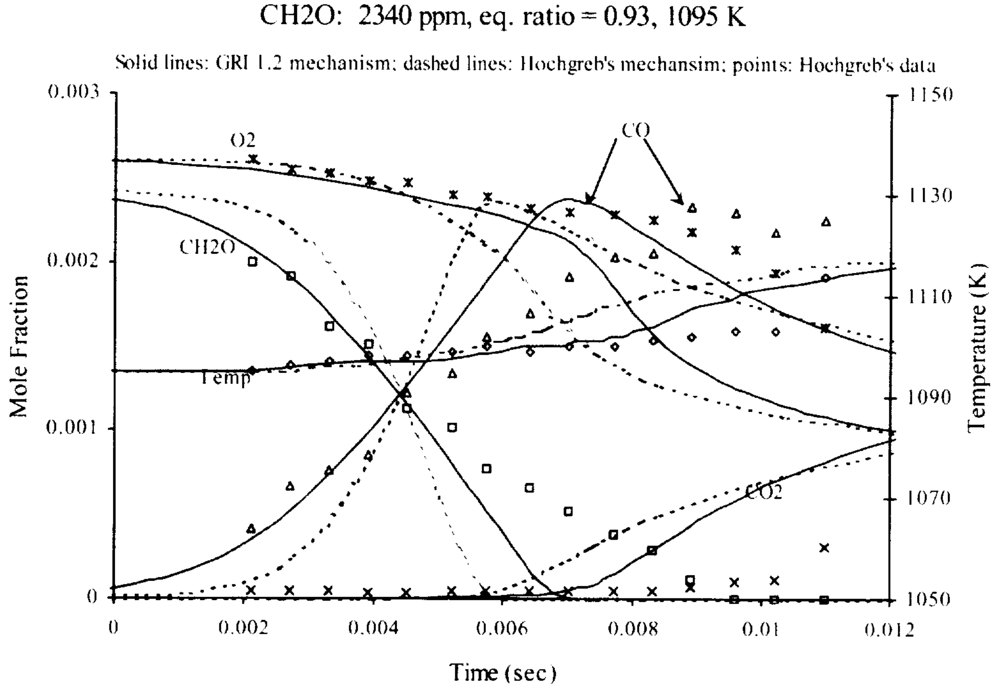

Figure 4-7: Comparison of kinetics mechanisms (Hochgreb vs. GRI 1.2) with experiments for 2340 ppm CH_2O, equivalence ratio=0.93, and flow reactor temperature T_{FR}=1095 K.

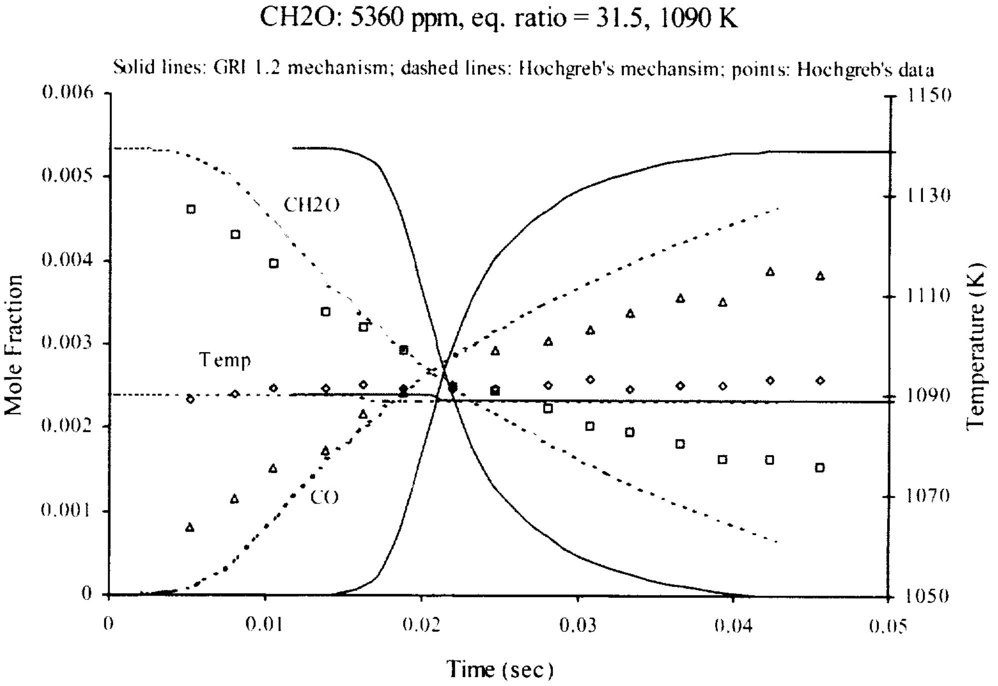

Figure 4-8: Comparison of kinetics mechanisms (Hochgreb vs. GRI 1.2) with experiments for 5360 ppm CH_2O, equivalence ratio=31.5, and flow reactor temperature T_{FR}=1090 K.

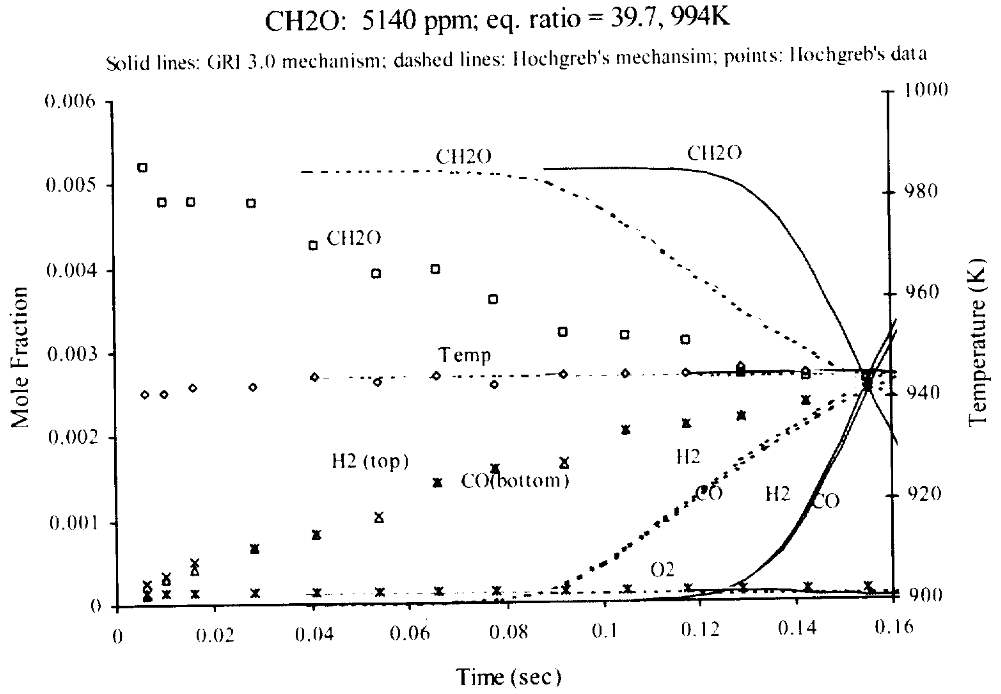

Figure 4-9: Comparison of kinetics mechanisms (Hochgreb vs. GRI 3.0) with experiments for 5140 ppm CH_2O, equivalence ratio=39.7, and flow reactor temperature T_{FR}=994 K.

4.4 Thermophysical Properties

Thermodynamic Data: CHEMKIN II [Kee et al. 1989] is the source for the thermodynamic data, with the following exceptions. Trioxane is not contained in the CHEMKIN II database, so thermodynamic data were obtained from Lay et al. [1997] and formatted using the THERM program package [Ritter and Bozelli 1987] into the NASA Gordon-McBride format. HO_2 thermodynamic data was specified on the input file using the data from Hills and Howard [1984] (Appendix 1).

Transport Properties: The OPPDIF [Lutz et al. 1996] package uses TRAN [Kee et al. 1986], which evaluates gas-phase transport properties using a polynomial fit to the temperature-dependent part of the transport property. The pure species properties are calculated from molecular collision data, including the dipole moment, the rotational relaxation collision parameter, the polarizability, the Lennard-Jones potential well depth, and the Lennard-Jones collision diameter. We added the known properties for trioxane (Table 4-3) to the TRAN [Kee et al. 1986] database for multicomponent evaluation of gas-phase viscosities, thermal conductivities, diffusion coefficients, and thermal diffusion coefficients. Polarizability and rotational relaxation data were not available for trioxane. We show these estimated parameters with the given rationale in Appendix 2.

The rotational relaxation collision parameter, Z_{rot}, for trioxane is here estimated to be 1.0. The quantity Z_{rot} is a measure of the number of collisions needed to establish rotational equilibrium of a molecule. Thermal conductivity is a weak function of the rotational relaxation collision parameter.

Trioxane concentration is highest near the surface, where it is rapidly decomposing to formaldehyde during burning. Thus, the effect of these assumptions being in error would be seen very near the surface and at relatively low temperatures (compared to the flame).

We estimate polarizability for trioxane to be 0.237 cubic Angstroms (see Appendix 2), using the method described by Hirschfelder et al. [1954]. The polarizability of the polar molecule affects diffusion coefficients between polar and nonpolar molecules. Transport properties of all other constituent gases were available from the existing database [Kee et al. 1986].

Surface Temperature: The Arrhenius law for the solid decomposition of trioxane is not known. If it were, we could estimate the surface temperature from this law, as shown in Appendix 4. Since this datum is not available, we estimate the surface temperature of the burning trioxane by using the boiling point of trioxane (Table 4-1) and keeping it as a constant.

Table 4-3: Thermophysical Properties of Trioxane

Quantity	Value
Lennard-Jones potential well depth, K	500
Lennard-Jones collision diameter, Angstrom	6.093
Dielectric Constant, (molten trioxane) Dielectric Constant, (solid trioxane)	8 3.2
Dipole moment, Debye (10^{-18}cm$^{3/2}$ erg$^{1/2}$)	2.18
Polarizability (estimated), Angstrom^3	0.237
Rotational relaxation collision number (estimated)	1.0

[Hochgreb and Dryer[1] 1992, Walker and Carlisle 1943, Maryott and Acree 1944]
See Appendix 3 for details on estimated quantities.

4.5 Radiative Properties

Participating Gases: The narrowband properties of CO, CO_2, and H_2O are taken from Soufiani and Taine [1997]. All other gases involved in the combustion do not contribute as participating media, either because they are not produced in sufficient quantity, or because they do not absorb or emit a significant amount of thermal radiation in the temperature range (spectra) of interest. As discussed in Section 3.4, soot is neglected.

5.0 Numerical Method

We used the set of computer codes developed at the Sandia National Laboratory for analyses of various problems that rely on solution of detailed kinetics models, and modified them as necessary to solve for the solid trioxane flame (OPPDIF, PSR, SENKIN, PREMIX). All of these codes rely on three core code packages: a chemical kinetics package (CHEMKIN II), a transport property package (TRAN), and a solver package that solves the boundary value problem (TWOPNT). This section contains a brief description of the code packages used, how they are modified, and the numerical techniques used to obtain the solutions.

The OPPDIF Program: Lutz et al. [1996] developed a computer program, called OPPDIF, to solve the system of differential equations posed by opposed jet diffusion flames. The governing equations outlined in Section 3 are solved by OPPDIF, modified to accommodate the solid surface boundary conditions described in Section 3. OPPDIF is formulated to solve the opposed jet problem using the constant velocity formulation described in Lutz et al. [1998], and summarized in Section 3. It solves the governing equations beginning with a coarse grid, and adds grid points along steep gradients or steep gradient derivatives, yielding a nonuniform mesh. New grid points are added until the solution is resolved with sufficient accuracy. The governing equations are discretized by finite difference, adjusting for the nonuniform grid. The diffusive terms in the energy and species equations are discretized using a second-order central difference; the convective terms are discretized using an upwind difference, to avoid artificial oscillations in the solution. The solution is first found using a given initial temperature profile (without solving the energy equation). This solution is then used as a starting point when the energy equation is added. The program creates a 'restart' file from the solution obtained from 'scratch,' so that all subsequent solutions can be started from the restart file. Both phases of solution use the two-point boundary value problem solver describe below.

OPPDIF uses a chemical kinetics package of programs called CHEMKIN II [Kee et al. 1989] and a transport property package called TRAN [Kee et al. 1986]. The CHEMKIN input file is listed in Appendix 1. The input file contains forward rate constants for the reactions. Backward rate constants are calculated from the forward rate data and the equilibrium constants. In the analysis, we considered all steps to be forward and backward reactions, with the exception of the decomposition of trioxane. This step is assumed a forward reaction only. The transport package input is described in Section 4.

The program allows a diffusion velocity calculation based on either the mixture-averaged formulation or the multicomponent formulation. We use the mixture-averaged formulation throughout this study in order to increase computational efficiency.

OPPDIF uses a two-point boundary value solver called TWOPNT [Grcar 1992] to solve the stiff system of equations typically posed by inclusion of detailed kinetics. TWOPNT uses hybrid Newton/time marching solution procedure. A damped Newton's method is attempted first, using user-specified convergence tolerances for both absolute and relative convergence. If the damped Newton's method does not produce a suitable solution, TWOPNT initiates time marching, where the user specifies step size and number of time steps. Time-stepping is used to arrive at a better initial solution; then Newton's method is attempted again; and so forth until a solution is obtained or time marching limits are reached. Since Newton's method is fast but fails to converge if the initial solution is too far away, and time marching does not have convergence problems, but is slow; this hybrid solution technique takes advantage of the strengths of both methods, while avoiding the weaknesses.

The time-stepping feature of TWOPNT is suppressed for the purposes of this study, primarily because of the possibility for dynamic instability near extinction, as described below.

Flame Controlling Method: Once a solution at a single set of jet velocities is found using OPPDIF, a modified version of OPPDIF, CFDF, created to accelerate convergence, is used to find all subsequent solutions. CFDF adapts the flame controlling methods described in Nishioka et al. [1996]; here the stretch rate (a) and solid surface blowing rate (u_F), and oxidizer velocity (u_0), are solved uniquely for a user-specified fixed temperature at a fixed location. In this method, the temperature at a given location is used as an internal "boundary" condition, while the stretch rate a, and solid surface blowing rate u_F and oxidizer velocity (u_0) become the flame response. Then by incrementally changing the fixed temperature, we can obtain a continuous mapping of the flame response. This has the advantage of solving the flame structure near the extinction turning point with a relatively small amount of computational time. The CFDF program can solve the flame response by fixing a temperature on either side of the maximum flame temperature and moving in either direction with respect to the surface.

Starting Conditions: Starting conditions are set within a subroutine of OPPDIF, which can start from ether an initial 'guess' at the solution, or a restart from a previously converged solution. This subroutine is modified to accommodate the solid surface boundary conditions as described in Section 3 and only used to generate initial solutions (including the energy equation) on coarse grids. For this solution, an initial guess at the temperature profile is included in the input file. Once a coarse grid solution is found, the program is restarted from these solutions and refined to obtain solutions that are more accurate. The more accurate solution is then used as the restart file for the CFDF program.

Boundary Conditions: Fuel side boundary conditions as described in Section 3.0 are modified in the FUN subroutine of OPPDIF (and CFDF), which sets up the solution to the governing differential equations. A version of the program is generated for the sets of boundary conditions listed in Table 3-1 and the boundary conditions used in Section 7.0 (Table 7-2). Note however that the flame controlling method modifies the boundary conditions. A temperature at a fixed point is used as an internal "boundary" condition, and the oxidizer velocity is solved, rather than specified as a boundary condition.

Domain Size: The physical domain under study needs to be large enough to accommodate the relatively wide flame structures of the solutions that include the full radiation model as well as the movement of the flame relative to the surface as the stretch rate changes. In particular, the flame thickness roughly inversely scales with the square root of stretch rate. To take advantage of computational efficiency, we determine the domain size by solving the optically thin model, because it gives rapid solutions that can be scaled to predict a domain size acceptable for use with the more accurate (narrowband) radiation model. Optically thin models are formulated with the assumption that the gas does not attenuate the radiation intensity in the optically thin limit; that is, it emits, but does not absorb. (Also note that the Planck mean absorption coefficients employed herein were generated based on the HITRAN '92 database [Rothman et al. 1992] in the optically thin limit, which are different from those used in Appendix 4.)

The desired domain is large enough that the solution is independent of the domain (no end effects). The results of these solutions are scaled to the expected domain increase required for the narrowband solutions from previous studies using both models. Based on scaling of the optically thin solutions, we chose a domain size of l=20 cm (from surface to oxidizer jet) for the adiabatic solutions. For these adiabatic solutions, the domain easily accommodates both extremes of high and low stretch rates, where the flame resides near the surface (0.04 cm at the blow-off stretch rate) or outward from the surface (1.5 cm at low stretch rate of 2.5 s^{-1}). This 20-cm domain is also used for the narrowband radiation solutions and is verified to be large enough (solution farthest from the surface located at 6 cm).

The surface radiation solutions, however, require a larger domain. We used a domain size criterion to ensure that effects from the boundaries would not change the solution. The domain is extended so that the domain-to-flame thickness ratio is at least 2.0. The flame thickness is estimated using the 'full width at half maximum temperature' method, where the distance between the points on either side of the flame that equal half the maximum flame temperature is used as the measure of the flame thickness.

Additionally, we examine solutions for an adequate 'tail' for the temperature profile at the oxidizer side, to ensure that heat loss from the boundary does not affect the solution. For a domain of 25 cm, this criterion is met for all solutions. The maximum flame temperature location for all solutions ranges from a minimum distance of 0.04 cm from the surface (at blow-off extinction) to a maximum distance of 9.7 cm (at a stable solution stretch rate of 0.025 s^{-1}, i.e., the upper part of the solution isola).

For completeness, the domain sizes are noted on the figures and text in the discussion sections.

Radiation: The statistical narrowband solver [Bedir 1998] is coupled with the CFDF program to obtain the solutions with gas phase radiation. The non-gray narrowband radiative transfer equation is solved with the S8 discrete ordinates method, using a 20-direction Gaussian quadrature set. The surface is modeled as a perfect (black-body) radiator, with absorptivity and emissivity equal to 1.0, as described in Section 3.3. The adiabatic solution at a=100 s^{-1} is used as a starting point to obtain the narrowband solutions. The radiation solver takes much more computational time, so the radiation solver is not called at each Newton computation. The solver is called whenever the maximum change in temperature exceeds a user-supplied limit.

Grid Independence: A study was performed to find a grid distribution that produces a solution independent of grid size and point distribution, but is also manageable from a computational standpoint. Solving the narrowband radiation cases consumes a relatively large amount of CPU time, which is primarily dependent on grid size. The grid is initially generated using OPPDIF for the adiabatic case. The grid was refined sequentially for representative stretch rates over the full flammability range using CFDF.

The GRAD and CURV criteria are used for evaluation. These are criteria used in the two-point boundary value problem solver (TWOPNT). "GRAD" is defined as a bound upon the range of change of a component C at grid point J such that:

GRAD = (C (J) – C (J+1)) / (C(maximum) - C(minimum))

"CURV" is defined as a bound upon the range of change of a component's derivative D such that:

CURV = (D (J) – D (J+1)) / (D (maximum) – D (minimum))

For cases where GRAD and CURV are 0.4 or less, there is little to no change in key parameters such as stretch rate and maximum flame temperature, indicating that the solution is independent of the grid. This grid is then checked against the full range of adiabatic solutions by evaluating GRAD and CURV. The grid is manually refined where necessary until an acceptable grid is found using the two gridding parameters. Unlike some of the opposed flow solutions, where the flame location is maintained at a fixed location between the jets by a balance between the jet velocities (based on density ratios), the peak flame temperature moves across the domain based on stretch rate. At high stretch rates, the flame is pushed close to the surface, requiring grid refinement close to the surface. As stretch rate decreases, the flame moves away from the surface, requiring a fine grid at a distance from the surface as well. The resulting grid used for the adiabatic solutions contains 174 points for the computational domain of 20 cm.

The surface radiation solutions necessitate a finer grid because the flame moves much further from the surface in the low stretch regime. The technique described above is used with the same GRAD and CURV criteria to develop a grid with 256 points. Additionally, the domain is extended from 20 cm to 25 cm as described previously.

For the narrowband radiation solutions, the adiabatic solution with the174-point grid is used to begin and to find the high stretch rate solutions. The grid is refined manually for the low stretch rate solutions to optimize computational time; as the flame moved away from the surface, points are added in this location and removed near the surface, while maintaining acceptable gridding parameters (GRAD and CURV).

Steady-state analysis: One limitation in using the above method, particularly in the extinction regions, is that the analysis is steady state. It is well documented [Sohn et al. 2000, Deitrich et al. 2000] that dynamic instabilities may occur near the low-stretch extinction limit. Indeed, these instabilities may induce extinction. Under strong radiative heat loss, the reaction rate is lowered exponentially due to lower temperature. As a result, reactants are consumed at a lower rate, allowing diffusion to occur at a higher rate, so that there is sufficient time to increase reactant concentrations. The increased concentrations led to increased reaction rate, increased radiation, and the oscillatory behavior observed by several researchers. Sohn et al. studied the nonlinear evolution of diffusion flame oscillations that are triggered by radiative heat loss. Deitrich et al. [2000] observed transient oscillations near the (low stretch) extinction limit in the candle flame experiments performed in low-gravity environments.

It should be noted therefore that, while extinction values are given in the following sections, these are based on steady-state solutions. A transient solution may slightly displace the extinction limit based on steady-state analysis.

For the narrowband cases, the exact turning point case at low stretch has not been pinned down. Solutions are obtained at a very low stretch rate ($a=0.068\ s^{-1}$), but no lower, because of numerical stiffness. On the other hand, such a numerical stiffness may be physical and reflect the inadequacy of the steady-state analysis when approaching the radiative extinction limit, as explained above. Nevertheless, this lowest obtainable solution is believed to be very close to the quench limit, for the following reasons, and is used as the case nearest the quench limit in the discussion of results (Section 6.0). This near limit case exhibits a 'leveling off' of the flame standoff distance, which is observed to be a precursor to extinction. It is also at a temperature lower than that of the surface radiation quench limit.

6.0 Discussion of Results

6.1 The Adiabatic Solution

We obtained solutions using the formulation described in Section 3 for the solid trioxane combustion and the numerical procedures described in Section 5 for the solid fuel trioxane diffusion flame. The solutions that do not contain the radiation terms are called the 'adiabatic' solutions. We compared all subsequent solutions with this 'base case.' All cases are run in standard air and standard atmospheric pressure. The surface temperature is set to 388 K, which is the boiling point of trioxane. Since this is the first detailed analysis of a solid trioxane flame, some commentary on the flame structure is warranted.

Flammability Domain: Figure 6-1 is a plot of the maximum flame temperature versus stretch rate for the entire flammability domain for the adiabatic flame. The figure shows that the flammable domain ranges from the blow-off stretch rate at 1952 s^{-1} at maximum flame temperature of 1417 K to the asymptotic low stretch maximum flame temperature at approximately 2200 K. The unstable solutions below the turning point at 1952 s^{-1} are shown for completeness. We observe the expected shape for the flammability curve where the solution at low stretch rate approaches a constant, maximum flame temperature (near 2200 K), and the blow-off occurs at a lower flame temperature (1417 K).

Flame Temperature Profiles: We calculated the maximum flame temperature for each solution in the domain (Figure 6-1(a)). Figure 6-1(b) gives several representative flame temperature profiles. Solutions at a low stretch rate (5 s^{-1}), middle stretch rate (99 s^{-1}), and the blow-off limit (turning point at 1952 s^{-1}) are shown. The figure shows that the temperature profiles are quite different, due to changes in the flow regime. At high stretch rates, the flame is blown against the surface, so the peak flame temperature (1417 K) is very near the fuel. The flame temperature is low, indicative of the low residence time at the blow-off turning point. As the stretch rate decreases, the flame moves away from the surface and broadens; and the temperature increases (1952 K at 99 s^{-1} and 2175 K at 5 s^{-1}). This is resultant from the more complete combustion occurring as the residence time increases. Note that the entire domain (20 cm) is not shown in order to show more detail of the temperature profiles.

Burning Rate: The nondimensional burning rate of the adiabatic flame is presented in Figure 6-2. Figure 6-2 presents the burning rate in a nondimensional form that is easily compared to the results of Appendix 4. Here, the burning rate is presented nondimensionally in an equivalent form to Equation (A4-13):

$$\frac{\dot{m}\,|_{x=0}}{\sqrt{\rho_o \mu_o a}} = \frac{2F\,|_{x=0}}{\sqrt{\rho_o \mu_o a}}$$

We see that the nondimensional burning rate for the adiabatic flame is relatively flat (around 0.8), except at the blow-off extinction limit, indicating that the dimensional burning rate scales with the square root of the stretch rate. The trend is consistent with the adiabatic PMMA solution (case 6) in Figure A4-8. (The dimensional form of the burning rate, $\rho u/_{x=0}$, which is more useful for engineering purposes, is given in Section 6.4 in comparison to the radiative flame results.)

Velocity profiles: Corresponding axial velocity profiles are shown for the low stretch rate (5 s^{-1}), middle stretch rate (99 s^{-1}), and the blow-off limit (turning point) cases in Figures 6-3 through 6-5. Note that the entire domain is not shown, and that the domain and velocity scales are different for each plot to show features of each profile. Each profile has similar characteristics: Near the surface, the axial velocity is in the positive x-direction, indicating fuel leaving the surface. The stagnation-point occurs where the velocity crosses the abscissa, indicating the change in direction of velocity from positive to negative. The local maxima in each curve indicate a local velocity increase due to heating by the flame. The location of the maxima (or minima in magnitude) corresponds to the location of the peak flame temperatures. The velocity then approaches the free stream (potential flow) velocity at the outer portion of the flame. In addition, the magnitude of the axial velocity gradient is twice that of the stretch rate, which is defined based on the radial velocity gradient.

Comparison of the velocity profiles shows that, at high stretch rates, the velocity profile is pushed nearer to the surface, so that the stagnation-point and local maxima (or minima in magnitude) are much closer to the surface than at low stretch rates. While the velocity profiles are similar, the changes occur over a much smaller portion of the domain for the high stretch rate cases. In addition, the blowing velocity from the surface, which is related to the fuel-burning rate, is larger at high stretch rate, even though the stagnation point is very close to the surface.

Species profiles: Figures 6-6 through 6-14 show species profiles for the same cases (low stretch rate (5 s^{-1}), middle stretch rate (99 s^{-1}), and the blow-off limit (turning point)). The species profiles are grouped by order of magnitude for ease of comparison. Note that the domain (x axis) is different for each plot so that the full range of species profiles is visible. Generally, the reaction occurs near the peak flame location so that, at high stretch rates, the reaction occurs much closer to the surface than at low stretch rates. The plots are scaled to locate the peak flame temperature at the center.

Figures 6-6 through 6-8 show profiles for $C_3H_6O_3$, CH_2O, CO, H_2, CO_2, H_2O, O_2 and the temperature profile for each of the three stretch rates. Trioxane gas is produced in approximately the same mole fraction from the surface, with only a slight increase of mole fraction at high stretch rate versus low stretch rate. The secondary fuel, formaldehyde, is produced in slightly higher quantities at lower stretch rate. As stretch rate increases, the 'overlap' region of reactants and products near the peak flame temperature expands so that, at very high stretch rate, reactants are not fully consumed near the maximum flame temperature due to the low residence time of the species in the reaction zone. The intermediate CO is produced in somewhat smaller quantity (peak mole fraction near 0.2 versus 0.25) and has a longer 'tail' from the reaction zone in the high stretch solution. Production of H_2 and CO_2 drops by half for the high stretch case, in comparison to the mid to low stretch cases. Production of H_2O decreases somewhat from the low stretch solution (peak mole fraction near 0.2) to the high stretch solution (peak mole fraction less than 0.15).

Figures 6-9 through 6-11 show profiles for the intermediates H, O, and OH and the temperature for each of the three stretch rates under consideration. First, we observe the similarity: the species peak in the same order (H, OH, O) over the domain. The differences again are due to both the lower residence times as stretch rate increases and the lower flame temperature. OH is produced in much smaller quantities at high stretch rate (approximate peak mole fraction 0.0025) versus low to mid stretch rate (approximate peak mole fractions of 0.0055, 0.007). The opposite is true of O and H: Larger quantities of these two are produced as the stretch rate increases.

Finally, Figures 6-12 through 6-14 show profiles for the intermediates HCO, HO_2, and H_2O_2 and the temperature for each of the three stretch rates. We observe first that the mole fraction scale is increased by an order of magnitude over each of the three plots. This indicates that these intermediates are produced in much greater quantities as stretch rate increases. HCO is produced first at lower stretch rate in the region between the surface and the peak flame temperature, but its mole fraction peaks at approximately $6X10^{-6}$ at the low stretch rate and peaks at approximate mole fraction $3.5X10^{-4}$ at the high stretch rate. At the low and mid stretch rate solutions, HO_2 and H_2O_2 are both produced primarily on the oxidizer side of the flame. Figure 6-14 shows a dramatic increase in mole fraction of HO_2 at the high stretch rate. Also, note the shift in the peak of these radicals (H_2O_2 and HO_2) to the fuel side of the flame. At high stretch, there is much more O_2 blown into the fuel side of the flame—while the absolute quantity of O_2 is small (order 10^{-3}) near the H_2O_2 and HO_2 peaks—it is sufficient to produce more of these radicals (order 10^{-4}). We explore the reasons for the chemical structures seen here in the following section.

Furthermore, the staged combustion of trioxane is quite evident. Its oxidation essentially follows the path: $C_3H_6O_3 \rightarrow CH_2O \rightarrow HCO \rightarrow H_2/CO \rightarrow H_2O/CO_2$. Important radicals, such as H, O, and OH, are produced in the regime of peak temperature. The controlling pathways for trioxane oxidation will be identified in the following section.

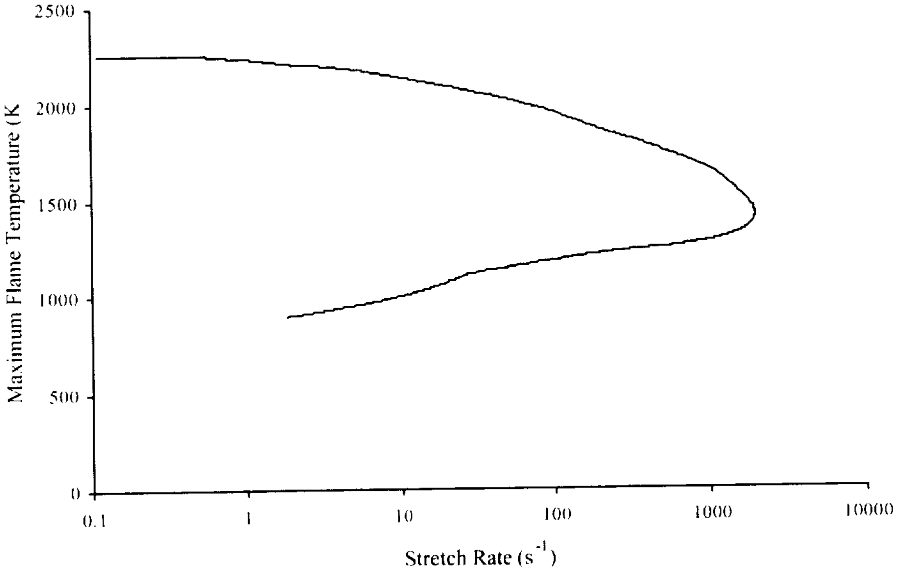

Figure 6-1(a): Maximum flame temperature vs. stretch rate for the adiabatic flame (20 cm domain).

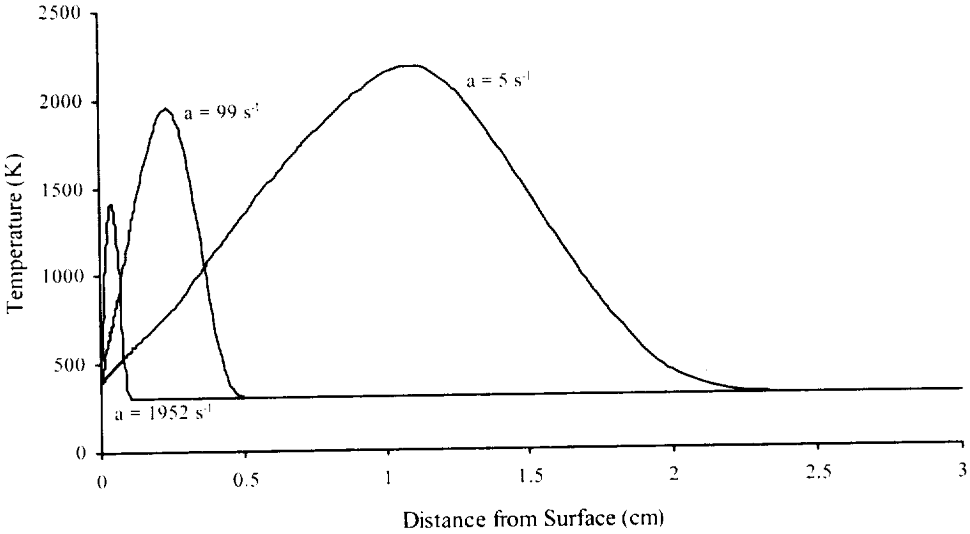

Figure 6-1(b): Temperature profiles for the adiabatic flame.

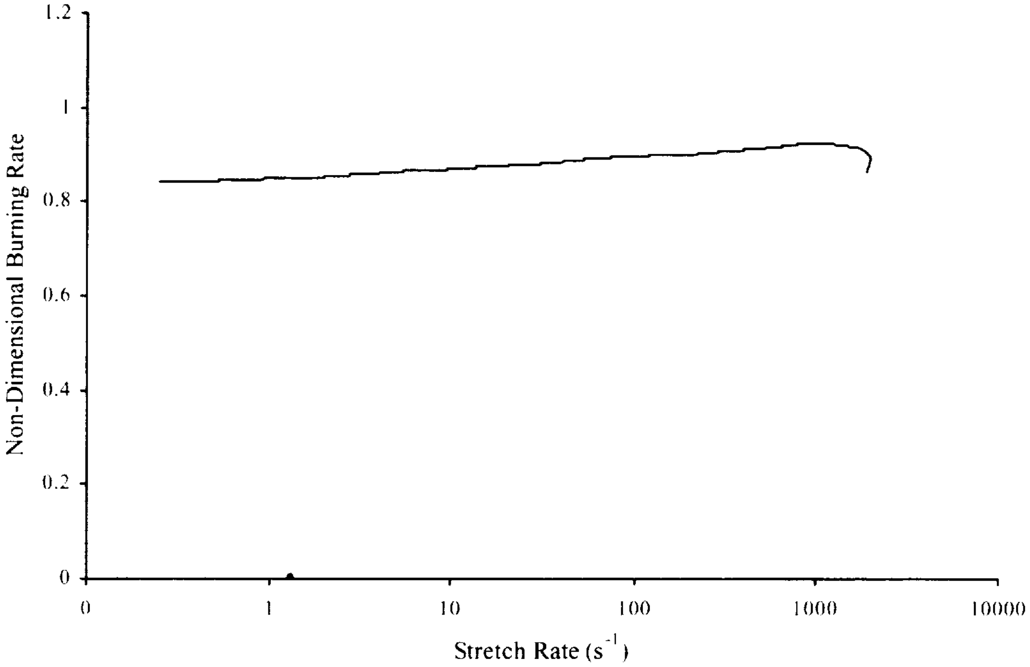

Figure 6-2: Nondimensional burning rate for the adiabatic flame.

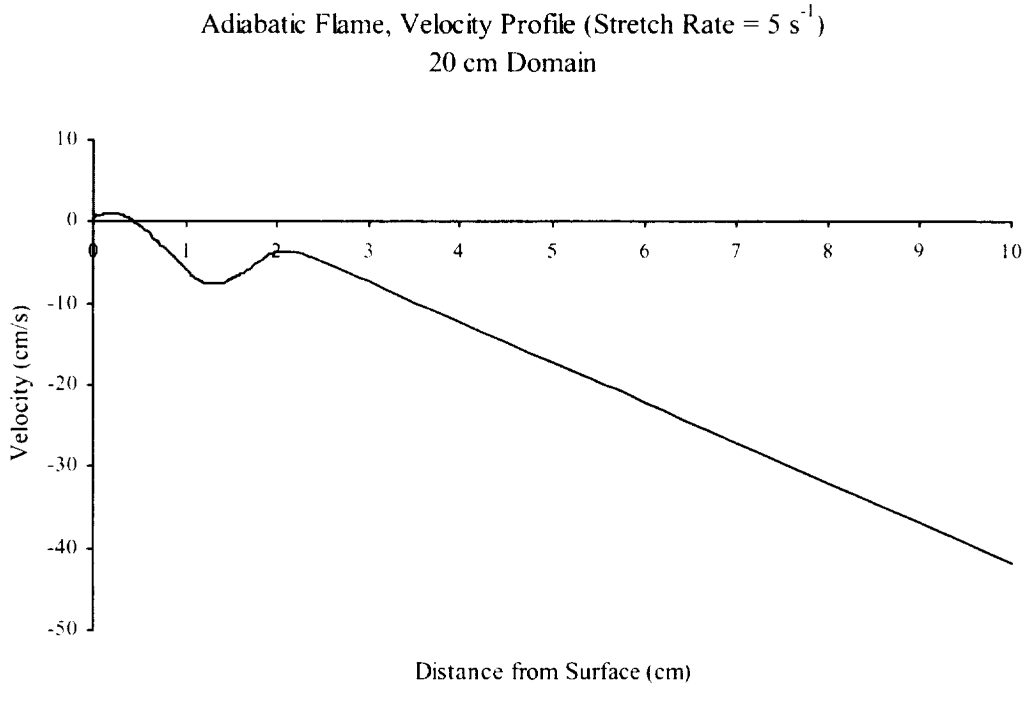

Figure 6-3: Axial velocity profile for low stretch adiabatic flame.

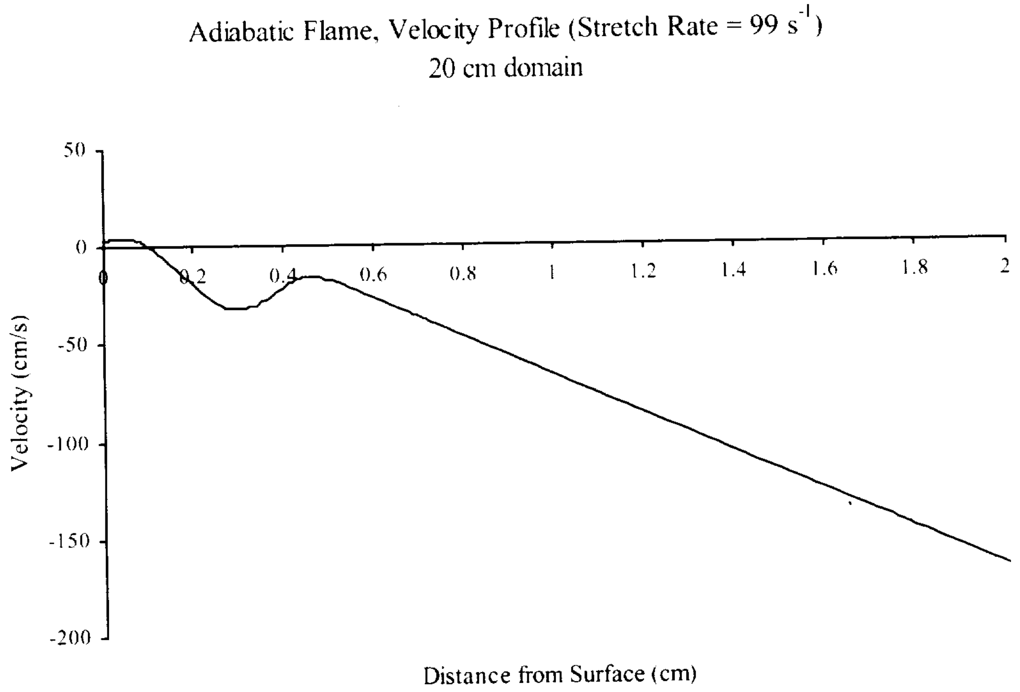

Figure 6-4: Axial velocity profile for mid-stretch rate adiabatic flame.

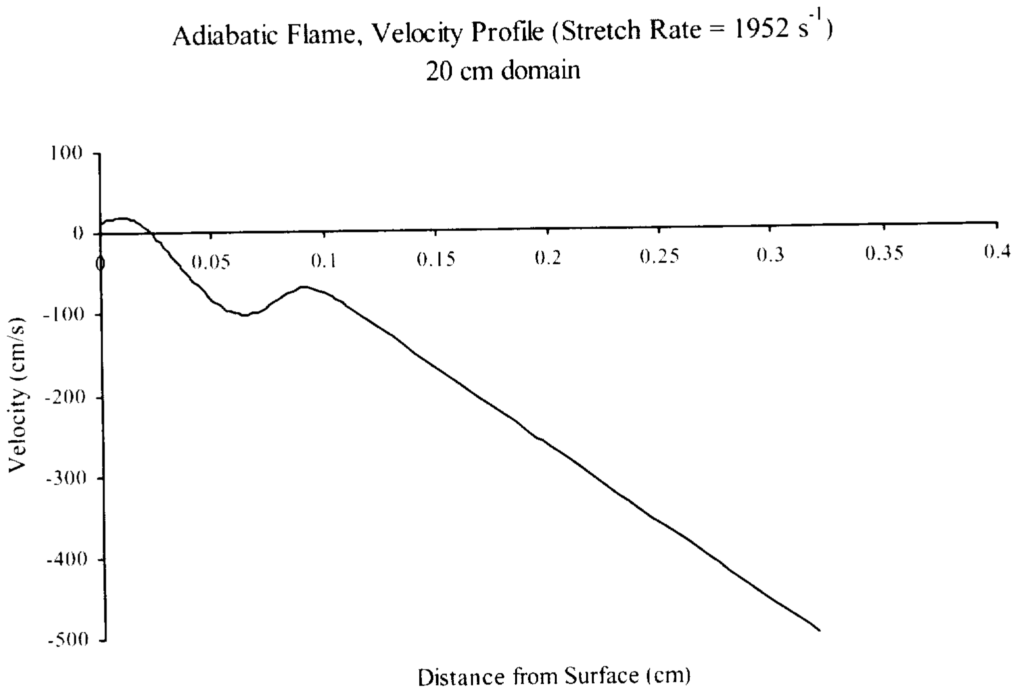

Figure 6-5: Axial velocity profile for high stretch rate turning point adiabatic flame.

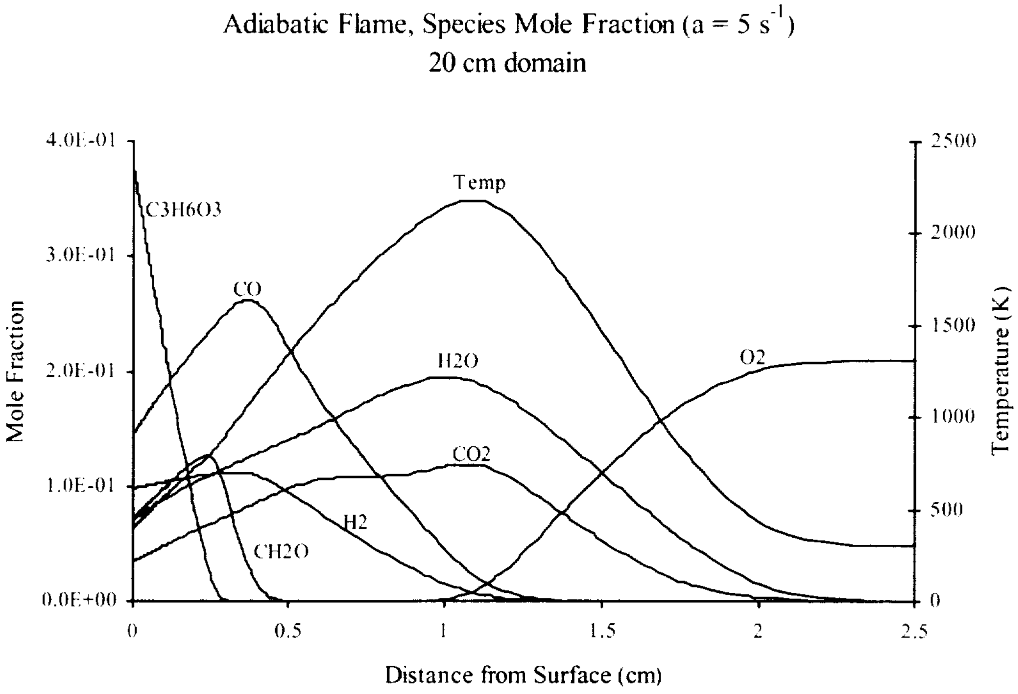

Figure 6-6: Major species profiles for low-stretch rate adiabatic flame.

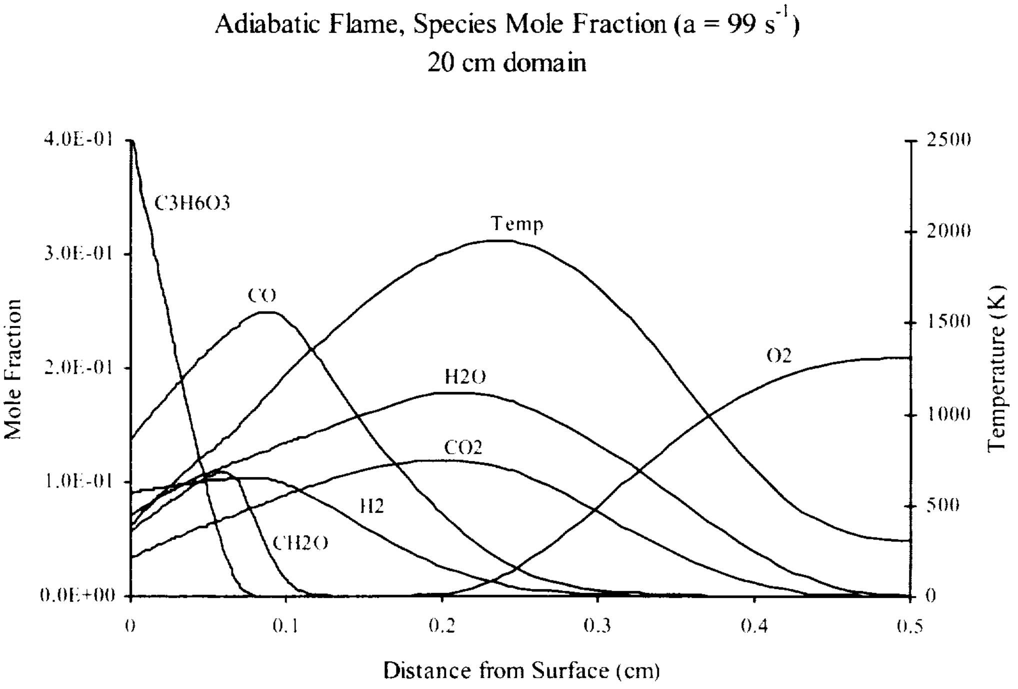

Figure 6-7: Major species profiles for middle stretch rate adiabatic flame.

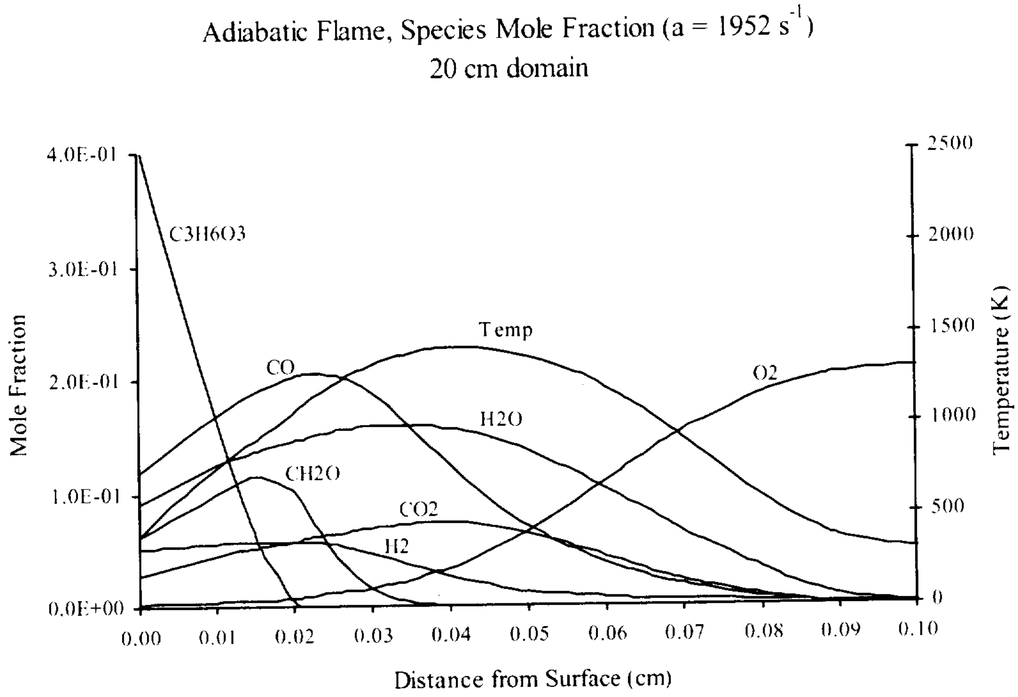

Figure 6-8: Major species profiles for high stretch rate (turning point) adiabatic flame.

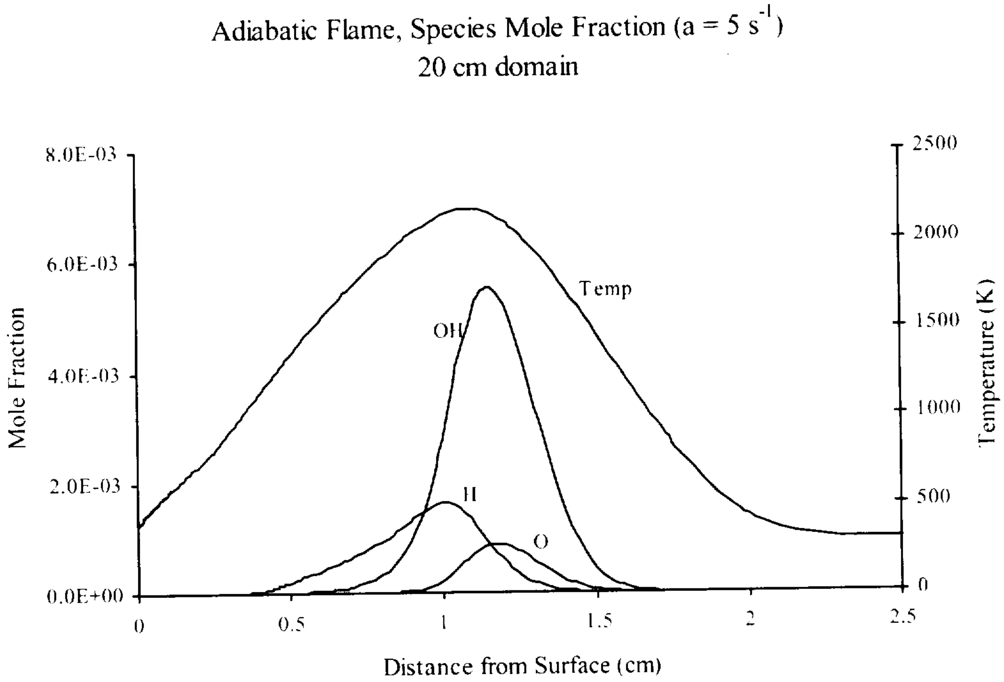

Figure 6-9: Species profiles of OH, H and O for low stretch rate adiabatic flame.

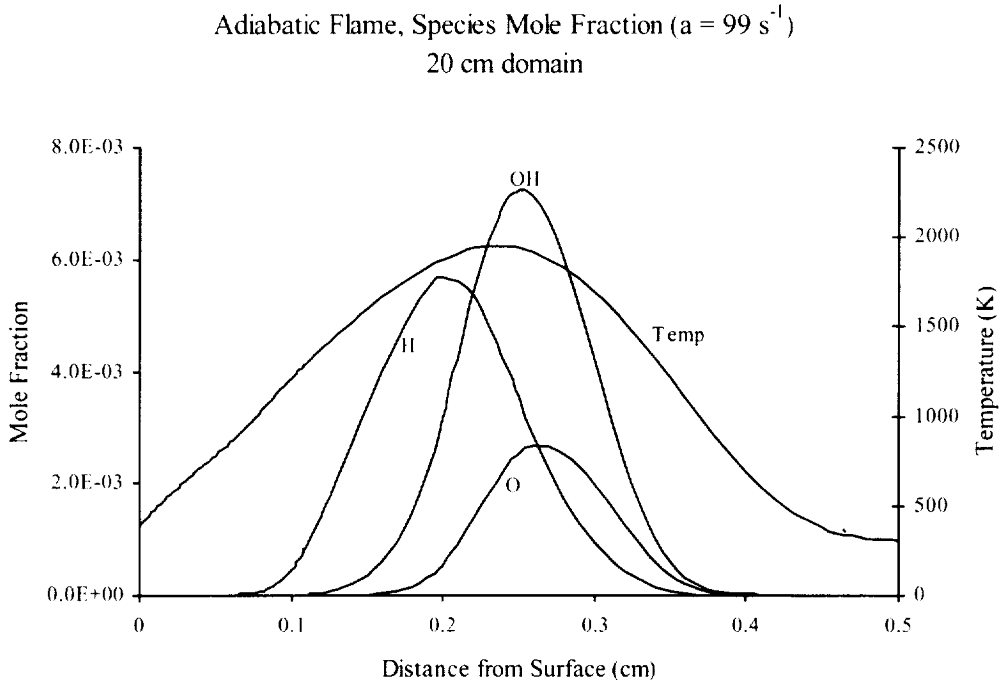

Figure 6-10: Species profiles of OH, H and O for middle stretch rate adiabatic flame.

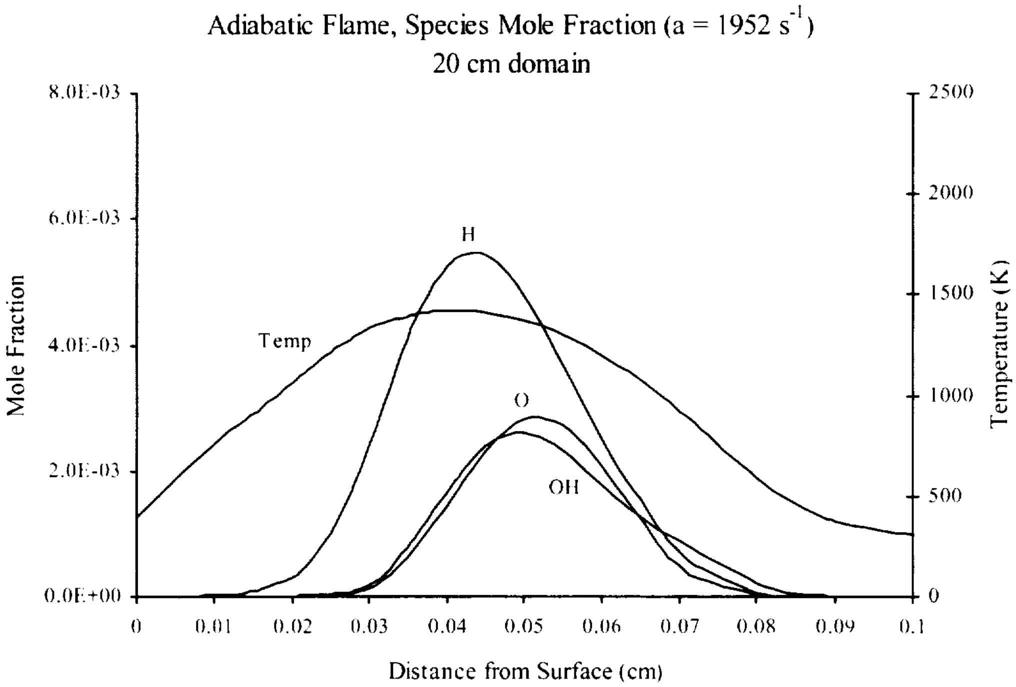

Figure 6-11: Species profiles for OH, H and O for high stretch rate (turning point) adiabatic flame.

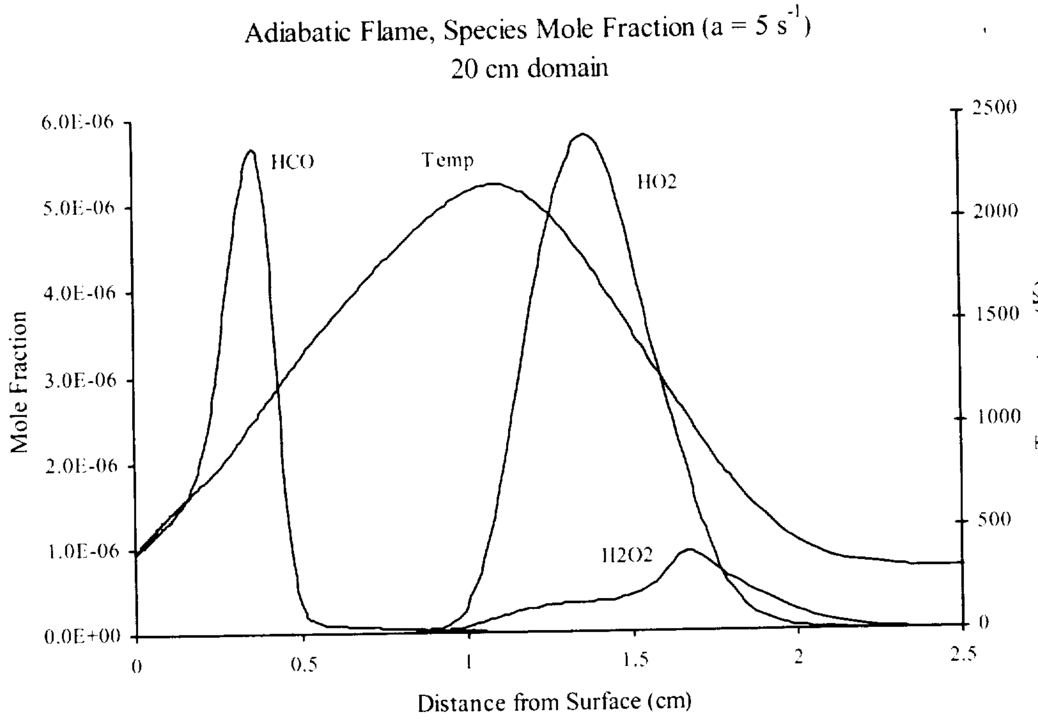

Figure 6-12: Species profiles of HCO, HO_2, and H_2O_2 for low stretch rate adiabatic flame.

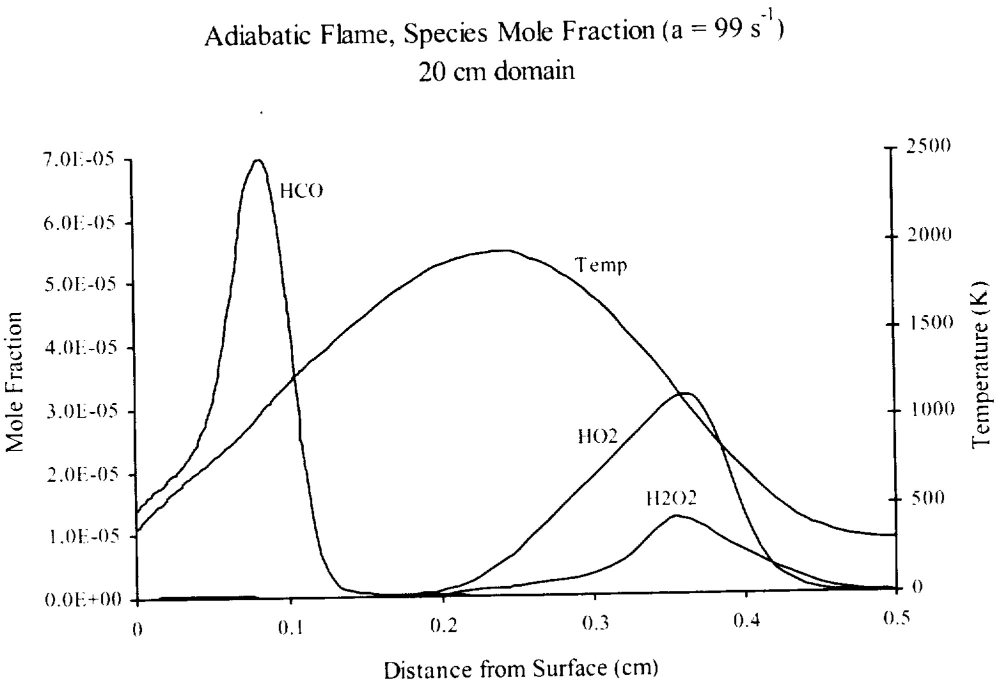

Figure 6-13: Species profiles of HCO, HO_2, and H_2O_2 for middle stretch rate adiabatic flame.

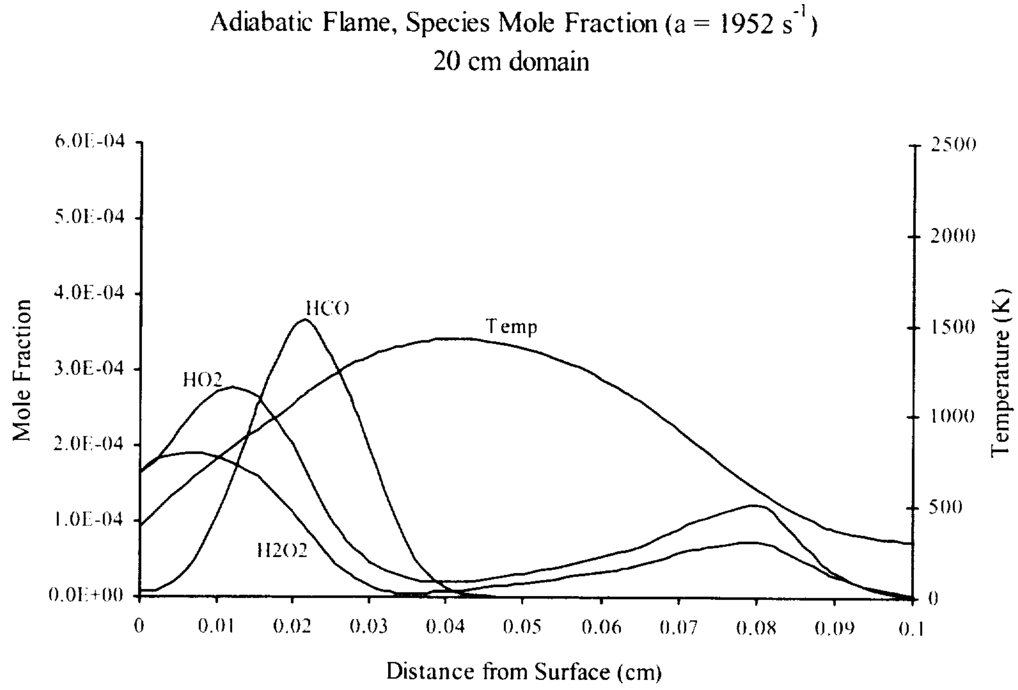

Figure 6-14: Species profiles of HCO, HO_2, and H_2O_2 for high stretch rate (turning point) adiabatic flame.

6.2 Adiabatic Flame Sensitivity and Reaction Path Analysis

We performed sensitivity and detailed analyses to discover the driving kinetic mechanisms responsible for the structure of the solid trioxane combustion in the stagnation-point flow. The flame structure is quite different from the homogeneous studies that established the kinetic mechanism, so these additional analyses are warranted. The adiabatic results are used as the 'baseline' with which to compare the response of the radiative flame in subsequent sections. The results are also compared where possible with the original kinetics study [Hochgreb 1991].

Several parameters are of interest in the sensitivity and detailed kinetics study: species production rates, reaction rates of progress, reaction heat release, and sensitivity to stretch rate. The following quantities are described here, using the definitions in the Nomenclature (Section 3.2).

While the species profiles were given in the previous section, we examined the production rates for the species to determine the location and magnitude of the major consumption and production zones. The production rate for species k is defined as:

$$\omega_k = \sum_i \nu_{ki} r_i \qquad \textbf{(6-1)}$$

We examined the rates of progress of the formaldehyde and formyl decomposition reactions to determine the dominant path(s) for CH_2O, HCO, and O_2 consumption. The rate of progress for reaction i is expressed as:

$$r_i = k_{fi} \prod_k [X_k]^{\nu'_{ki}} - k_{ri} \prod_k [X_k]^{\nu''_{ki}} \qquad \textbf{(6-2)}$$

We examined the reaction heat release to determine both the total heat release and the primary reactions that contribute to the heat release over the flame domain. The heat release for reaction i is given by:

$$Q_i = \sum_k \nu_{ki} r_i h_k \qquad \textbf{(6-3)}$$

and the total heat release is

$$Q_T = \sum_i Q_i = \sum_k \varpi_k h_k \qquad \textbf{(6-4)}$$

This total heat release term is equivalent to the source term in the energy equation (Equation 3-1(f)).

We examined the variables discussed above for three stretch rates over the adiabatic domain (a=5 s^{-1}, a= 99 s^{-1}, and a=1952 s^{-1}). For consistency, these are the same low, medium, and high stretch rates used in the foregoing discussion of the flammable domain, flame temperature profiles, velocity profiles, and species profiles.

Since the response of the flame at extinction is of particular interest here, we chose the radial pressure curvature, E, for sensitivity analysis. Recall from the formulation section (Equation 3-1(c)), that E is the eigen-value of the solution and is related to the stretch rate by:

$$E = -\rho_o a^2$$

The sensitivity gives a quantitative measure of how a solution to a model depends on parameters in the model. The sensitivity is calculated using the residual solution vector, F, and computing its sensitivity to the reaction rate constants, k_i. The vector Φ satisfies

$$F(\Phi, k_i) = 0$$

where Φ is the vector containing the parameters of the solution, including E. F can be differentiated to give

$$\frac{\partial F}{\partial \Phi}\frac{\partial \Phi}{\partial k_i} + \frac{\partial F}{\partial k_i} = 0$$

Where the matrix $\partial F/\partial \Phi$ is the Jacobian of the original system, $\partial F/\partial k_i$ is the matrix of partial derivatives of F with respect to the parameters of the solution, and $\partial \Phi/\partial k_i$ are the sensitivity coefficients. These are calculated in a similar manner as that used in the PREMIX [Kee et al. 1998] code, and the sensitivity to a particular parameter can be extracted from the sensitivity matrix. We calculated the sensitivity to E at the extinction state (E_{ext}) and normalized it to form logarithmic derivatives:

$$\frac{k_i}{E_{ext}}\frac{\partial E_{ext}}{\partial k_i} = \frac{\partial(\ln E_{ext})}{\partial(\ln k_i)}$$

This expression is then normalized in a post-processor by the maximum value of the sensitivity,

$$\frac{\partial(\ln E_{ext})}{\partial(\ln k_i)} \Big/ \max\left[\frac{\partial(\ln E_{ext})}{\partial(\ln k_i)}\right]_{among\ all\ i} \qquad \textbf{(6-5)}$$

so that the resulting sensitivity parameters are relative to +/- 1.0. Since E is negative and its magnitude is proportional to a^2 in this analysis, the negative (positive) values of sensitivity coefficient represent the promoting (retarding) nature of the corresponding reaction, with respect to the overall reactivity. We can therefore employ the normalized *E* sensitivity examined at the extinction turning points to identify the dominant reactions controlling the flame extinction.

Species Production Rates and Reaction Rates of Progress: The production rates for each species are given in Figures 6-15, 6-16 and 6-17 for the sample stretch rates. In each plot, positive production rates indicate species production, and negative production rates indicate species consumption. Following these plots are the relevant reaction rates of progress of the sample stretch rates (Figures 6-18(a-c), 6-19(a-c), 6-20(a-e)). Positive values indicate a forward progressing reaction and negative values indicate a reverse progressing reaction.

In general, we see in each production rate plot that trioxane decomposes in the same region that formaldehyde is produced, via reaction 1. This occurs in a relative low-temperature region of the flame (840 K, 950 K and 1060 K at the location of maximum consumption of fuel for a=5, 99, and 1952 s^{-1}, respectively). This is followed by consumption of formaldehyde, with the primary products being CO and H_2. This occurs at somewhat higher temperatures (1150 K, 1170 K, and 1270K for a=5, 99 and 1952 s^{-1}, respectively). CO and H_2 are eventually converted to CO_2 and H_2O, respectively in the high-temperature region of the flame.

The rates of progress for the formaldehyde decomposition, reactions 2 through 8, are presented in Figures 6-18(a), 6-19(a), and 6-20(a) for each of the sample stretch rates. Reactions 5 and 7 consistently dominate the major formaldehyde consumption, with reaction 5 having the primary role. Note that the consumption zones for H and CH_2O coincide to promote reaction 5.

(5) $CH_2O+H \rightarrow HCO+H_2$
(7) $CH_2O+OH \rightarrow HCO+H_2O$

Subsequently, formyl radical is consumed to form H_2 and CO. The production of H_2 and CO is attributed to the decomposition of HCO via reactions 9 and 11, rather than formaldehyde decomposition (reaction 3).

(9) $HCO+M \rightarrow H+CO+M$
(11) $HCO+H \rightarrow CO+H_2$

This is validated by examining the HCO reaction rates of progress, Figures 6-18(b), 6-19(b), and 6-20(b). Finally, there is a zone of radical pool formation and then recombination into final products, CO_2 and H_2O.

The primary O_2 consumption zone is located downstream of the fuel consumption zone. Figures 6-18(c), 6-19(c), and 6-20(c) show the O_2 reaction rates of progress. Reaction 20 is the dominant reaction, and is the primary source of radical pools, producing OH and O. Reaction 20 is highly endothermic (see heat release discussion), so the local temperature of the maximum O_2 consumption is of interest. The local temperatures are 2175 K, 1950 K, and 1410 K for a= 5, 99, and 1952 s^{-1}, respectively, indicating that O_2 consumption peaks in the high-temperature region of each sample flame. Also, note that H production peaks in opposition to O_2 consumption.

Recall that Hochgreb [1991] found the rate of formaldehyde consumption in the fuel-rich zone below 1100 K to be particularly sensitive to the concentration of O_2. She observed that, in the presence of oxygen, the formaldehyde is consumed in a branching mechanism, in addition to the straight chain, as described in Section 4, allowing multiple pathways for radical attack of the fuel. The region between the surface and the flame fits the characterization of a low-temperature, fuel-rich zone. In contrast to this, we see a consistent dominance of reactions 5 and 7 in the decomposition of formaldehyde, with HCO consumed via 9 and 11, i.e., the straight-chain mechanism.

The production rates increase by an order of magnitude for each sample stretch rate, starting from the low stretch case and increasing. The turning point is characterized by overlap of the formaldehyde consumption and radical production zones, ascribed to the shortened residence time at the high stretch rate.

Only at the turning point does reaction 6, $CH_2O+O \rightarrow HCO+OH$, have any importance in the decomposition of formaldehyde—resulting from the overlap of formaldehyde consumption and the radical pool. This is in contrast to the previous premixed homogeneous study [Hochgreb 1991], where reaction 5 is the straight-chain decomposition reaction, and reaction 8, $CH_2O+HO_2 \rightarrow HCO+H_2O_2$, is the branching path decomposition reaction. Since the primary product of these reactions is HCO, we examined the rates of progress of the HCO decomposition (reactions 9 through 15) as well.

The rate of progress for the HCO consumption in Figures 6-18(b), 6-19(b), and 6-20(b) confirms that reaction 9 is the dominant path for HCO decomposition over the flame domain. Note that reaction 9 is plotted on the right-hand scale for Figures 6-18(b) and 6-19(b). Rate of progress for reaction 11 is an order of magnitude less than reaction 9 at the low and middle stretch cases. This confirms the foregoing supposition that the presence of CO and H_2 suggested HCO decomposition via reactions 9 and 11. Only for the high stretch case does reaction 10 ($HCO + O_2 \rightarrow CO+HO_2$) appear with any significance. Note that reaction 10 also appears as an important O_2 rate of progress reaction at the high stretch, particularly near the surface. This indicates that reaction 10 is the culprit for the increased HO_2 that appears near the surface in Figure 6-14.

While we see no evidence of Hochgreb's low-temperature reaction path in the analysis of the CH_2O decomposition pathway, the emergence of reaction 10 in the HCO and O_2 pathways is a telltale footprint of an alternate pathway. This, as well as the increase in production of HO_2 and H_2O_2 on the fuel side of the flame, is further explored in Figures 6-20(d) and 6-20(e). Figure 6-20(d) gives the primary rates of progress for the HO_2 reactions. Since we seek an explanation for the changes in the HO_2 concentrations on the fuel side of the flame, we note that reaction 10 dominates in this region, and is the primary producer of HO_2. Indeed, the other dominant reaction here (reaction 28) consumes HO_2. Figure 6-20(e) presents the rates of progress for the major H_2O_2 reactions. Again, focusing on the fuel side of the flame, the dominant reactions are 8 and 36. While reaction 8 does not appear significant in Figure 6-20(a), it is the primary source of H_2O_2 in this portion of the flame. Reaction 36 consumes the H_2O_2 in this region.

Thus, we see the emergence of Hochgreb's low-temperature reaction pathway in a portion of the high stretch flame. This is attributed to several factors: While the maximum flame temperature is greater than 1100 K, a large portion of the flame is not; the region of the flame near the surface is fuel-rich; and finally, at the high stretch extinction limit, enough O_2 is blown into the fuel-rich region to support the low-temperature reaction pathway.

In conclusion, the main reaction paths follow the route illustrated in Figure 6-25. This is essentially Hochgreb's 'high temperature' mechanism. A portion of the high stretch extinction limit flame exhibits the 'low temperature' reaction pathway. This is noteworthy in that the reaction path exists in one region of the heterogeneous diffusion flame at the high stretch extinction limit. This pathway is further explored with the radiative flame in Section 6.5.

Heat Release: Figures 6-21(a), 6-22(a), and 6-23(a) show the total heat release over the domain for the sample stretch rates. Temperature profiles are included for comparison. Figures 6-21(b), 6-22(b), and 6-23(b) contain the heat release by reaction to understand the primary contributors to the total heat release. Positive values indicate exothermicity; negative values indicate endothermicity.

All of the profiles exhibit an endothermic zone nearer to the surface, and an exothermic zone beyond. The endothermic zone is comparable in magnitude to the exothermic zone, which is unusual for hydrocarbon combustion. As can be observed in the reaction heat release, the endothermic zone corresponds to the fuel pyrolysis region. In the formaldehyde consumption zone, the exothermicity of reaction 5 counterbalances the endothermicity of reaction 9.

Beginning with the low stretch solution, the endothermic region coincides with the decomposition of trioxane (reaction 1). The consumption of formaldehyde (reaction 5) is opposed by the thermal decomposition of HCO (reaction 9), so that the initial part of the exothermic region resembles a small plateau. Reactions 16 and 23 also contribute to this plateau. The recombination zone releases much more heat in comparison, with reaction 35 (producing H_2O from the recombination of H and OH) accounting for more than half of the heat release. Reactions 35, 38, and 23 all lead to H_2O formation, indicating that the primary heat release is due to formation of H_2O, rather than CO_2 via reaction 16, which is a major source of heat release in most hydrocarbon combustion. The branching reaction 20 represents the dominant endothermicity in the heat release zone, while it is also the controlling branching reaction generating the radical pool.

The middle stretch rate case is similar to the low stretch rate case, except that reaction 11 contributes to the smaller of the two exothermic peaks. This indicates that HCO is consumed via reaction 11 as well as reaction 9 (as seen in the reaction progress discussion). The second, larger peak occurs in the recombination zone, and again, reaction 35 contributes to more than half of the heat release. Reactions 35, 38, 23, 16, and 28 contribute to the heat release in this zone, and again, the primary heat release in this zone is due to formation of H_2O. Reaction 20 accounts for the primary endothermic response in this zone.

At the turning point, the endothermic peak is reduced in relative magnitude, and the exothermic peaks reverse in magnitude. The first exothermic peak is larger than the second one. This is due to the overlap of the fuel and formaldehyde decomposition with the radical pool zones, as well as the contribution of reaction 7 to the decomposition of formaldehyde. The flame is blown against the surface, and the residence time is short, so that these zones overlap. Reaction 11 exceeds reaction 9 in heat release in this case due to the increased importance of reaction 11 (see rate of progress discussion) as a secondary path for HCO decomposition at high stretch. Previously, H is consumed in the radical pool zone, but with the overlap (or compression) of these zones at high stretch, H is available for reaction with HCO. In the radical pool zone, with the reduced presence of OH (Figure 3-21), reaction 35 is no longer significant, and the major heat release comes from reaction 38.

Eigen-Value Sensitivity: The results of the normalized E_{ext} sensitivity are presented in Figure 6-24 for the high stretch turning point. At the high stretch turning point (a=1952 s^{-1}), where the temperature is relatively low, the residence time is low as well, and the flame is very near the surface, the extinction stretch rate is sensitive to a number of reactions. Reaction 5 is the primary path for formaldehyde decomposition, and reaction 9 is the primary path for HCO decomposition. Reaction 11 promotes HCO decomposition but consumes H, thereby retarding the reaction. Additionally, E_{ext} is sensitive to reactions 16, 20, 21, 28, 29, and 38. We know from Figure 6-20(c) that the reactions 20 and 38 have a net rate of progress in the forward direction, and are competing chain branching and termination reactions. Unraveling these reactions reveals a common thread: The presence of the highly reactive, low molecular weight radicals, in particular, the H radical, controls the reaction progress. Reactions 11 and 29 consume H radical and retard the reaction. Reactions 16 and 20 produce H (reaction 16 is a direct production, while reaction 20 produces H via a net cycle with OH and O via reactions 21 and 23). Production of these radicals, particularly H radical, is an important control mechanism here because these radicals are highly reactive in the short residence time available, and these are the reactants more likely to be forced out of the reaction zone due to high stretch rate. Also, we observe from the species profiles in Figure 6-11 that the peaks for O, OH, and H are shifted somewhat past the peak temperature location to the lean side of the flame with respect to the lower stretch rate solutions in Figures 6-9 and 6-10, indicating that the radical pool zone is extended past the peak temperature location. Analyzing production rates also confirms this. Note that E_{ext} is *not* sensitive to reaction 1, the trioxane decomposition, since it is well separated from the formaldehyde decomposition.

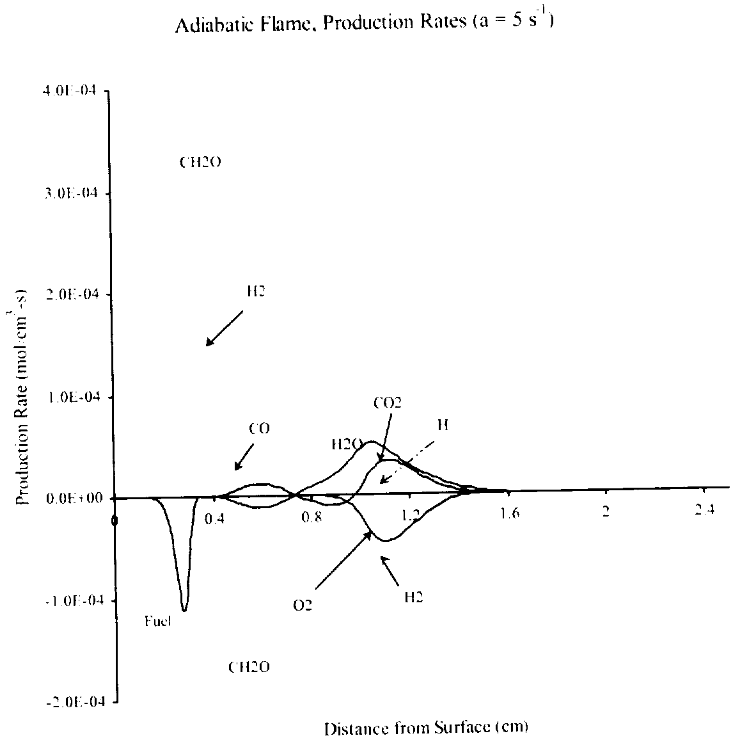

Figure 6-15: Adiabatic flame, species production rates for low stretch rate.

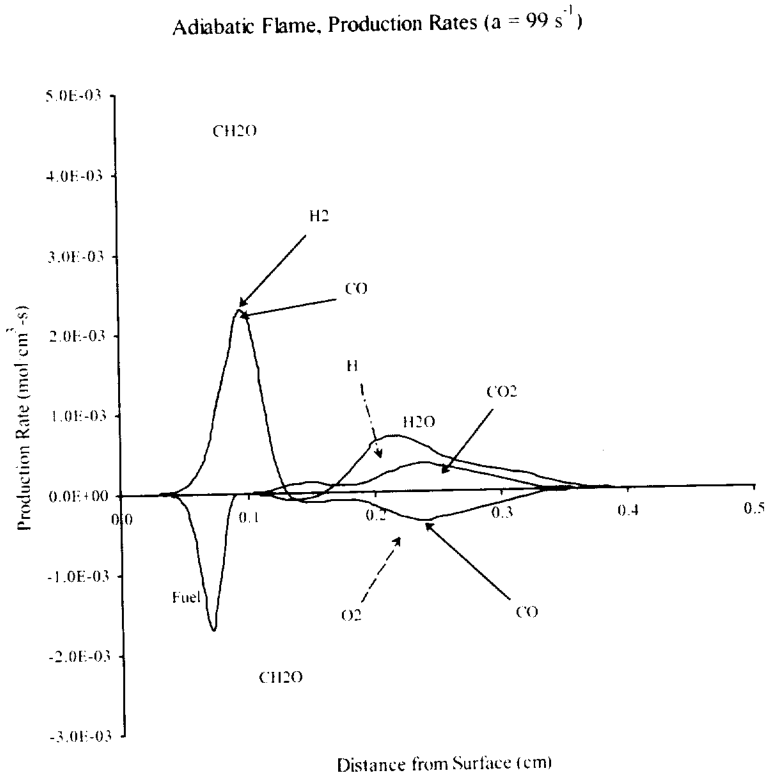

Figure 6-16: Adiabatic flame, species production rates for mid stretch rate.

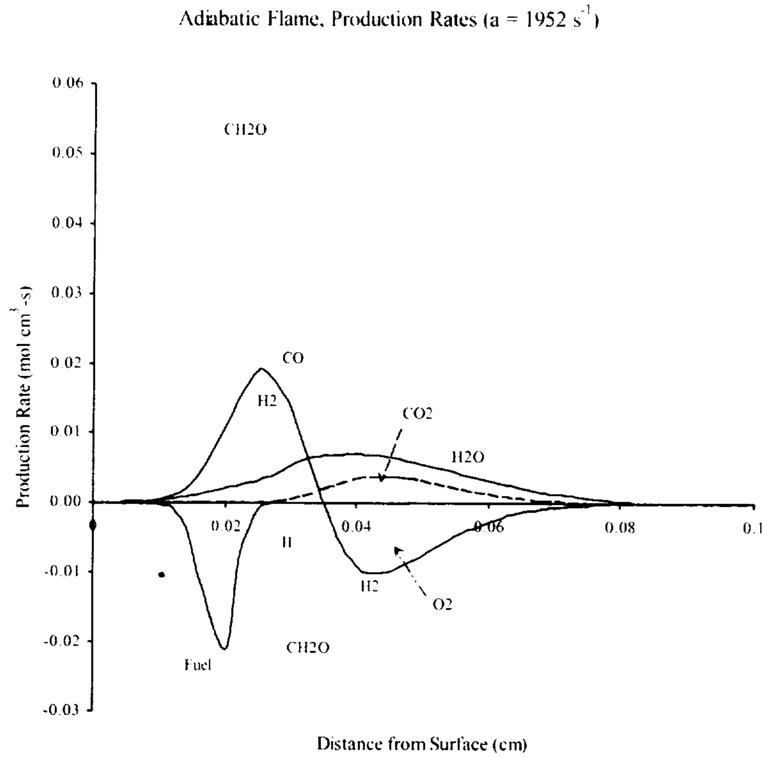

Figure 6-17: Adiabatic flame, species production rates at the blow-off extinction limit.

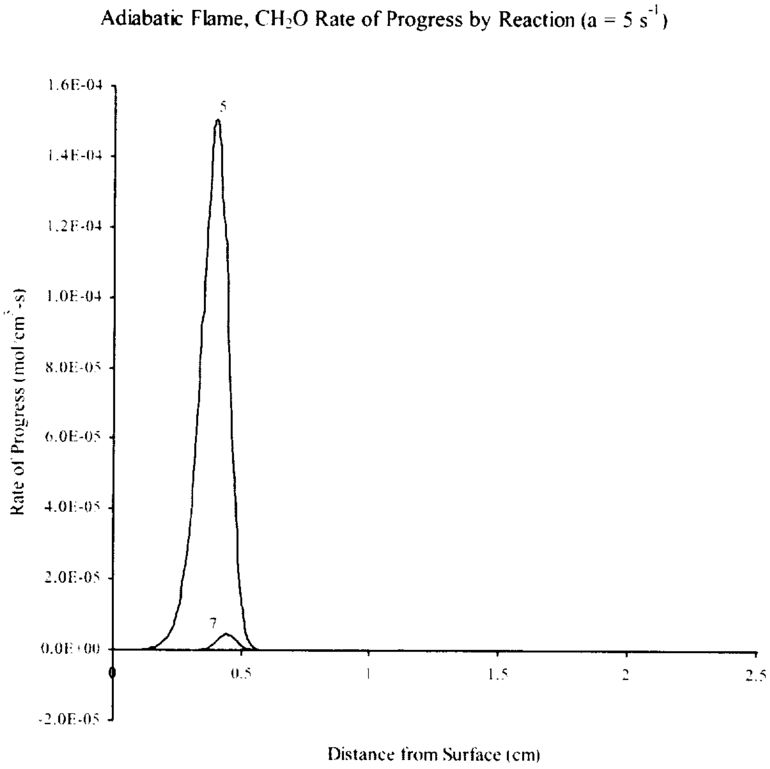

Figure 6-18(a): Adiabatic flame, CH_2O consumption rate of progress by reaction for low stretch rate.

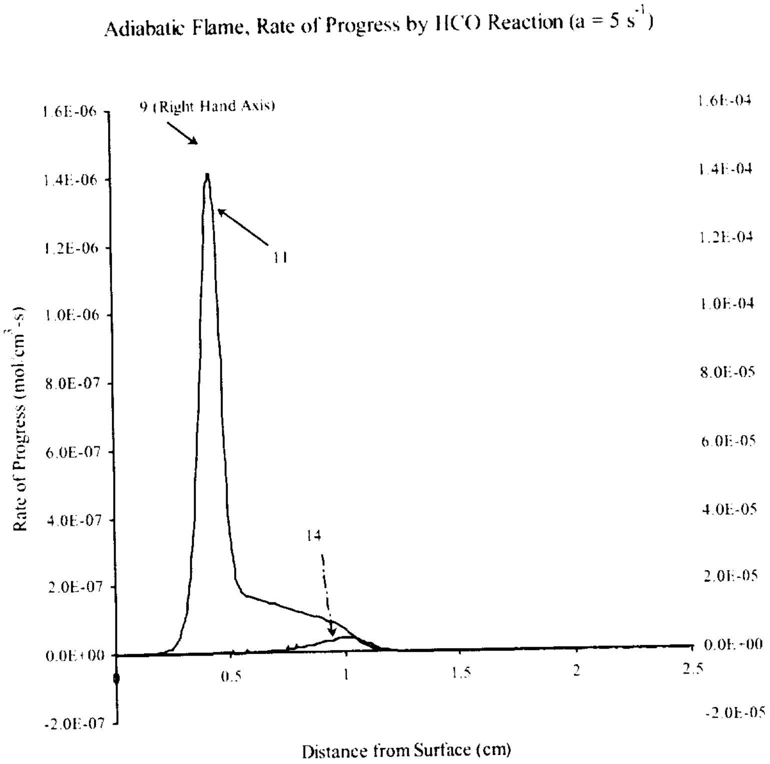

Figure 6-18(b): Adiabatic flame, HCO consumption rate of progress by reaction for low stretch rate.

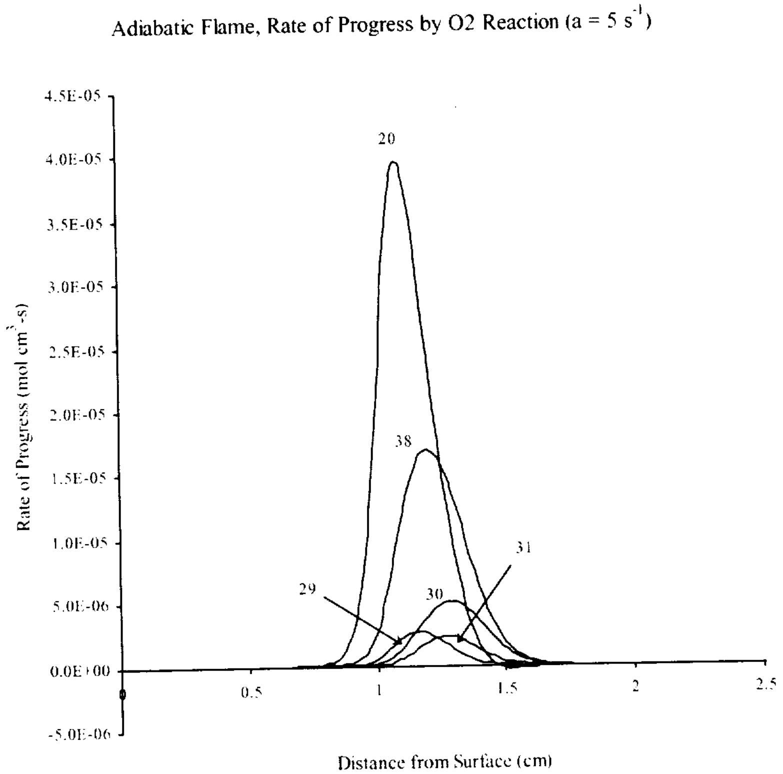

Figure 6-18(c): Adiabatic flame, O_2 consumption rate of progress by reaction for low stretch rate.

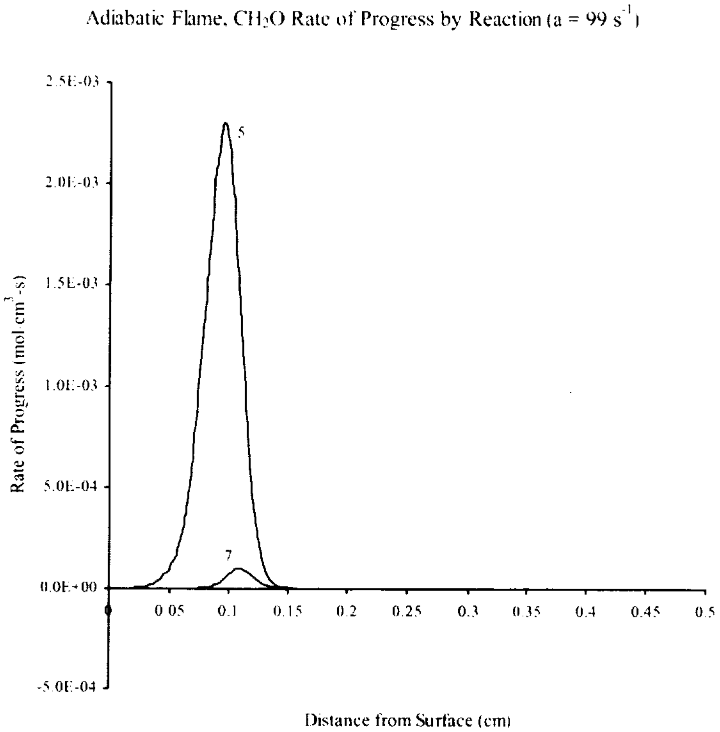

Figure 6-19(a): Adiabatic flame, CH_2O consumption rate of progress by reaction for mid stretch rate.

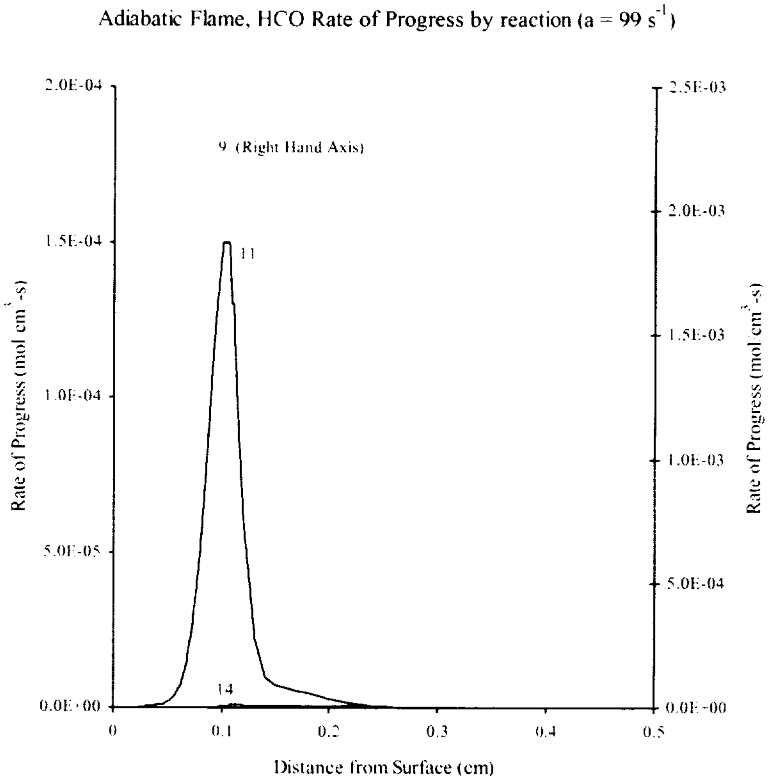

Figure 6-19(b): Adiabatic flame, HCO consumption rate of progress by reaction for mid stretch rate.

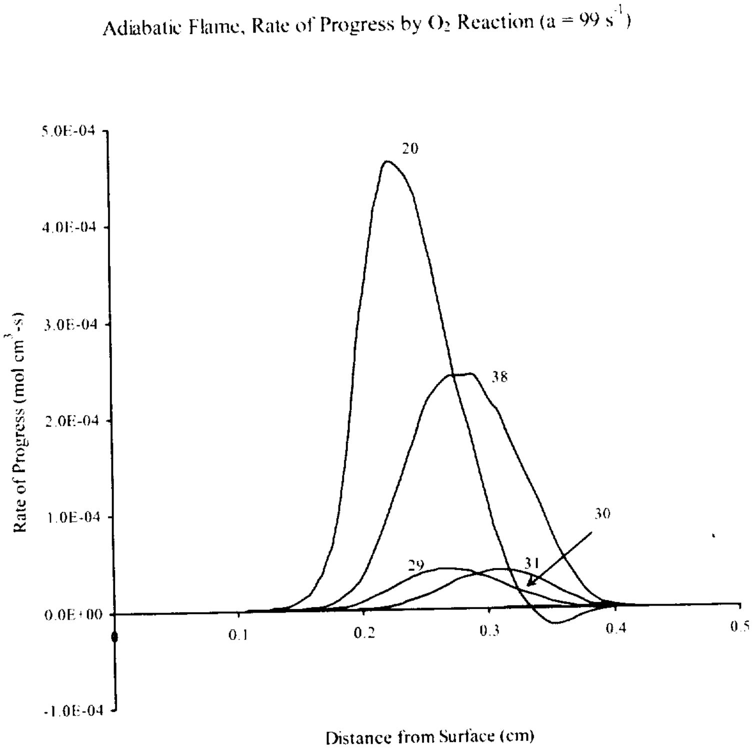

Figure 6-19(c): Adiabatic flame, O_2 consumption rate of progress by reaction for mid stretch rate.

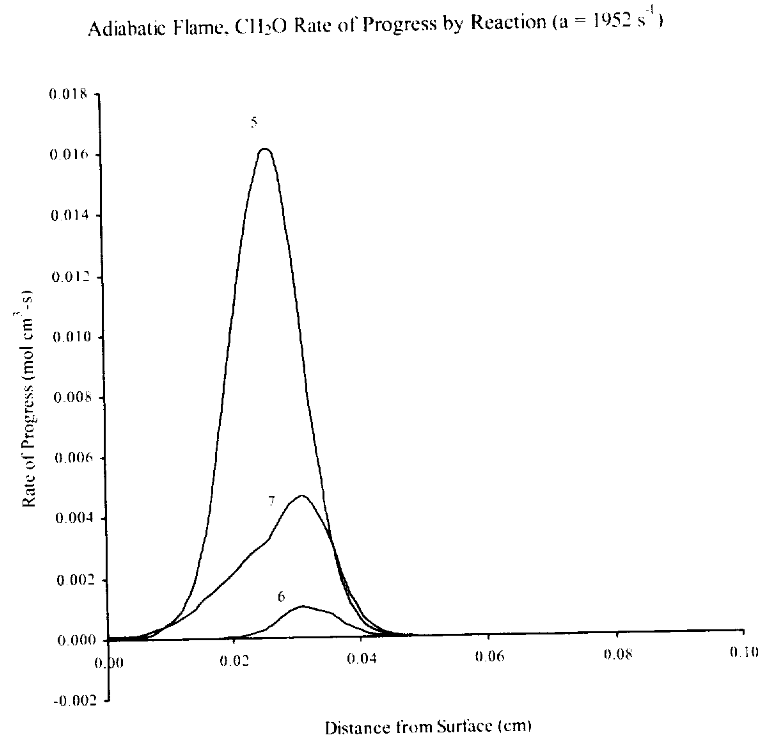

Figure 6-20(a): Adiabatic flame, CH_2O consumption rate of progress by reaction at the blow-off extinction limit.

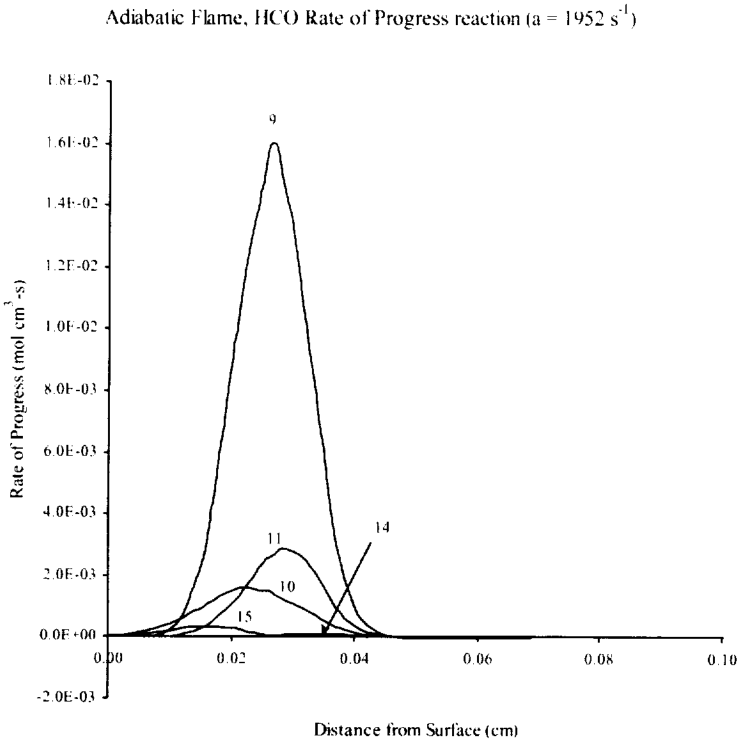

Figure 6-20(b): Adiabatic flame, HCO consumption rate of progress by reaction at the blow-off extinction limit.

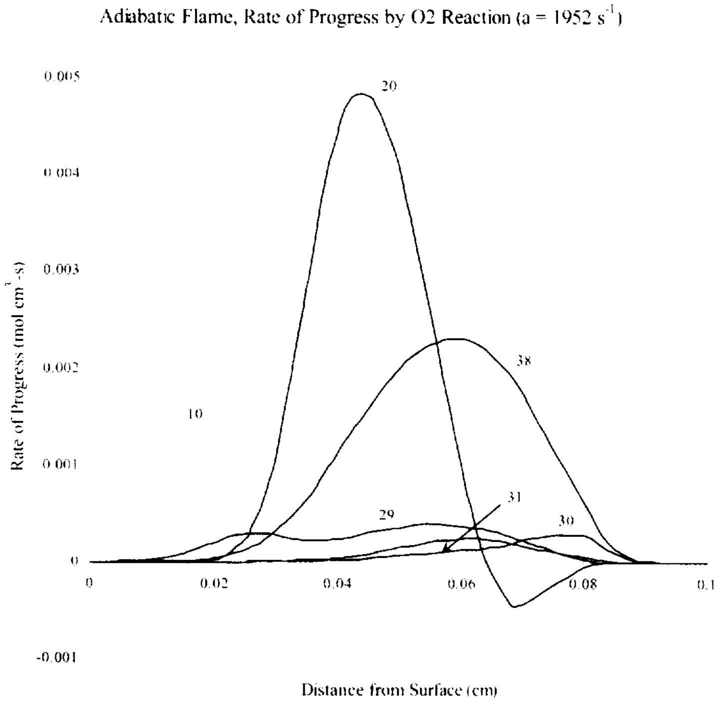

Figure 6-20(c): Adiabatic flame, O_2 consumption rate of progress by reaction at the blow-off extinction limit.

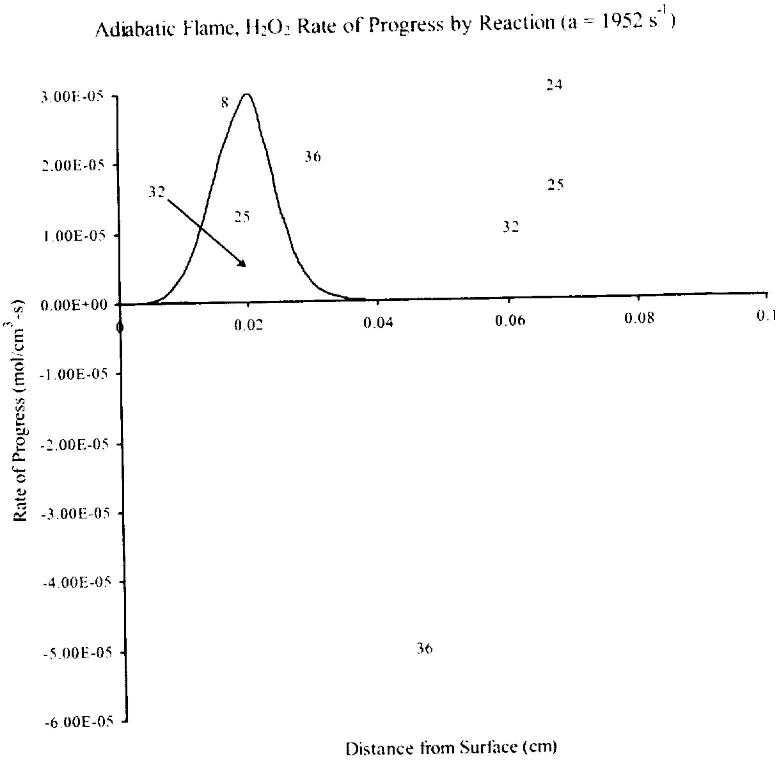

Figure 6-20(d): Adiabatic flame, H_2O_2 consumption rate of progress by reaction at the blow-off extinction limit.

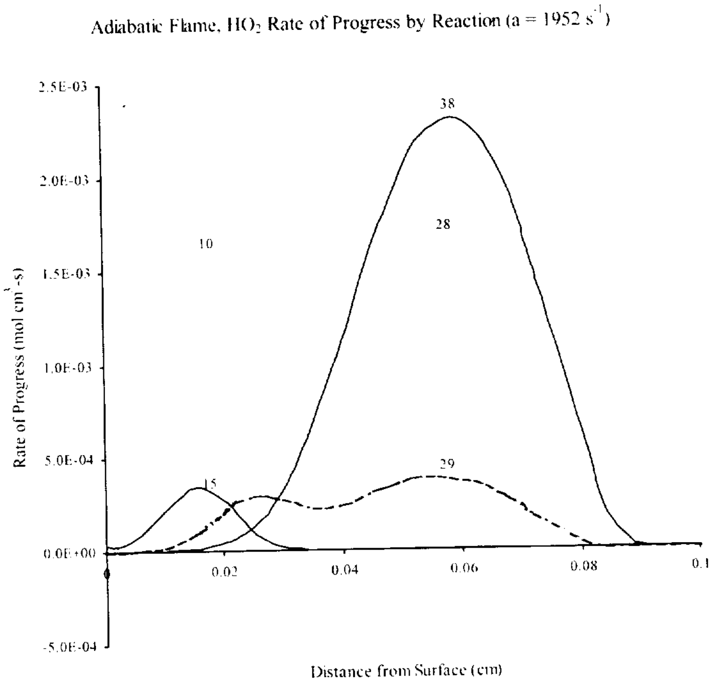

Figure 6-20(e): Adiabatic flame, HO_2 consumption rate of progress by reaction at the blow-off extinction limit.

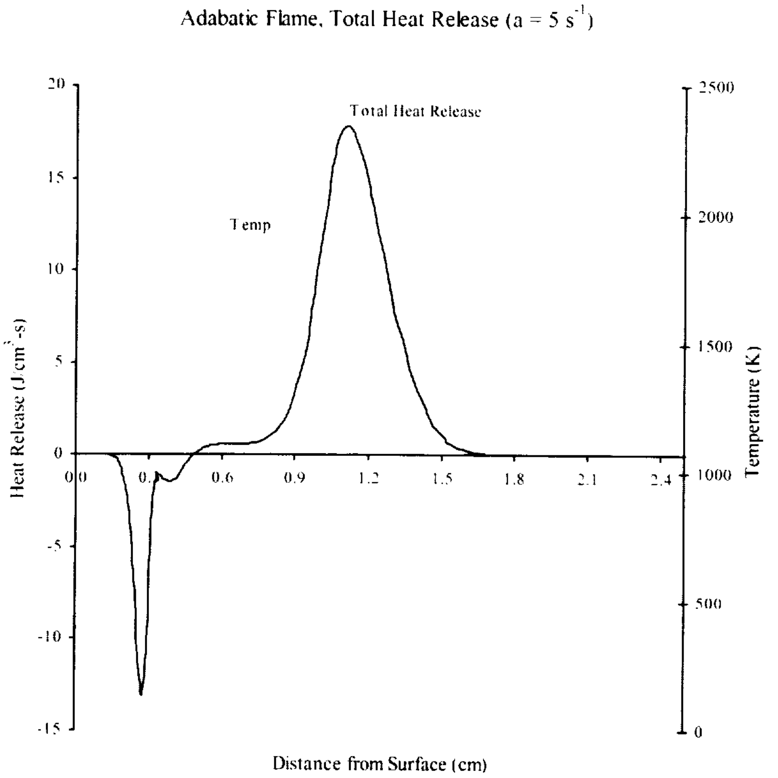

Figure 6-21(a): Adiabatic flame, total heat release for low stretch rate.

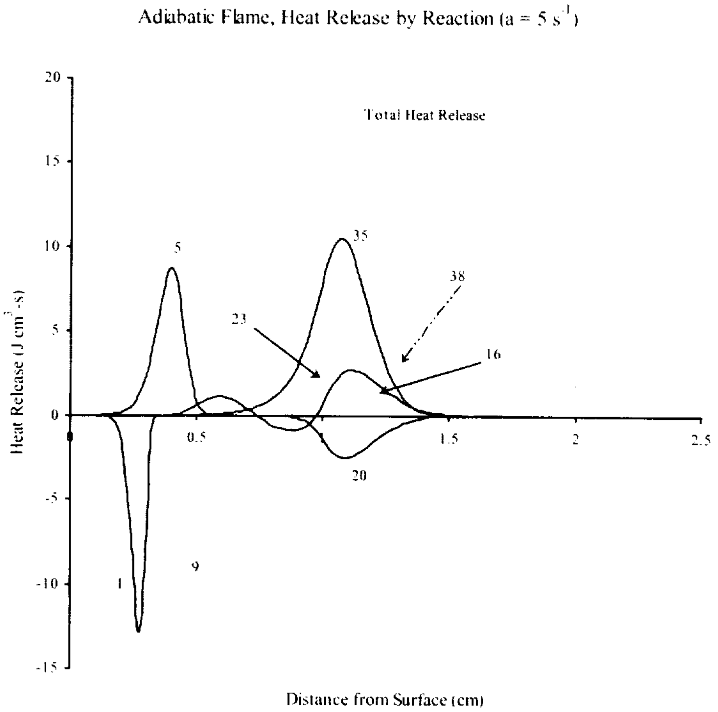

Figure 6-21(b): Adiabatic flame, heat release by reaction for low stretch rate.

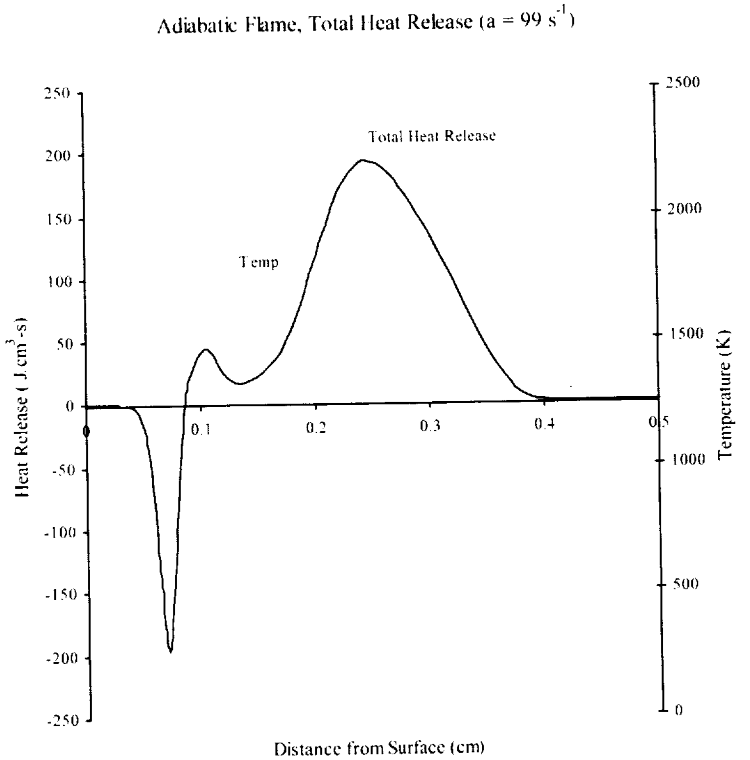

Figure 6-22(a): Adiabatic flame, total heat release for mid stretch rate.

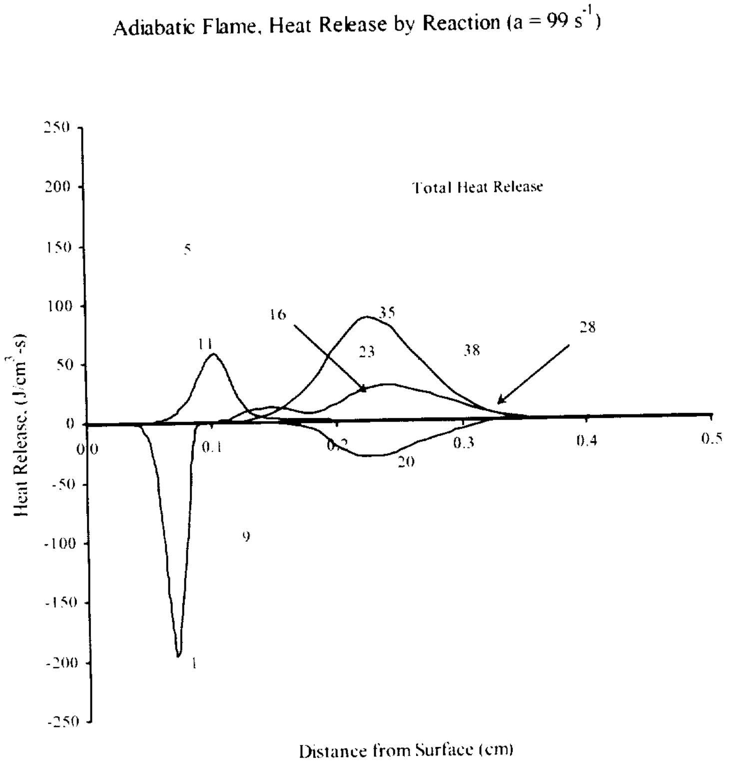

Figure 6-22(b): Adiabatic flame, heat release by reaction for mid stretch rate.

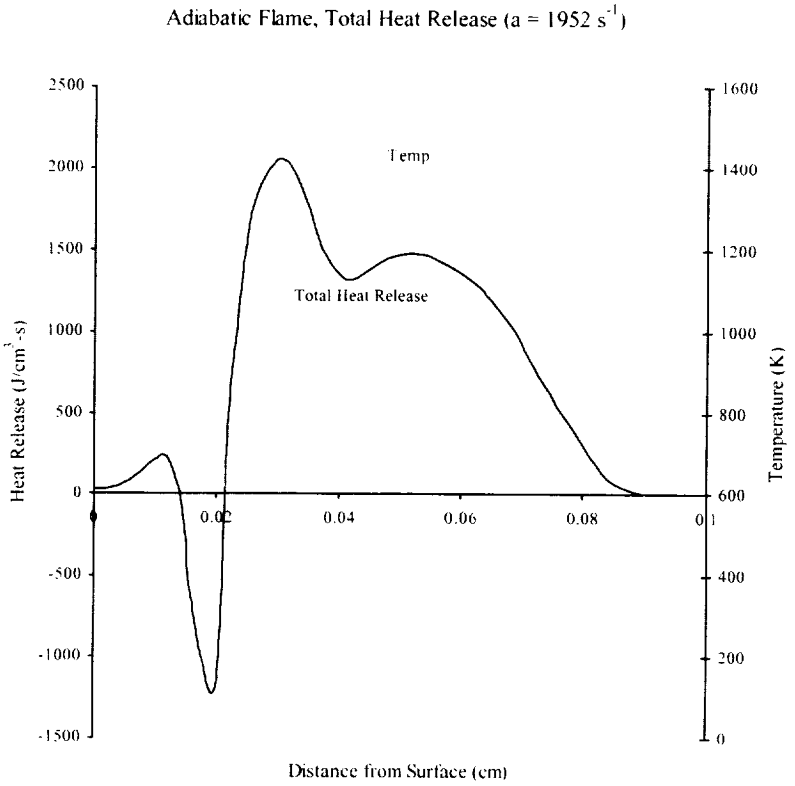

Figure 6-23(a): Adiabatic flame, total heat release at the blow-off extinction limit.

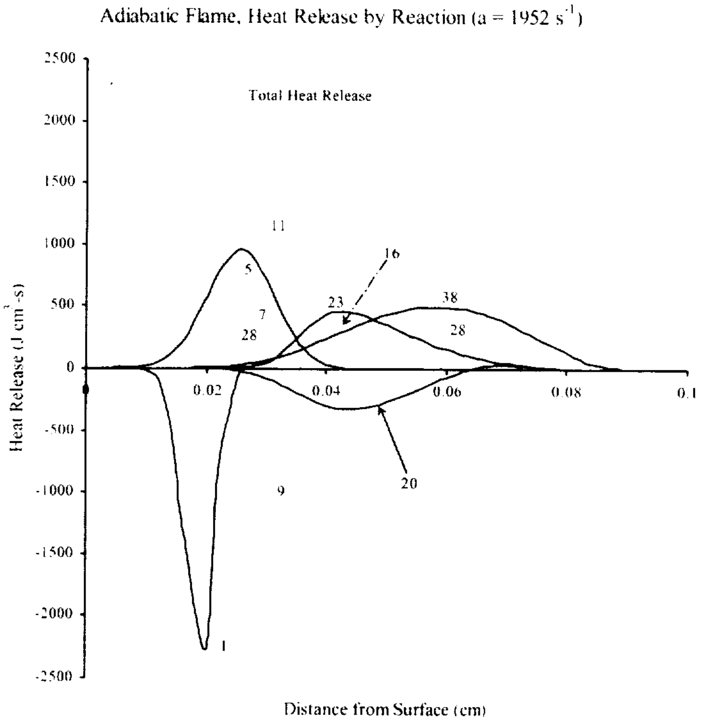

Figure 6-23(b): Adiabatic flame, heat release by reaction at the blow-off extinction limit.

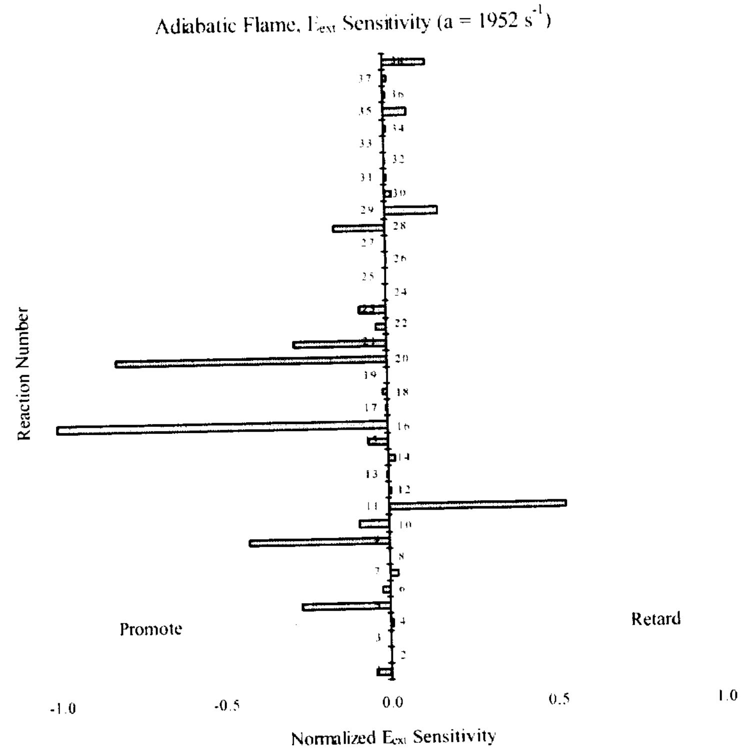

Figure 6-24: Adiabatic flame, normalized E_{ext} sensitivity by reaction at the blow-off extinction limit.

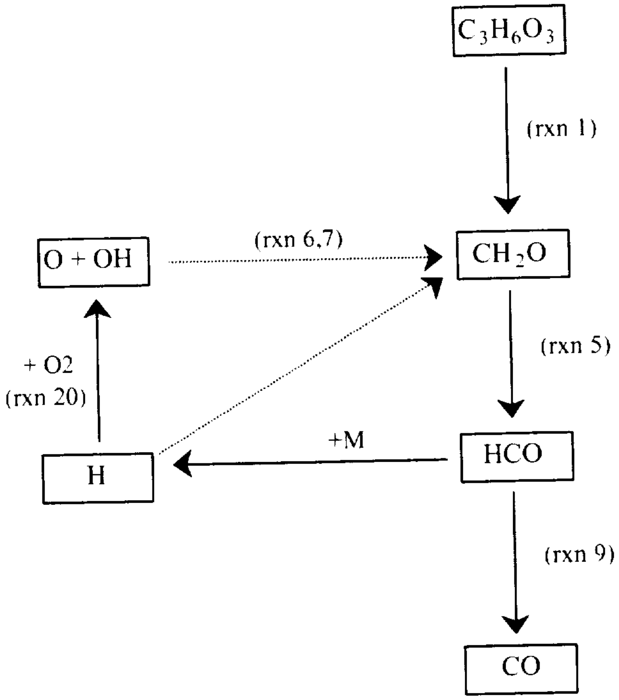

Figure 6-25: Main reaction path for adiabatic trioxane diffusion flame.

6.3 Effects of Surface Radiation

As discussed in Appendix 4, including radiative emission from the solid surface gives a qualitative picture of the radiative contribution, and is useful for comparison purposes in order to separate surface radiation effects from flame radiation effects. In this section, we compare the trends documented in Appendix 4 for the simpler PMMA model to those in the trioxane flame and to the adiabatic solution as well.

Solutions are obtained using the formulation for an emitting surface described in Section 3, that includes black-body emission ($\varepsilon = 1.0$) from both boundaries. The domain is increased from 20 cm for the adiabatic solution to 25 cm, as described in Section 5. All cases are run in standard air and at standard atmospheric pressure. The surface temperature is set to 388 K, which is the boiling point of trioxane. We refer to these solutions in the discussion as the 'surface radiation' solutions.

Flammability Domain: Figure 6-26 is a plot of the maximum flame temperature versus stretch rate for the entire flammability domain for the trioxane 'surface radiation' flame. In this case, the full solution isola, including the unstable solutions (i.e. the lower branch solution in Figure 6-26), is presented. The figure shows the expected low stretch extinction limit observed in Appendix 4, in contrast to the adiabatic solutions. While the materials and the surface temperatures are quite different, the trend is the same.

The blow-off extinction limit (1942 s^{-1} at T_{max}=1405 K) is nearly identical to that of the adiabatic solution (1952 s^{-1} at T_{max}=1417 K). In this regime, the surface emission has virtually no effect. We contrast this with Figure A4-7, where surface radiation effects are small, but noticeable at the high stretch regime. Although the materials are different, and therefore the heat transfer characteristics are different as well, the primary reason for the larger effect on the PMMA solutions in comparison to the trioxane solutions at high stretch is the surface temperature (see Table A4-2 for PMMA with surface radiation). The trioxane surface is 388 K. The surface temperature of the PMMA solutions was calculated from the Arrhenius equation for the solid and was found to be 675 K at the extinction limit shown in Figure A4-7. Since emission is proportional to the fourth power of temperature, the surface emission effect is much stronger for the PMMA solutions.

Following the curve from right to left, we observe a peak temperature of 2216 K at a stretch rate of 0.4 s^{-1}. As stretch rate decreases, the radiative emission begins to dominate the solution, leading to lower temperatures and weaker flames. Radiative quenching occurs at 0.011 s^{-1} and a maximum flame temperature of 1013 K. Again, the trioxane flame is sustained at a lower stretch rate than that observed in Figure A4-7 for PMMA primarily due to surface temperature differences, resulting in weaker surface emission for the trioxane flame.

Flame Temperature Profiles: We calculate the maximum flame temperature for each solution in the domain (Figure 6-26a). Figure 6-26b gives several representative flame temperature profiles. We choose solutions to compare with the adiabatic temperature profiles in Figure 6-2, at a low stretch rate (5 s^{-1}), middle stretch rate (98 s^{-1}), and the blow-off limit (turning point at 1942 s^{-1}). We also include the radiative extinction turning point temperature profile (a=0.011 s^{-1}), along with a profile from the region on the left side of the isola, above the turning point (a=0.025 s^{-1}). The figure shows that the temperature profiles are quite different, due to changes in the flow regime as well as radiative emission from the surface. As before, the high stretch solutions are blown against the surface. As stretch rate decreases, the flame moves away from the surface, and reaches a maximum temperature. In the region where surface radiation effects become important, the flame temperature decreases, while the flame continues to move away from the surface. Prior to extinction, the flame can no longer sustain the large standoff distance, and 'falls back' towards the surface. This drop-off toward the surface before extinction was also observed in the PMMA study (Figure A4-5) for all but the absorbing, non-emitting surface.

Consistent with the results of Appendix 4, including surface radiation in the trioxane flame has introduced a flame structure not seen in the adiabatic solution; that is, a low temperature, low stretch rate regime.

Burning Rate: The burning rate of the flame is presented in a format that allows comparison with the results of Appendix 4. Figure A4-8 gives the nondimensional burning rate for the PMMA fuel. Figure 6-27(a) presents the burning rate in a nondimensional form that is easily compared to the results of Appendix 4. Here, the burning rate is presented nondimensionally in an equivalent form to Equation A4-13:

$$\frac{\dot{m}\,|_{x=0}}{\sqrt{\rho_o \mu_o a}} = \frac{2F\,|_{x=0}}{\sqrt{\rho_o \mu_o a}}$$

It allows us to observe the trend of the burning rate of trioxane in comparison with the PMMA results. Figure 6-27(a) shows this quantity versus the stretch rate for both the adiabatic flame and the flame with surface radiation. When compared to the PMMA solution in Figure A4-8, we see that the radiative trioxane flame behaves very much the same. The flame with surface radiation has a uniformly lower burning rate. At very low stretch, the burning rate decreases toward the extinction limit, due to the low flame temperatures.

Figure 6-27(b) illustrates the dimensional burning rate, $\rho u|_{x=0}$, since this is of more interest for engineering purposes. Note this is plotted on a log-log scale, and the effects of the surface radiation flame is apparent at the lower stretch rates.

Species Profiles: The species profiles for the five stretch rates under examination are presented in Figures 6-28 through 6-43. They are ordered by increasing stretch rate, and the species are grouped by order of magnitude. Note changes in domain so that the full range of species profile is visible. The flame temperature profiles are included for reference.

The species profiles at a=5, 98, and 1942 s^{-1} (Figures 6-28 through 6-43), along with the foregoing temperature profiles, establish that the surface radiation solutions are virtually identical to the adiabatic solutions for these stretch rates. They are presented here to confirm this fact; the reader is referred to the foregoing discussion on the adiabatic solutions for these stretch rates.

We turn to the lower stretch solutions (Figures 6-28, 6-29, 6-30, 6-31, 6-34, 6-35, 6-36, 6-39, 6-40, 6-41) to examine the effects of surface radiation on the species distribution in the flame. Scaling necessitates a different grouping of species for the low stretch cases. Starting with the fuel, we observe that the initial mole fraction of fuel at the surface is greatly reduced at the lower stretch rates, from approximately 0.35 at a =5 s^{-1} to 0.09 and 0.03 for $a = 0.025$ s^{-1} and 0.011 s^{-1}, respectively. Mole fractions of formaldehyde are reduced accordingly, however, the shape of the formaldehyde curve differs at low stretch. Rather than peaking away from the surface, the formaldehyde mole fractions are relatively constant close to the surface, and then decrease. This indicates that formaldehyde accumulates (it is produced faster than it is consumed) in the low temperature region near the surface, and is not rapidly depleted until it reaches the higher temperature region of the flame, which is located at a large standoff distance. CO, CO_2, H_2O, and H_2 behaviors are similar, for the same reasons.

HCO, because it is the primary product of the formaldehyde decomposition, appears nearer to the surface than other intermediate radicals. The reduced mole fractions of fuel and formaldehyde result in reduced mole fractions of HCO.

Among the intermediate radicals H, O, and OH, we see the emphasis on the OH radical continued from a=5 s^{-1} to a=0.025 s^{-1}. However, at the low stretch turning point, H dominates, echoing the emphasis on H at the high stretch turning point. The profiles of H_2O_2 and HO_2 at the low stretch turning point exhibit a different character than the other low stretch cases, indicating that a different reaction path is present here. This is explored further in the following sections. The H_2O_2 profile is similar to the high stretch turning point, rather than other low stretch cases. On the other hand, HO_2 is present in the high temperature region of the low stretch turning point flame, as opposed to the low temperature, fuel-rich region of the high stretch turning point flame. Note that these two HO_2 peaks do occur at the same local temperature (around 1000 K).

The primary purpose of the surface radiation solution is to distinguish the effects of surface and gas phase radiation, and the surface radiation solution is somewhat artificial. Therefore, we do not pursue the reaction path analysis here. Reaction path analysis and turning point sensitivity are discussed for the flame with gas phase and surface radiation.

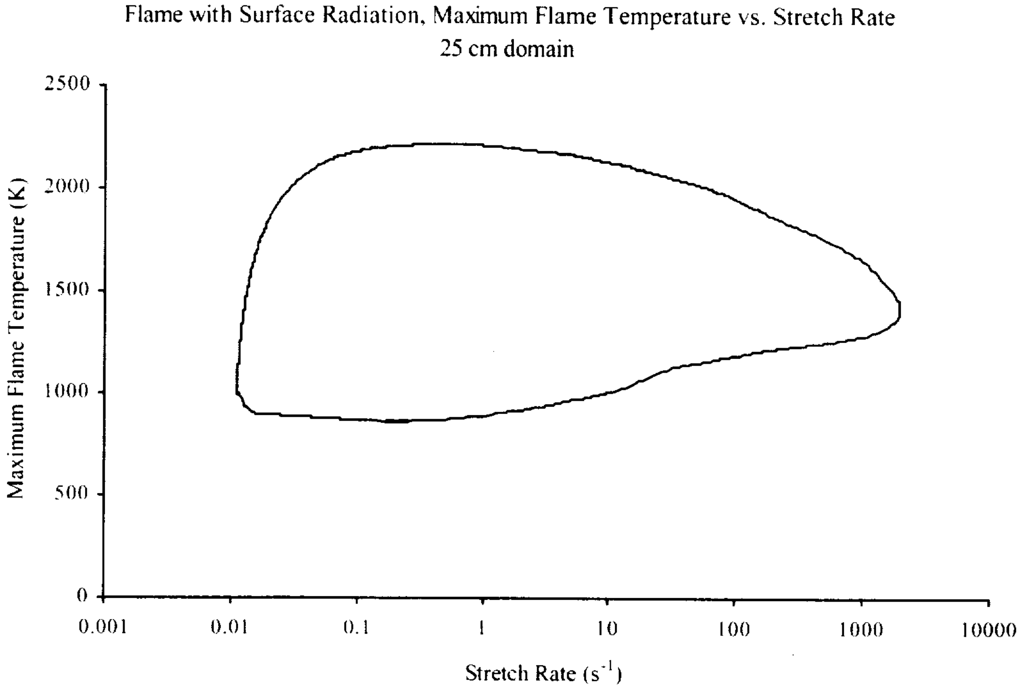

Figure 6-26(a): Maximum flame temperature vs. stretch rate for flame with surface radiation.

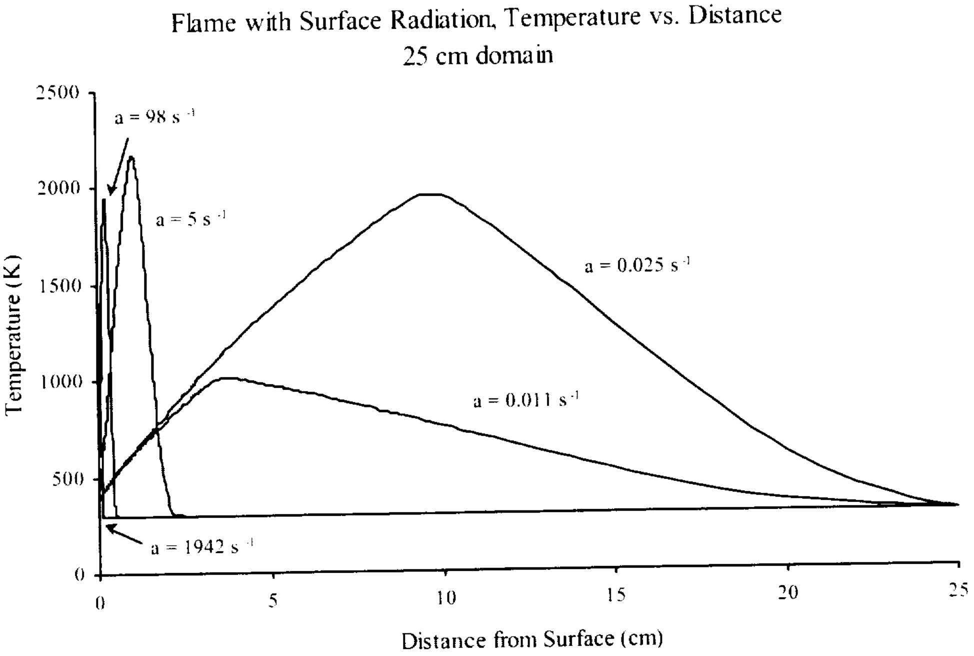

Figure 6-26(b): Temperature profiles for flame with surface radiation.

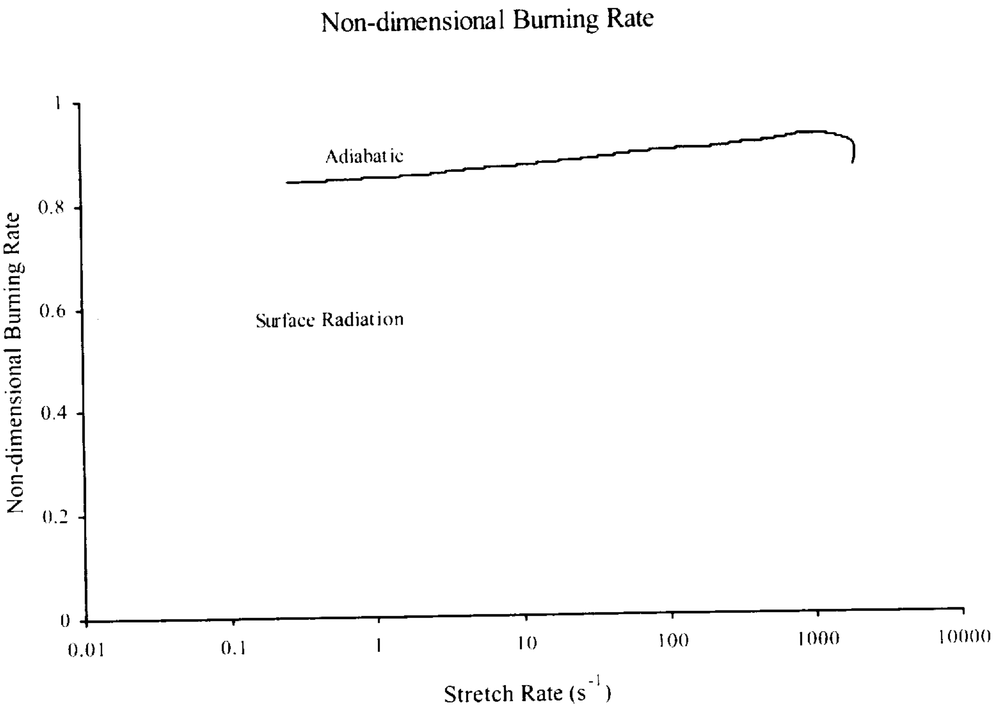

Figure 6-27(a): Nondimensional burning rate vs. stretch rate for adiabatic flame and flame with surface radiation.

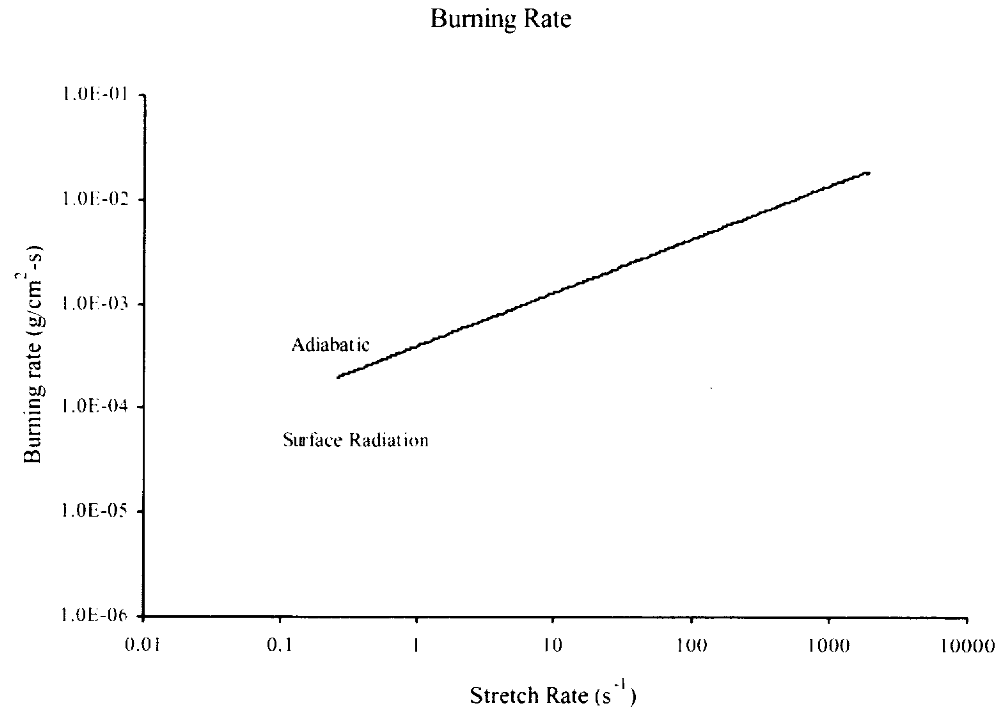

Figure 6-27(b): Dimensional burning rate vs. stretch rate for adiabatic flame and flame with surface radiation.

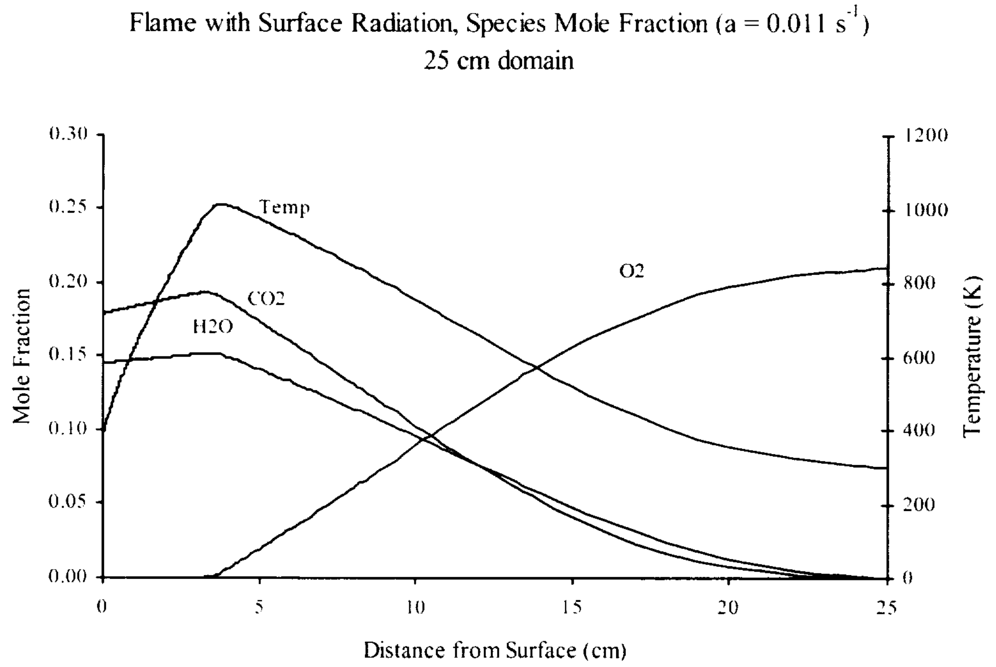

Figure 6-28: Species profiles of O_2, CO_2, and H_2O for radiative extinction turning point (flame with surface radiation).

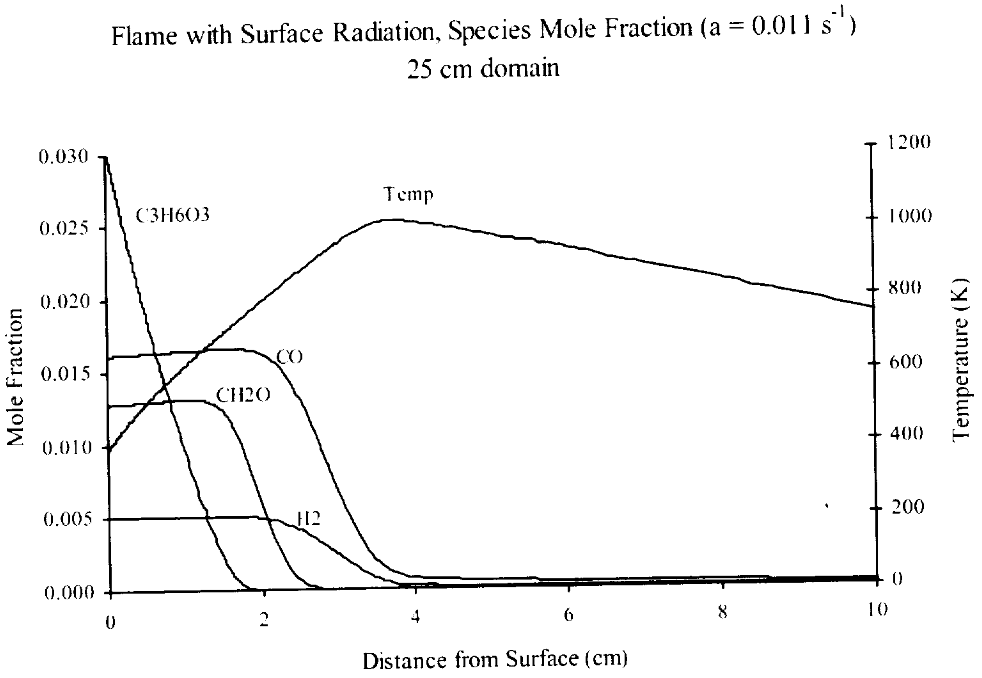

Figure 6-29: Species profiles of $C_3H_6O_3$, CO, CH_2O, and H_2 for radiative extinction turning point (flame with surface radiation).

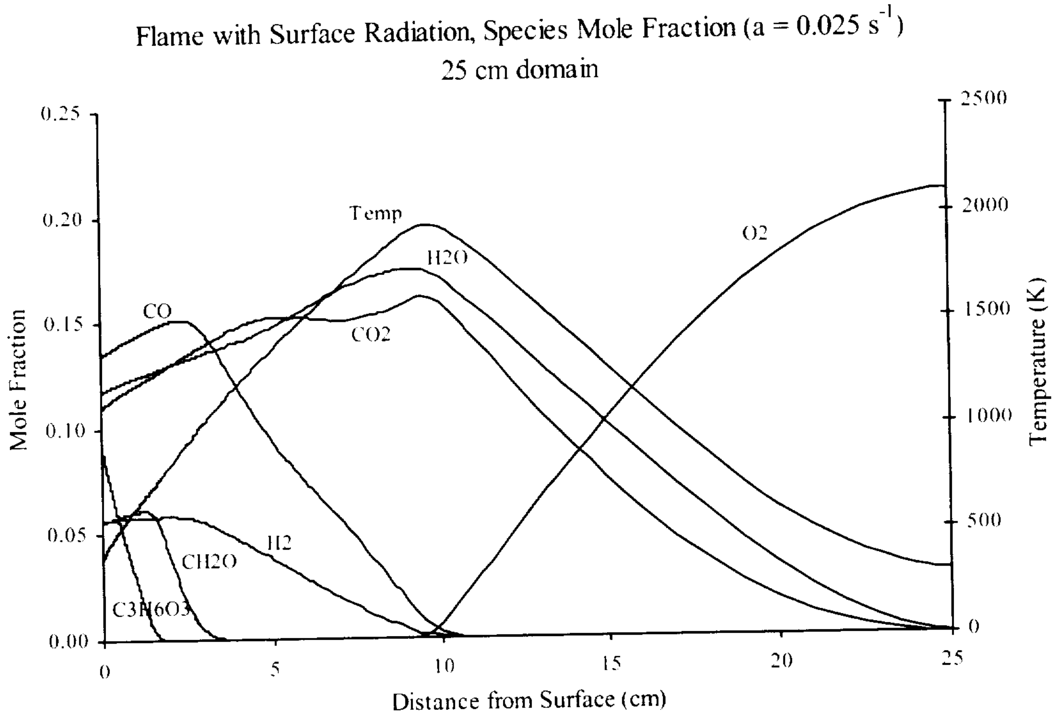

Figure 6-30: Major species profiles for very low stretch rate (flame with surface radiation).

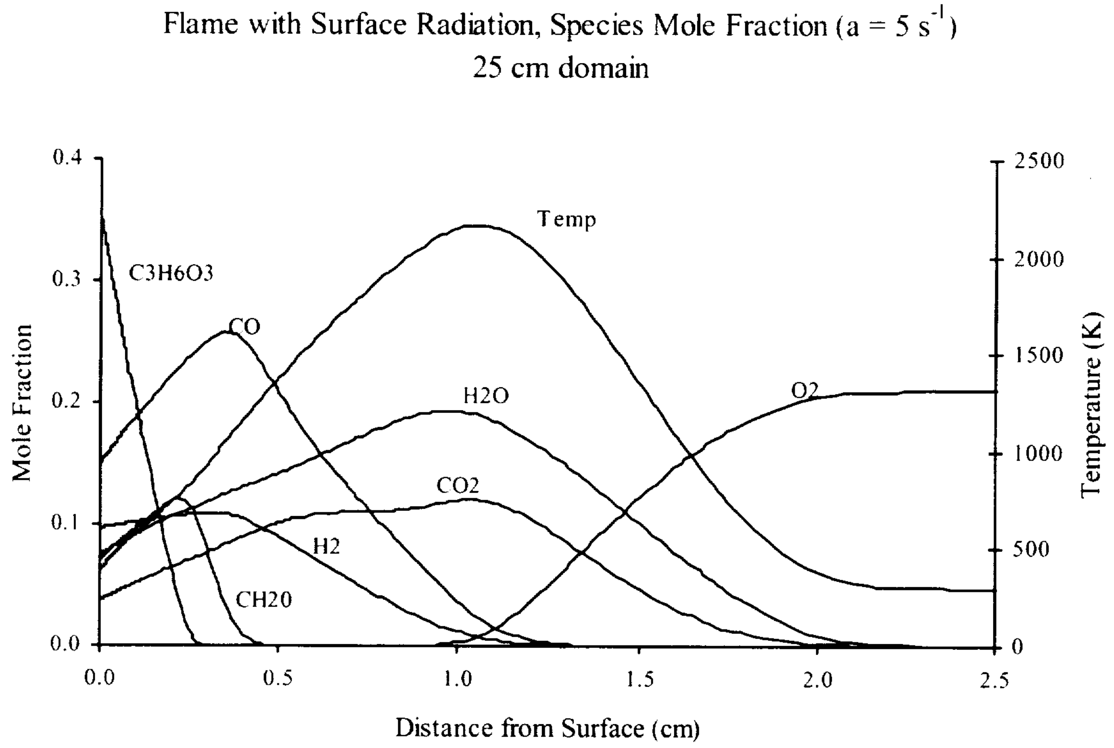

Figure 6-31: Major species profiles for low stretch rate (flame with surface radiation).

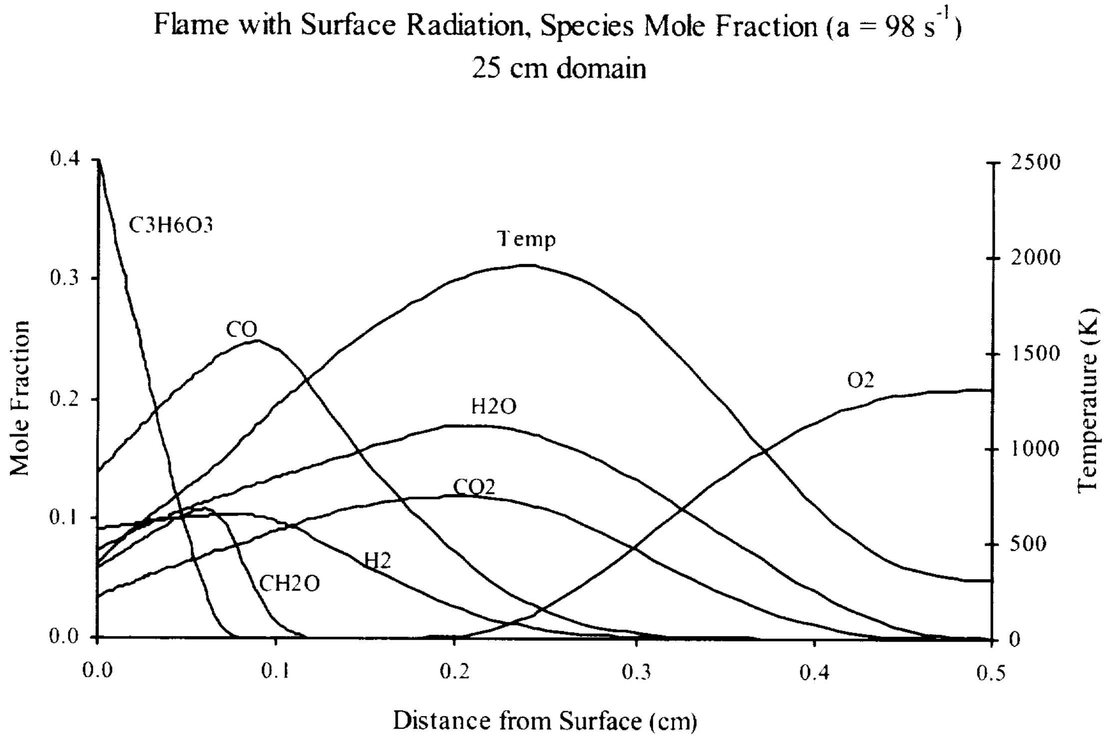

Figure 6-32: Major species profiles for mid-stretch rate (flame with surface radiation).

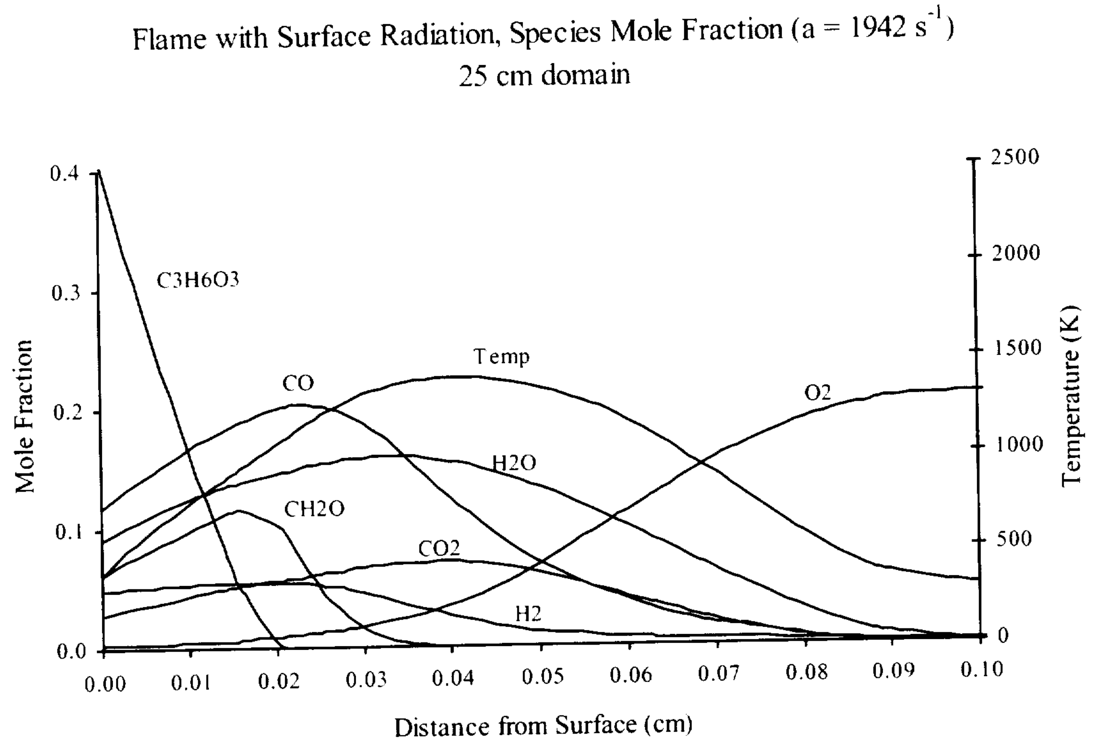

Figure 6-33: Major species profiles for blow-off turning point (flame with surface radiation).

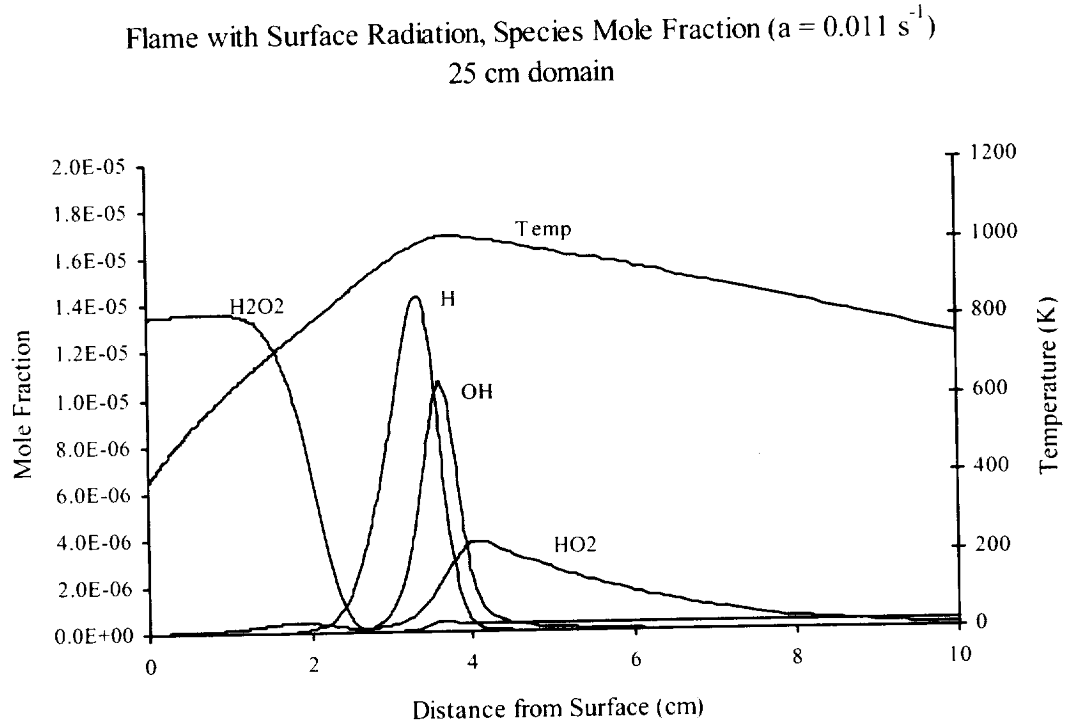

Figure 6-34: Species profiles of H_2O_2, H, OH, and HO_2 for radiative extinction turning point (flame with surface radiation).

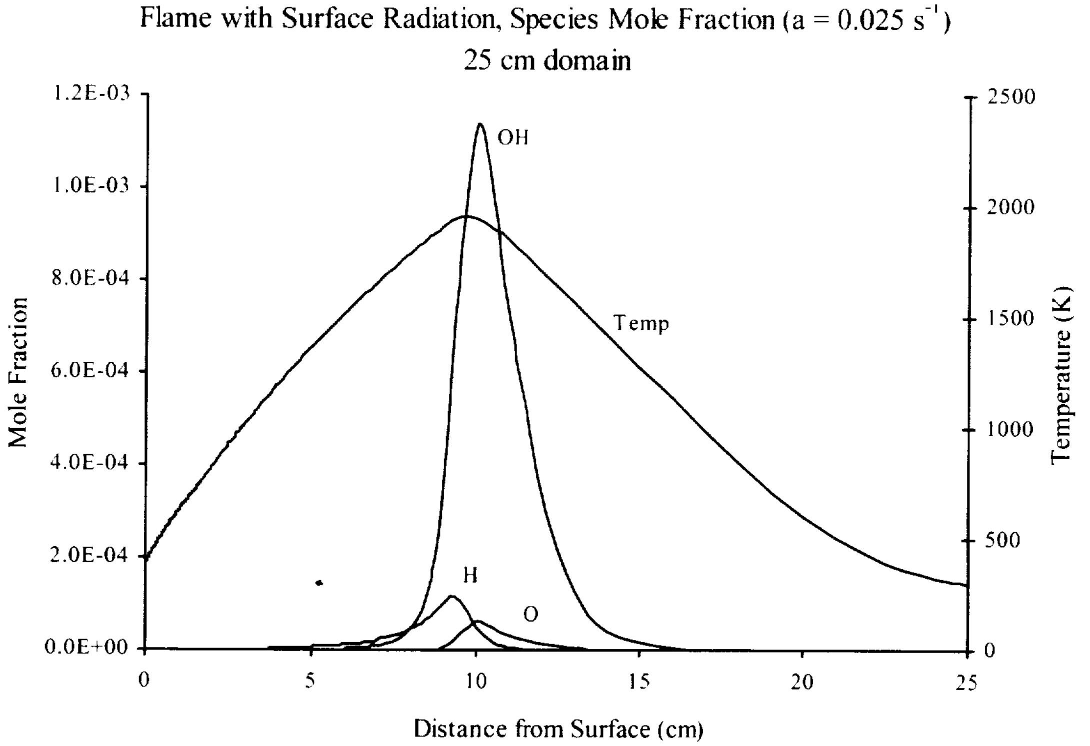

Figure 6-35: Species profiles of H, O, and OH for very low stretch rate (flame with surface radiation).

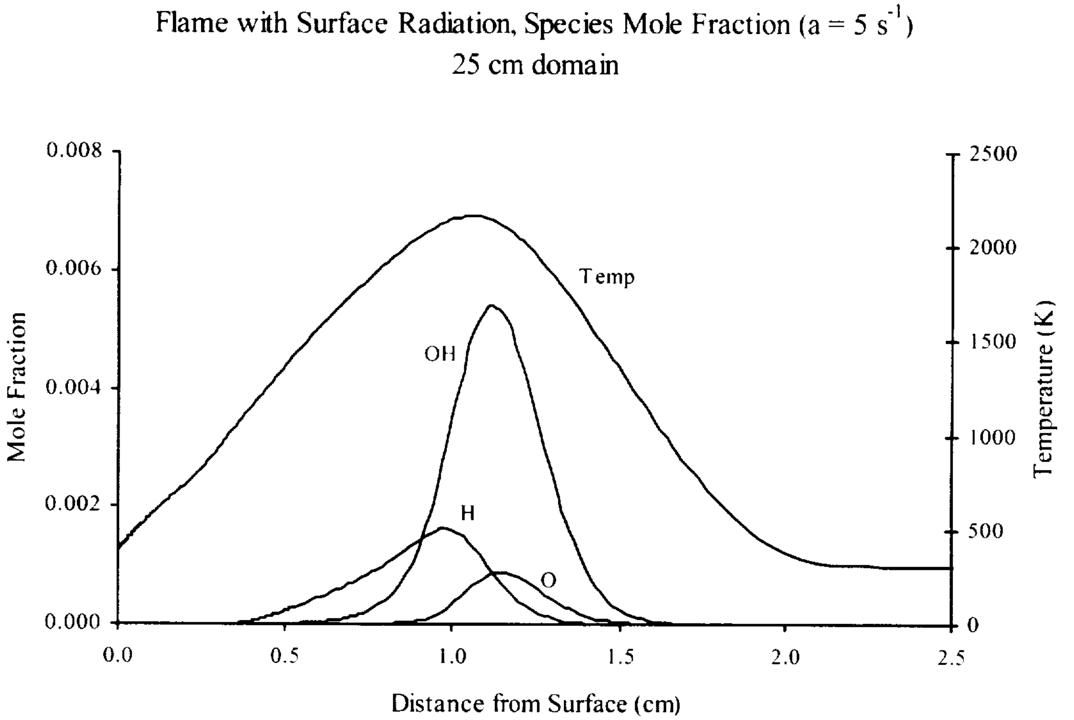

Figure 6-36: Species profiles of H, O, and OH for low stretch rate (flame with surface radiation).

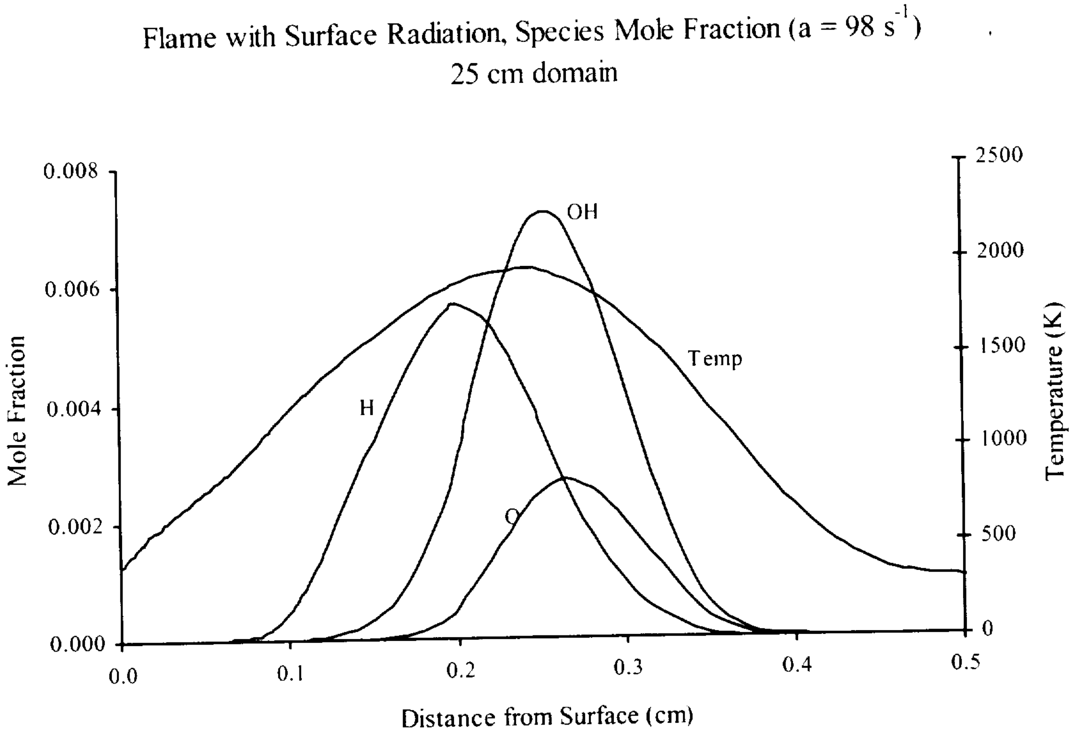

Figure 6-37: Species profiles of H, O, and OH for middle stretch rate (flame with surface radiation).

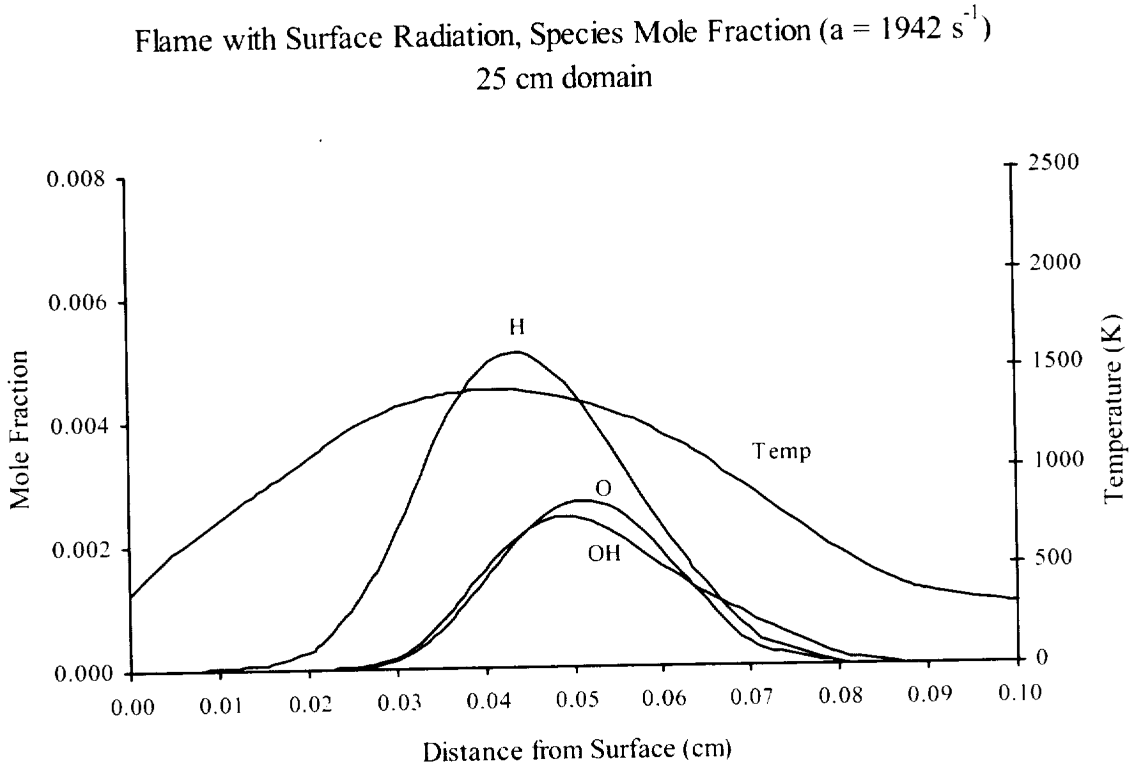

Figure 6-38: Species profiles of H, O, and OH for blow-off turning point (flame with surface radiation).

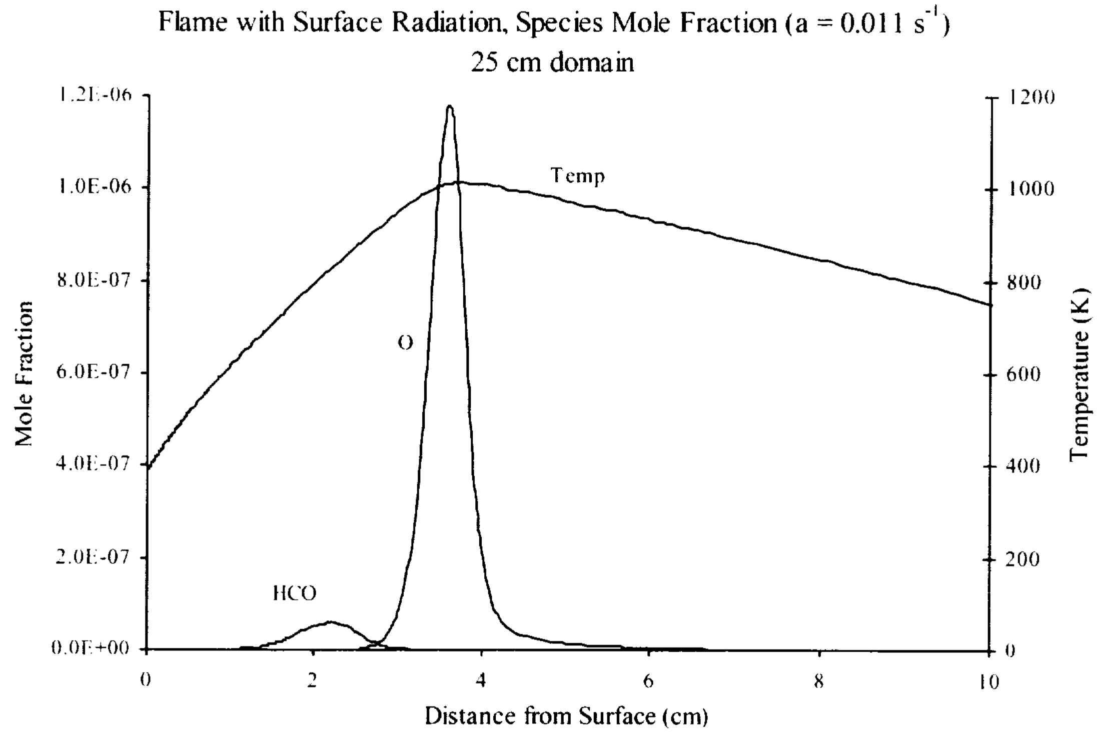

Figure 6-39: Species profiles of HCO and O for radiative extinction (flame with surface radiation).

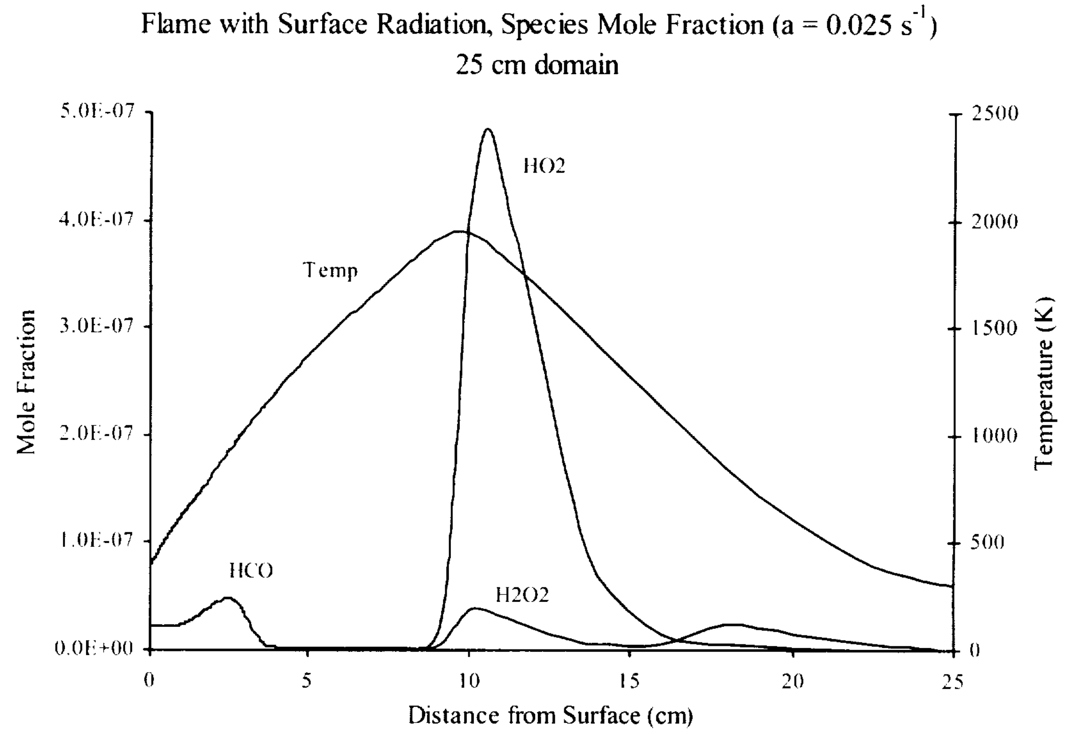

Figure 6-40: Species profiles of HO_2, H_2O_2, and HCO for very low stretch rate (flame with surface radiation).

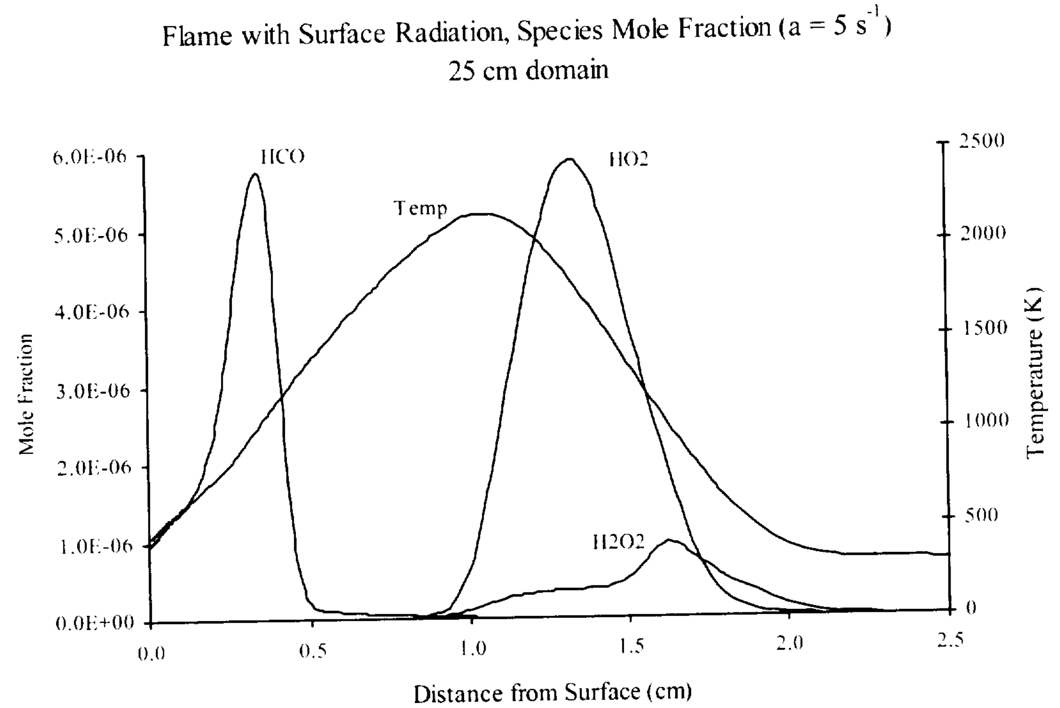

Figure 6-41: Species profiles of HO_2, H_2O_2, and HCO for low stretch rate (flame with surface radiation).

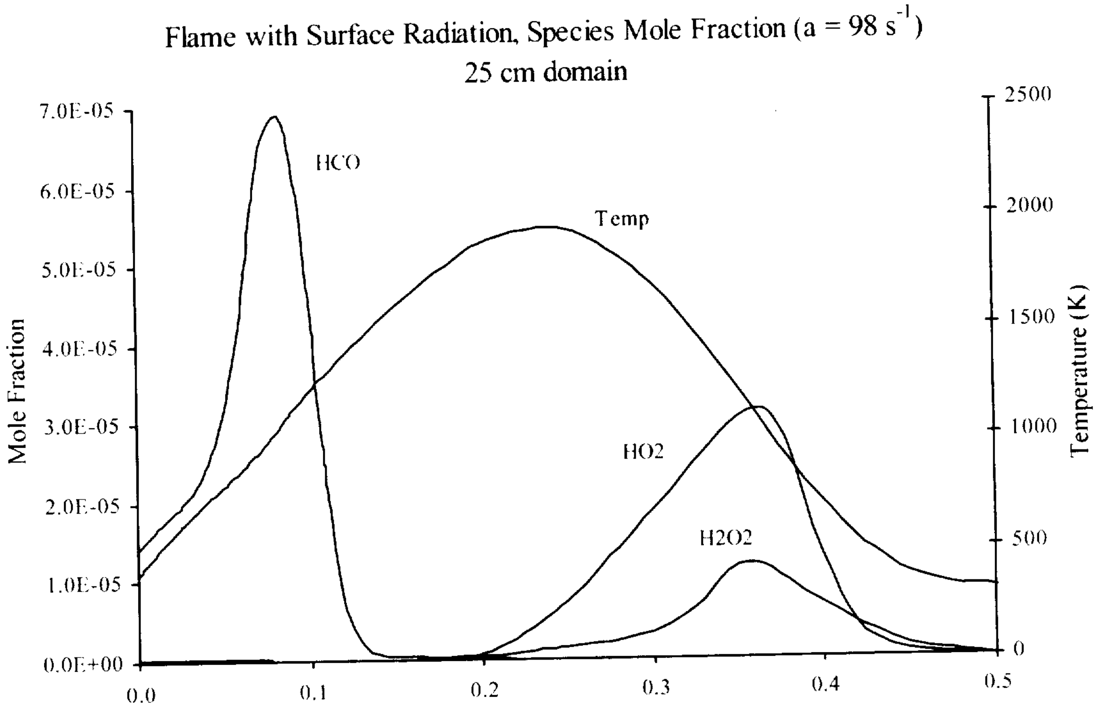

Figure 6-42: Species profiles of HO_2, H_2O_2, and HCO for middle stretch rate (flame with surface radiation).

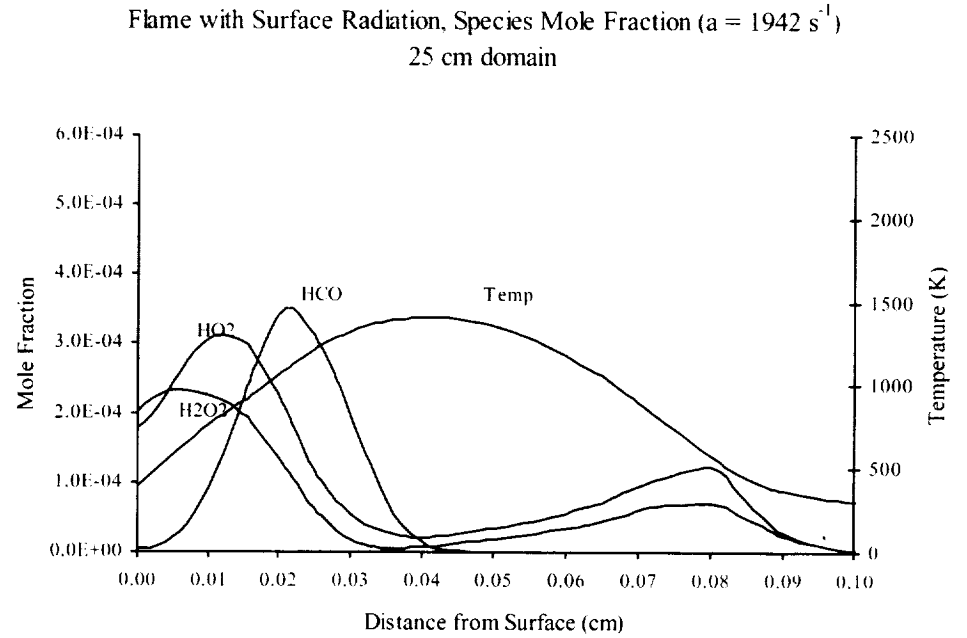

Figure 6-43: Species profiles of HO_2, H_2O_2, and HCO for blow-off extinction (flame with surface radiation).

6.4 Effects of Gas-Phase and Surface Radiation

We now turn to the 'full solution' that includes both surface and gas-phase radiation in the stagnation-point diffusion flame. This solution, using both detailed kinetics and the narrowband radiative model, yields the most accurate model available for the solid trioxane flame.

We solved, using the narrowband formulation for gas-phase radiative participation by CO_2, CO, and H_2O described in Section 3.4. The model includes black-body emission ($\varepsilon = 1.0$) and absorption ($\alpha=1.0$) by the surface, as well as black-body emission at the oxidizer side boundary. We also use the domain of 20 cm, used for the adiabatic flame. All cases are run in standard air and at standard atmospheric pressure. The surface temperature is set to 388 K, which is the boiling point of trioxane. We refer to these solutions in the discussion as the 'flame and surface radiation' solutions.

Flammability Domain: Figure 6-44 is a plot of the maximum flame temperature versus stretch rate for the entire flammability domain that compares the three global flame cases: 'adiabatic,' 'surface radiation,' and 'flame and surface radiation' for the trioxane flame. The full solution isolas, including the unstable solutions, are presented. Note that the low stretch extinction turning point for the flame and surface radiation case is not shown, due to numerical difficulties described in Section 5.0 that are possibly caused by the transient instability at the low stretch turning point. The figure shows the expected low stretch extinction limit observed in Appendix 4, in contrast to the adiabatic solutions. In comparison to Figure A4-7, while the materials and the surface temperatures are quite different, the trend is the same. We observe that the solutions for the 'flame and surface radiation' at low stretch rates are uniformly lower in temperature than the 'surface radiation' cases, and that extinction occurs at a higher stretch rate.

The blow-off extinction limit (1944 s^{-1} at T_{max}=1415 K) is nearly identical to that of the adiabatic solution (1952 s^{-1} at T_{max}=1417 K) as well as the 'surface radiation' solution. In this regime, the gas-phase and surface losses have virtually no effect (This is further explored in the radiative flux analysis section that follows.). We contrast this with Figure A4-7, where surface radiation effects are small, but noticeable in the high stretch regime. As with the surface radiation solutions, the emission is proportional to the fourth power of temperature, and the surface emission effect is much stronger for the higher surface temperature PMMA solutions. Furthermore, even though gas-phase radiation is included, the flame is so thin in the high stretch region, that the rate of gas radiative loss is negligible in comparison to the rate of combustion heat generation.

Following the curve from right to left, we observe a peak temperature of 2001 K at a=22 s^{-1}. As stretch rate decreases, the radiative losses begin to dominate the solution, leading to lower temperatures and weaker flames. Radiative quenching occurs near a=0.068 s^{-1} and a maximum flame temperature of 997 K. This quench limit is higher stretch than that of the 'surface radiation' case, due to the additional flame radiation heat losses. The differences in the shapes of the low stretch curves are entirely due to flame radiation losses. The quench limit and the blow-off limit are not the same temperature, and both quench limits are due to reaction rate limitations [Bedir 1998]. The blow-off limit is due to limited reaction time at high stretch, while the quench limit results from too low a flame temperature because of radiative loss. This is further explored in the global radiative flux discussion that follows.

Flame Temperature Profiles: We calculated the maximum flame temperature for each solution in the domain, as shown in Figure 6-44. Several representative flame temperature profiles are given in Figure 6-45. We then chose solutions to compare with the adiabatic and surface radiation temperature profiles in Figure 6-2, at the blow-off limit (turning point at a=1942 s^{-1}) and the low stretch case (a=5.0 s^{-1}). We also include the case near the radiative extinction turning point temperature profile (a=0.068 s^{-1}), along with a profile from the region on the left side of the isola, above the turning point (a=1.0 s^{-1}). The figure shows that the temperature profiles are quite different, due to changes in the flow regime as well as radiation from the system. As before, the high stretch solutions are blown against the surface. As stretch rate decreases, the flame moves away from the surface, and reaches a maximum temperature. The gas radiation effects become apparent where the flame temperature begins to deviate from the adiabatic and surface radiation curves ($a\approx100$ s^{-1}). Flame temperature begins to drop where $a<$ 25 s^{-1}. The drop-off in the standoff distance toward the surface before extinction that is observed in the PMMA study (Figure A4-5) is not observed here, although the solutions near the turning point demonstrate a leveling off of the flame standoff distance, indicative of an imminent 'fall' toward the surface at extinction.

Burning Rate: The burning rate of the flame is presented in a format that allows comparison with the results of Appendix 4. Figure A4-8 gives the nondimensional burning rate for the PMMA fuel. Figure 6-46a presents the burning rate in a nondimensional form that is easily compared to the results of Appendix 4. Here, the burning rate is presented nondimensionally in an equivalent form to Equation (A4-13):

$$\frac{\dot{m}\big|_{x=0}}{\sqrt{\rho_o \mu_o a}} = \frac{2F\big|_{x=0}}{\sqrt{\rho_o \mu_o a}}$$

Figure 6-46(a) shows this quantity versus the stretch rate for both the adiabatic flame and the flame with gas phase and surface radiation. When compared to the PMMA solution in Figure A4-8, we see that the radiative trioxane flame behaves somewhat differently. Referring to Figure A4-6, the radiative trioxane flame behavior is similar to that of Case 2 (α=1,ε=0). This result is significant in that it confirms the findings of Appendix 4. The radiative burning rates (considering both flame and surface radiation) can be higher than the adiabatic burning rates, in the low stretch regime. This is the first demonstration of this phenomenon with a realistic solid fuel. The increased burning rate is due to the combination of the absorption of incident radiation from the flame, and the low surface temperature of the trioxane. In this case, the flame radiation absorbed by the surface dominates the surface emission. The resulting emission is much lower than that of the PMMA flame, so that the burning rate behavior is more like a non-emitting surface. At very low stretch, the burning rate decreases toward the extinction limit due to the low flame temperatures.

Figure 6-46(b) illustrates the dimensional burning rate, $\rho u/_{x=0}$, since this is of more interest for engineering purposes. Note this is plotted on a log-log scale, and the effects of the radiative flame are apparent at the lower stretch rates.

Species Profiles: The species profiles for the four stretch rates under examination are presented in Figures 6-47 through 6-59. They are ordered by increasing stretch rate, and the species are grouped by order of magnitude. Note changes in domain so that the full range of species profile is visible. The flame temperature profiles are included for reference.

The species profiles at 1944 s^{-1}, along with the foregoing temperature profiles, establish that the 'flame and surface radiation' solutions are virtually identical to the adiabatic solutions at high stretch rates (greater than a=100 s^{-1}). We present them here to confirm this fact; the reader is referred to the foregoing discussion on the adiabatic solutions for this stretch rate. When we compare the 'flame and surface radiation' case at a=5 s^{-1} to the adiabatic case at the same stretch, we see that flame radiation has reduced the maximum flame temperature (from 2175 K to 1906 K), but that the species profiles are as yet unaffected because they demonstrate the same character as the adiabatic flame.

We turn to the lower stretch solutions to examine the effects of flame and surface radiation on the species distribution in the flame. Scaling necessitated a different grouping of species for the low stretch cases. Starting with the fuel, we observe that in contrast to the 'surface radiation' solutions, the initial mole fraction of fuel at the surface is *increased* at the lower stretch rates, from approximately 0.55 at a =5 s^{-1} to 0.7 for a = 1.0 s^{-1} and 0.068 s^{-1} (due to the increase of the nondimensional burning rate at low stretch). Mole fractions of formaldehyde are reduced as stretch decreases, indicating that the conversion of fuel to formaldehyde is slowed at decreased stretch rate (in contrast to the formaldehyde accumulation observed at low stretch in the surface radiation flame).

Mole fractions of CO are reduced as stretch rate decreases, although they peak uniformly after the formaldehyde mole fraction peak. In addition, at higher stretch (e.g. a=5 s^{-1}), CO is produced in larger quantities than formaldehyde. At a=1 s^{-1}, they are produced in approximately equal quantities, and at a=0.068 s^{-1}, formaldehyde is produced in larger quantities. This is indicative of an alternate reaction path at very low stretch, and is examined in the detailed reaction path analysis that follows. We observe a similar trend with products CO_2 and H_2O. H_2O is produced in larger quantities at higher stretch (a=5 s^{-1}), but equivalent quantities at very low stretch (a=0.068 s^{-1}), further supporting an alternate reaction path at very low stretch. H_2 is produced in much smaller quantities at very low stretch, in contrast to the higher stretch cases.

HCO, because it is the primary product of the formaldehyde decomposition, peaks closer to the surface than other intermediate radicals, except near the quench limit. Near radiative extinction, the HCO peak is located closer to the other radical peaks (Figure 6-53). Note also that, near the quenching turning point, the characters of the HO_2 and H_2O_2 profiles change dramatically. The combination of changes in these profiles (HO_2. H_2O_2, and HCO) lends further support to an alternate (branching) reaction path near the quench limit, with HO_2 and H_2O_2 featured with formaldehyde. This is further addressed in the reaction pathway analysis that follows.

Among the intermediate radicals H, O, and OH, we see the emphasis on the OH radical continued from a=5 s^{-1} to a=1 s^{-1}. However, near the low stretch turning point, H dominates, echoing the emphasis on H at the high stretch turning point. The H_2O_2 profile has a similarity to the high stretch turning point, rather than other low stretch cases. Also, comparing HO_2 for both turning points, both exhibit two peaks, one before the peak flame temperature, and one behind the peak flame temperature, although the peaks are reversed in relative magnitude. The peak of HO_2 on the fuel side at the high stretch limit (Figure 6-59) is a result of low temperature and more O_2 leakage (order 10^{-3}) into the fuel side, as pointed out in Section 6.1. In comparison, the O_2 present at the smaller fuel side HO_2 peak due to diffusion at low stretch (Figure 6-53) is order 10^{-4}.

Radiative Flux Analysis: The radiative fluxes and radiative source term are examined for each of the sample stretch rates (Figures 6-60 through 6-67) to shed some light on the effect of radiation on the solutions. The fluxes are labeled as follows:

- The q^+ is the radiative flux from the surface in the positive x direction. At the surface, this flux is representative of the surface emission. Observe that q^+ at $x=0$ is constant, due to the constant surface temperature. As temperature increases away from the surface, and the concentrations of the participating gases increase, the q^+ increases as well. The subsequent decrease in q^+ is due to absorption. At the flame edge, this flux is representative of the radiative loss from the system. Note that this loss at the flame edge is larger at higher temperatures (higher emission).
- The q^- is the radiative flux toward the surface. At the edge of the flame, this is representative of the background black-body radiation. Moving from the edge to the flame, the q^- increases due to emission from the flame. At the surface, the q^- represents the incident radiation at the surface, which is fully absorbed by the black surface ($\alpha=1$).
- The q_{net} is the net radiative flux: $q_{net}=q^+-q^-$. A negative q indicates a net radiative gain by the surface, because more radiation is absorbed than emitted.
- The dq_{net}/dx is the radiative source term that appears in the energy equation (Equations (3-1(f)) and (3-6). A positive dq_{net}/dx indicates a loss due to emission from the participating species in the flame, and a negative dq_{net}/dx indicates a gain due to absorption by the participating species.

Temperature profiles are provided in the plots as well for convenience. Comparing the radiative fluxes over the sample stretch rates, we see that for all but the blow-off turning point, there is a negative net radiation between the surface and the flame, indicating that emission from the flame dominates the surface emission. At the blow-off limit, radiation is relatively unimportant. This is more apparent in the following section, where radiative flux is compared to conductive flux. The q_{net} is positive beyond the flame in the presence of larger amounts of H_2O and CO_2 and high temperatures. This is where the flame emits the most radiation, as indicated by the increase in q^+. The almost flat q_{net} profile at the blow-off turning point indicates that the flame is optically thin, with very little absorption.

The radiative source term, dq_{net}/dx, increases with increasing temperature, and peaks at the maximum temperature location. In the center of the flame, the gas is emitting radiation, indicated by the positive source term. For all but the blow-off limit, we see a small negative region on either side of the flame, where the slope of q_{net} is negative. These are the regions where the gas is absorbing radiation.

Global Radiative Fluxes: The radiative fluxes over the entire stretch rate regime are presented in Figure 6-68. The radiative fluxes (similar to Section A4.4.3) presented are:

- $q_{net,e}$: net radiative flux from the flame edge to the surroundings (loss from the system)
- q^-_w: radiative flux from the flame to the surface (absorbed by black surface)
- q^+_w: radiative flux from the surface to the flame (emission from surface)
- $q_{net,w}$: net radiative flux from the surface

Note that, since the surface temperature is held constant, q^+_w is constant. The net system radiative loss, $q_{net,e}$, peaks between a=1 and 10, and is lower at both the high stretch and low stretch limits. The maximum loss is not at the location of maximum flame temperature (a=22 s^{-1}), but somewhat lower stretch rate; showing that the flame is not optically thin in this region and that the flame has significant absorption. The radiation absorbed by the surface, q^-_w, follows the same trend, for the same reasons, since its source is the flame, as well. The net radiative flux from the surface, $q_{net,w}$, illustrates the feedback from the flame that leads to the burning rate increase at low stretch rate. The feedback from the flame to the surface is negative for most of the domain, indicating that the flame heat loss is a heat gain for the surface.

To fully understand the effect of the radiation, however, we must compare it to both the conduction at the surface and the heat generation in the flame. It is the decrease in the conduction to the fuel and flame heat generation terms *in comparison* to the radiation losses that lead to quenching of the flame. That is, the conduction to the fuel and the heat generation by the flame each decrease more rapidly than the radiation, so that the *relative importance* of the radiation increases. Figures 6-69(a), 6-69(b) and 6-69(c) illustrate this point.

Figure 6-69(a) is a plot of the net radiative heat flux to fuel/conductive heat flux to fuel

$$\frac{-q_{net,w}}{\lambda_g\left(\frac{dT}{dx}\right)_{x=0}}$$

versus the stretch rate. At high stretch rate, the radiation is negligible, but as stretch decreases, the importance of the radiation flux from the surface becomes apparent. Figure 6-69(b) is a plot of the surface conduction (denominator of above) versus stretch rate. Note the log-log scale. Conduction falls off at low stretch rate due to the increase of flame standoff distance. The ratio in Fig 6-69(a) peaks between a=0.1 and 1, as the flame radiation peaks, and the conduction diminishes. At very low stretch, the net radiative flux to the surface falls off (Figure 6-68), leading to radiative quenching.

Figure 6-69(b) shows the ratio, net radiative heat loss/heat generation

$$\frac{q_{net,e}}{\int_{x=0}^{x=l}\sum_k \omega_k h_k\,dx}$$

versus stretch rate. Here, the ratio monotonically increases with decreased stretch rate, illustrating that the increase in radiative loss as heat generation decreases leads to flame extinction.

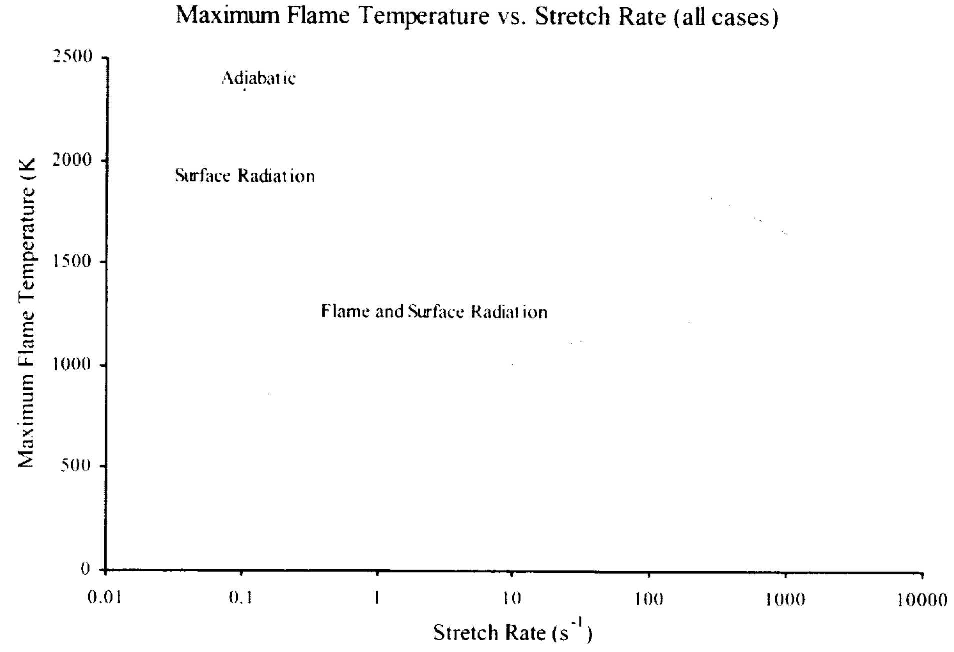

Figure 6-44: Maximum flame temperature vs. stretch rate for adiabatic flame, flame with surface radiation, and flame with gas phase and surface radiation.

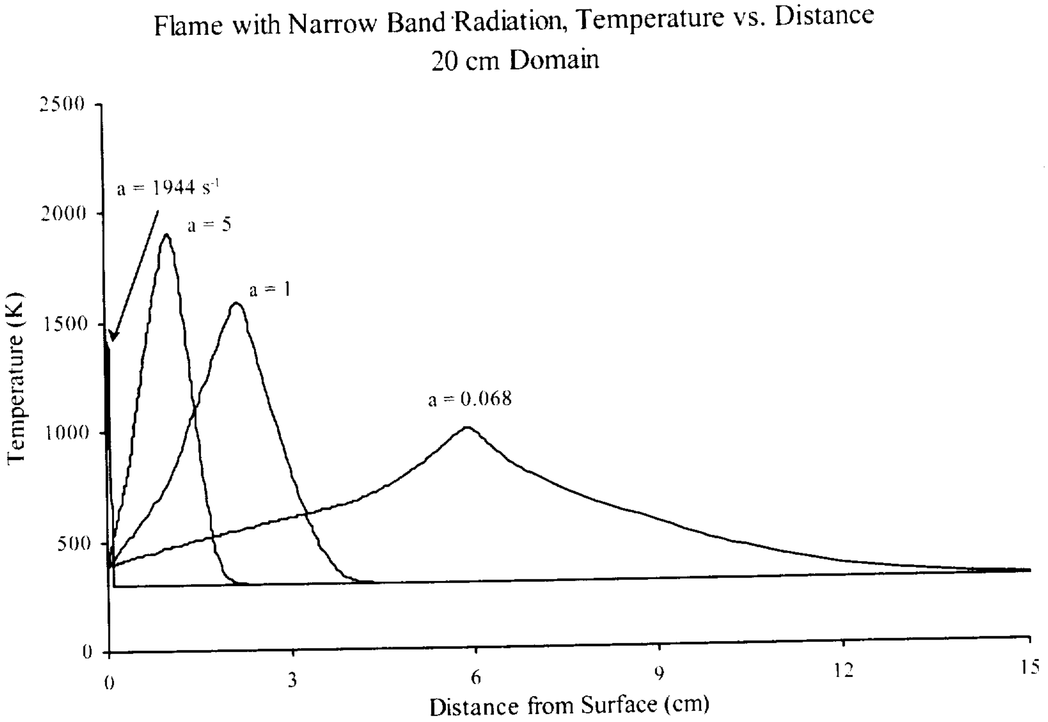

Figure 6-45: **Temperature profiles for flame with gas phase and surface radiation.**

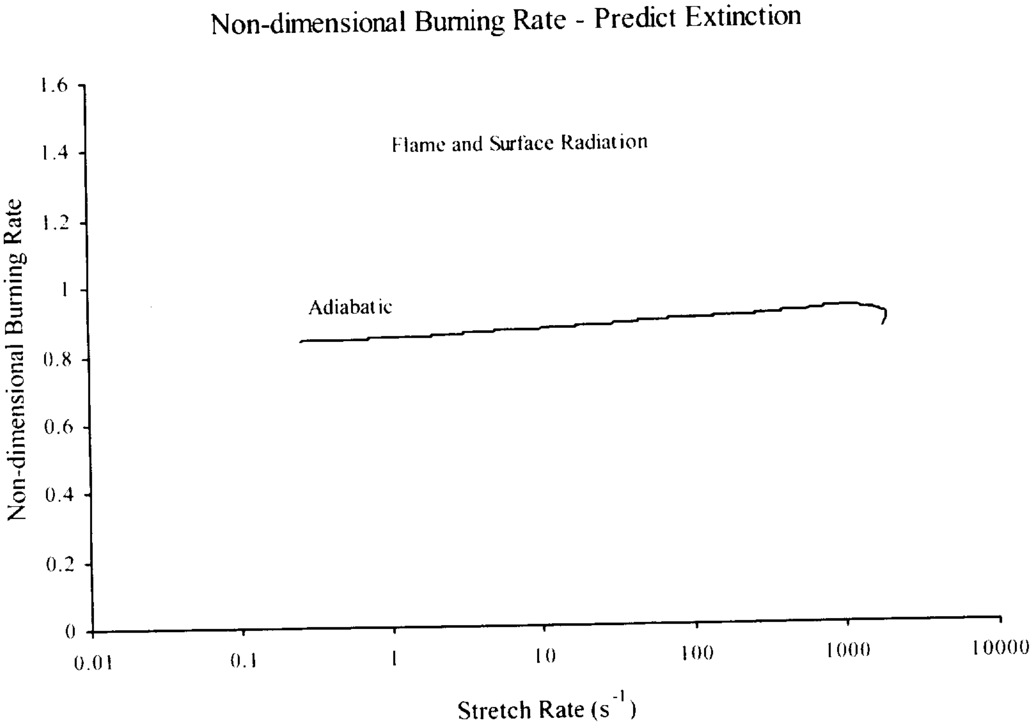

Figure 6-46(a): Nondimensional burning rate vs. stretch rate for adiabatic flame and flame with gas phase and surface radiation.

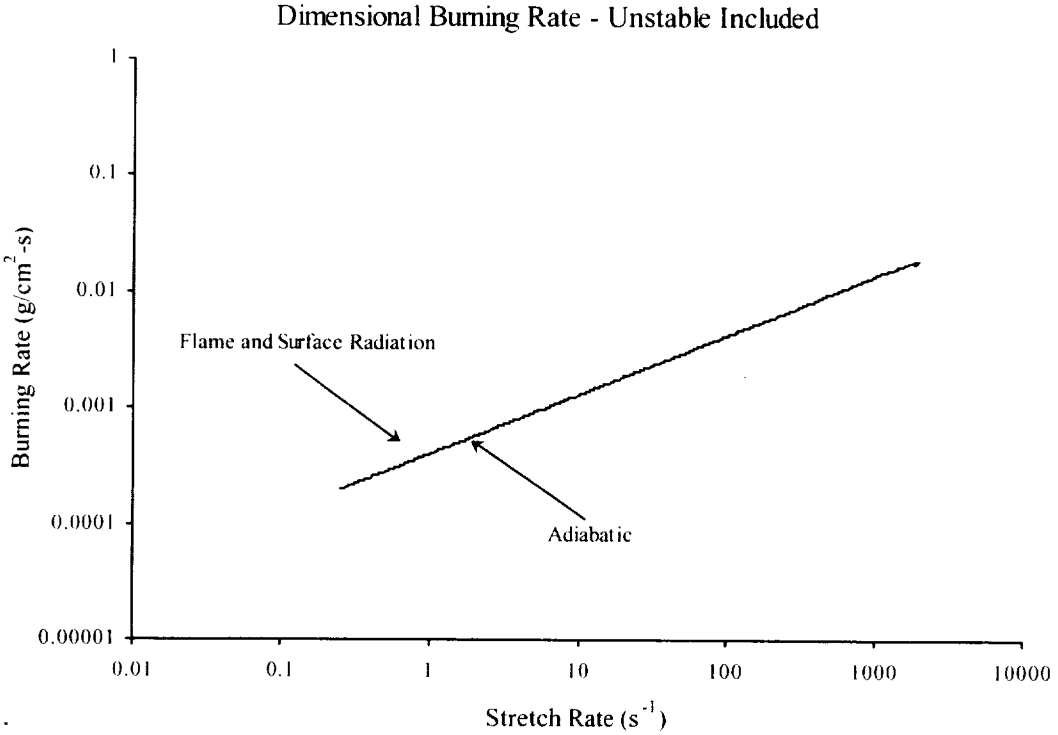

Figure 6-46(b): Dimensional burning rate vs. stretch rate for adiabatic flame and flame with gas phase and surface radiation.

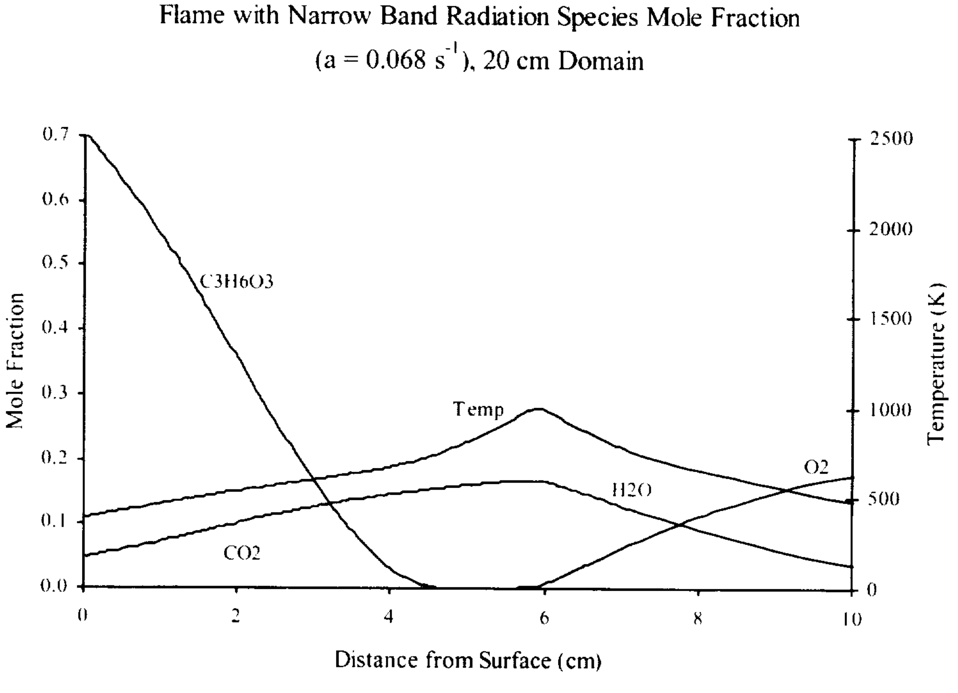

Figure 6-47: Species profiles of $C_3H_6O_3$, CO_2, O_2, and H_2O for radiative extinction turning point (flame with gas phase and surface radiation).

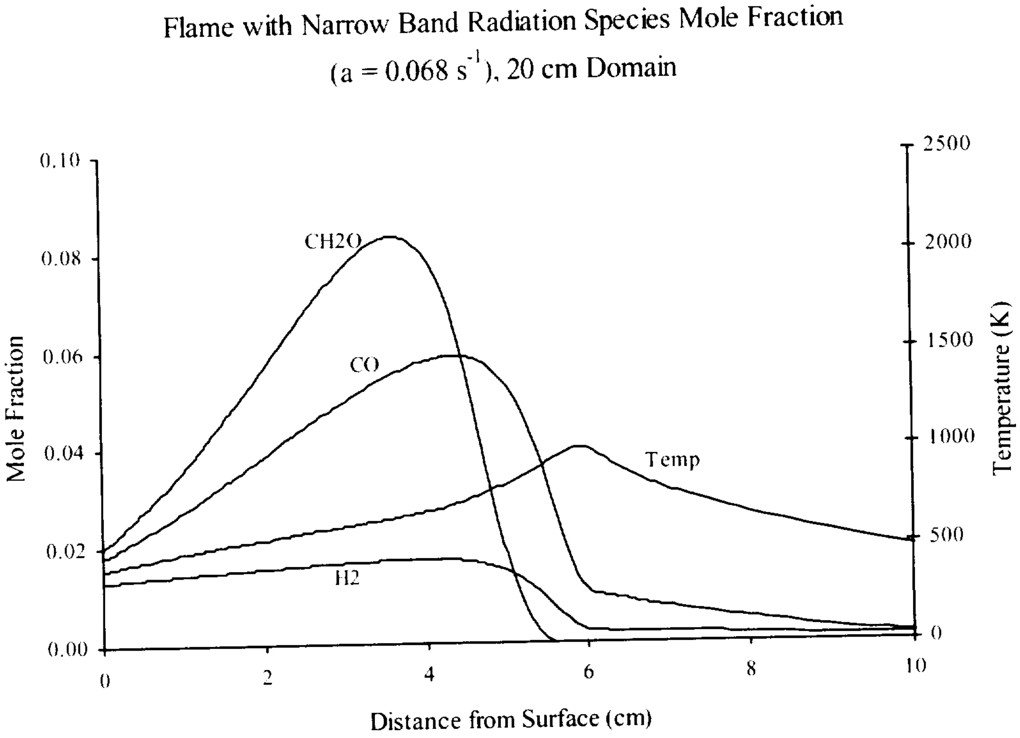

Figure 6-48: Species profiles of CH_2O, CO, and H_2 for radiative extinction turning point (flame with gas phase and surface radiation).

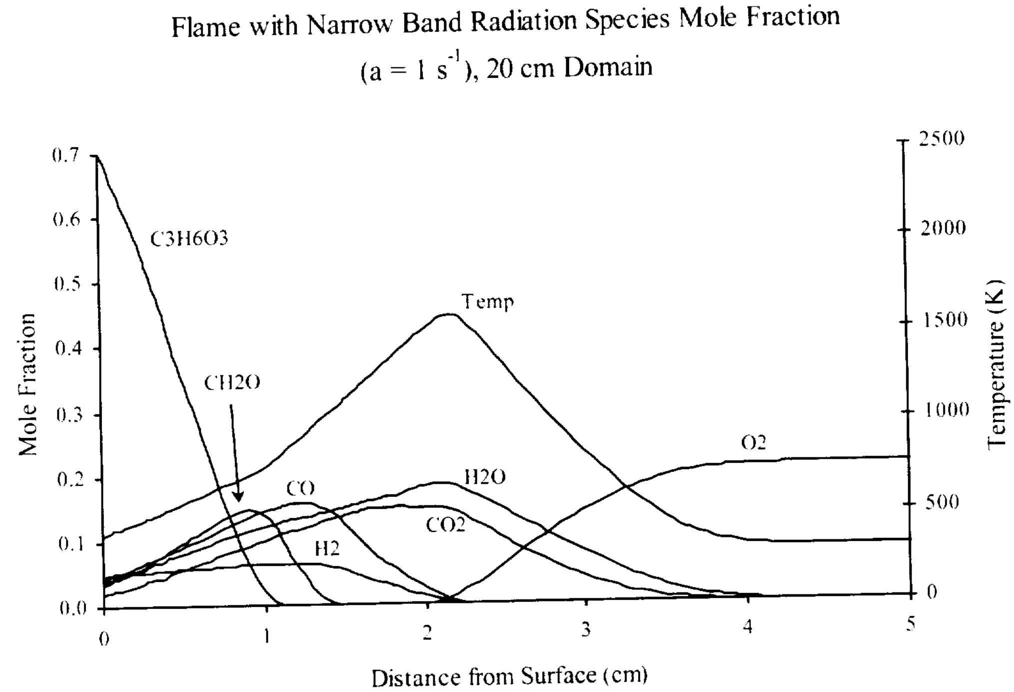

Figure 6-49: Major species profiles for low stretch rate (flame with gas phase and surface radiation).

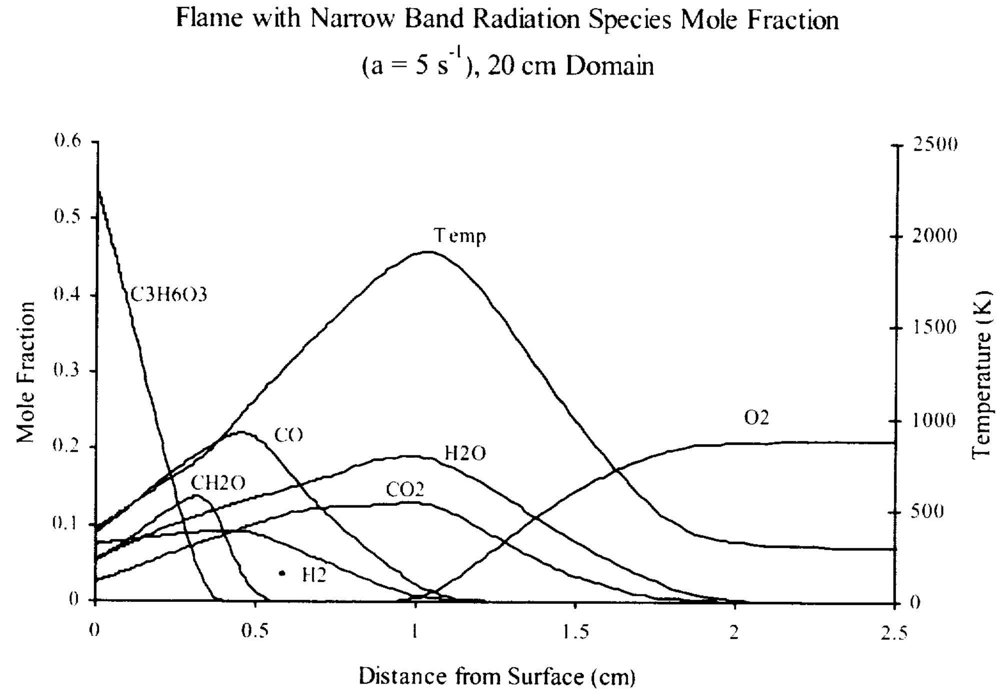

Figure 6-50: Major species profiles for mid-stretch rate (flame with gas phase and surface radiation).

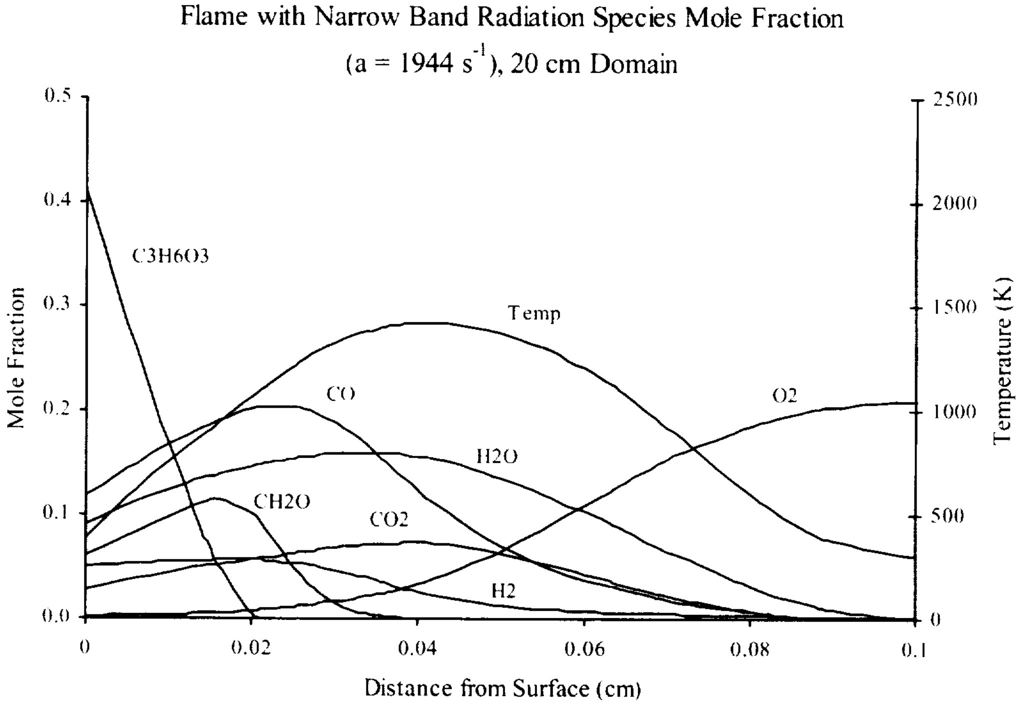

Figure 6-51: Major species profiles at the blow-off extinction limit (flame with gas phase and surface radiation).

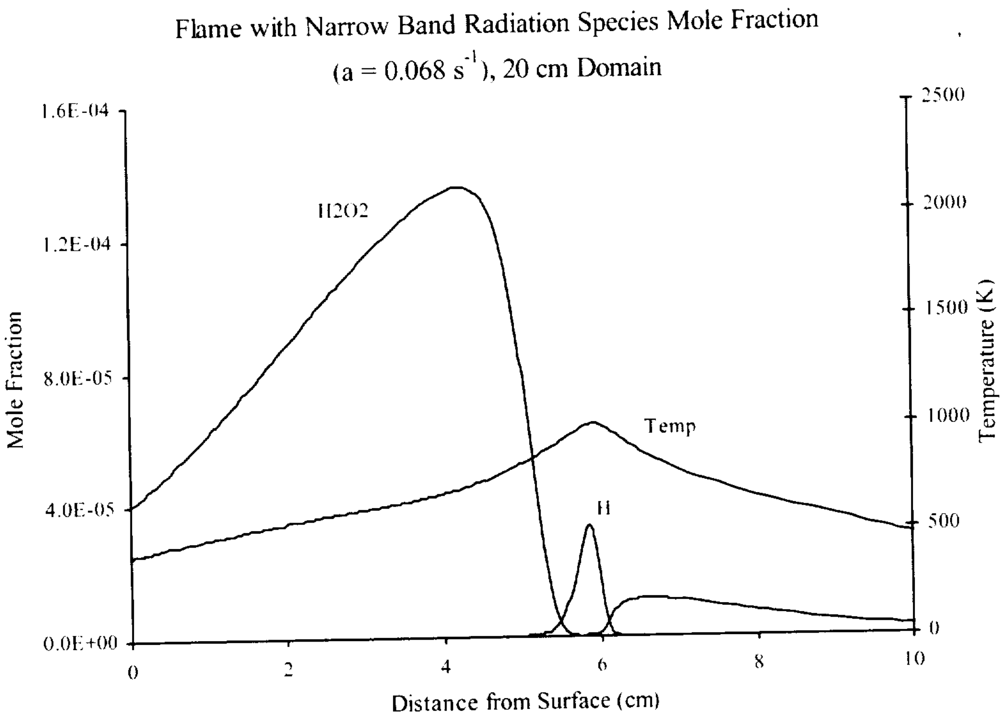

Figure 6-52: Species profiles of H_2O_2, and H for radiative extinction turning point (flame with gas phase and surface radiation).

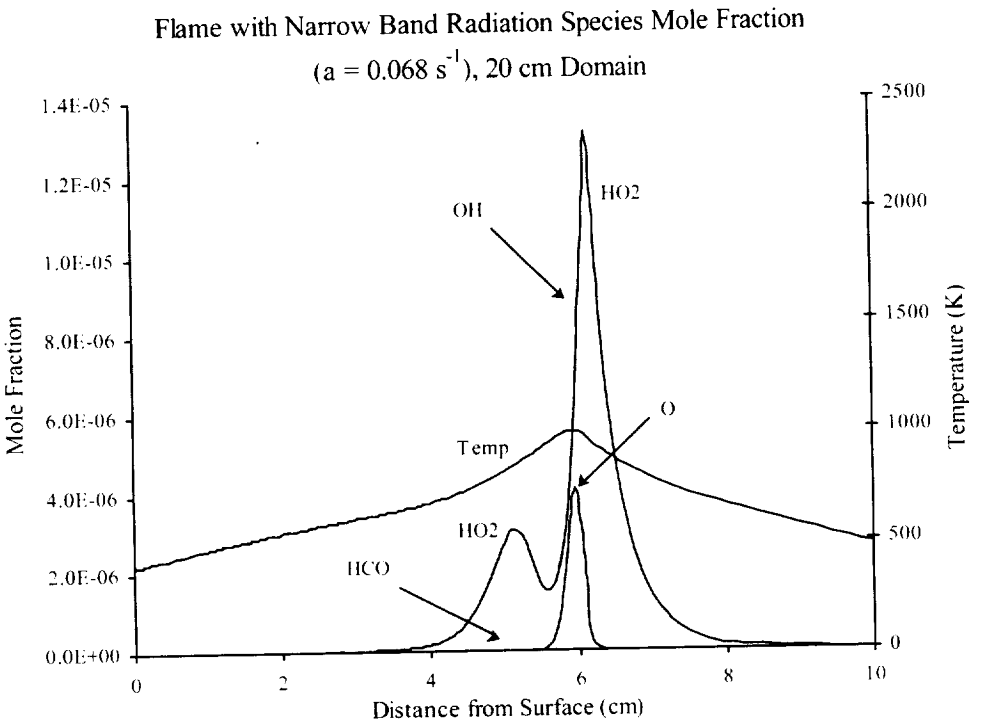

Figure 6-53: Species profiles of HCO, OH, O, and HO_2 for radiative extinction turning point (flame with gas phase and surface radiation).

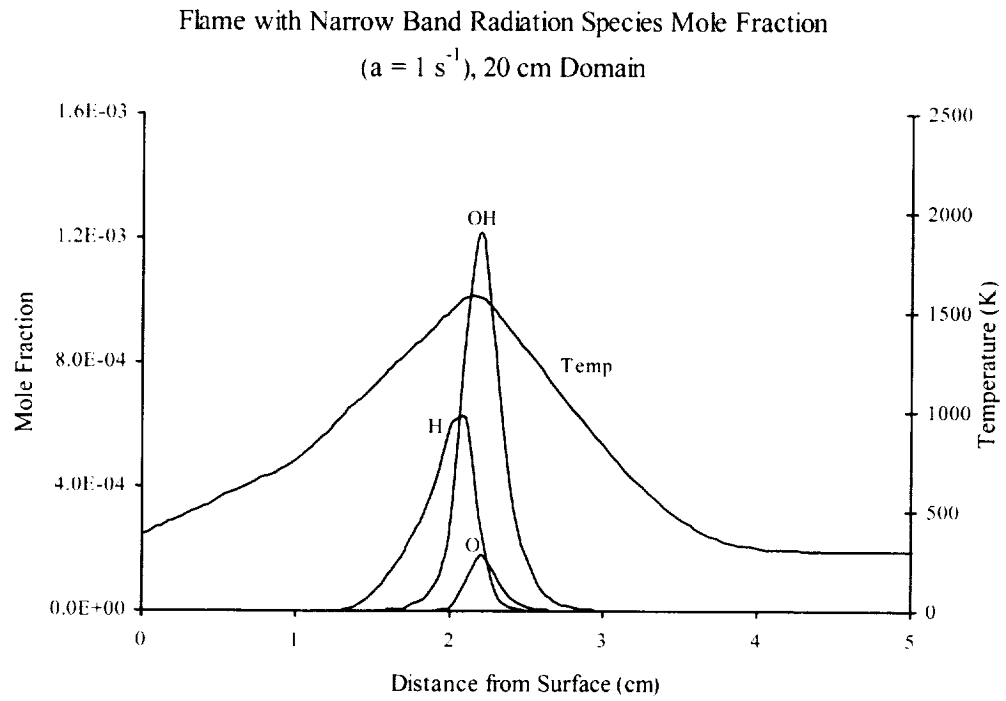

Figure 6-54: Species profiles of H, O, and OH for low stretch rate (flame with gas phase and surface radiation).

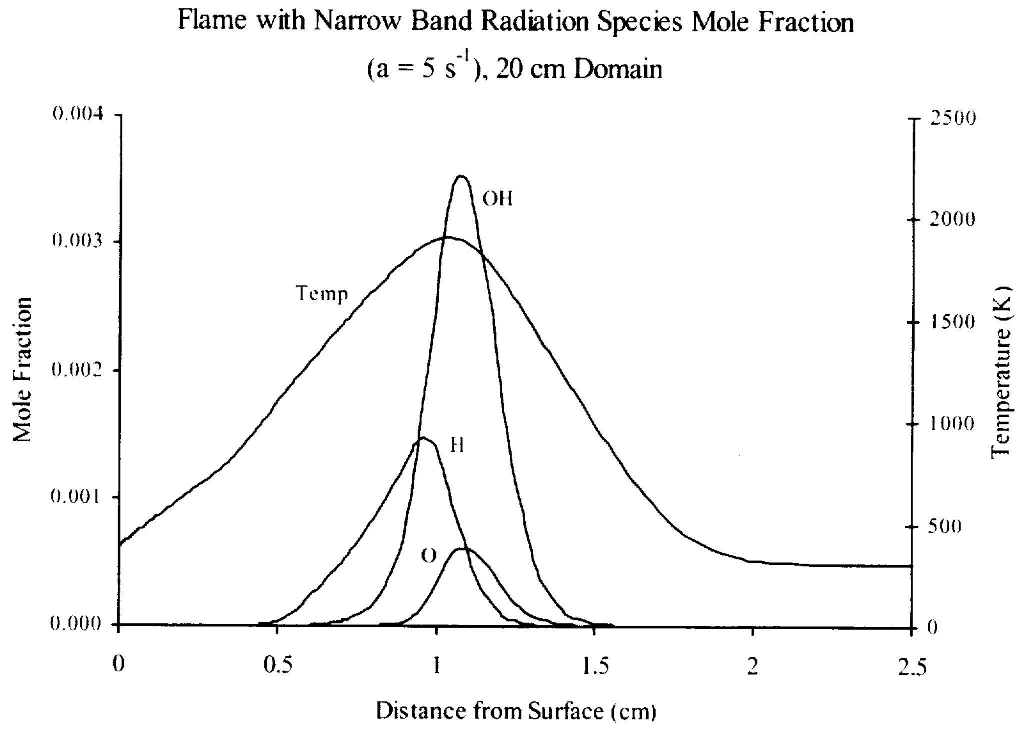

Figure 6-55: Species profiles of H, O, and OH for mid-stretch rate (flame with gas phase and surface radiation).

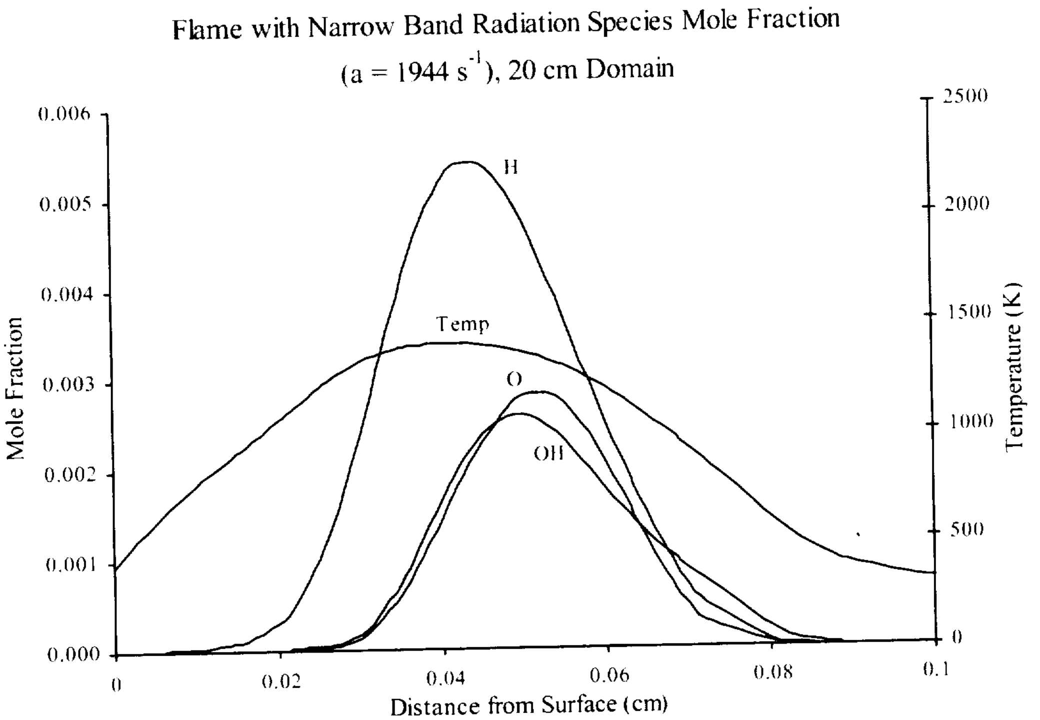

Figure 6-56: Species profiles of H, O, and OH at the blow-off turning extinction limit (flame with gas phase and surface radiation).

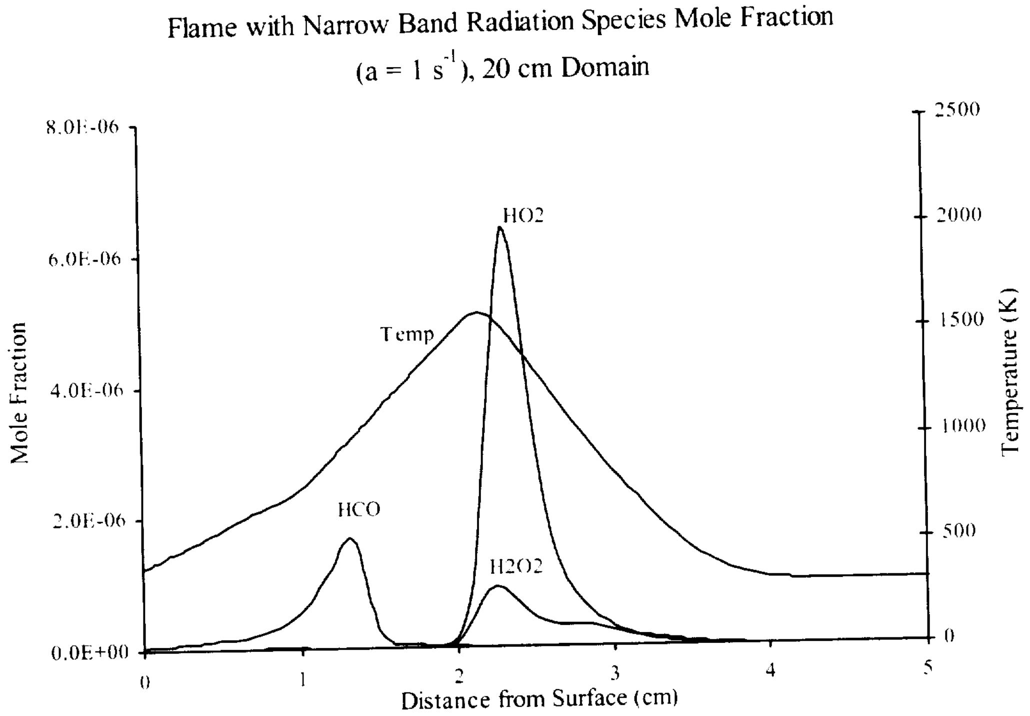

Figure 6-57: Species profiles of HO_2, H_2O_2, and HCO for low stretch rate (flame with gas phase and surface radiation).

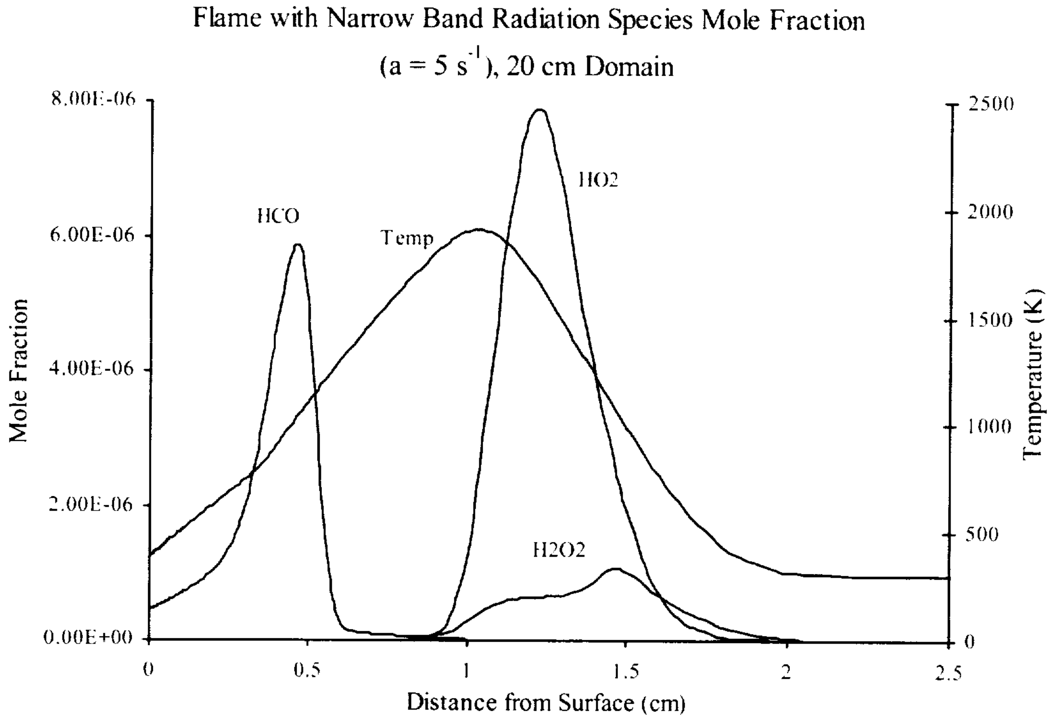

Figure 6-58: Species profiles of HO_2, H_2O_2, and HCO for mid-stretch rate (flame with gas phase and surface radiation).

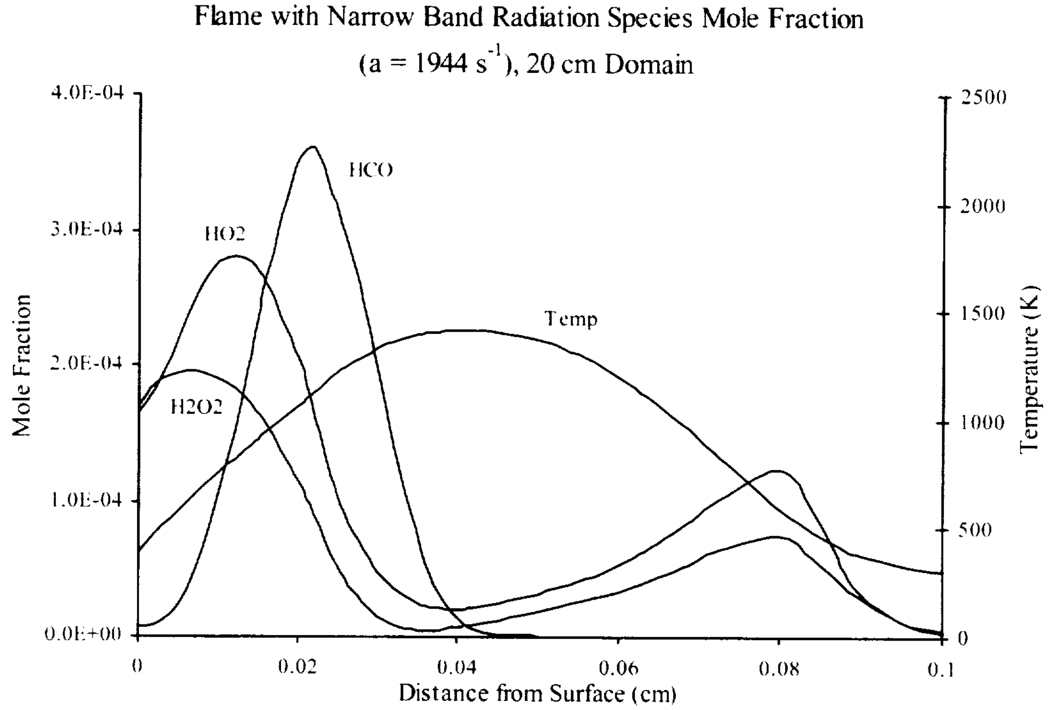

Figure 6-59: Species profiles of HO_2, H_2O_2, and HCO at the blow-off extinction limit (flame with gas phase and surface radiation).

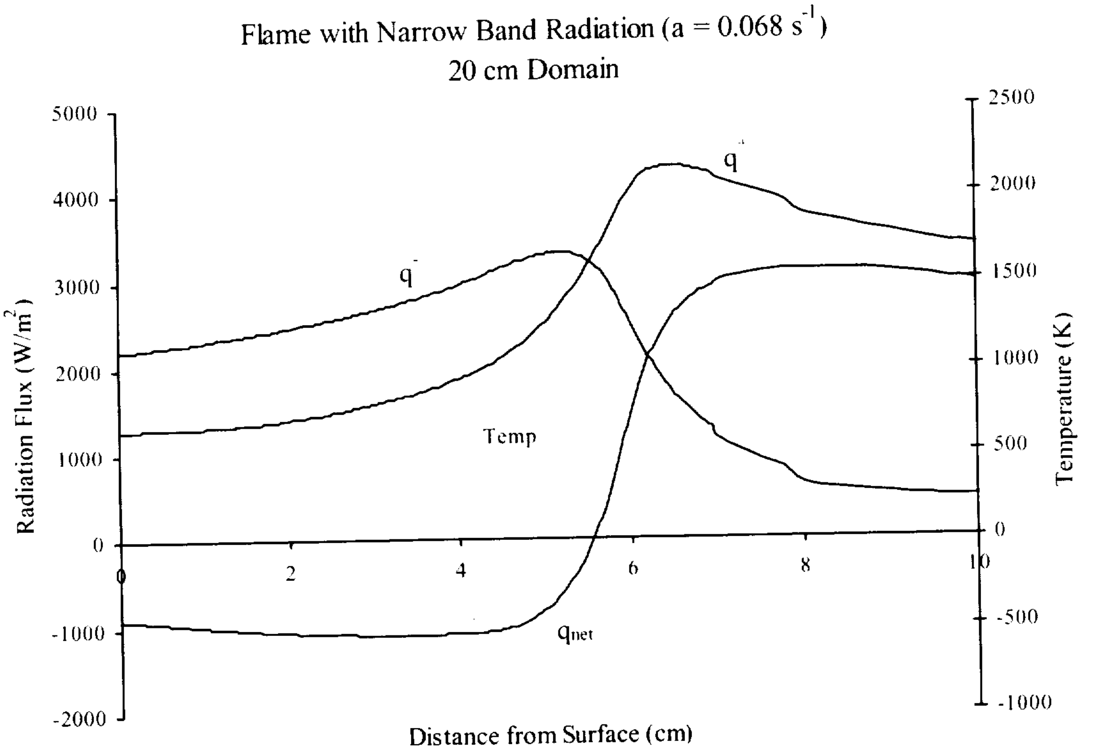

Figure 6-60: Radiation flux for radiative extinction point (flame with gas phase and surface radiation).

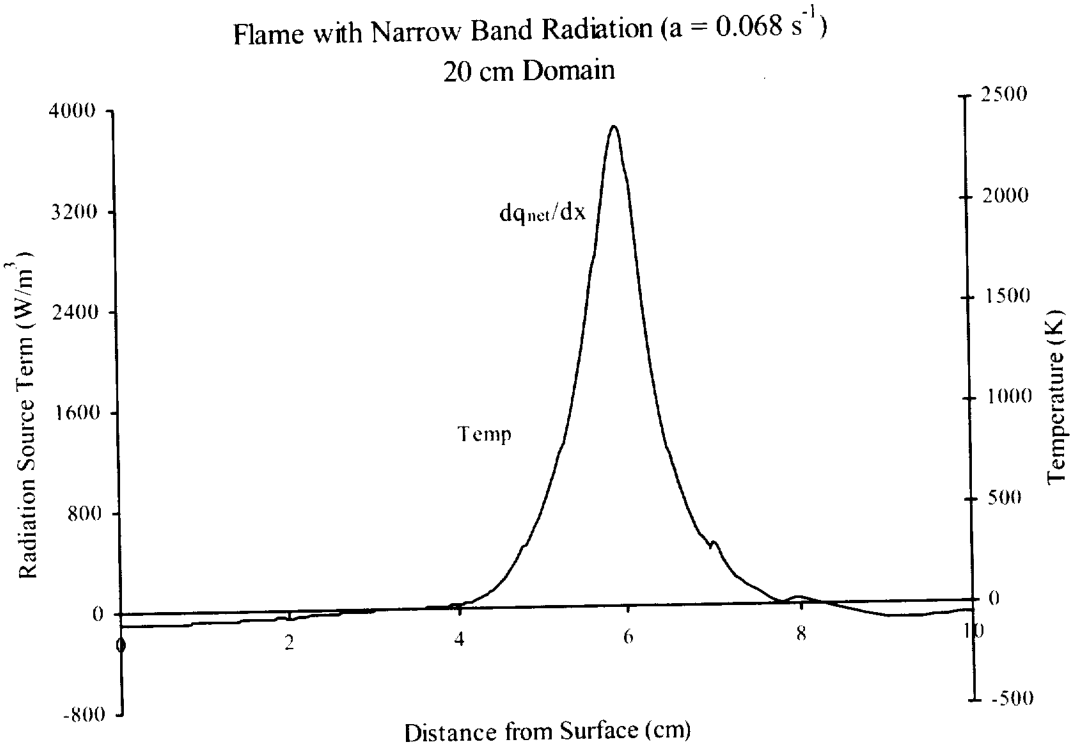

Figure 6-61: dq$_{net}$/dx for radiative extinction point (flame with gas phase and surface radiation).

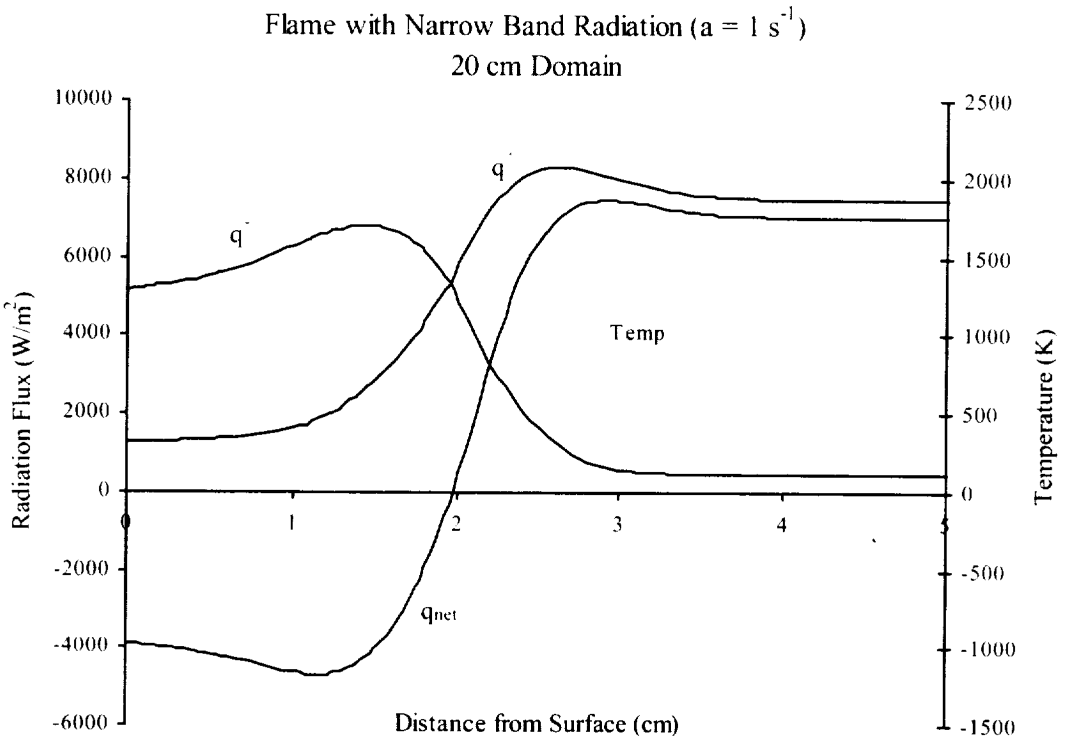

Figure 6-62: Radiation flux for low stretch rate (flame with gas phase and surface radiation).

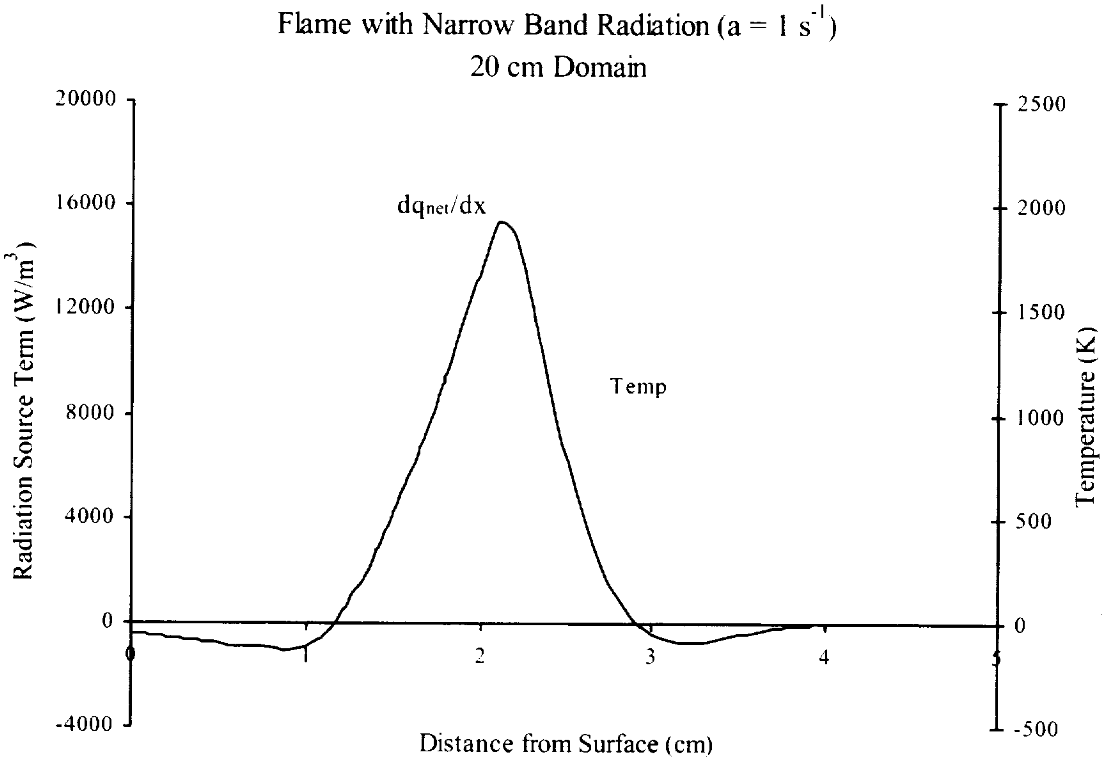

Figure 6-63: dq_{net}/dx for low stretch rate (flame with gas phase and surface radiation).

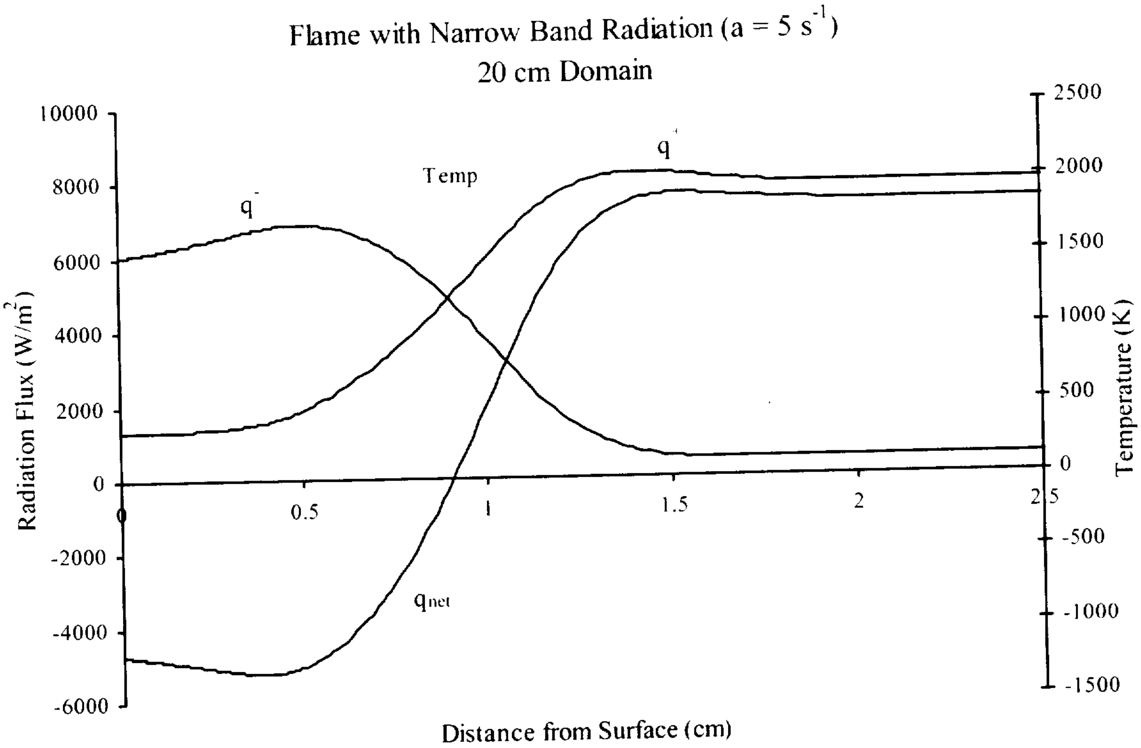

Figure 6-64: Radiation flux for mid-stretch rate (flame with gas phase and surface radiation).

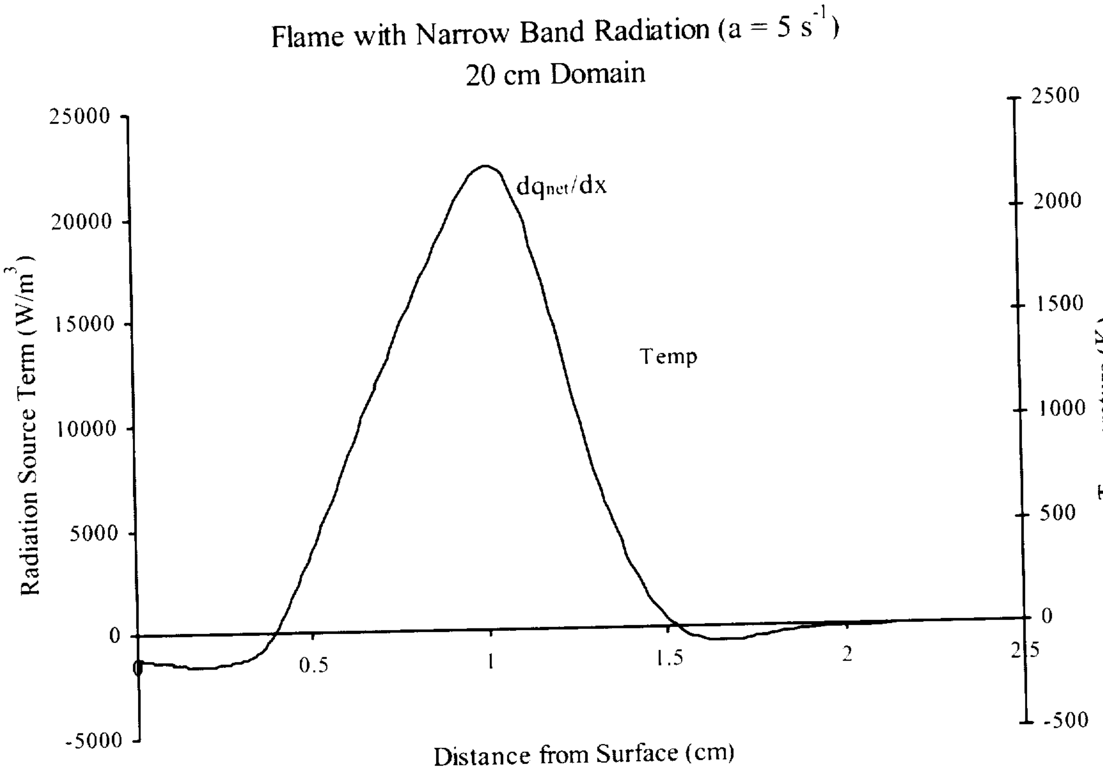

Figure 6-65: dq$_{net}$/dx for mid-stretch rate (flame with gas phase and surface radiation).

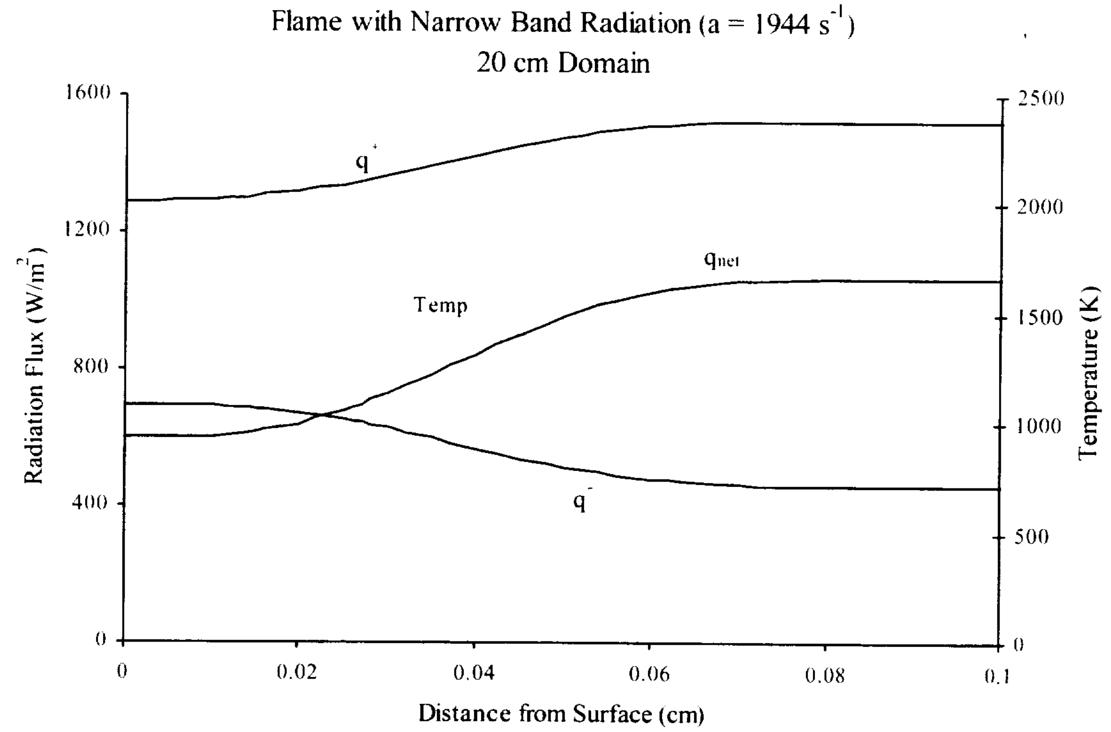

Figure 6-66: Radiation flux at the blow-off extinction limit (flame with gas phase and surface radiation).

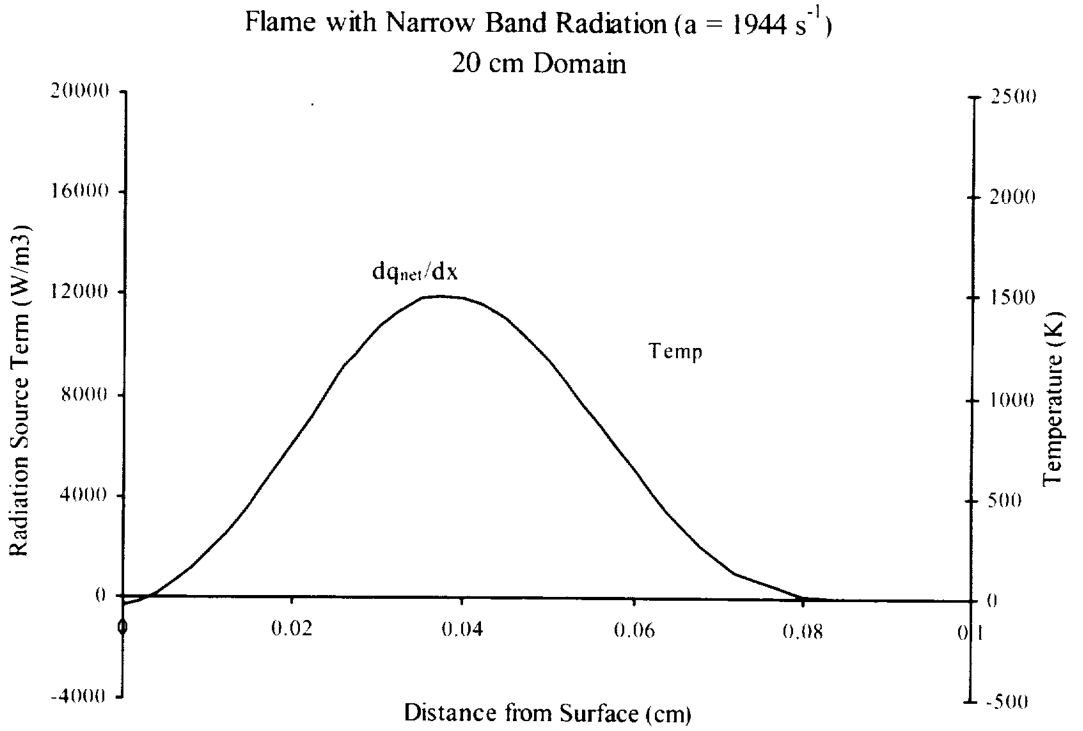

Figure 6-67: dq_{net}/dx at the blow-off extinction limit (flame with gas phase and surface radiation).

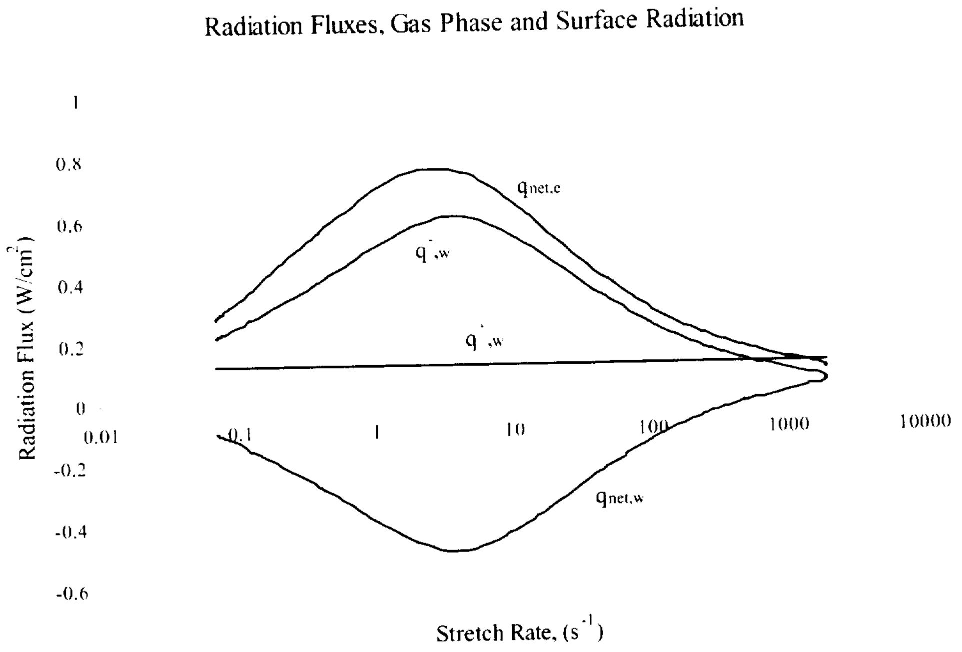

Figure 6-68: Heat flux breakdown vs. stretch rate for the flame with gas phase and surface radiation.

($q_{net,c}$=net radiative flux from flame edge to the surroundings; q^{-}_{w}= radiative flux from flame to surface; q^{+}_{w}=radiative flux from surface to flame; $q_{net,w}$=net radiative flux from surface).

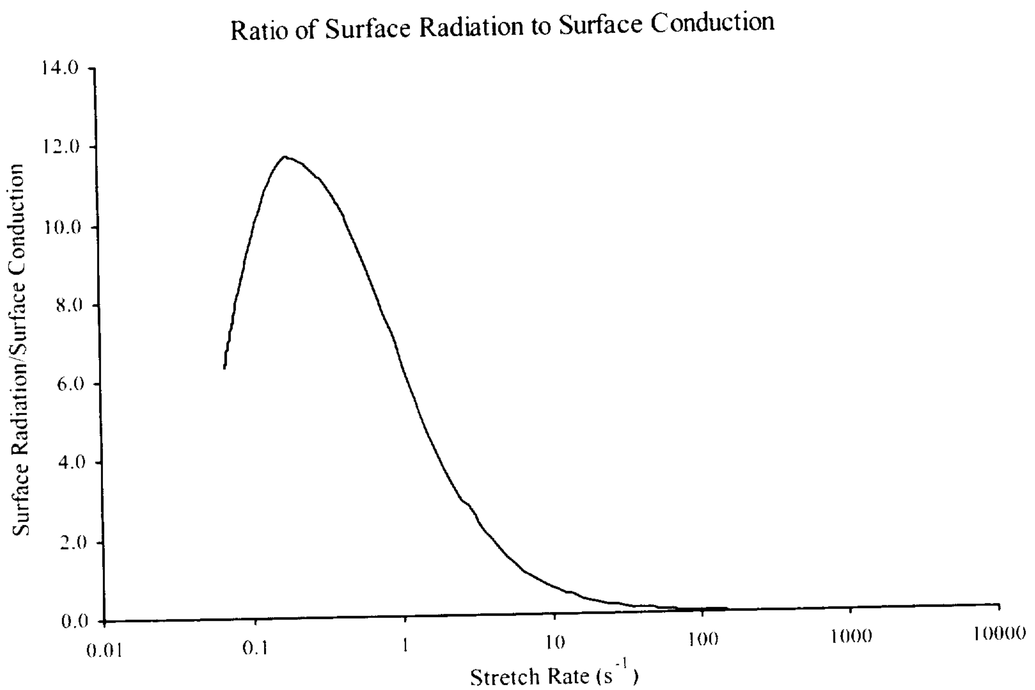

Figure 6-69(a): Ratio of net radiative heat flux to the solid to conductive heat flux to the solid vs. stretch rate.

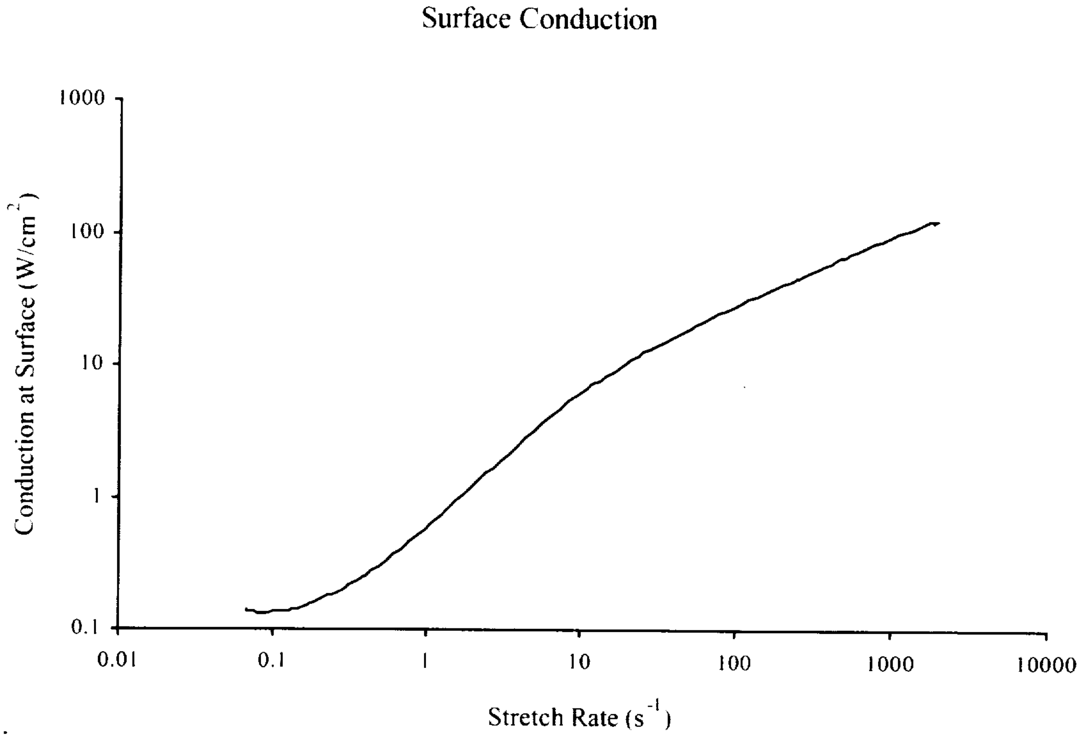

Figure 6-69(b): Surface conduction vs. stretch rate.

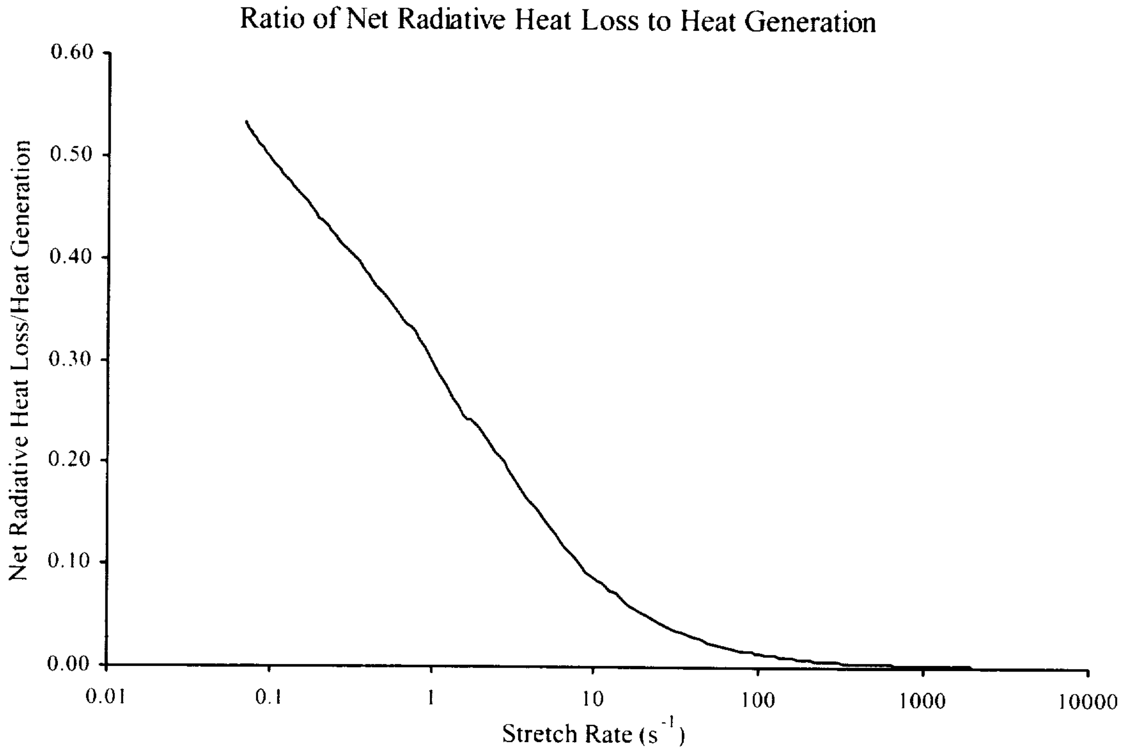

Figure 6-69(c): Ratio of net radiative heat loss to the total heat generation vs. stretch rate.

6.5 Sensitivity and Reaction Path Analysis for Flame With Gas Phase and Surface Radiation

We performed sensitivity and detailed analyses on the narrowband flame results to discover the differences in the driving kinetic mechanisms responsible for the structure of the solid trioxane combustion in the stagnation-point flow. We also compared the results, where possible, with the original homogeneous kinetics study [Hochgreb 1991].

The parameters of interest here are the same as outlined in Section 6.2; namely: species production rates, reaction rates of progress, reaction heat release, and sensitivity to stretch rate. These are examined for three stretch rates (a=0.068 s^{-1}, a= 1 s^{-1}, and a=5 s^{-1}). For consistency, these are the same stretch rates used in the discussion in Section 6.4. The reader is referred to the adiabatic discussion for the higher stretch cases, since the 'flame and surface radiation' case and adiabatic case are identical at high stretch (greater than a=100 s^{-1}).

Species Production Rates and Reaction Rates of Progress. The production rates for each species are given in Figures 6-70, 6-71, and 6-72 for the sample stretch rates. In each plot, positive production rates indicate species production, and negative production rates indicate species consumption. Following these plots are the relevant reaction rates of progress of the sample stretch rates (Figures 6-73(a-c), 6-74(a-c), 6-75(a-e)). Positive values indicate a forward progressing reaction and negative values indicate a reverse progressing reaction.

As before, we see in each production rate plot that trioxane decomposes in the same region in which formaldehyde is produced, via reaction 1. This occurs at reduced rates, as stretch rate decreases. The temperatures are low in this region of the flame (715 K, 823 K and 847 K at the location of maximum consumption of fuel for a=0.068, 1, and 5 s^{-1}, respectively). This is followed by consumption of formaldehyde, with the primary products being CO and H_2. This occurs at somewhat higher temperatures (895 K, 1035 K, and 1105 K for a=0.068, 1, and 5 s^{-1}, respectively). CO and H_2 are eventually converted to CO_2 and H_2O, respectively, in the high-temperature region of the flame.

The rates of progress for the formaldehyde decomposition, reactions 2 through 8, are presented in Figures 6-73(a), 6-74(a), and 6-75(a) for each of the sample stretch rates. As with the adiabatic flame, reactions 5 and 7 consistently dominate the major formaldehyde consumption, with reaction 5 having the primary role. Subsequently, formyl radical is consumed to form H_2 and CO. At a=1 and 5 s^{-1}, consistent with the adiabatic flame, the production of H_2 and CO is attributed to the decomposition of HCO via reactions 9 and 11, rather than formaldehyde decomposition (reaction 3). However, near the quench limit stretch rate, while reaction 9 remains important, reaction 10 overtakes reaction 11 as the branching path due to the increasing leakage of O_2 when approaching the quench limit.

(9) $HCO+M \rightarrow H+CO+M$
(10) $HCO+O_2 \rightarrow CO+HO_2$

This is seen in the HCO reaction rates of progress (Figures 6-73(b), 6-74(b), and 6-75(b)) and is suggestive of Hochgreb's 'low-temperature' reaction path, discussed in Sections 4 and 6.4. (Note that reaction 9 is plotted on the right-hand scale for Figures 6-73(b), 6-74(b) and 6-75(b).) Also, near the turning point, CO is produced at almost the same rate as CH_2O, which is explained by the emphasis here on reactions 9 and 10. As before, there is a zone of radical pool formation and then recombination into final products, CO_2 and H_2O.

The primary O_2 consumption zone is located after the fuel consumption zone. The O_2 reaction rates of progress are shown in Figures 6-73(c), 6-74(c), and 6-75(c). For a=5 s^{-1}, reaction 20 is the dominant reaction, and is the primary source of radical pools, producing OH and O. At the lower stretch rates, reaction 38 asserts itself as the dominant reaction for O_2 consumption. At a=1 s^{-1}, reactions 20 and 38 have very similar rates of progress; near the quench limit (a=0.068 s^{-1}), reaction 38 dominates. In contrast to reaction 20, reaction 38 is exothermic (see heat release discussion). Another interesting feature is the O_2 consumption layer on the fuel side of the flame. We see evidence of this by reaction 10. This reaction asserts itself in the two low temperature regions of the flame. We see some evidence at the high stretch turning point (illustrated and discussed in Sections 6.1, 6.2, and 6.4). At the low temperature quench limit (6-73(b) and (c)), it is more apparent.

Figures 6-73(d) and 6-73(e) illustrate the main reaction pathways for H_2O_2 and HO_2, respectively, for the case near the quench limit. There are two distinct reaction zones for H_2O_2 here. In the radical pool (near the peak temperature), reaction 26 is the main producer of H_2O_2 and reaction 36 is the main consumer. Closer to the flame, reaction 8 produces H_2O_2 in the decomposition of formaldehyde via the branching path. We again see reaction 8 in the consumption of HO_2, as shown in Figure 6-73(e). Reaction 38 is the primary producer of HO_2 in the radical pool, while reaction 28 is the primary consumer here. HO_2 is also active on the fuel side of the flame, with reactions 10 and 8 noteworthy on the fuel side of the radical pool.

The production rates increase by an order of magnitude for each sample stretch rate, starting from the low stretch case and increasing. The low stretch extinction limit retains the distinct zones of formaldehyde consumption and radical production; unlike the high stretch extinction limit, which is characterized by overlap of the formaldehyde consumption and radical production zones, ascribed to the shortened residence time at the high stretch rate.

In conclusion, the main reaction paths follow the route illustrated in the adiabatic flame discussion. However, a branching path appears near the quench limit, illustrated in Figure 6-80. As noted earlier, traces of this path are also observable at the high stretch extinction limit in the low-temperature portion of the flame. This is Hochgreb's 'low-temperature' mechanism.

Low stretch radiative branching path:

(5) $CH_2O+H \rightarrow HCO+H_2$
(9) $HCO+M \rightarrow H+CO+M$
(10) $HCO+O_2 \rightarrow CO+HO_2$
(8) $CH_2O+HO_2 \rightarrow HCO+H_2O_2$
(36) $H_2O_2+M \rightarrow OH+OH+M$

Heat Release: The total heat release over the domain for the sample stretch rates is presented in Figures 6-76(a), 6-77(a), and 6-78(a). Temperature profiles are included for comparison. Figures 6-76(b), 6-77(b), and 6-78(b) contain the heat release by reaction to understand the primary contributors to the total heat release. Positive values indicate exothermicity; negative values indicate endothermicity.

As with the adiabatic solutions, all of the profiles exhibit an endothermic zone nearer to the surface, and an exothermic zone beyond. However, as stretch rate decreases, the endothermic zone is greatly reduced, so that it is no longer comparable to the exothermic zone. The endothermic zone corresponds to the fuel pyrolysis region, and since less fuel is pyrolyzed, the endothermicity is reduced. In the formaldehyde consumption zone, the exothermicity of reaction 5 counterbalances the endothermicity of reaction 9, although at low stretch, the magnitudes are much reduced in comparison to the adiabatic flame.

The small plateau created by the consumption of formaldehyde (reaction 5) being opposed by the thermal decomposition of HCO (reaction 9) at a=5 s^{-1} essentially disappears near the quench limit. Reactions 16 and 23, which also contribute to this plateau, are only visible in the primary heat release zone near the quench limit.

At the higher stretch cases (a=1, 5 s^{-1}), reaction 35 (producing H_2O from the recombination of H and OH) accounts for more than half of the heat release, consistent with the adiabatic flame. Also, as before, reactions 35, 38, and 23 all lead to H_2O formation, indicating that the primary heat release is due to formation of H_2O, rather than CO_2. Reaction 20 accounts for the primary endothermic response in this zone.

At the low stretch quenching limit, reaction 38 replaces reaction 35 as the major source of heat release, consistent with the low temperature path described above. Reaction 20 no longer plays a part in the heat balance, so that there is no longer a large endothermic response to counter the endothermic reactions.

Eigen-Value Sensitivity: The results of the normalized E_{ext} sensitivity are presented in Figure 6-79 for the low stretch turning point (quench limit). At the low stretch turning point (a=0.068 s^{-1}), the temperature is very low (T_{max} =997 K) and the flame is far from the surface, and the molecular interaction is inhibited more than anywhere in the flame domain due to low flow and low temperature. In contrast to the high stretch turning point sensitivity, the formaldehyde and HCO decompositions are not emphasized here. E_{ext} is instead sensitive to reactions 16, 20, 28, 29, and 38. While these reactions also appear in the high stretch sensitivity, they receive more emphasis here. We know from Figure 6-73(c), that reactions 20 and 38 have a net rate of progress in the forward direction and are competing chain branching and termination reactions, with reaction 38 playing the stronger role. Reactions 16, 20, and 28 promote the reaction, producing radicals H and OH (reaction 20 produces H via the net cycle with OH and O via reactions 21 and 23). Reactions 29 and 38 are chain terminators and retard the reactions, consuming H. The highly reactive H radical appears to be the key to reaction progress here as well as at the high stretch turning point, although the OH radical (via forward reaction 28) has more of a role than at the high stretch turning point. Figures 6-52 and 6-53 from Section 6.4 show the species profiles for H, O and OH at the quench limit, and H has by far the largest mole fraction in the flame zone among the three radicals, with OH next in importance. Unlike the high stretch limit, where the radical pool extends past the peak temperature location, the radical pool zone at the low stretch limit is located with the peak temperature zone. Also note that here, as with the high stretch extinction limit, no sensitivity to reaction 1 is evident, because the trioxane decomposition is well separated from the formaldehyde decomposition.

Another feature of note here is reaction 36. This reaction, while of minor importance in terms of sensitivity, has switched directions of progress from the blow-off extinction results. At blow-off, the reaction progresses in the reverse direction, producing H_2O_2, and slightly retarding the overall reaction. At the low stretch radiative quench limit, the reaction progresses in the forward direction, producing OH, and thereby promotes the overall reaction progress.

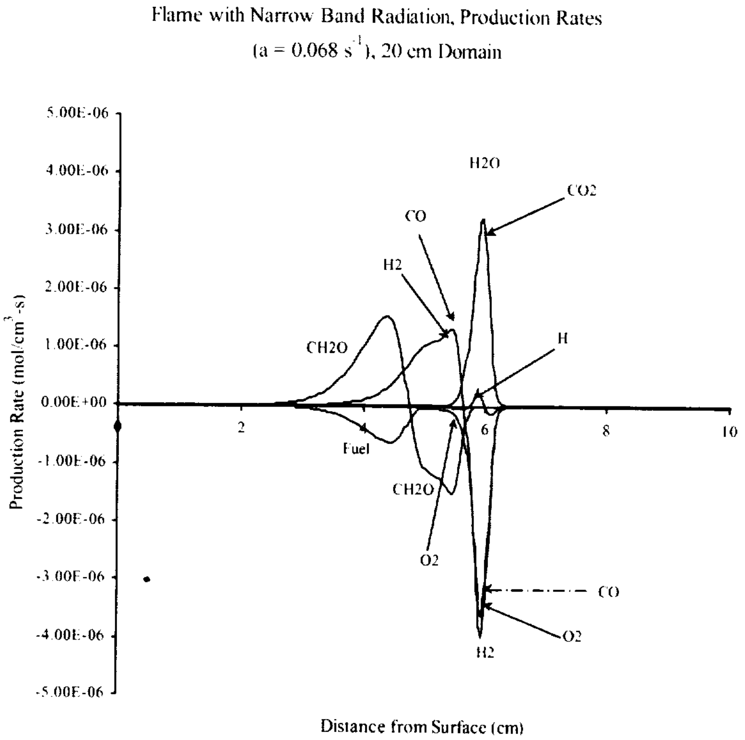

Figure 6-70: Flame with gas phase and surface radiation, production rates by reaction for radiative extinction.

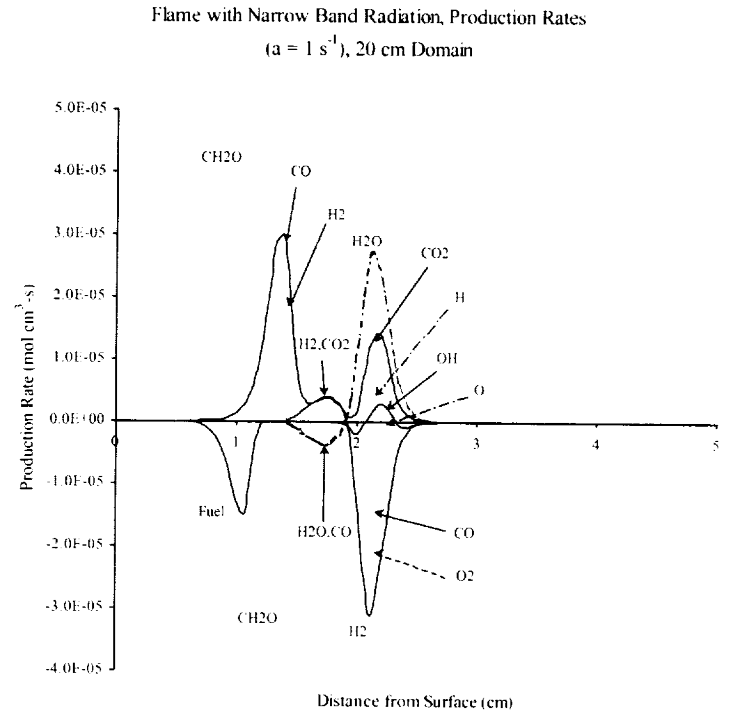

Figure 6-71: Flame with gas phase and surface radiation, production rates by reaction for low stretch rate.

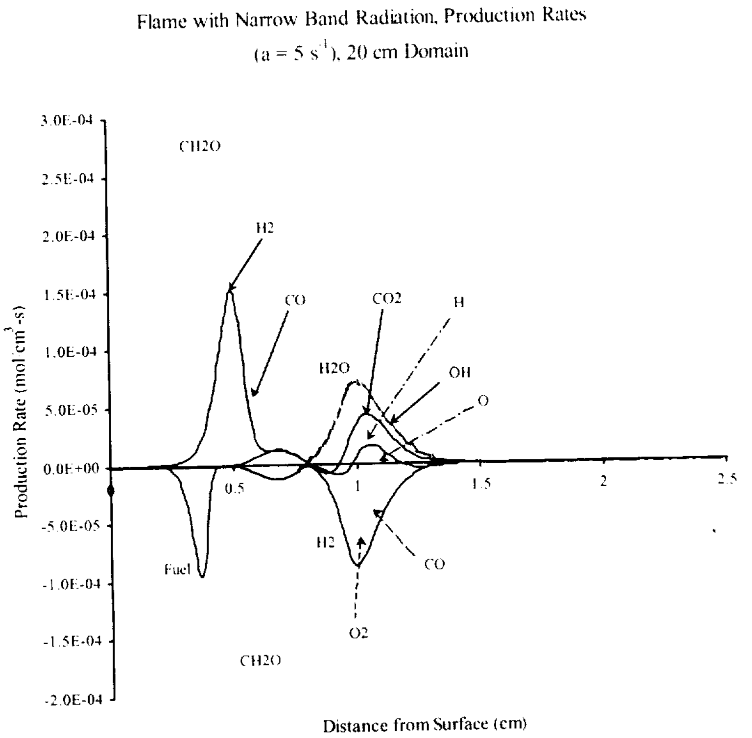

Figure 6-72: Flame with gas phase and surface radiation, production rates by reaction for mid stretch rate.

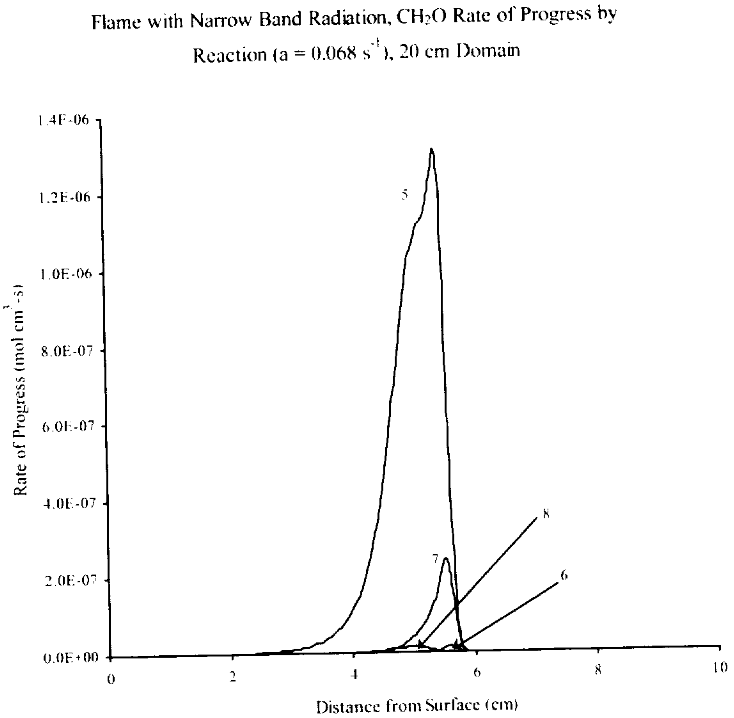

Figure 6-73(a): Flame with gas phase and surface radiation, CH_2O consumption rate of progress by reaction for radiative extinction.

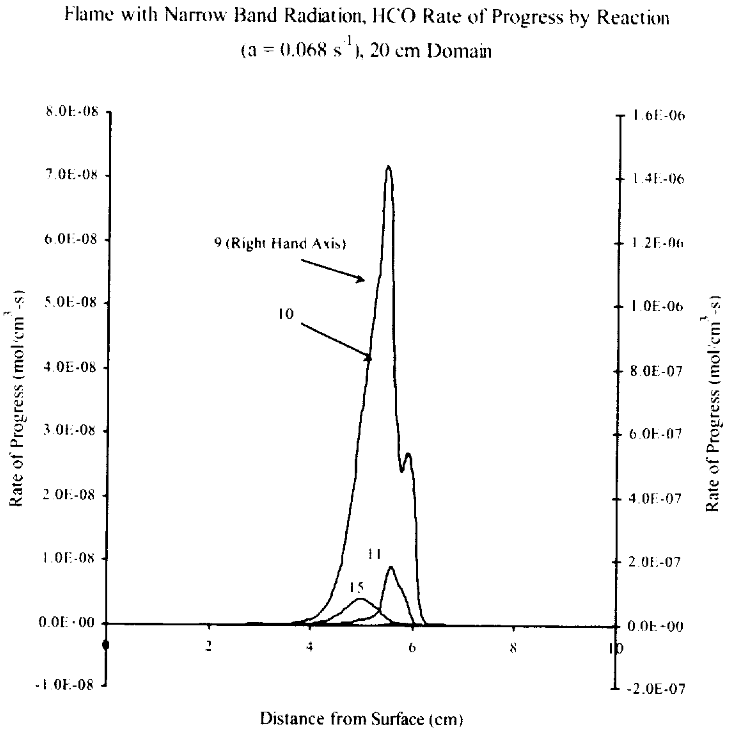

Figure 6-73(b): Flame with gas phase and surface radiation, HCO consumption rate of progress by reaction for radiative extinction.

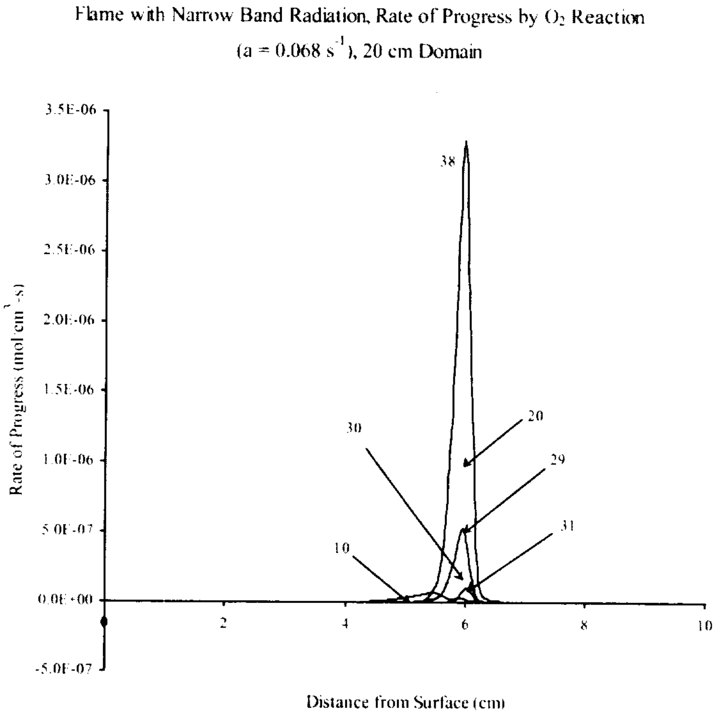

Figure 6-73(c): Flame with gas phase and surface radiation, O_2 consumption rate of progress by reaction for radiative extinction.

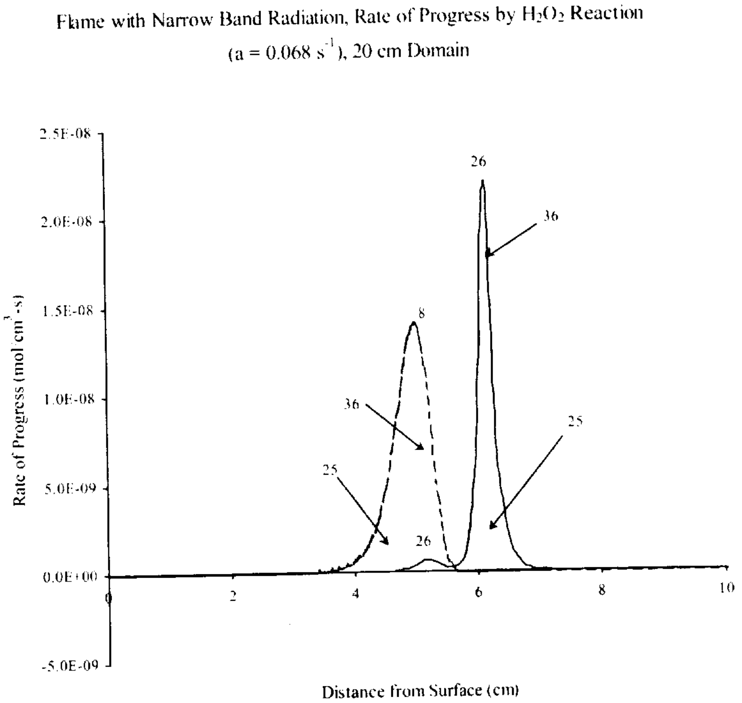

Figure 6-73(d): Flame with gas phase and surface radiation, H_2O_2 consumption rate of progress by reaction for radiative extinction.

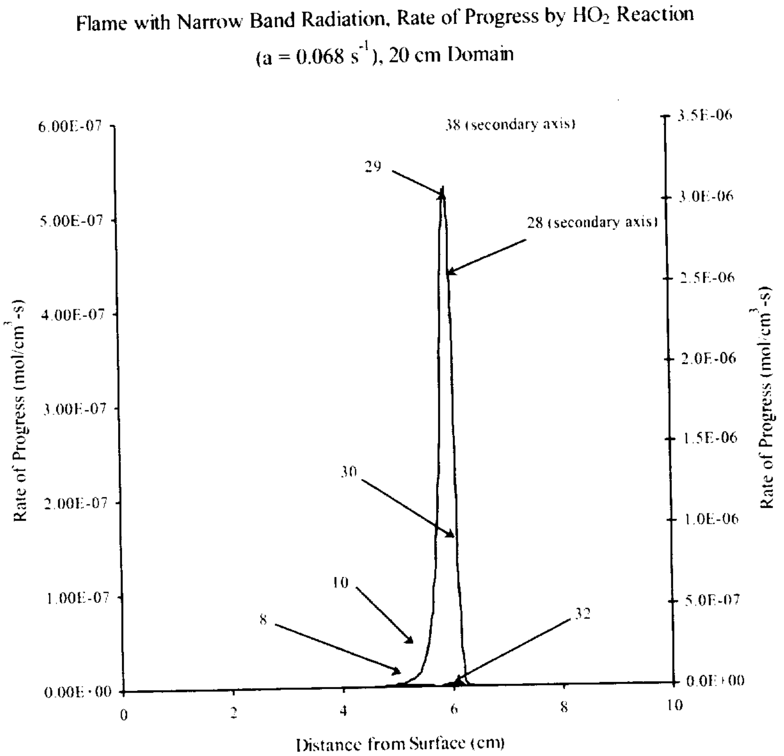

Figure 6-73(e): Flame with gas phase and surface radiation, HO_2 consumption rate of progress by reaction for radiative extinction.

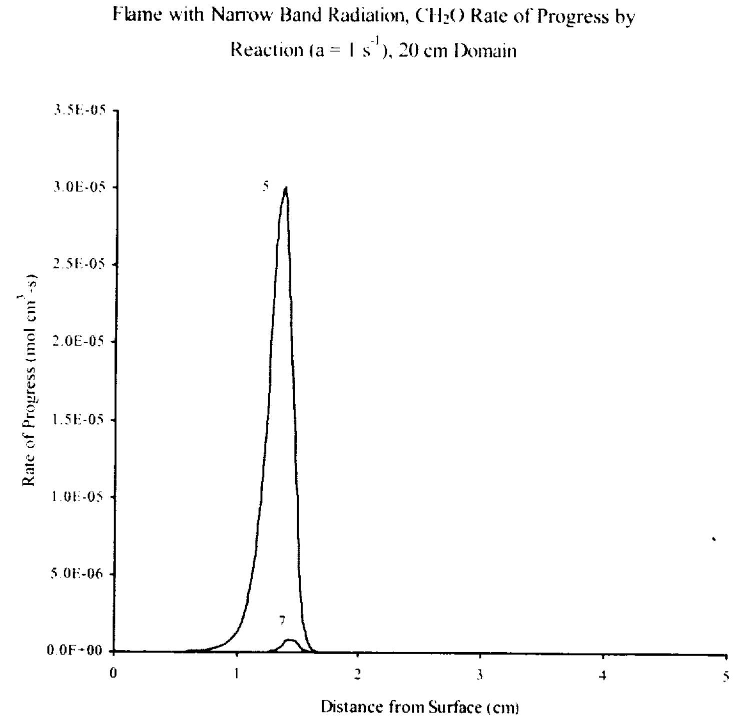

Figure 6-74(a): Flame with gas phase and surface radiation, CH_2O consumption rate of progress by reaction for low stretch rate.

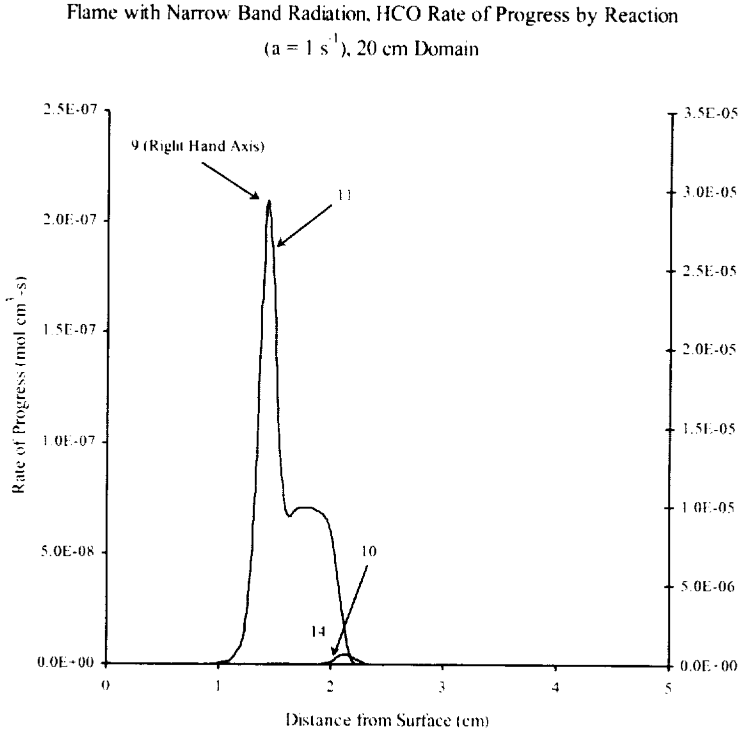

Figure 6-74(b): Flame with gas phase and surface radiation, HCO consumption rate of progress by reaction for low stretch rate.

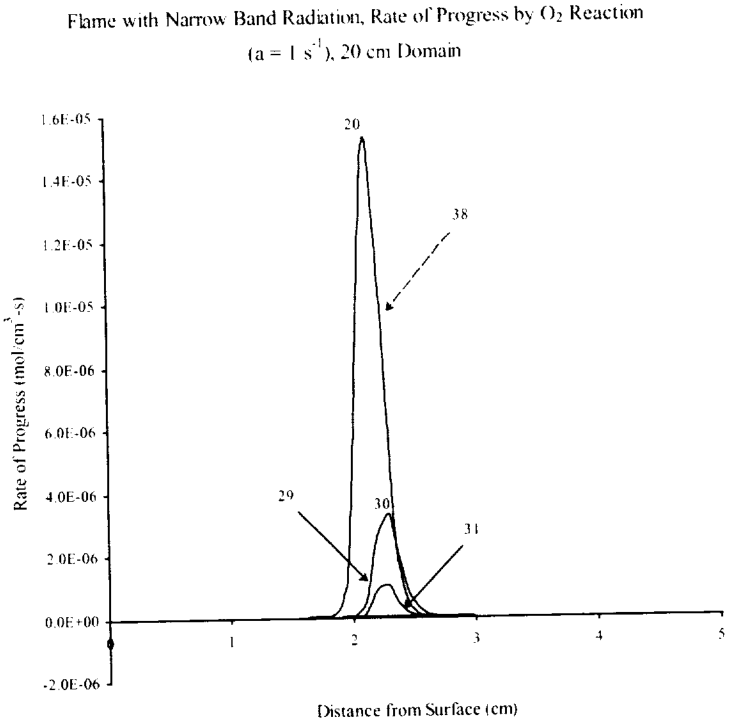

Figure 6-74(c): Flame with gas phase and surface radiation, O_2 consumption rate of progress by reaction for low stretch rate.

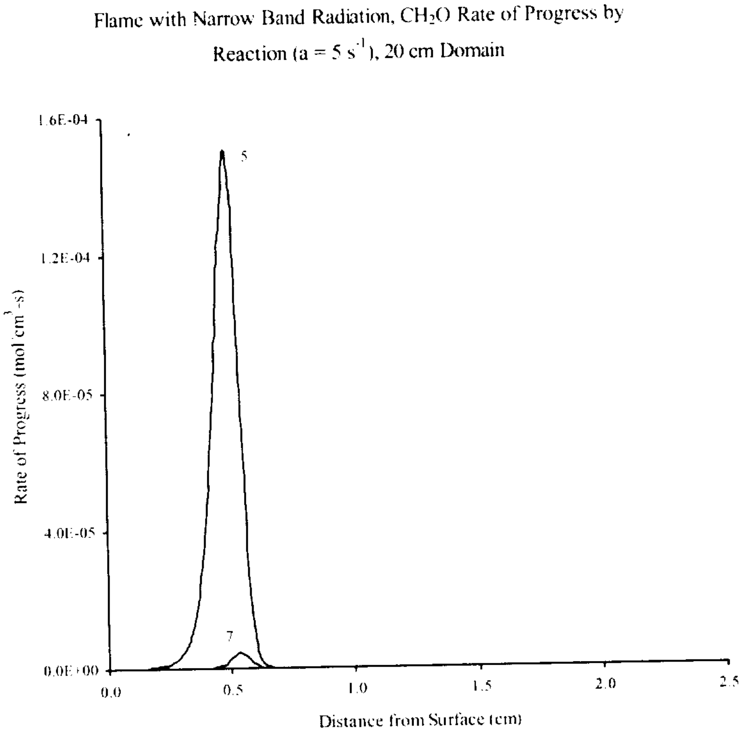

Figure 6-75(a): Flame with Gas Phase and Surface Radiation, CH_2O Consumption Rate of Progress by Reaction for Mid Stretch Rate.

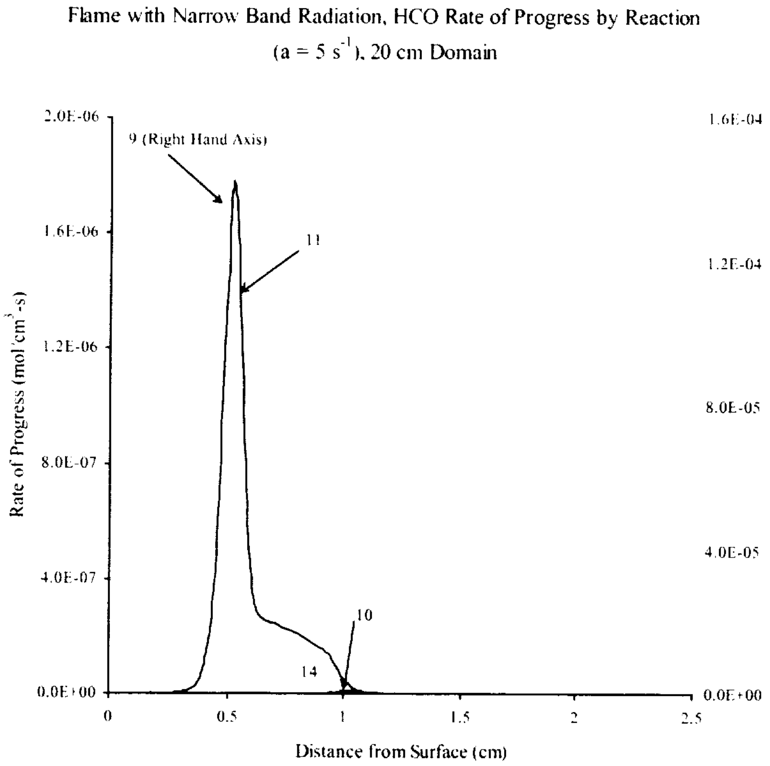

Figure 6-75(b): Flame with gas phase and surface radiation, HCO consumption rate of progress by reaction for mid stretch rate.

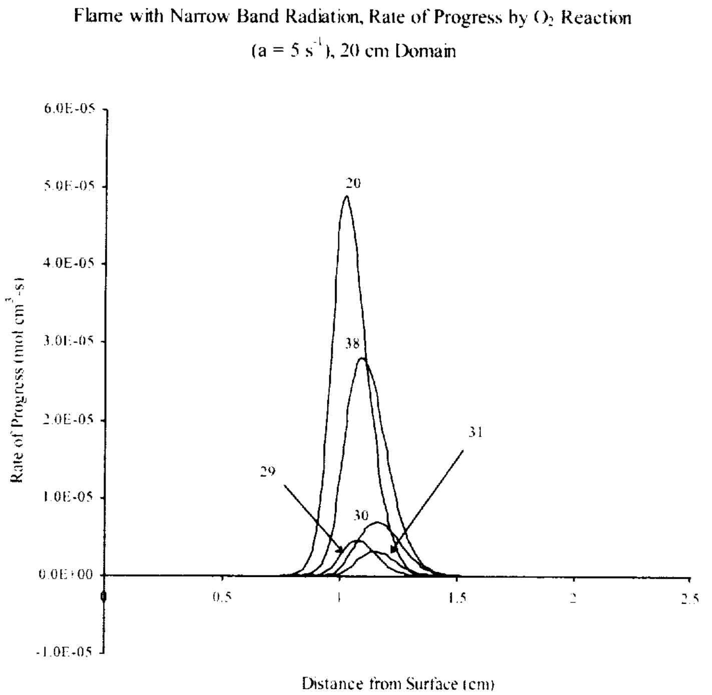

Figure 6-75(c): Flame with gas phase and surface radiation, O_2 consumption rate of progress by reaction for mid stretch rate.

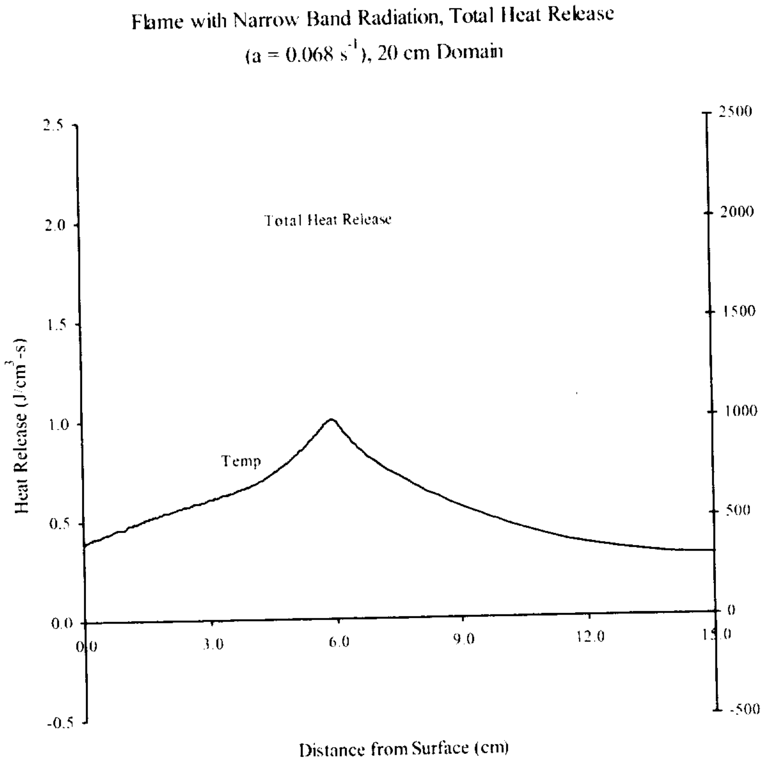

Flame with Narrow Band Radiation, Total Heat Release

(a = 0.068 s^{-1}), 20 cm Domain

Figure 6-76(a): Flame with gas phase and surface radiation, total heat release for radiative extinction.

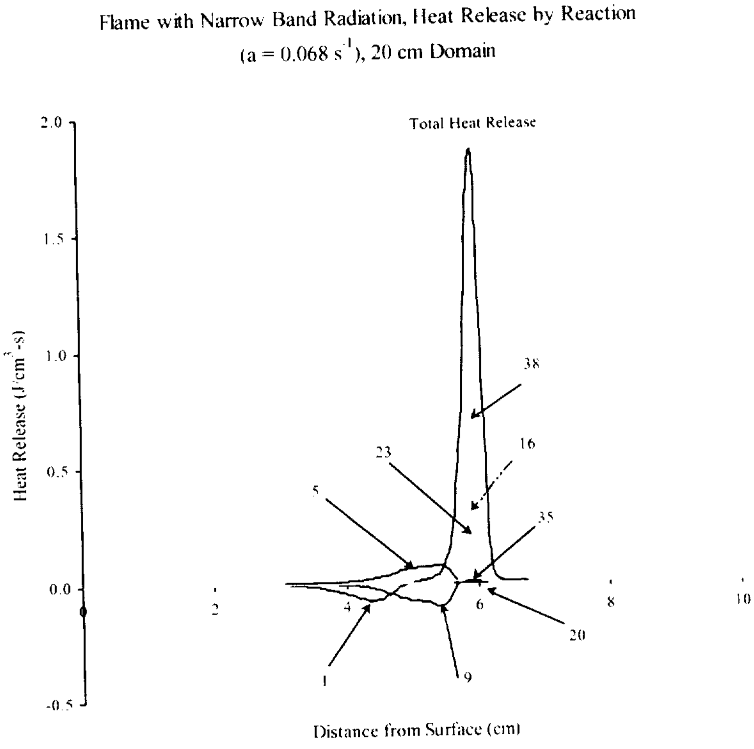

Flame with Narrow Band Radiation, Heat Release by Reaction

(a = 0.068 s^{-1}), 20 cm Domain

Figure 6-76(b): Flame with gas phase and surface radiation, heat release by reaction for radiative extinction.

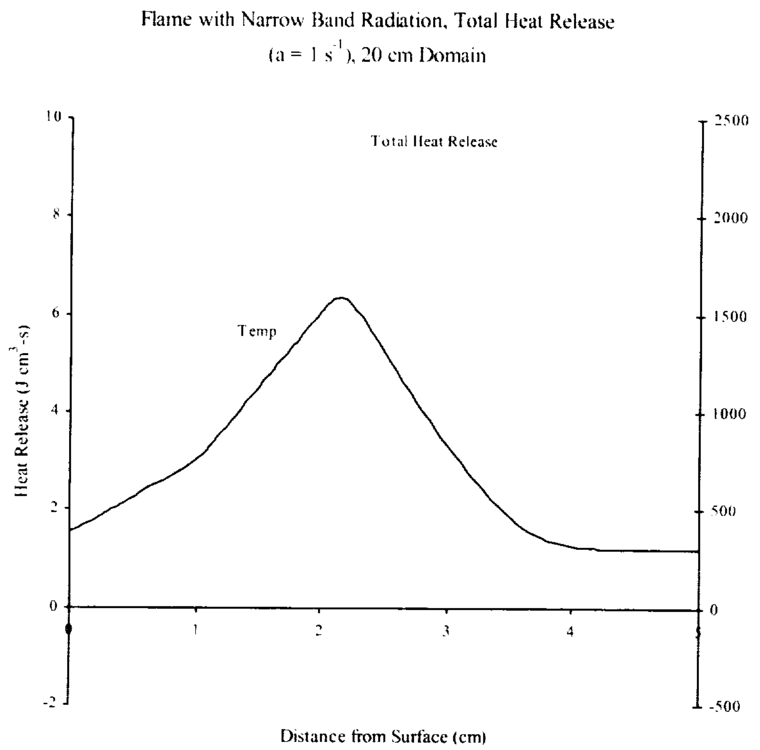

Figure 6-77(a): Flame with gas phase and surface radiation, total heat release for low stretch rate.

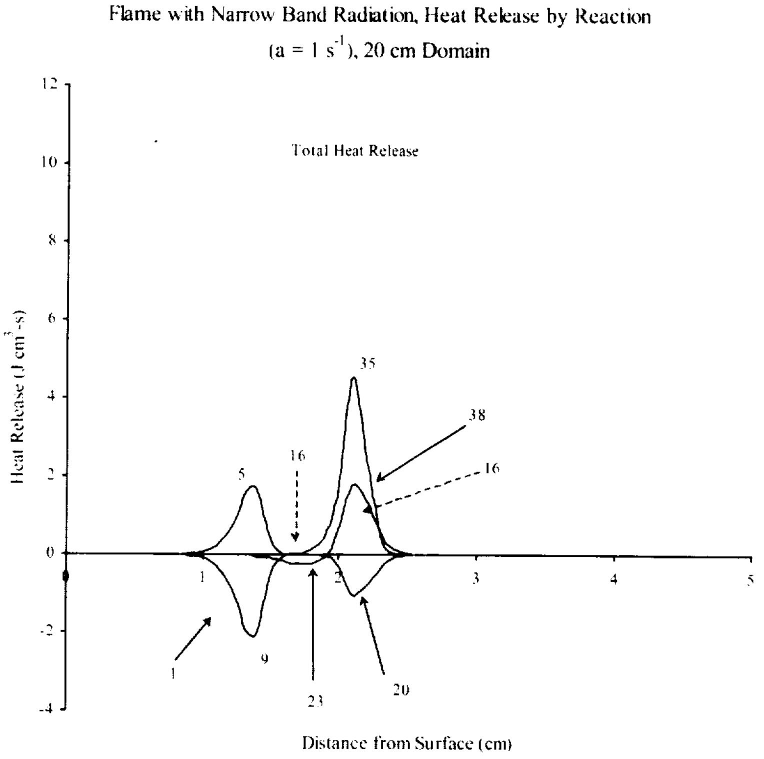

Figure 6-77(b): Flame with gas phase and surface radiation, heat release by reaction for low stretch rate.

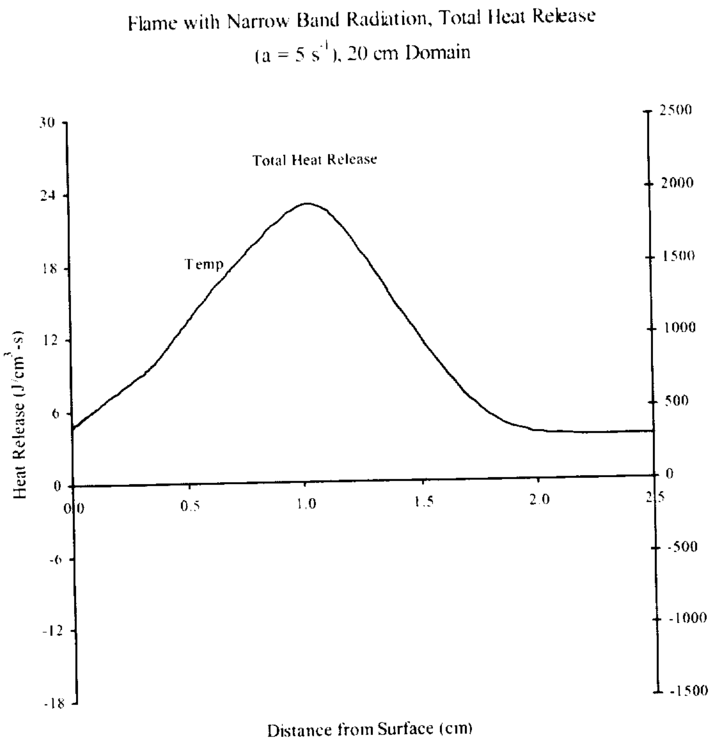

Figure 6-78(a): Flame with gas phase and surface radiation, total heat release for mid stretch rate.

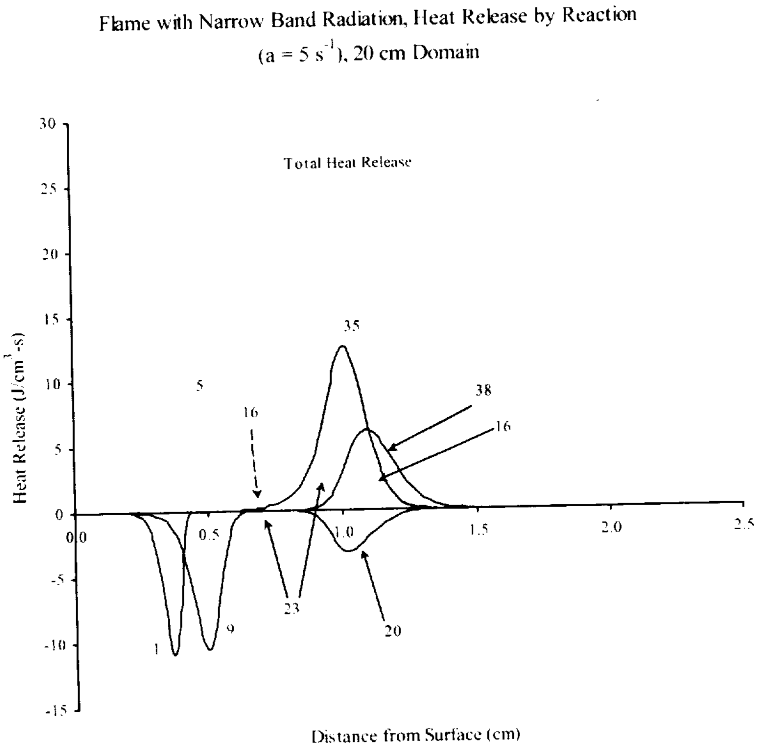

Figure 6-78(b): Flame with gas phase and surface radiation, heat release by reaction for mid stretch rate.

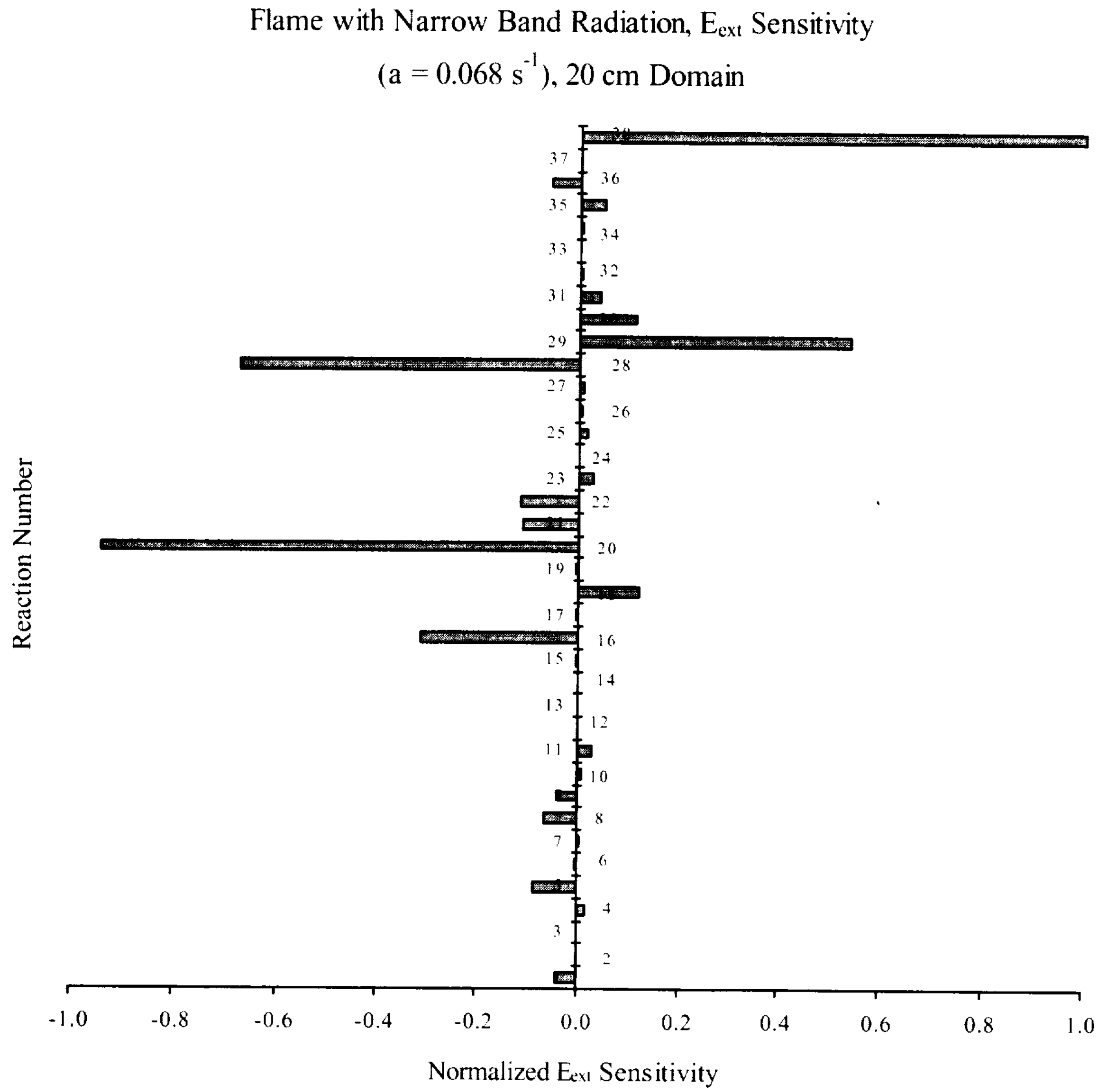

Figure 6-79: Flame with gas phase and surface radiation, normalized E_{ext} sensitivity by reaction for radiative extinction.

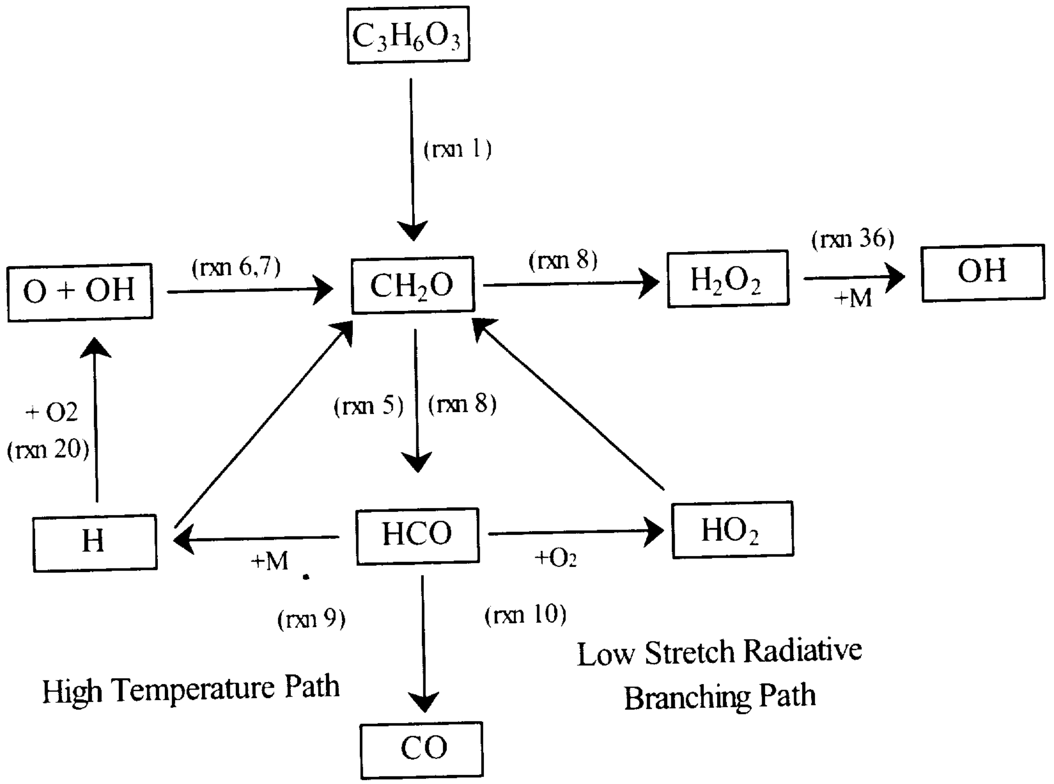

Figure 6-80: Reaction pathways for high-temperature path and chain-branching reaction paths for trioxane diffusion flame near low stretch extinction limit.

6.6 Conclusions

We presented an accurate and comprehensive model of the solid trioxane combustion in a stagnation-point flow configuration, using the narrowband model for the radiative heat transfer and detailed kinetics for the trioxane decomposition. In addition, we presented detailed reaction path analyses and sensitivity at the extinction turning points for the trioxane diffusion flame.

The flame with gas phase and surface radiation was compared to the adiabatic solution and a solution with surface radiation only. This study confirms and emphasizes previous parametric results (Appendix 4) showing that radiative effects (both gas phase and surface) are amplified at low stretch rate and can lead to extinction (quenching). Gas phase radiation effects are amplified at low stretch due to (1) a decrease in flame heat generation, brought about by the large flame standoff distance and (2) a longer optical length, also due to the thicker radiating layer. But the increasing loss from the flame lowers the flame temperature. Thus, the net amplification of gas radiation at low stretch is somewhat modulated by this interactive flame-radiation effect.

The stagnation-point trioxane diffusion flame in air has two distinct extinction limits. The high stretch blow-off turning point was found to occur at a=1952 s^{-1} at a maximum flame temperature of 1417 K. The low stretch turning point (quench limit) is near a=0.068 s^{-1} at a maximum flame temperature of 997 K.

Reaction path analysis shows that a straight-chain process dominates the trioxane decomposition over the entire flammability regime with the exception of near the extinction limits. Here, a branching path asserts itself due to low temperatures. Sensitivity analysis at the turning points shows that the extinction flow parameter (the radial pressure curvature) is sensitive to the fuel, formaldehyde, and formyl radical decomposition reactions at the high stretch extinction limit, but not near the low stretch extinction limit. The key to the rate of progress at both extinction limits is the H radical, because of its high reactivity. Table 6-1 is a summary of the key features of the extinction limits.

Table 6-1: Summary of the Key Features of the Trioxane Extinction Limits

Trioxane Flame Type	Extinction Characteristics	
	High Stretch	Low Stretch
Adiabatic	Low temperature (1400K) Low residence time Close to Surface Narrow flame Straight-chain reaction path	No extinction
Surface Radiation	Low temperature (1400K) Low residence time Close to surface Narrow flame	Low temperature (1000K) High residence time Very far from surface Very wide flame
Surface And Gas Phase Radiation	Low temperature (1400K) Low residence time Close to surface Narrow flame Straight-chain reaction path	Low temperature (1000K) High residence time Far from surface Wide flame Branching 'low temperature' reaction path

We conclude that, while the parametric studies of Appendix 4 give much insight into the radiative physics of the flame, including detailed kinetics with an equally accurate radiation model allows more accurate extinction analysis and yields insight into the detailed chemistry and sensitivity at extinction.

While Appendix 4 gave us some indication that it is possible for a radiative flame to have a higher burning rate than the adiabatic counterpart, here we have demonstrated this fact with a realistic fuel. Moreover, we see that flame radiation must be included to observe this effect—the flame with surface radiation only does not exhibit the higher burning rate, since the increase in burning rate at low stretch is due to feedback of the flame radiation to the surface.

The activity of the radical intermediate species, particularly at high stretch, where these species are blown against the surface, lead us to question the role these may play in the surface heat balance. In the next section, we investigate the possible effects of radical recombination at the solid surface.

7.0 Surface Radical Interactions in Solid Trioxane Combustion

7.1 Overview

As observed in Section 6, the flame interaction with the solid surface can be critical in the determination of the flame structure and extinction boundaries. In Appendix 4, we parametrically examined the role of gas-phase radiation and the extremes of surface radiative properties on the solid surface combustion. In Section 6, we examined in detail the role of flame radiation and detailed kinetics in combustion of a solid. We now turn to the examination of intermediate radical interaction with the solid surface. Solid surfaces can induce chemical reactions via either catalytic behavior or third-body behavior. Here we investigate the possible effects of surface-induced radical recombination in the solid trioxane flame.

Evidence indicates that intermediate radicals produced during combustion may have an effect on the flame structure and extinction boundaries because of recombination at the surface. We investigate the role of surface quenching of radicals in this section to determine whether this effect plays a significant role in the heat balance at the trioxane flame surface. We also consider the combined effects of surface radical interactions and surface radiative emission over the flammability regime of solid trioxane burning in air. The trioxane flame computational model of Section 3 is adapted to allow for surface radical recombination.

7.2 Nomenclature

The nomenclature in this section is adapted from Section 3, with the following additions:

Subscripts:

k	non-fuel species (as in Section 3)
l	non-fuel species that do not react at the surface (inert)
r	radical species that may react at the surface

7.3 Background

Vlachos and coworkers are leading an effort [Bui-Pham and Seshardri 1990, Vlachos et al. 1993, and Vlachos et al. 1994, Aghalayam et al. 1998, Fernandes et al. 1999, Gummalla et al.[1], Gummalla et al.[2], Park et al.] to understand the effects of interactions of radicals with a solid surface on flame structure, particularly on the ignition and extinction behaviors of various flames. Vlachos et al. examined the role of intermediate species interacting with a solid surface in a methane-air flame [1994] and a hydrogen-air flame [1993]. The surface is modeled as a sink for various radicals in order to gauge the effect of radical absorption by the surface. Each radical species is selectively removed from the surface (its surface concentration is set to zero) and the effect on ignition and extinction temperatures is observed in the pre-mixed flame. We assume an infinitely fast radical destroying mechanism at the surface. This model is not intended to simulate a physical situation, but to indicate the potential effect of each radical on the kinetics when surface recombination can occur. The investigators found that ignition and extinction temperatures can be altered significantly by surface chemistry. For the case of extinction in a hydrogen-air flame, the H radical had by far the largest effect in increasing extinction temperature, while O and OH had lesser effects. For the case of extinction in a methane-air flame, again the H radical plays the largest role in increased extinction temperature, particularly under fuel-rich conditions. O and OH also increase extinction temperature, but to a lesser extent. Other radicals, particularly CH_3, have a strong role in increasing ignition temperature.

Aghalayam et al. [1998] extended the treatment of the surface reactions to a cycle of absorption-surface reaction-desorption (of stable species) and included the heat of reaction. They investigated the role of wall quenching in ignition, extinction, and auto-thermal behavior in a premixed hydrogen-air flame impinging on a flat surface. They found that, for ignition, radical quenching retards the system due to the kinetics of the surface reaction. Extinction is also retarded due to thermal feedback from the recombination of radicals at the wall.

The investigators propose a mechanism that involves removing H, O, OH, HO_2, and H_2O_2 radicals at the surface via reaction at vacant sites. 'Sticking' coefficients are assumed to be unity (a surface 'clean' of radicals), to provide the fastest rate of radical removal (the most extreme case). The pre-exponential term is taken to be 10^{13} s^{-1}, which the authors estimate from transition state theory. The surface recombination reactions have zero activation energy. These assumptions result in an extreme (maximum) estimate of the potential effects of surface radical recombination on the heat balance and flame structure.

All real surfaces behave as sources and sinks for radicals. To determine the potential effect of a chemically reactive surface, the investigators [Aghalayam et al. 1998] looked at three cases for the premixed flame:

1. A reactive surface. Capable of absorbing out radicals from the gas phase (a sink for radicals). In this case, surface diffusion assists radical recombination into stable species. Since the formation of the stable species is exothermic, heat is released by the surface to the flame.

2. An inert surface. This is the base case used for comparison. Only the gas-phase reactions are used and the diffusive flux of each species at the wall is zero. This can be considered an 'extreme' case in the same sense as a radiatively nonparticipating surface (no absorption or emission).

3. A reactive surface with heat of reaction set to zero, to understanding the effect of the heat of surface reaction (as compared to case 1).

The investigators also examined the recombination of one radical at a time at the wall to isolate the most important radicals.

The investigators found that, while the actual mechanism used for the radical recombination may be debated, these details are less important to the outcome than the specific radical that is quenched and the effect of the heat of recombination.

Quenching of H radicals: For ignition, the radical recombination case requires higher temperature and power to ignite, indicating that the radical quenching of H radicals at the wall tends to make the mixture less ignitable (retards ignition). The heat of reaction at the surface shows no effect so that the ignition retardation is due entirely to the kinetics of radical quenching at the surface.

For extinction, heat loss due to radical recombination does have an effect. The flame is sustained at a lower power (supplied to the surface) due to heat feedback from the surface reactions. Temperatures across the flame are higher (due to the heat of absorption of H). Concentrations of H are lower, and H_2 higher near the surface when the radical recombination is considered. *The investigators found a trade-off effect for extinction: Radical recombination kinetically retards the flame; however, the heat feedback from the radical recombination counters this effect and sustains the flame.*

The closer a flame is to extinction, the more important the thermal and chemical coupling between the gas-phase and the surface becomes. Away from the extinction limit, the coupling is weak.

Quenching of other radicals: Fuel-rich and fuel-lean cases were considered in evaluation of the effect of other radicals. For the fuel-lean case, H, O, and OH have important effects (as discussed above) on ignition and extinction. The effect of H radical is the most pronounced, with O and OH having decreasing effects in that order. For the fuel-rich case, only the H radical played any significant role in ignition and extinction effects because the concentrations of O and OH are relatively small in a fuel-rich situation. *The effect of thermal feedback on extinction behavior is only important in cases where the radical concentrations are sufficiently high.*

The role of strain rate: An increase in strain rate tends to contract the non-extinction zone of the flame (making ignition harder), and thus the effect of wall radical recombination has the same qualitative effect, although more pronounced. Ignition near a reactive surface requires a higher ignition source at higher strain rates, compared to an inert surface at the same conditions.

Effect of surface radiation: The investigators studied surface radiation in the auto-thermal regime (self-sustained flame) using a surface emissivity of 0.3 and a surface temperature of 1000 K. Since they considered only emissivity, which represents a heat loss to the system, they found the auto-thermal regime greatly reduced and the effect of surface radical recombination is thus less significant.

Mass balance adjustments: A comment is warranted here on maintaining a mass balance in the model. When the mass fraction of a species is set to zero at the solid boundary to simulate a reactive surface (sink), the mass balance is not strictly maintained unless the product of the recombined species is adjusted as well. Warnatz [1978] noted that, for a species, or combination of species, having significant interactions at the surface, the reactants and products need to be accounted for in the mass balance so that the mass is adjusted for strict accounting of radicals reacting at the surface. The studies cited here did not make use of this adjustment because the mass of the species of interest did not change enough to necessitate this adjustment.

7.4 Formulation of Surface Radical Interactions in Solid Trioxane Combustion

Application to solid trioxane combustion: Here we examine the effect of radical recombination on the solid trioxane surface by adapting the 'radical sink' technique. Nothing is known about the activity of surface radicals on the burning of trioxane, so we consider the potential extremes in this situation to investigate if further study into this effect is merited.

Starting with the approach described by Vlachos et al. [1993, 1994], we examine the effect of the radicals produced in the trioxane decomposition, namely H, O, OH, HO_2, H_2O_2, and HCO, in order to observe the effect on the flame.

We also consider the role of formaldehyde as an intermediate radical. Formaldehyde has a duel role in the trioxane flame. Trioxane decomposes directly to formaldehyde, so that formaldehyde can be considered a secondary fuel. However, formaldehyde also behaves like an intermediate, in that its concentration is initially small at the surface, increases rapidly, and then is entirely consumed. While CH_2O is more stable than the other radicals examined (as evidenced by the gas chromatography data produced by Hochgreb [1991]), we examine this potential effect in order to encompass all possible surface radical interactions.

Table 7-1 is a comparison of surface mole fractions of trioxane, formaldehyde, and intermediate radicals for several oxidizer velocities using an inert trioxane surface. Three stretch rates are shown for each species. These data are identical to the 'adiabatic' cases described in Section 6.1. They represent the range of possible stretch rates for this flame. At the high stretch rate, the flame is at the extinction turning point (blow-off), where it is driven very close to the surface. The middle stretch rate case represents a flame further from the surface and not near the extinction limit. The low stretch rate case is a flame with a larger standoff distance whose temperature is approaching the flame sheet limit.

The concentration of CH_2O is roughly an order of magnitude smaller than that of trioxane at each stretch rate, but relatively large at the surface compared to the other radicals (at least two orders of magnitude), so the effect of formaldehyde is of particular interest for study. HCO is more concentrated at the surface than the other species. In addition, the concentrations of radicals at the surface are generally larger at the high stretch rate, which is the blow-off extinction point. This is also of particular interest for study, since the temperature is low enough in the flame (1415 K peak) for the 'low-temperature' reaction path discussed in Section 3.0 to dominate, and produce higher concentrations of radical intermediates that may interact at the surface. Another item of note is that the mole fractions at the surface in the solid trioxane flame are generally smaller than the surface mole fractions in the cited references. This is primarily due to the larger surface temperatures studied in the cited references.

Surface radical sink boundary condition: In order to gauge the importance of surface reaction effects, we begin with the mole fraction at the surface set to zero; all other boundary conditions remain as before (Section 3.0). This approach assumes an infinitely fast radical absorption mechanism at the surface. Some commentary on the species boundary conditions is necessary. While the boundary conditions do not change from the solid fuel stagnation-point formulation (with the exception of the radical species), the rationale for using these boundary conditions does change.

For the reactive surface, we can no longer use the same rationale as in Section 3 in the mass balance. Recall that at x=0 we used the following condition for the nonreactive surface:

$$\dot{m} = \rho_f u_f = \rho_F u_F = 2F$$

For a reactive surface, the mass flux not only includes fuel, but also radicals involved in the surface reactions. (Realistically, it would also include products of the radical recombination, but here we are using the 'radical sink' approximation and neglect the products). We separate the non-fuel species, k, into two types: those that are inert, I, and the radicals that react at the surface, r. Then the full mass balance for the reactive surface is expressed by:

$$\dot{m} = \rho_f u_f + \sum_I \rho_I u_I + \sum_r \rho_r u_r$$

We use the boundary condition from Section 3.0, where the nonreactive, non-fuel species $u_I=0$, but we no longer claim that u_r=0, so that

$$\dot{m} = \rho_f u_f - \sum_r \rho_r u_r$$

However, we can claim, as a first-order approximation, that

$$\rho_f >> \rho_r$$

so that

$$\dot{m} \approx \rho_f u_f$$

and the boundary conditions, Equations 3.3 and 3.4, on the fuel species remain the same. We verify the validity of this assumption by examining the mole fractions of the radicals at the surface. Table 7-1 lists example mole fractions for the fuel and the intermediates of interest in the trioxane flame (trioxane, and potential 'r' species: formaldehyde, H, HCO, H_2O_2, HO_2, O and OH). Inert, or 'I,' species include the rest of the species, such as H_2, O_2, H_2O, CO, CO_2, and N_2. Since both the mole fraction and the molecular weight of the fuel are large compared to the intermediates at the surface, we deduce that the fuel density is also much larger at the surface, since

$$\frac{\rho_f}{\rho_r} = \frac{X_f}{X_r}\frac{M_f}{M_r} >> 1$$

For the radical species, the Y_r are set to zero to simulate a species sink. The boundary conditions for the simple surface sink approximation are summarized in Table 7-2.

Table 7-1: Example Mole Fractions of Radicals at the Inert Surface for Low, Middle, and High Stretch Rates*

Mole Fractions for Adiabatic Trioxane			
Stretch rate, s^{-1}	**5**	**99**	**1952**
C3H6O3	3.79E-01	4.05E-01	4.12E-01
CH2O	7.08E-02	5.77E-02	6.12E-02
H	5.24E-11	4.14E-09	2.36E-06
HCO	9.31E-07	1.39E-05	7.49E-06
H2O2	1.40E-09	1.29E-07	1.65E-04
HO2	1.18E-11	1.41E-08	1.64E-04
O	0.00E+00	0.00E+00	1.44E-12
OH	6.36E-16	1.35E-11	1.70E-07

*Adiabatic cases in standard air; surface temperature 388K; 20 cm separation distance.

Table 7-2: Boundary Condition Comparison at x=0 Between the Formulation With the Inert Solid Surface and With Radical Interaction at the Surface (sink)

Dependent Variable	Inert Surface Boundary Condition at x=0	With Radical Interaction
F	$\dfrac{\lambda_g \left(\dfrac{dT}{dx}\right)_{x=0+}}{2\left(L^o + \int_{T^o}^{T_s} c_{p,f}\,dT\right)}$	$\dfrac{\lambda_g \left(\dfrac{dT}{dx}\right)_{x=0+}}{2\left(L^o + \int_{T^o}^{T_s} c_{p,f}\,dT\right)}$
G	0	0
T	T_s	T_s
Y	$fuel: Y_f = \dfrac{u_F}{(u_F + V_f)}$ $other: u_F = -V_k$	$fuel: Y_f = \dfrac{u_F}{(u_F + V_f)}$ $radical: Y_r = 0$ $other: u_F = -V_k$

Surface heat balance: As noted previously, the extreme situation to examine for our flame is the radical sink case, since including heats of reaction tends to have a trade-off effect in sustaining the flame near the extinction limit. Moreover, the effect of thermal feedback from radical recombination heats of reaction on extinction behavior is not significant unless radical concentrations are sufficiently high. Therefore, our study attempts first to determine the potentially important radicals via the 'surface sink' method described above. Heats of reaction from the surface reactions are not included here. Only a case found to have significant radical recombination effect using the sink method would warrant examination of the potential for thermal feedback due to heats of reaction from the radical recombination at the fuel surface.

7.5 Numerical Method

We adapted the CFDF program described in Section 5 to accommodate the radical interaction model for the surface boundary conditions. The surface radical sink is simulated by setting the mass fraction of the radical of interest to zero at the surface in the subroutine FUN. The solutions are run using the fixed temperature method described in Section 4. We used the domain size (20 cm) and number of grid points (174) throughout the study for the inert and reactive surface cases.

We adapted the surface radiation model of Section 3 to include the reactive surface in the same manner. For these cases, a domain of 25 cm is used, and 256 grid points are necessary to achieve accuracy over the entire domain.

7.6 Discussion of Results

7.6.1 The Surface Modeled as a Radical Sink

We solve over the entire flammability range from a stretch rate of approximately 2 s^{-1} to the blow-off extinction limit. In all cases, solutions are for standard air and atmospheric pressure, with the surface temperature set to 388 K. We first solve for the surface simulated as a radical sink, for one radical of interest at a time. Then we run the extreme case, called 'all sink', where the surface is a sink for all radicals (except formaldehyde). We first discuss results for all radicals and the 'all sink' case, since these are similar. We address results for the intermediate formaldehyde separately.

Individual radical sink: Results indicate that individual radical recombination at the surface has little to no effect on the flame compared to the inert surface case. We examined formaldehyde separately because of its unique role in the kinetics of the flame. Plots are of no use in examining the results because the differences are indistinguishable from the inert case. We therefore present the data in tables for sample stretch rates. Table 7-3 and 7-4 illustrate results at the two extremes of the domain, where any differences are most apparent. Table 7-3 gives results at the very low stretch rate, where the flame is not near the surface and the maximum flame temperature approaches the flame sheet limit. Table 7-4 presents the comparison at the blow-off extinction turning point, where the flame is blown against the surface, and the flame temperature is low. The tables list the stretch rates, fuel, and oxidizer side velocities, and maximum flame temperature for the inert case (adiabatic case of Section 6) and each case of radical surface sink.

The only difference worthy of mention is the turning point of HO_2. For the HO_2 radical, the turning point occurs at a stretch rate slightly lower than the inert surface case (1945 s^{-1} versus 1952 s^{-1}). Referring back to Figure 6-14, we see that for the inert surface, the HO_2 radical is produced in relatively large quantities near the surface at the blow-off limit due to the low temperature of the flame. This explains why we notice a slight decrease in the blow-off limit when the HO_2 radical is suppressed at the surface. The effect is small because the concentration of the radical is still very small in an absolute sense.

The effects of the radical sink in the trioxane flame are very slight compared to previous findings for the following reasons. First, the surface temperature of the trioxane is low (388 K) in comparison to that studied by previous researchers. Second, the lower temperature leads to smaller mole fractions of radicals at the surface. The most important radicals (OH, O and H) in Vlachos et al. [1994] have surface mole fractions in the 10^{-2} to 10^{-3} range. Aghalayam et al.'s study [1998] include somewhat lower radical mole fractions: $X_{OH}=O(10^{-3}$ to $10^{-4})$ and $X_H=O(10^{-5})$. Here, these radicals are far less concentrated at the surface, as indicated by the inert surface mole fractions given in Table 7-1.

'All sink': Cases are also run for the surface acting as a sink for all of the radicals of interest in combination. This case is called 'all sink' in Tables 7-3 and 7-4. The 'all sink' case also blows off at a stretch rate very slightly lower (1943s^{-1} versus 1952 s^{-1}), primarily due to the effect of HO_2 described above. Otherwise, the data are virtually identical. We conclude that the surface behaving as a pure sink for radicals is an insignificant effect for the solid trioxane flame, due to the low surface temperature and resulting low concentrations of radicals.

Formaldehyde: As discussed in Section 4.3, formaldehyde has a unique role in the kinetics of the solid trioxane flame. For the case where the surface is modeled as a sink for formaldehyde, the turning point occurs at a stretch rate somewhat lower than the inert surface (1761 s^{-1} versus 1952 s^{-1}), although the turning point temperatures are very close (Table 7-4). At the low stretch end of the regime, the difference is smaller; Table 7-3 shows that, at a stretch rate near 5 s^{-1}, the maximum flame temperatures are 2148 K for the formaldehyde sink case, and 2175 K for the inert case. The formaldehyde sink case gives uniformly lower maximum flame temperatures across the flammability domain, as illustrated in Figure 7-1. We conclude that the effect of formaldehyde being absorbed by the surface is very small in spite of the relatively large concentration at the surface in the inert (adiabatic) flame. Since formaldehyde is produced in larger quantities between the surface and the flame, as shown in Figures 6-6 through 6-8, the surface absorption effect is minor. In a true cycle of absorption-desorption of formaldehyde on a trioxane surface, we would expect the observed effect to be even smaller than the extreme sink model, because formaldehyde is more stable than the other radicals involved, and its recombination into higher molecular weight species requires higher energy bonds, and is thus less likely to occur.

Aghalayam et al. [1998] suggest that surface chemistry plays a minor role at lower surface temperatures; but at high surface temperatures the surface recombination of radicals can be important for accurate prediction of wall heat flux. This study demonstrates their commentary to be true for a lower surface temperature reactive surface in the solid trioxane diffusion flame.

Table 7-3: Effect of the Surface Modeled as Radical Sink for Stretch Rate Near 5 s^{-1}

	a (s^{-1})	u_F (cm/s)	u_O (cm/s)	T_{max} (K)
Inert	5.1	0.6	-94.0	2175.4
H	5.0	0.6	-92.9	2176.2
HCO	5.1	0.6	-94.2	2175.5
H_2O_2	5.1	0.6	-93.8	2175.5
HO_2	5.1	0.6	-95.1	2175.0
O	5.0	0.6	-92.7	2176.2
OH	5.1	0.6	-94.7	2175.2
CH_2O	5.0	0.5	-96.6	2147.9
All sink	5.1	0.6	-94.2	2175.3

Table 7-4: Effect of the Surface Modeled as Radical Sink for the Blow-Off Extinction Limit

	a (s^{-1})	u_F (cm/s)	u_O (cm/s)	T_{max} (K)
Inert	1951.9	11.3	-38913.9	1416.6
H	1951.5	11.3	-38907.0	1416.4
HCO	1951.7	11.3	-38910.6	1416.8
H_2O_2	1949.5	11.3	-38867.8	1416.8
HO_2	1945.0	11.2	-38776.3	1416.6
O	1951.9	11.3	-38913.9	1416.6
OH	1951.8	11.3	-38913.7	1415.7
CH_2O	1761.0	9.8	-35106.5	1415.3
All sink	1943.0	11.2	-38736.8	1417.0

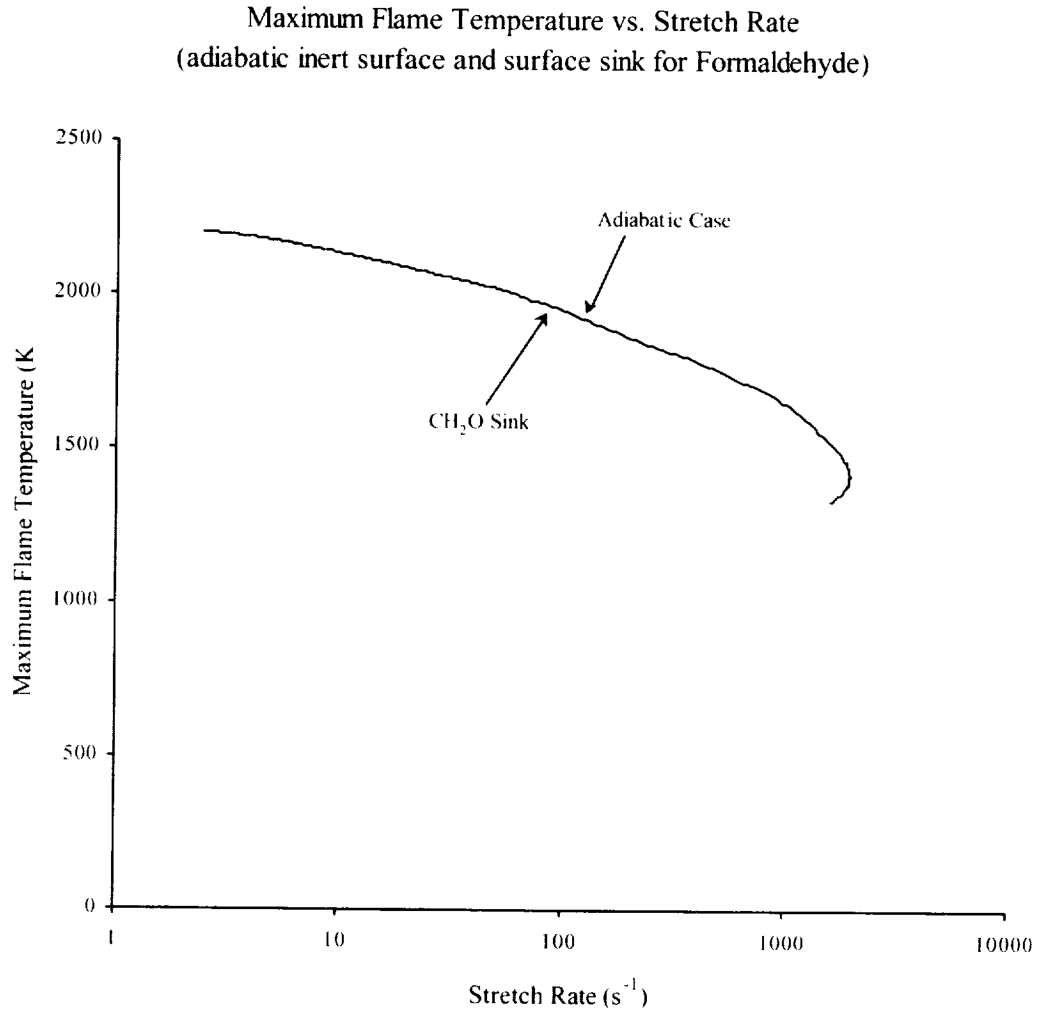

Figure 7-1: Maximum flame temperature vs. stretch rate for the adiabatic (inert surface) trioxane flame and the surface sink for formaldehyde.

7.6.2 Surface Radical Interaction Coupled With Surface Emission

The 'all sink' case described above is coupled with the model for a surface emitting radiation (as described in Section 3) in order to gauge the potential effects of radical interactions in the presence of surface radiation. Figure 7-2 contains two cases: the full isola of the inert surface that emits as a black body, and the surface that both absorbs radicals and emits as a black body. The full isola of the 'all sink' case is not produced—but the blow-off and radiative extinction turning points are shown. Figure 7-2 illustrates that there is virtually no difference if surface radical interaction is included with surface radiation. Surface radiation is clearly the dominant effect when compared to the radical recombination at the surface. This is consistent with Aghalayam et al.'s [1998] observations with partial surface emission. Although they studied a higher surface temperature (1000 K), they observed a decreased significance of radical recombination in the presence of surface emission.

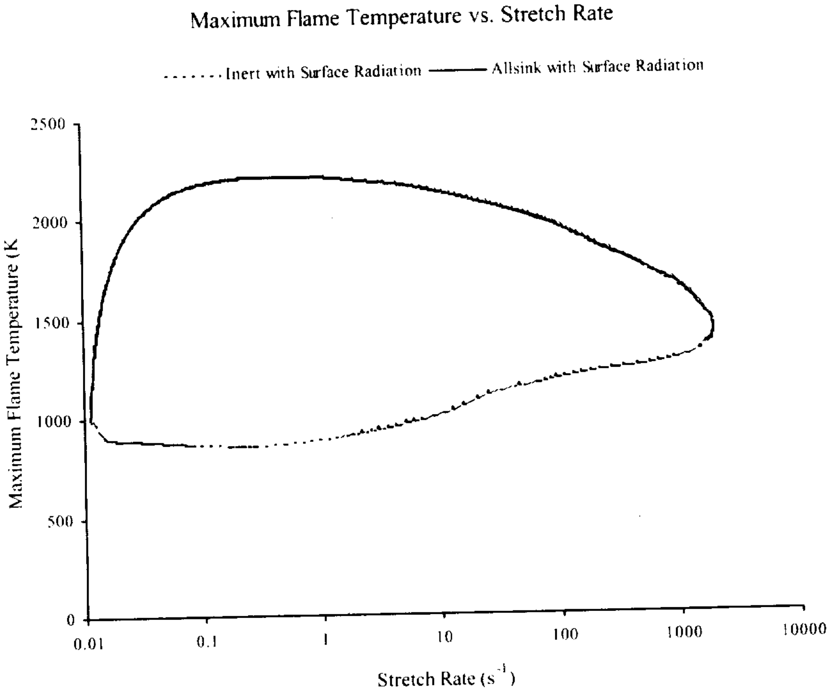

Figure 7-2: Maximum flame temperature vs. stretch rate for an inert surface including surface radiation and a surface that absorbs radicals and radiates.

7.7 Conclusions

We conclude that the effect of radical interactions at the surface in a solid trioxane flame is not significant, and that the only observable effect is near the extinction turning point. Even in the extreme case, where the surface absorbs all radicals, the effect is very small. In comparison to previous studies that found that surface radical interactions could be important, the trioxane flame has a relatively low surface temperature, and resulting smaller mole fractions of intermediates. When coupled with surface radiation effects, the surface radiation dominates and no surface radical interaction effect is observable. We conclude that the inert model of the solid trioxane diffusion flame is adequate and no representation of radical recombination at the surface is necessary to accurately represent the physics of the flame under study. While including heats of reaction as in Aghalayam et al. [1998] and mass compensations, ala Warnatz [1978], is acknowledged to be more accurate representations, these are not necessary in this study because the most extreme surface sink model yields very minor differences.

8.0 Summary

The goal of this work has been to add to the increasing body of knowledge on microgravity combustion so that space travel will be both safer and more feasible. Knowledge of how fires burn and extinguish in the unique microgravity environment of space is an essential component of spacecraft fire safety. Two numerical models were developed for the study of gas-phase radiation effects on the burning and extinction of a solid fuel in a stagnation-point diffusion flame configuration.

Early studies described in Appendix 4 present a relatively simple model formulation using PMMA in a stagnation-point configuration with one-step kinetics and Planck mean absorption coefficient. Results showed that both the gas-phase and solid surface radiation become more important as flame stretch rate decreases. The interaction of gas-phase and surface radiation, flame temperature, solid burning rate, extinction limits, and flammability boundaries were examined parametrically. The nondimensional analysis shows that the gas radiation parameter is inversely proportional to the stretch rate. Moreover, the nondimensional surface radiation parameter is inversely proportional to the square root of stretch rate. Even though, at high stretch rates, surface radiative losses can be large (and thus more important), gas-phase radiation can be comparable or dominant at low stretch rates.

The body of this thesis presents a solid trioxane stagnation-point diffusion flame model enhanced by detailed kinetics coupled with a narrowband radiation model, with carbon dioxide, carbon monoxide, and water vapor as the gas-phase radiation participating media. This model validates several of the assumptions of the first model, and expands the results to include detailed reaction path analysis and sensitivity.

Gas phase radiation effects are amplified at low stretch due to (1) a decrease in flame heat generation, brought about by the large flame standoff distance and (2) a longer optical length also due to the thicker radiating layer. But the increasing loss from the flame lowers the flame temperature. Thus, the net amplification of gas radiation at low stretch is somewhat modulated by this interactive flame-radiation effect.

The stagnation-point trioxane diffusion flame in air has two distinct extinction limits. The high stretch blow-off turning point is found to occur at $a=1952\ s^{-1}$ at a maximum flame temperature of 1417 K. The low stretch turning point (quench limit) is near $a=0.068\ s^{-1}$ at a maximum flame temperature of 997 K.

Reaction path analysis shows that a straight-chain process dominates the trioxane decomposition over the entire flammability regime with the exception of near the extinction limits. Here, a branching path asserts itself due to low temperatures. Sensitivity analysis at the turning points shows that the extinction flow parameter (the radial pressure curvature) is sensitive to the fuel, formaldehyde, and formyl radical decomposition reactions at the high stretch extinction limit, but not near the low stretch extinction limit. The key to the rate of progress at both extinction limits is the H radical, because of its high reactivity.

We demonstrated with a realistic fuel that it is possible for a radiative flame to have a higher burning rate than the adiabatic counterpart. Moreover, flame radiation must be included to observe this effect—the flame with surface radiation only does not exhibit the higher burning rate, since the increase in burning rate at low stretch is due to feedback of the flame radiation to the surface.

The trioxane diffusion flame model is extended to include surface absorption of radicals from the gas phase and the results compared to the inert surface case. Surface radiation is also included both with and without surface radical interactions. Results indicate that, for the model studied, surface absorption of radicals from the gas phase is unimportant.

Some comments on potential improvements that could be undertaken in future work are appropriate. The radiation model could be improved by including the fuel and formaldehyde as participating species.

While we believe we have included the primary participating species, including the fuel can have an effect on the results [Bedir 1998, Kashiwagi 1979]. Accurate measurements of these species absorbing and emitting bands could be included if made available.

The trioxane surface was assumed to absorb and emit as a black-body in this model; measurements of real surface absorption and emission could improve the model. The polarizability and the rotational relaxation collision parameter for trioxane were estimated for this analysis. While the solutions presented are not greatly dependent on either quantity, availability of accurate measurements of these two quantities could improve our confidence in the results. Finally, knowledge of the surface temperature relationship to the trioxane burning rate would be useful—a solid pyrolysis law (Arrhenius relationship) similar to that used in Appendix 4 for PMMA could be implemented in the model to include a surface temperature solution, rather than an imposed surface temperature.

The computer codes that generated these solutions were adapted for trioxane specifically. These codes could be generalized so that any solid (or liquid) fuel could be studied in the future.

Finally, and most importantly, experimental study on trioxane flames should be undertaken in order to validate the model predictions.

Appendix 1: CHEMKIN input file

```
ELEMENTS
C H O N
END
SPECIES
C3H6O3 CH2O CO CO2 H HCO H2 H2O H2O2 HO2 O OH O2 N2
END
THERM
! All of the thermodynamic data are from the CHEMKIN database except:
! The heat of formation for HO2 (H(f)=3.0kcal/mol), from
! Hills and Howard. J.Chem. Phys. 81, 4458, 1984. The fit below is from NASA
! Gordon-McBride.
HO2                   L 5/89H   1O   2   00   00G   200.000  3500.000 1000.000    1
 4.01721090E+00 2.23982013E-03-6.33658150E-07 1.14246370E-10-1.07908535E-14    2
 1.11856713E+02 3.78510215E+00 4.30179801E+00-4.74912051E-03 2.11582891E-05    3
-2.42763894E-08 9.29225124E-12 2.94808040E+02 3.71666245E+00 1.00021620E+04    4
!
! Trioxane data from Lay et al, J Phys Chem A, 101: 2471-2477, 1997.  Curve fit
! to NASA format using THERM (Bozelli)
C3H6O3      9/28/98 THERMC   3H   6O   3      G   300.000  5000.000 1390.000   01
 1.35345410E+01 1.75029470E-02-6.07166082E-06 9.51875850E-10-5.56106710E-14    2
-6.32346609E+04-5.25370825E+01-4.03811034E+00 5.69255009E-02-3.89747992E-05    3
 1.30526128E-08-1.70320983E-12-5.70209398E+04 4.23309293E+01                   4
!
REACTIONS
!Trioxane decomposition:
C3H6O3=>3CH2O     1.90E15  0       47500
!Hochgreb and Dryer, J PHYS CHEM, 96: 295-297, 1992.
!
!Oxidation of CH2O:
!Following rxns from Hochgreb and Dryer, Comb. and Flame, 91: 257-284, 1992.
!except as noted.  References listed in above are noted with HD prefix.
!All data from HD fitted to 700-2500 K; Uncertainty Factors listed with UF
!prefix
!Third body efficiency of N2 assumed to be 1.0 in all rxns
!
!Consumption of CH2O:
CH2O+M=HCO+H+M     4.21E23  -1.66    92170  !UF 3
CH2O+M=H2+CO+M         8.25E15     0      69540   !UF 3
!HD:  Roth and Just, 20th Symposium, 1984, p. 807.
!HD:  Third body efficiencies for above 2 rxns are all 1.0
CH2O+O2=HCO+HO2    2.05E13  0      38920  !UF 3
!HD:  Tsang and Hampson, J PHYS CHEM REF DATA 15: 1087-1279, 1986.
CH2O+H=HCO+H2   5.18E07    1.66    1834   !UF 2
!HD:  best fit for 300<T<1700K used, since CH20 conc. highest near surface.
CH2O+O=HCO+OH   1.81E13    0       3078   !UF 1.5
!HD:  Tsang and Hampson, 1986
CH2O+OH=HCO+H2O    3.43E09  1.18     -447   !UF 3
!HD:  Tsang and Hampson, 1986
CH2O+HO2=HCO+H2O2 1.47E13  0      15200   !UF 1.5
!HD
!
!Formation and Consumption of HCO:
HCO+M=H+CO+M    1.85E17    -1.00  17000   !UF 2
!HD:  Timonen, Ratajczak, Gutman,& Wagner, J PHYS CHEM, 91: 5325-5332,1987.
CO/1.9/ CO2/1.9/ H2O/16/ H2/1.89/
HCO+O2=CO+HO2   4.22E12     0      0       !UF 2
!HD:  Timonen, Ratajczak, Gutman, & Wagner, J PHYS CHEM, 92: 651-655, 1988.
HCO+H=CO+H2     7.23E13     0      0       !UF 2
!HD:  Timonen, Ratajczak, Gutman, & Wagner, J PHYS CHEM, 91: 692-694, 1987.
HCO+O=CO+OH     3.00E13     0      0       !UF 3
```

```
!HD: Tsang and Hampson, 1986
HCO+O=CO2+H      3.00E13     0       0       !UF 2
!HD: Tsang and Hampson, 1986
HCO+OH=CO+H2O    3.00E13     0       0       !UF 3
!HD: Tsang and Hampson, 1986
HCO+HO2=CO2+OH+H  3.00E13  0       0       !UF 3
!HD: Tsang and Hampson, 1986
!
!Oxidation of CO:
CO+OH=CO2+H      9.29E03     2.23   -2625   !UF 1.5
!HD:  Yetter, Dryer & Rabitz, Comb Sci Tech, 79: 97-128, 1991.
!HD:  fit from the original non-Arrhenius expression
CO+HO2=CO2+OH    6.63E13     0       22950   !UF 2
!HD: Yetter et al, 1991
CO+O+M=CO2+M     4.00E13     0       -4540   !UF 4
!HD: Yetter et al, 1991
CO/1.9/ CO2/1.9/ H2O/16/ H2/2.5/
CO+O2=CO2+O      2.53E12     0       47690   !UF 3
!HD: Yetter et al, 1991
!
!H2-O2 Chain Reactions:
H+O2=OH+O            3.52E16        -.70     17070
!HD: corrected Ref. 26; Masten, Hanson & Bowman (J PHYS CHEM, 94:
!7119-7128, 1990).
H2+O=OH+H        5.08E04     2.67    6292   !UF 2
!HD: Yetter et al, 1991
OH+OH=H2O+O      2.88E00     3.66   -4313   !UF 2.5
!HD: Yetter et al, 1991
OH+H2=H2O+H      2.16E08     1.51    3430   !UF 2
!HD: Yetter et al, 1991
!HD:  fit from the original non-Arrhenius expression
!
!Formation and Consumption of H2O2 and HO2:
H2O2+OH=H2O+HO2          7.00E12     0       1430   !UF 2
!HD: Yetter et al, 1991
H2O2+H=H2O+OH    1.00E13     0       3590   !UF 2
!HD: Yetter et al, 1991
HO2+HO2=H2O2+O2    4.20E+14    0.00        11980   !UF 1.5
DUP
HO2+HO2=H2O2+O2    1.30E+11    0.00        -1629
DUP
!HD:   Hippler, Troe, & Willner, J.Chem.Phys.93: 1755-1760, 1990.
!      Rate constant is the sum of the above two rates.
H+HO2=OH+OH      1.69E14     0        874   !UF 3
!HD: Yetter et al, 1991
H+HO2=H2+O2      6.63E13     0        2126   !UF 3
HO2+OH=H2O+O2    1.45E16     -1.00  0        !UF 2.5
HO2+O=O2+OH      1.81E13     0        -397   !UF 2
H2O2+H=H2+HO2    4.82E13     0        7948   !UF 2
O+O+M=O2+M       6.17E15     -.50   0        !UF 3
CO/1.9/ CO2/1.9/ H2O/16/ H2/2.5/
H2+M=H+H+M       4.58E19     -1.40   104400   !UF 2
CO/1.9/ CO2/1.9/ H2O/16/ H2/2.5/
H+OH+M=H2O+M     2.25E22     -2.00  0        !UF 2
CO/1.9/ CO2/1.9/ H2O/16/ H2/2.5/
H2O2+M=OH+OH+M           1.20E17     0        45500   !UF 2
CO/1.9/ CO2/1.9/ H2O/16/ H2/2.5/
O+H+M=OH+M       4.72E18     -1.00  0        !UF 30
CO/1.9/ CO2/1.9/ H2O/16/ H2/2.5/
H+O2+M=HO2+M     2.00E15     0       -1000   !UF 3
CO/1.9/ CO2/1.9/ H2O/16/ H2/2.5/
END
```

Appendix 2: Transport Property Estimates for Trioxane

This appendix outlines the rationale for the estimations of rotational relaxation collision parameter and polarizability for trioxane. These data were not available for trioxane after an extensive literature search, nor could an estimate be made by back calculating from other known properties. The effect of these two quantities on transport properties is also discussed, along with potential effects of estimation error on the results.

Rotational Relaxation, Z_{rot}

The quantity Z_{rot} is a measure of the number of collisions needed to establish rotational equilibrium of a molecule when it has been excited out of equilibrium by addition of energy to the system. This quantity was first defined by Parker [1959] and the theory was expanded by Brau and Jonkman [1970]. Their analyses are applicable to diatomic gases only; however, certain analogies may be drawn to more complex species, such as trioxane. Gas-phase thermal conductivity can be thought of as a measure of the collision efficiency of a species in the transmission of thermal energy, and indeed, thermal conductivity is a weak function of Z_{rot} [Kee et al. 1986].

The quantity Z_{rot} for a same species collision of a diatomic gas is given by Parker [1959] as:

$$Z_{rot} = \frac{1}{16}\left(a\frac{d}{e}\right)^2$$

In this expression, a is a constant characterizing the spatial rate of variation of the collision force between two molecules, d is the nuclear separation distance, and e is a parameter based on the geometry of the collision. The quantities a and e are typically estimated by fitting experimentally known values of the *vibrational* relaxation collision parameter, Z_{vib}. None of these quantities is available for trioxane.

Z_{rot} is zero for monatomic species and some linear molecules with no rotational component. Since trioxane is a nonlinear molecule, we know that its rotational component is non-zero. The vast majority (all but one of 100 +) of the nonlinear molecules in the TRAN database have rotational relaxation collision parameter greater than or equal to 1.0; a large portion of these are equal to 1.0. That is, it takes one or more collisions for the molecule to relax to the equilibrium state. Another molecule, benzene, has an analogous molecular weight (benzene m. wt. = 78, trioxane m. wt. = 90) and structure (ring) to trioxane. Z_{rot} for benzene (and all other high molecular weight molecules in the TRAN database) is one collision. Therefore the quantity $Z_{rot} = 1$ was chosen for trioxane because it is a high molecular weight, nonlinear molecule, and is similar in structure and molecular weight to benzene.

We evaluated the thermal conductivity of trioxane with the TRAN program using the values of Z_{rot} equal to one and zero, to gather further insight into the effect of rotational relaxation on thermal conductivity. The value of thermal conductivity at 300 K was increased by 6 percent for $Z_{rot} = 1$. We compared the value to that of benzene and found it to be comparable, but somewhat larger—which is expected, given its larger molecular weight.

With the known information outlined above, the selection of $Z_{rot} = 1$ is reasonable and conservative. Larger estimates ($Z_{rot} > 1$), while possible, would be unsupportable by the known data.

The effect of this assumption being in error would be to slightly increase thermal conductivity if $Z_{rot} > 1$. During burning of the solid, the gas-phase trioxane is formed through pyrolysis very near the surface and rapidly decomposes to formaldehyde. Thus, an underestimation of thermal conductivity of trioxane would have the largest effect at the surface and tend to underestimate the conduction heat transfer from the gas to the surface. Any potential error then would be most noticeable at low stretch rates, where heat feedback between the flame and the surface is increasingly important, and where the concentration of trioxane would tend to be larger due to increased residence time at low velocities. Thus, the effect of a small underestimation of thermal conductivity would also somewhat underestimate the flammable region of trioxane.

Polarizability, α_p

Trioxane is a dielectric molecule with a permanent dipole [Walker and Carlisle 1943]. These electrical characteristics are important in molecular collisions, because they affect the intermolecular forces present between molecules of trioxane and other species when they collide. Transport properties are thus affected by molecular electrical characteristics. The polarizability, α_p, is used in the calculation of binary diffusion coefficients (for polar-nonpolar collisions only) in the transport package, TRAN [Kee et al. 1986].

An excellent and exhaustive discussion of polarizability and other electrical characteristics of molecules is given by Hirschfelder et al. [1954]. The following discussion is a brief summary from Hirschfelder et al. [1954] of the pertinent information necessary to understand the effect of polarizability.

If E is an electric field strength applied to a molecule, and μ^{ind} is the dipole moment induced by the electric field, then

$$\mu^{ind} = \alpha_p \mathrm{E}$$

and α is the polarizability.

There exists a quantity called the electric susceptibility, X, that relates polarizability, dipole moment, and the dielectric constant. X is expressed via the dielectric constant, ε, by the Clausius-Mosotti relation:

$$X = \frac{3}{4\pi}\frac{M}{N\rho}\left(\frac{\varepsilon - 1}{\varepsilon + 2}\right)$$

where M is the molecular weight, N is Avagadro's number, and ρ is the density.

X for molten trioxane is calculated from the dielectric constant and found to be 0.237 cubic Angstroms. For solid trioxane, the value is 0.143. We can use the electric susceptibility to predict the variation of the dielectric constant with density, as shown in the above expression, since the electric susceptibility remains constant with respect to these two quantities.

We can find polarizability and dipole moments by measuring the dielectric constant, as a function of temperature. If μ is the dipole moment, and k is the Boltzman constant, then

$$X = \alpha + \frac{\mu^2}{3kT}$$

When we plot this expression as 1/T, the result is a straight line, with α as the intercept and $\mu^2/3k$ as the slope. Polarizability is then defined at the intercept, where $1/T \to 0$. (Or $X \approx \alpha$).

Then the intercept gives α, the polarizability, as approximately 0.237 cubic Angstroms.

In the calculation of the binary diffusion coefficient in the TRAN program [Kee et al. 1986], the polarizability for a polar molecule appears in the calculation of a collision integral, which is internal to the TRAN computational package. A priori insight into the variation of the diffusion coefficient with polarizability of a polar molecule is therefore not available. For this reason, we used the TRAN program to assess differences in diffusion coefficients with different polarizabilities.

The differences in polar-nonpolar diffusion coefficients for trioxane were assessed for polarizabilities of zero and 0.237. The value for solid trioxane lies within this range, so that the extremes of the range of known values of polarizability for trioxane are included. (The dielectric constant for gas phase trioxane is unknown, possibly because trioxane decomposes so rapidly to formaldehyde in the gas phase. It is possible that gas phase trioxane has a higher dielectric constant, and thus a higher polarizability, but we don't consider this possibility here because no evidence for this exists.) The results showed no differences to the third significant figure in the binary diffusion coefficients. Thus, we conclude that the polarizability does not significantly affect the transport characteristics of this problem, and any error in the estimate will have little effect. The value $\alpha = 0.237$ is retained in the database for trioxane.

Appendix 3: Latent Heat of Solid Fuel

This appendix contains the detailed latent heat calculation for a solid fuel (generalized), and the specific application for trioxane.

Generalized latent heat calculation: We desire the change in latent heat (enthalpy) of the fuel for the heat balance at the surface. The surface has temperature T_s, and the enthalpy is calculated from reference quantities, designated by the 'o' superscript. Figure A3-1 illustrates the change in enthalpy.

The total enthalpy of the solid, where $c_{p,s}$ is the constant pressure specific heat of the solid fuel, is:

$$h_s(T_s) = h_s^o + \int_{T^o}^{T_s} c_{p,s} dT$$

The total enthalpy of the gas-phase fuel, where $c_{p,f}$ is the constant pressure specific heat of the gas-phase fuel, is:

$$h_f(T_s) = h_f^o + \int_{T^o}^{T_s} c_{p,f} dT$$

Here the subscripts refer to the phase of the fuel: s refers to the solid phase, and f refers to the gas phase. Then the change in enthalpy for the fuel at the solid-gas interface is:

$$\Delta h_{fs} = h_f^o + \int_{T^o}^{T_s} c_{p,f} dT - h_s^o - \int_{T^o}^{T_s} c_{p,s} dT$$

For simplicity, allow

$$L = \Delta h_{fs}$$

and

$$L^o = h_f^o - h_s^o$$

Then the general expression for the enthalpy at the fuel interface is:

$$L = L^o + \int_{T^o}^{T_s} c_{p,f} dT - \int_{T^o}^{T_s} c_{p,s} dT$$

Specific application to trioxane: Now for most solids, including trioxane, we approximate c_s as a constant, particularly when T_s is not large compared to T^o, so that

$$L = L^o + \int_{T^o}^{T_s} c_{p,f} dT - c_{p,s}\left(T_s - T^o\right) \qquad \textbf{(A3-1)}$$

For trioxane, L^o=55.6 kJ/mol (6.17x10^9 erg/g), T^o=300 K, T_s=388 K (boiling point of trioxane), and the integral can be calculated.

When the integration is carried out numerically using the transport data for trioxane (referenced in Section 4) the result is:

$$\int_{300}^{388} c_{p,f}\,dT = 9.445x10^{8}\,erg/g$$

Approximating the integral from the NIST database [National Institute of Standards Chemistry Web book], we start with:

$C_{p,f}$(trioxane gas, 300 K) = 82.38 J/mol/K (9.145x10^{6} erg/g/K)

and

$C_{p,f}$(trioxane gas, 400 K) = 109.75 J/mol/K (1.218x10^{7} erg/g/K)

Assuming a linear profile for specific heat over the temperature range 300 to 400 K, we can interpolate to get the midpoint value over the range of integration:

$C_{p,f}$(trioxane gas, 344 K) = 94.42 J/mol/K (1.048x10^{7} erg/g/K)

Then approximating the integral:

$$\int_{300}^{388} c_{p,f}\,dT \approx c_{f,midpoint}\,\Delta T = c_{p,f}(344K)(388K - 300K) = 9.224x10^{8}\,erg/g$$

This is less than 3 percent different from the value calculated from numerical integration. We conclude that the specific heat is a near-linear function of temperature over the range evaluated and that the transport data used in Section 4 are consistent with the NIST data for trioxane. The data from references [Lay et al. 1997] and [National Institute of Standards Chemistry Web book] used to approximate the integral are compared in Figure A3-2. Upon investigation, we found that both references use a single source [Dorofeeva 1992], so this result is not surprising. It does confirm that the polynomial approximation used to convert the data from Lay et al. [1997] via the THERM program into the NASA format is accurate.

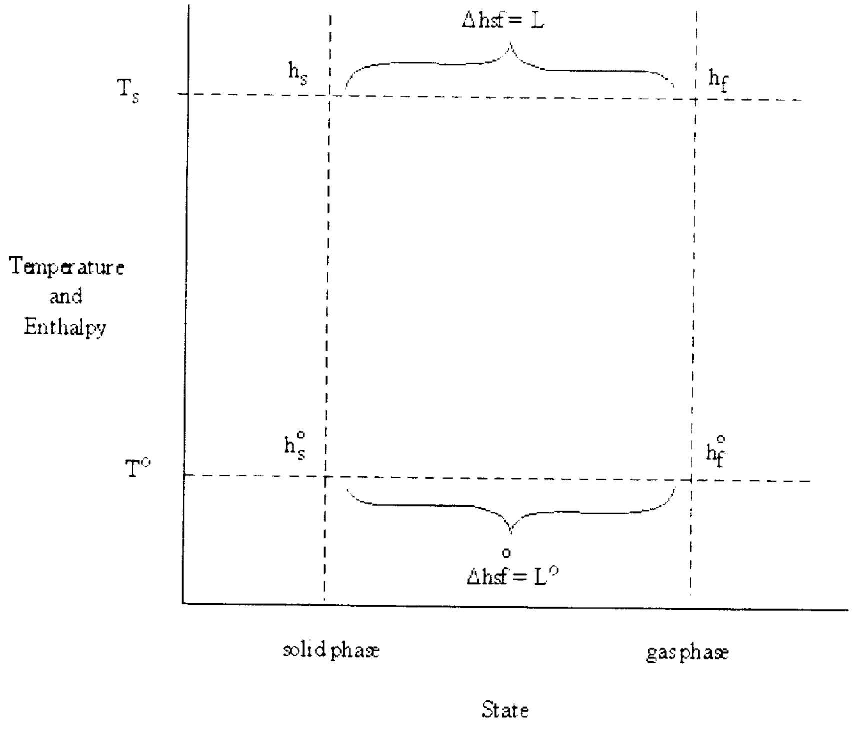

Figure A3-1: Illustration of enthalpy calculation.

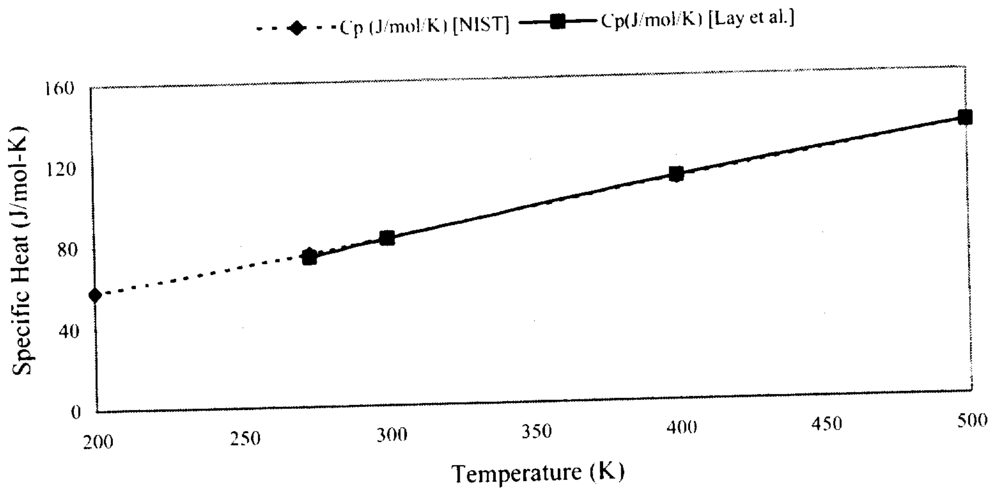

Figure A3-2: Comparison of specific heat data from references.

[Lay et al. 1997] and [NIST Chemistry Web book]

Appendix 4: Surface and Gas-Phase Radiation Effects on the Burning and Extinction of a Solid Fuel

A4.1 Background

Radiative loss from flames has long been recognized as a mechanism for flame extinction. For example, in the early theory of flammability limits for premixed flames, gaseous radiative loss was included in the one-dimensional analysis [Spalding 1957]. Surface radiative loss was introduced for a solid monopropellant to explain the observed low-pressure deflagration limit of ammonia perchlorate [Friedman et al. 1959].

In analyses of diffusion flame extinction, research has concentrated on the high stretch regime, which most often occurs in higher speed flows. In the absence of convective flow, Bonne [1971] hypothesized that radiation can lead to diffusion flame extinction in microgravity. Surface radiative loss has also been included in a flat-plate boundary layer combustion analysis of a solid [Silbulkin et al. 1981 and 1982]. Unfortunately, the parabolic equations used are unsuitable for flame extinction analysis [Chen and T'ien 1986], and the extinction condition found appears to be the artificial consequence of the local similarity assumption.

T'ien [1986] used flame stretch rate as the flow parameter to investigate combustion and extinction characteristics of a diffusion flame anchored to a solid surface in the stagnation-point region. Only surface radiative loss was included. He found that the importance of surface radiative loss is inversely proportional to the square root of the stretch rate. At low stretch rate, he found a radiatively quenched flammability boundary in a map using oxygen percentage and stretch rate as the coordinates.

Heat loss from gas-phase radiation has been included in several studies of diffusion flames. Negrelli et al. [1977] used the exponential wide-band gas radiation model and assumed the flame chemistry to be infinitely fast. Liu and Rogg [1991] employed detailed chemical kinetics for methane and air using the optically thin radiation approximation in the gas-phase. Sohrab and Williams [1981] assumed one-step kinetics and used asymptotic techniques. All of these studies concluded that radiation lowers the flame temperature, as expected, but did not examine the radiation quench limit.

Chao et al. [1990] studied the spherical droplet combustion problem using an asymptotic expansion, and treated gas radiation as a pure loss. They identified a large droplet diameter limit beyond which flame quenching occurs. Kinoshita and Pagni [1981] studied a gray radiation diffusion flame above a gray pyrolyzing solid fuel in the stagnation-point region using the optically thin model. They recognized flame and surface radiation interaction, and that flame radiation effects may cancel surface emission effects. In a series of papers [Bhattacharjee[1] and Altenkirch 1990, Bhattacharjee[2] and Altenkirch 1990, Bhattacharjee and Altenkirch 1992], Bhattacharjee and Altenkirch included both gas-phase and solid surface radiation in their model of opposed-flow flame spread over a solid. They pointed out that gas-phase emission is not a pure heat loss from the flame system because the portion of the gas-phase radiation incident on the fuel surface may be absorbed. They assumed in their model that the amount of incident radiation is balanced by the surface emission, thus detailed gas-surface radiative interaction analysis was not performed.

Chen and Cheng [1994], in their model of downward flame spread over a solid, incorporated a two-flux, optically thin model to study the effect of gas-phase radiation from CO_2 and H_2O. Although the accuracy of the two-flux model is somewhat questionable in this two-dimensional configuration, the method provides a direct coupling between the gas-phase radiative flux and the solid radiative flux. For surface radiative properties, they selected an absorptivity and emissivity equal to 0.92, and presented detailed radiative and convective heat fluxes along the solid surface.

The objective here is to study the influence of gas-phase radiation from carbon dioxide and water vapor on the burning and extinction of solid fuels. In particular, we are interested in the interaction between gas-phase radiation and the solid surface. In the analysis, we vary not only flame stretch rate but also the surface radiant properties to obtain a more complete understanding of the effect of gas-phase and solid surface radiation. This study is unique in that it offers the only parametric variation over the comprehensive set of surface radiation parameters—including the gas-phase flame radiation so that surface absorption as well as emission can be evaluated. Also, this section provides insights into the calculations for a real fuel with detailed chemistry that is taken up in the following sections.

A4.2 Nomenclature

a	Stagnation-point flow radial velocity gradient, $U_e = ar$, s^{-1} (r = radius)
c_p	Specific heat of the gas, J/kg-K
c_s	Specific heat of the solid, J/kg-K
D_k	Ratio of local radiative emission length to flame thickness, Equation A4-2
F	Nondimensional parameter of the two-flux radiation model, see Equation (A4-4)
f	Modified stream function [T'ien et al. 1978]
$-f_w$	Nondimensional burning rate, see Equation (A4-13)
K_p	Planck mean absorption coefficient, 1/m
L	Latent heat of the condensed fuel scaled to c_pT_e
m	mass burning rate of the condensed fuel, kg/m-s
Pr	Prandtl Number, $\mu c_p/\lambda$
Q	Nondimensional heat loss to solid, see Equation (A4-10)
q_f	Nondimensional heat of combustion
q^+	Nondimensional gas-phase radiative flux away from the surface, scaled to σT_e^4
q^-	Nondimensional gas-phase radiative flux towards the surface, scaled to σT_e^4
q_{net}	Nondimensional net heat flux away from the surface, see Equation (A4-8)
S	See Equation (A4-3)
T	Temperature, degrees Kelvin
U_e	Radial velocity at edge of boundary layer
w	Nondimensional reaction rate
Y	Species mass fraction
y	direction normal to surface
α	Total hemispherical absorptivity of the surface
ε	Total hemispherical emissivity of the surface
η	Nondimensional distance normal to the fuel surface [T'ien et al. 1978], $\eta = \dfrac{U_e}{2\sqrt{\int_0^r \rho_e \mu_e U_e dr}} \int_0^y \rho dy$
Θ	Nondimensional temperature, $\Theta = T/T_e$, where T_e = 300K
Θ_c	Nondimensional temperature far inside the condensed fuel
λ	Thermal conductivity, kJ/m-s-K
μ	Viscosity, kg/m-s
ρ	Density, kg/m^3
σ	Stefan-Boltzman constant, 5.6696×10^{-8} W/m^2-K^4
τ	Nondimensional optical thickness, see Equation (A4-12)

Subscripts

e	Edge of boundary layer
F	Fuel
f	Flame
o	Oxidizer
P	Product
w	Wall (fuel surface)

Superscripts

'	d/dη

A4.3 Combustion Model

An axi-symmetric stagnation-point configuration is adopted for the solid-fuel laminar diffusion flame analysis. The flame model, with one-step finite-rate chemical kinetics, is similar to that described in references T'ien et al. [1978] and T'ien [1986]; here we add a two-flux gas-phase radiation model (Figure A4-1). The modified energy equation, the surface boundary conditions and the two-flux radiation equations are described as follows.

The nondimensional energy equation is identical to T'ien et al. [1978] except that the gas-phase radiation has been included:

$$\frac{1}{\mathrm{Pr}}\Theta''+f\Theta'+\frac{2SD_k}{\mathrm{Pr}}(F-\Theta^4)=-q_f w \qquad \textbf{(A4-1)}$$

The last term on the left-hand side is the gas-phase radiative contribution, where

$$D_k=2\sqrt{\frac{\mu_e}{\rho_e a}}K_p\Theta \qquad \textbf{(A4-2)}$$

and

$$S=\frac{\sigma T_e^3}{\lambda_e}\sqrt{\frac{\mu_e}{\rho_e a}} \qquad \textbf{(A4-3)}$$

The nondimensional parameter D_k can be regarded as the ratio of local radiative emission length to flame thickness. The nondimensional parameter S represents the rate of black-body radiative heat transfer to gas-phase conduction. (The coefficient term S/Pr is similar to that defined by Ozisik [1973] relating the Boltzman number and the Reynolds number.) K_p is the local Planck mean absorption coefficient of the mixture, adjusted for local partial pressures. In this work, only combustion products H_2O and CO_2 are assumed to participate radiatively. The Planck mean absorption coefficients are taken from data in Seigel and Howell [1981] and T'ien and Lee [1982] and modeled as polynomial functions of temperatures and summed using the partial pressure of the gases as the weighting factor. Soot and fuel vapor contributions are neglected.

The quantity a in Equations (A4-2) and (A4-3) is the flame stretch rate which is the flow parameter in this problem. Note that the product SD_k is inversely proportional to stretch rate, a. Therefore, the importance of the gaseous radiation term in Equation (A4-1) increases at small stretch rate.

The gas-phase radiation flux is modeled using the two-flux (Schuster-Schwartzchild) radiation model [Ozisik 1973, Siddall 1974, Seigel and Howell 1981, Lee and T'ien 1989], chosen because of its simplicity and its capability to model both gas-phase absorption and emission. In addition, the method allows for detailed accounting of the radiative fluxes (versus a global approach) and permits study of the interaction between gas-phase and surface radiation. The quantity F in Equation (A4-1) is given by

$$F = \frac{1}{2}(q^+ + q^-) \qquad \textbf{(A4-4)}$$

where q^+ is the nondimensional gas-phase radiative flux away from the surface (in the positive η direction) and q^- is the nondimensional gas-phase radiative flux toward the surface (in the negative η direction); see Figure A4-1. These nondimensional fluxes are scaled to the background radiative flux, σT_e^4. The two-flux radiation equations are:

$$\frac{dq^+}{d\eta} = D_k(\Theta^4 - q^+) \qquad \textbf{(A4-5)}$$

and

$$\frac{dq^-}{d\eta} = D_k(q^- - \Theta^4) \qquad \textbf{(A4-6)}$$

with boundary conditions:

$$\begin{aligned} &\eta = 0 : q_w^+ = (1-\alpha)q_w^- + \varepsilon\Theta_w^4 \\ &\eta \to \infty : q_e^- = \Theta_e^4 = 1 \end{aligned} \qquad \textbf{(A4-7)}$$

where α and ε are the surface absorptivity and emissivity. At the surface, the radiation flux leaving is equal to the reflection of incident radiation plus the radiation emitted from the surface. Transmission of radiation through the solid surface is negligible. At the outer boundary of the flame, the radiation entering the system is the background emission from the surroundings. The net flux of gas-phase radiation is the difference between the flux away from the surface and the flux toward the surface:

$$q_{net} = q^+ - q^- \qquad \textbf{(A4-8)}$$

The energy balance at the fuel surface, with radiation, is:

$$\Theta'_w = -f_w \Pr Q + Sq_{net,w} \qquad \textbf{(A4-9)}$$

where Θ_w' is the temperature gradient at the surface from the gas phase, $f_w PrQ$ is the heat transferred to the solid and to pyrolyze it to fuel gas [T'ien 1986, Oh et al. 1994], and $Sq_{net,w}$ is the net radiation from the surface. Also,

$$Q = \Theta_w - \frac{c_s}{c_p} + L \qquad \textbf{(A4-10)}$$

Note that the radiation parameter S appears in the surface boundary condition (Equation A4- 9) as well as the energy equation (Equation A4-1). It is inversely proportional to the square root of the stretch rate, so the effect of surface radiative transfer is also amplified at small stretch rate. However, this amplification rate is smaller than that of the gas-phase radiation (which is proportional to the inverse stretch rate).

A4.4 Discussion of Results

A4.4.1 Variation of the Flow Parameter (stretch rate)

The dependency of Equations (A4-1) and (A4-9) on S and D_k, and thus stretch rate, a, suggests the relative importance of radiation to the heat balance. At higher stretch rate, surface radiative effects are more significant than gas-phase radiation effects, because the optical thickness of the gaseous flame is smaller at higher stretch rate. Note that

$$\begin{aligned} S &\propto 1/\sqrt{a} \\ SD_k &\propto 1/a \end{aligned} \qquad \textbf{(A4-11)}$$

Moreover, gas-phase radiation effects could take precedence due to larger amplification by SD_k at low stretch rates. This is due to an increase of the optical thickness of the flame as stretch rate decreases. Figure A4-2 shows the quantity D_k, as given by Equation (A4-2), over a range of stretch rates, and illustrates the dependence of optical thickness on stretch rate. D_k can be interpreted as the ratio of the local radiation absorption length to the flame thickness. The nondimensional optical thickness of the entire flame, τ, is related to D_k by

$$\tau = \int_0^{\infty} (D_k) d\eta \qquad \textbf{(A4-12)}$$

Figure A4-2, which is a plot of D_k versus nondimensional distance from the surface, η, for a range of stretch rates, illustrates the increased importance of gas-phase radiation emission at low stretch rate for a typical case that includes full surface absorption and emission. One can see that, as stretch rate decreases, the peak values of D_k increase. This means that the optical thickness τ (the integrated value of D_k) increases as stretch rate decreases as well. While the flame is considered optically thin ($\tau << 1$), the *relative* optical thickness increases almost tenfold between a stretch rate of 60 and 1.4 s^{-1}. Thus at the low stretch limit, gas-phase radiation (particularly gas-phase emission) becomes increasingly important in the heat balance. The significance of this increased emission is shown later.

A4.4.2 Parametric Variation of the Surface Radiation Properties

The model equations are solved numerically by the time-marching scheme described in T'ien et al. [1978], using the properties of PMMA from T'ien [1986] (with the exception of surface radiative properties, which are varied parametrically) and the two-flux radiation equations are solved by integration in η, the nondimensional spatial coordinate. To understand how gas-phase radiation interacts with the surface processes (absorption, emission, reflection) and the consequences of this interaction on the flame, we chose four cases with the extreme combinations of surface absorptivity and emissivity. We computed these cases with variation of absorptivity and emissivity in Equation (A4-7) over the range of stretch rates from blow-off to low speed quenching. These cases are:

Case 1: $\alpha = 1$; $\varepsilon = 1$; full absorption and full emission (a 'black' surface)
Case 2: $\alpha = 1$; $\varepsilon = 0$; full absorption and no emission (i.e., largest radiation energy gain to surface; a 'cold' surface)
Case 3: $\alpha = 0$; $\varepsilon = 0$; no absorption (fully reflecting) and no emission

Case 4: $\alpha = 0$; $\varepsilon = 1$; no absorption (fully reflecting) and full emission (largest radiation energy loss from the surface)

These parametric extremes permit us to consider a series of interesting questions: What is the importance of surface absorption in both the presence and absence of surface emission? How does a fully reflecting surface affect the flame heat balance? How does the flame respond in the presence of large surface radiation loss (non-absorbing; fully emitting surface)? Additionally, these cases could represent some physically realizable situations. For example, Case 2 mimics a liquid surface behavior, with little emission (due to low surface temperature) but full absorption.

A4.4.3 Radiative Heat Fluxes

Radiative heat fluxes, normalized by the background flux σT_e^4, are plotted on a semi-log scale as functions of stretch rate in Figure A4-3(a), (b) and (c) and can be described as follows (refer to Figure A4-1 for illustration):

q^-_e: radiative flux from flame outer boundary to surroundings (loss from system)
q^-_w: radiative flux from the gas-phase to the surface
q^+_w: radiative flux from the surface to the gas-phase (includes both surface emission and reflection of incident radiation)

Figure A4-3(a) illustrates the radiative flux at the flame outer boundary toward the ambient for the four combinations of surface absorptivity and emissivity. The radiative flux at the flame boundary is the total (global) heat loss from the system (including the gas flame and the solid radiation). Case 2 has the smallest loss, because of full absorption by the surface and no surface emission. Case 4, that of no surface absorption and full emission, has the largest loss to the ambient. This is due to loss of both the gas-phase and surface emissions, less a small amount of gas-phase absorption. Case 3, that of no surface emission or absorption, represents the situation where the system heat loss is from gas-phase radiation only. At high stretch rate, Figure A4-3(a) shows that q_e^+ is small due to the smaller optical thickness and consequently smaller gas emission, $D_k\Theta^4$. At low stretch rate, D_k is amplified and q_e^+ correspondingly increases until it peaks at $a = 5\ s^{-1}$. The decrease of q_e^+ at extremely low stretch rate is due to decreased flame temperature (to be discussed later).

The difference between Cases 2 and 3 is as follows. In Case 2, the gas-phase radiation to the surface is absorbed; while in Case 3, it is reflected (and since these flames are optically thin, most of this reflected radiation is lost to the ambient environment). Case 1: full emission and full absorption, has high q_e^+ at large stretch rate due to large surface emission. Note that surface emission depends on surface temperature and is independent of optical thickness. The value of q_e^+ is amplified at lower stretch rate due to the increased gas-phase emission (and loss). The curves for Cases 1 and 3 almost coincide for $a < 5\ s^{-1}$. In this range of stretch rate, the reflected gas-phase radiative flux from the surface in Case 3 is almost equal to the emitted surface radiative flux in Case 1. Consequently, the overall losses from the flame are approximately equal. This is considered a coincidence rather that a general observation since the result can be altered by material properties such as the solid pyrolysis surface temperature.

The nature of the difference between Case 1 and 4 is the same as that between Cases 2 and 3. While the incident gas-phase radiation is fully absorbed on the surface in Case 1, this incident flux is fully reflected from the surface in Case 4, and most of it is lost to the ambient environment. Therefore, Case 4 has the highest possible radiative loss from the system.

The trend of flame radiative loss (q_e^+) versus stretch rate, as shown in Figure A4-3(a), correlates very well with the maximum flame temperature curves shown in Figure A4-4. Higher loss results in lower flame temperature and vice versa. Since the curves in Figure A4-3 represent the full flammable range from blow-off to extinction, the flammability ranges can be compared: higher loss results in a narrower flammable range (i.e., higher a at the quenching limit and lower a at the blow-off limit).

The radiative fluxes at the solid fuel surface are given in Figures A4-3(b) and A4-3(c). Figure A4-3(b) shows the incident gas-phase radiative flux onto the fuel surface. The four curves also correlate well with the flame temperature curve shown in Figure A4-4 (i.e., at a given stretch rate, high flame temperature produces high q_w^-). Figure A4-3(c) shows the total radiative flux from the surface to the gas phase. It is the sum of surface emission ($\varepsilon\Theta_w^4$) and reflection $(1-\alpha)q_w^-$ (Equation A4-7). For Case 2, q_w^+ is zero and for Case 4, q_w^+ is the highest. As mentioned previously, Figure A4-3(c) shows that q_w^+ for Cases 1 and 3 are approximately equal for $a < 5$ s^{-1} for the particular solid fuel properties chosen in the computation.

Using the two-flux radiation model, approximately half of the radiation emitted from the gas phase goes toward the flame edge (ambient environment) *directly* and the other half goes toward the fuel surface. Our model includes absorption, but the amount of absorption is small. (The amount of absorption is greater when the more accurate spectral radiation models are employed [Bedir et al 1997]. This will be discussed in more detail in later sections.) Therefore, for simplicity in this discussion, we will neglect the effect of gas-phase absorption. The fate of the incident flux and the amount of surface radiation emitted depend on the values of surface absorptivity and emissivity. The total amount of radiative flux from the surface, q_w^+, for the four cases is shown in Figure A4-3(c). For each case, the difference between q_e^- in Figure A4-3(a) and q_w^+ in Figure A4-3(c) should be approximately one-half of the radiation emitted in the flame (i.e., the portion emitted directly to the ambient) which in turn should be approximately equal to q_w^-. A check between Figure A4-3(a), A4-3(b), and A4-3(c) shows this is indeed the case. The approximation is more exact at higher stretch rate because the gas-phase absorption is less.

A4.4.4 Flame Standoff Distance and Solid Burning Rate

The distance between the solid fuel surface and the location of maximum temperature (very close to the location of maximum consumption rate of fuel vapor) is referred to as the flame standoff distance. Here we use the nondimensional flame standoff distance, η_f, which is a function of $(a)^{1/2}$. This distance is shown in Figure A4-5 for the four cases as a function of stretch rate. (Note that the trend in the physical coordinate is different than in the nondimensional coordinate.) The curves for Cases 1, 3 and 4 all display a maximum at an intermediate stretch rate. Case 2, however, monotonically increases with decreased stretch rate. This is related to the increase of nondimensional burning rate, f_w, as follows. Here the burning rate is an eigenvalue of the solution and the nondimensional solid burning rate, f_w, is related to the mass burning rate by:

$$-f_w = \frac{m}{\sqrt{\rho_e \mu_e a}} \qquad \textbf{(A4-13)}$$

Note that the nondimensional burning rate varies with the inverse square root of the stretch rate. Figure A4-6 gives the nondimensional solid burning rate as a function of stretch rate for the four cases studied. For Cases 1, 3, and 4, $-f_w$ displays a maximum at high stretch rate, then decreases at lower stretch rate until the quenching limit is reached. For an adiabatic system (no radiative loss) and infinitely fast chemical kinetics, $-f_w$ is a constant (approximately 1.2 for the present fuel in air). The nondimensional solid burning rate falls at low stretch rate for these three cases due to radiative loss. (Note that the mass burning rate, m, (which is dimensional) falls at a more rapid rate, because it is dependent on the product $-f_w(a)^{1/2}$. For Case 2 in the dimensional domain, the radiative burning rate can be *higher* than the adiabatic limit—see discussion below).

The nondimensional burning rate is determined by the heat transfer rate to the solid surface which, according to Equation (A4-9), is the sum of two terms: the conduction flux, Θ_w', and the net radiative flux at the surface, $Sq_{net,w}$. To obtain a rough estimate of Θ_w', we can use Figures A4-4 and A4-6 and $\Theta_w'=(\Theta_f - \Theta_w)/\eta_f$ and $q_{net,w}$ can be obtained from Figures A4-3(b) and A4-3(c) and Equation (A4-8).

Case 3 is radiatively neutral at the solid surface ($q_{net,w}$=0), so $-f_w$ is determined by the conduction flux only. Radiation, however, has an influence through the flame temperature. Since gas-phase radiation loss (emission) lowers the flame temperature (see Figure A4-4 discussion), the conductive flux is smaller, yielding a smaller $-f_w$ at low stretch rate.

Case 1 is approximately radiatively neutral at the solid surface for $a < 5\ s^{-1}$, as previously discussed. At higher stretch rates, q_w^+ is larger while flame temperature is lower than that of Case 3, due to surface emission. Both the conductive and radiative fluxes are lower, which produces a lower $-f_w$ compared with Case 3.

Case 4 has the highest q_w^+, the lowest q_w^-, and the lowest Θ_f. Therefore, both the conductive and radiative fluxes are the lowest of the four cases, resulting in the lowest nondimensional burning rate.

The curve for Case 2 in Figure A4-6 displays a qualitatively different trend: nondimensional burning rate increases monotonically with decreasing stretch rate. Furthermore, the value exceeds that given by the adiabatic, fast-kinetic limit ($-f_w = 1.2$). This is because gas-phase radiative feedback becomes dominant at low stretch rate. Note that q_w^+=0. Comparing with the other three cases, this case has the smallest radiative loss (FigureA4-3a), the highest flame temperature (Figure A4-4), and the largest q_w^- (Figure A4-3). Note also that $q_{net,w}$ is negative (it is positive in all other cases), which means that there is a net radiative heat input to the solid. This radiative heat feedback is especially pronounced at low stretch. The corresponding standoff distance, η_f, is also larger at low stretch rate than the other cases, due to the larger nondimensional burning rate (a blowing effect).

This unusual behavior for Case 2 can have implications to the burning of a liquid fuel. For many liquids, the vaporization temperature is close to that of ambient, so the surface radiative emission is negligible, but the surface can be radiatively absorbing. Case 2 mimics this situation. Therefore, gas-phase radiation can overdrive the liquid burning rate above the classical adiabatic value, particularly at low stretch rate. This "anomaly" will be further explored in the following sections using a realistic solid fuel.

A4.4.5 Comparison to Identical Systems With No Gas-Phase Radiation

The effects of gas-phase radiation on flame temperature, burning rate, and flammability are discussed in comparison with identical systems with no gas-phase radiation (Cases 5 and 6) in order to elucidate the fundamental physical processes affected by gas-phase radiation. Here we compare the case with both gas-phase and surface radiation (i.e., Case 1: full absorption and full emission) to the case with surface emission only (no gas radiation) (Case 5: $K_p = 0$; $\varepsilon = 1$) and the adiabatic case, which neglects all of the radiation effects (Case 6: $K_p = 0$; $\varepsilon = 0$).

Figures A4-7 and A4-8 compare the effects of surface radiation only (Case 5) and the combination of surface and gas-phase radiation (Case 1) to the case where radiation effects are neglected (Case 6). When radiation heat transfer is entirely neglected in the heat balance, no extinction limit at low stretch rate is observed. Adding surface emission (Case 5) leads to extinction at low stretch rates [T'ien 1986]. Adding gas-phase radiation further narrows the flammable range.

Figure A4-7 is a plot of nondimensional maximum flame temperature versus stretch rate. The addition of gas-phase radiative participation yields reduced flame temperatures over the range of stretch rates, due to the increased gas-phase radiative heat loss from the system. Compared with the surface radiation case, the temperature reduction is small at high stretch rates but becomes increasingly large at low stretch rates.

Figure A4-8 is a plot of the nondimensional burning rate versus stretch rate for the three cases discussed above. When radiative effects are entirely neglected (Case 6), the nondimensional burning rate approaches a constant level as stretch rate decreases. When surface emission is added (Case 5), the nondimensional burning rate is lower than the adiabatic case due to radiative heat loss from the surface.

The addition of gas-phase radiation to the model yields increased burning rate over the case with surface emission only. This is a reverse of the trend of the nondimensional flame temperature, Figure A4-7, and due to the absorption of radiation by the fuel surface. This burning rate increase is more pronounced at lower stretch rates, although it is diminished somewhat at the quenching limit due to the flame temperature drop there.

Tables A4-1, A4-2, and A4-3 contain nondimensional maximum flame temperatures, and species mass fractions at the surface for various stretch rates, ranging from low to high stretch (Cases 1, 5, and 6, respectively). These are included primarily for comparison to the model with detailed chemistry in the following chapters. We observe that, for both the adiabatic surface and the radiating surfaces, more oxygen reaches the surface when approaching the high stretch extinction limit, which is indicative of incomplete combustion. Also note that, for the radiating surface, less fuel is pyrolyzed at the surface in the low stretch regime.

A4.4.6 Flammability

Using oxygen mass fraction at the edge of the boundary layer (Y_{oe}), and stretch rate as parameters, Figure A4-9 presents the comparison of flammability boundaries for three cases: adiabatic (Case 6), surface radiation only (Case 5) and gas-phase and surface radiation (Case 1). As pointed out first in T'ien [1986], the flammable boundary for the adiabatic case is monotonic—the solid is flammable in a very low oxygen stream as long as the stretch rate is sufficiently low. With surface radiative loss, this is no longer true. A low-stretch quenching branch exists and the U-shaped flammability boundary defines a minimum oxygen percentage below which the stagnation-point region is not flammable for any stretch rate.

The extinction boundary with gas-phase radiation added (Case 1) has a similar shape to the one with surface radiation only. The flammable range is narrower, however, because of the additional system heat loss. The difference between these two cases is largest in the quenching branch at low stretch rate. At high stretch rates, the blow-off boundaries are close. We note that this is opposite to the findings in Oh et al. [1994] which report a large difference at high stretch rate and little difference at low stretch rate. Due to a series of complex mathematical transformations and approximations used in Oh et al. [1994], we were not able to pin down the source of this discrepancy. The results we obtained are compatible with the flame temperature drops and are consistent with the notion (as reflected by the nondimensional parameters) that gas-phase radiation takes precedence over surface radiation as stretch rate decreases.

A4.5 Conclusions

We have extended the model of an axi-symmetric stagnation-point diffusion flame for a solid fuel [T'ien 1986, Oh et al. 1994] to include a gas-phase radiation model in order to investigate the effect of surface absorption and emission on flame temperature, burning rate, radiative fluxes, and the extinction limit of an optically thin flame. This study has demonstrated analytically and numerically that radiation effects (both gas-phase and surface) are amplified at low stretch rate.

The increase of surface radiative influence is due to the increase of flame standoff distance at low stretch rate ($\propto a^{-1/2}$). The increase of the gas-phase radiative effect is due to an increase of the optical thickness of the gas at low stretch rate. The rate of increase of the gas-phase radiative effect is more than that of the surface radiative effect ($\propto 1/a$). Thus, although at high stretch rate, surface radiation is more important than that in the gas phase, the latter may become comparable or more dominant at low stretch rates, as illustrated in our numerical study.

The radiation emitted from the surface results in a heat loss to the flame. Depending on the nature of the interaction with the surface, the influence of gas-phase radiation on the burning of a solid fuel is more complicated, as pointed out in De Ris [1979] and Bhattacharjee and Altenkirch [1992]. For a quasi-one-dimensional, flat flame like the one we have here, approximately half of the radiation emitted from the gas-phase is lost to the ambient environment; the other half is incident to the surface. This incident portion can be reflected at the surface (and lost to the ambient environment in an optically thin flame), or can be absorbed by the surface, or a combination of these, depending on surface absorptivity. In addition, the emissivity of the surface will determine how much radiative flux will join the reflected flux as a system loss to the ambient environment (less the small amount of flux absorbed in the gas-phase in the optically thin flame). In this work, we have studied the four limiting cases of surface radiative properties. In reality, solid fuels will have characteristic surface radiative properties bounded by these four extreme cases. Nevertheless, these cases help us to identify and understand the physics involved in the radiative exchange.

We have also used the results of Case 1 (gas-phase radiation with surface emission and absorption equal to unity) as a 'model' solid to compare with those of Case 5 (surface radiation only) in order to separate the effect of gas-phase radiation. With gas-phase radiation, the computed results show a lower flame temperature, a narrower flammable domain, but a slightly higher solid fuel burning rate.

A4.6 Further Studies

Using the two-flux radiation model along with the Planck mean absorption coefficient has led to fundamental understanding of the effects of flame radiation on the burning and extinction of a solid fuel. Computationally this model is very efficient. However, it does have well known limitations. Bedir et al [1997] and Rhatigan et al. [1998] have shown that, while the use of Planck mean absorption coefficient gives a qualitatively correct trend for many of the combustion problems, it over-predicts the radiative heat flux. The amount of over-prediction depends on the stretch rate (related to the optical length) and can be as much as 100% near the low-stretch quench limit. In the following sections, the combustion model has been extended, using the methods established by Bedir [1998], to include the more accurate narrowband radiation model with a discrete ordinate solution. When quantitative results are required, it is recommended that, unless numerical simplicity and computational time are major factors, the more accurate radiation models (i.e., narrowband and a discrete ordinate solution) be used.

The surface radiative fluxes for Case 1 show that, at low stretch, the incident flux is approximately equal to the surface radiative emission, so that the surface is radiatively neutral. This may not be true for multidimensional situations. In Jiang [1995], where gas-phase radiation is modeled using the S-N discrete ordinate scheme for a concurrent-flow flame spread problem, Jiang found that the incident flame radiation is always smaller than that emitted from the surface. We note that the radiatively neutral assumption was used in Bhattacharjee and Altenkirch [1992] for their opposed-flow flame spreading analysis.

Although we believe we have captured the essential influence of gas-phase radiation on the burning of a solid fuel in this work, quantitatively more accurate results can be predicted by improving the present models (e.g., Rhatigan et al. [1998]). The combustion model can be improved by including detailed kinetics for the gas and solid phases (as described in Section 3). A more sophisticated radiation model, which includes spectral analysis, was used to demonstrate the limitations of the results using the Planck mean absorption coefficient model. In this work, soot radiation has not been included. In low oxygen and/or low stretch rate situations, soot is not observed [Grayson et al. 1994, Olson 1997]; but in higher oxygen streams, soot may be present. To be consistent with the spirit of this work, accounting for the soot radiation effect requires that we predict the soot concentration, which is a difficult and contemporary research problem.

The other important limitation in this analysis is the use of one-step kinetics. The extension of the model to include detailed kinetics is taken up in the body of the thesis. This brings the accuracies of the radiation model (using narrowband spectral analyses) and the kinetics model (using detailed kinetics) to an equivalent level for study of the stagnation-point diffusion flame.

Table A4-1: Sample Surface Species Mass Fractions (Y_w) and Nondimensional Temperature (Θ) for Adiabatic Case (Case 6), Over Various Stretch Rates

stretch rate, s^{-1}	Θ_{max}	$\Theta_{surface}$	$Y_{F,w}$	$Y_{O,w}$	$Y_{CO2,w}$	$Y_{H2O,w}$
6.25	7.815	2.024	0.5927	4.46E-12	0.09692	3.17E-02
101	6.87	2.291	0.576	1.28E-04	0.1008	3.29E-02
133.7	6.086	2.311	0.5706	1.41E-03	0.1008	3.29E-02

Table A4-2: Sample Surface Species Mass Fractions (Y_w) and Nondimensional Temperature (Θ) for the Surface Radiation Case (Case 5), Over Various Stretch Rates

stretch rate, s^{-1}	Θ_{max}	$\Theta_{surface}$	$Y_{F,w}$	$Y_{O,w}$	$Y_{CO2,w}$	$Y_{H2O,w}$
0.88	4.923	1.734	0.1062	1.73E-03	2.11E-01	6.89E-02
6.25	7.214	1.993	0.3794	1.86E-08	1.48E-01	4.83E-02
25	7.261	2.128	0.4651	1.69E-06	1.27E-01	4.16E-02
100	6.371	2.245	0.5054	7.25E-04	1.17E-01	3.82E-02
106.3	6.097	2.252	0.5039	1.53E-03	1.17E-01	3.81E-02

Table A4-3: Sample Surface Species Mass Fractions (Y_w) and Nondimensional Temperature (Θ) for the Gas-Phase and Surface Radiation Case (Case 1), Over Various Stretch Rates

stretch rate, s^{-1}	Θ_{max}	$\Theta_{surface}$	$Y_{F,w}$	$Y_{O,w}$	$Y_{CO2,w}$	$Y_{H2O,w}$
1.33	6.296	2.035	0.2529	2.72E-02	1.75E-01	5.72E-02
6.25	6.381	2.055	0.4678	1.5E-06	1.26E-01	4.14E-02
100	6.139	2.255	0.5088	1.23E-03	1.16E-01	3.78E-02
101.1	6.034	2.256	0.5075	1.59E-03	1.16E-01	3.78E-02

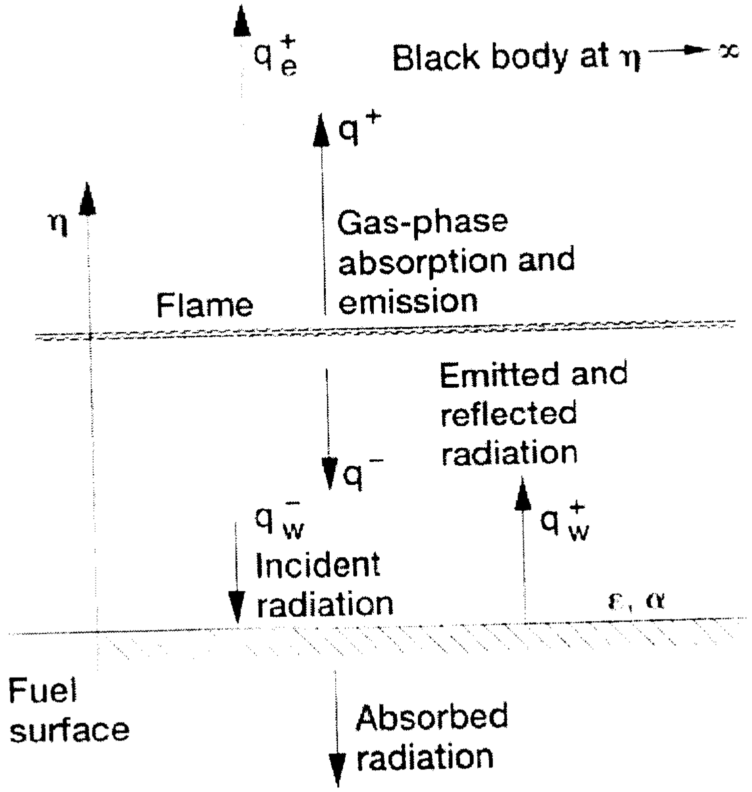

Figure A4-1: Illustration of geometry and radiation model.

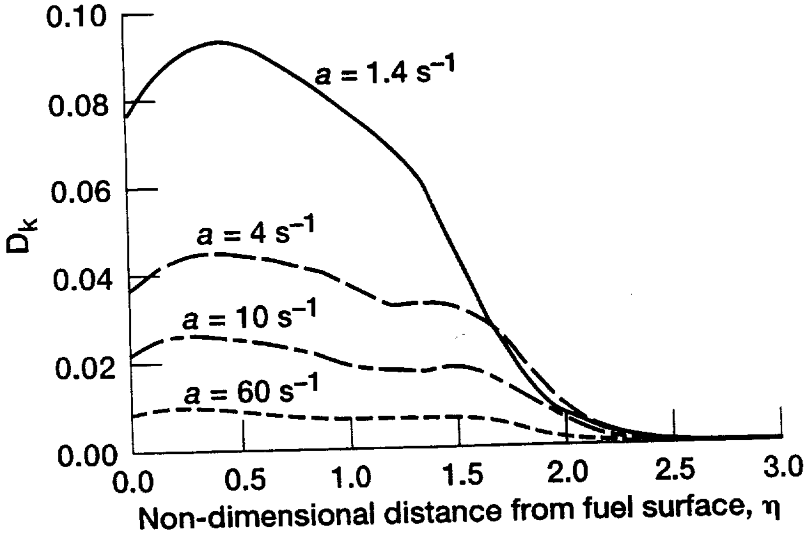

Figure A4-2: Effect of stretch rate (a) on ratio of local radiative absorption length to flame thickness (D_k).

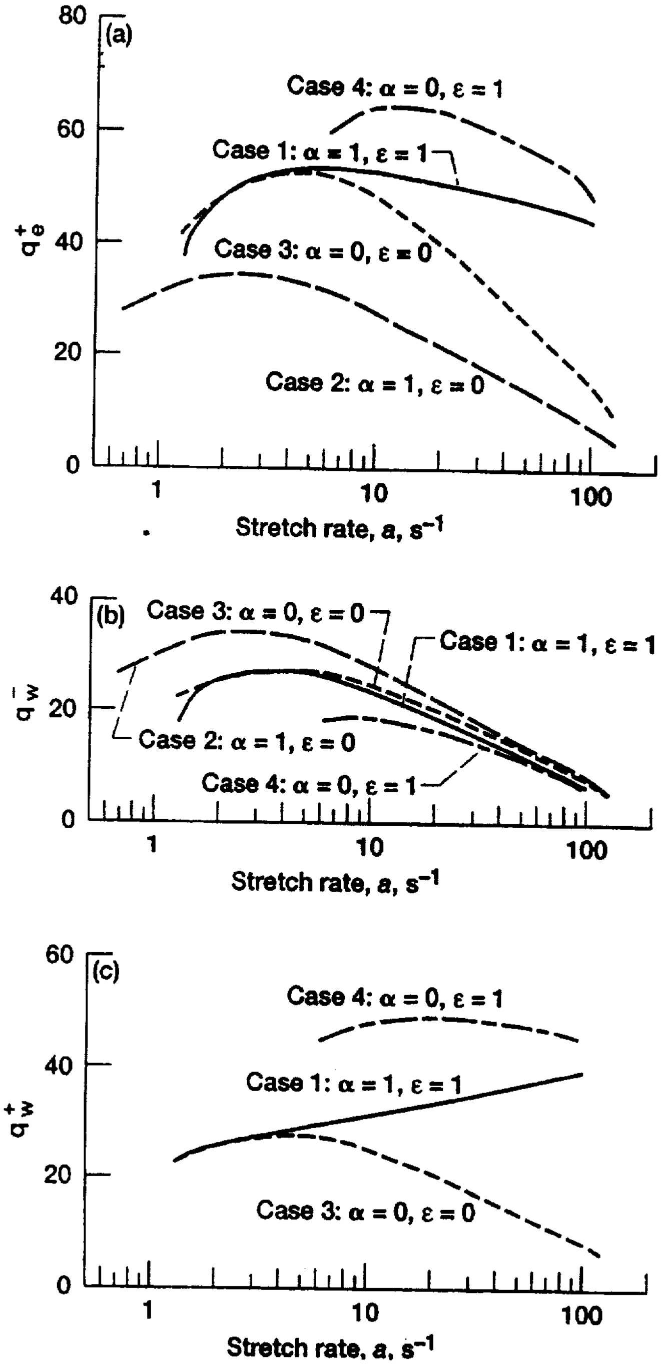

Figure A4-3: Nondimensional radiative fluxes vs. stretch rate.

(a): Radiative Flux from the Flame Edge to the ambient (q_e^+), (b): Radiative Flux from the Gas-phase to the Surface (q_w^-), (c): Radiative Flux from the Surface to the Gas-phase (q_w^+)

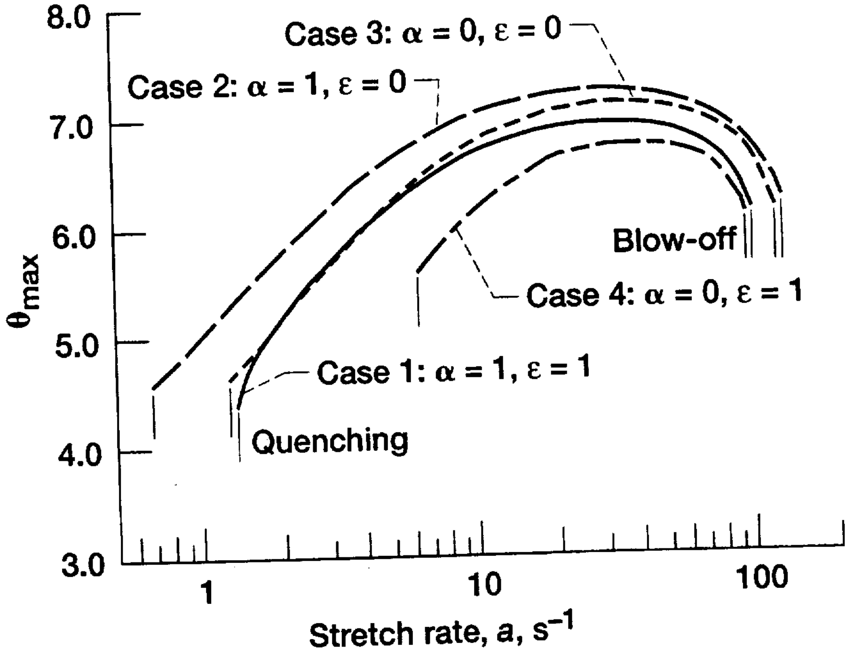

Figure A4-4: Nondimensional maximum flame temperature vs. stretch rate.

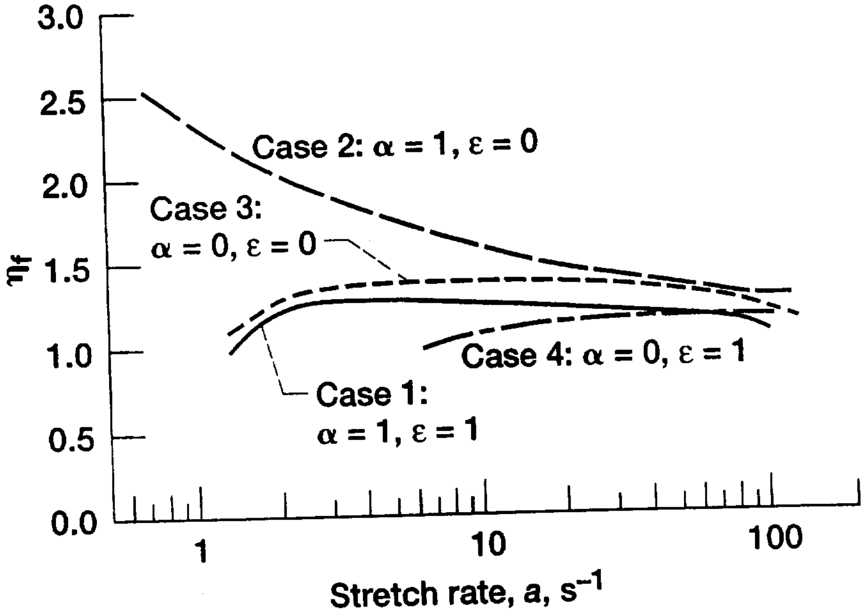

Figure A4-5: Nondimensional flame standoff distance vs. stretch rate.

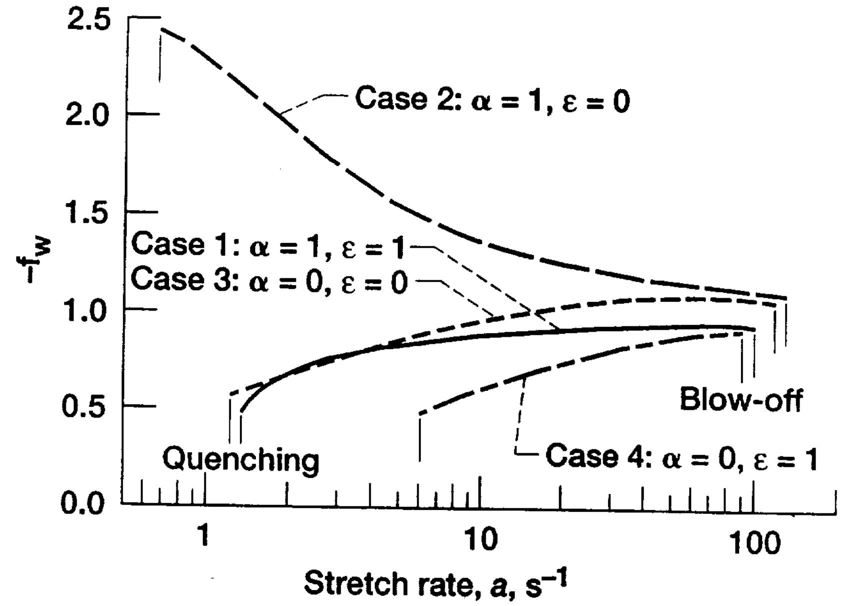

Figure A4-6: Nondimensional fuel burning rate vs. stretch rate.

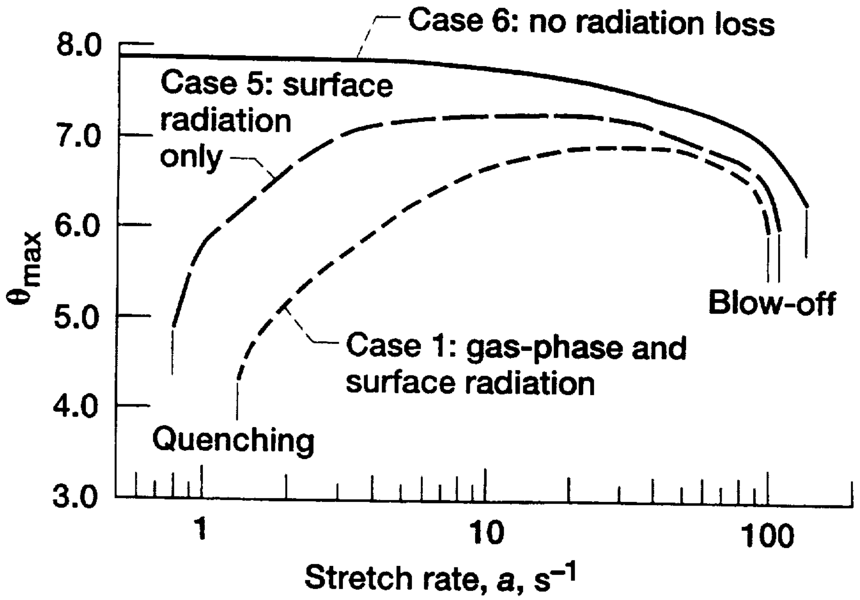

Figure A4-7: Effect of gas-phase radiation on nondimensional maximum flame temperature.

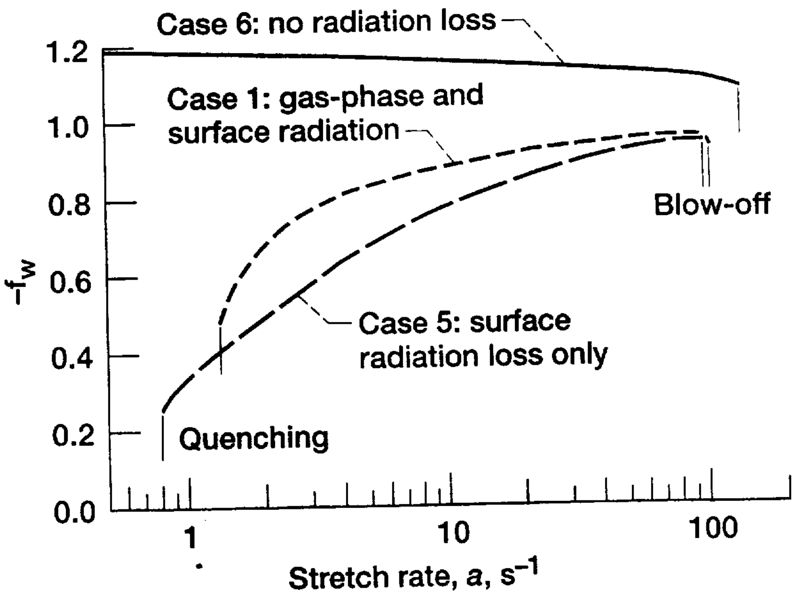

Figure A4-8: Effect of gas-phase radiation on nondimensional burning rate.

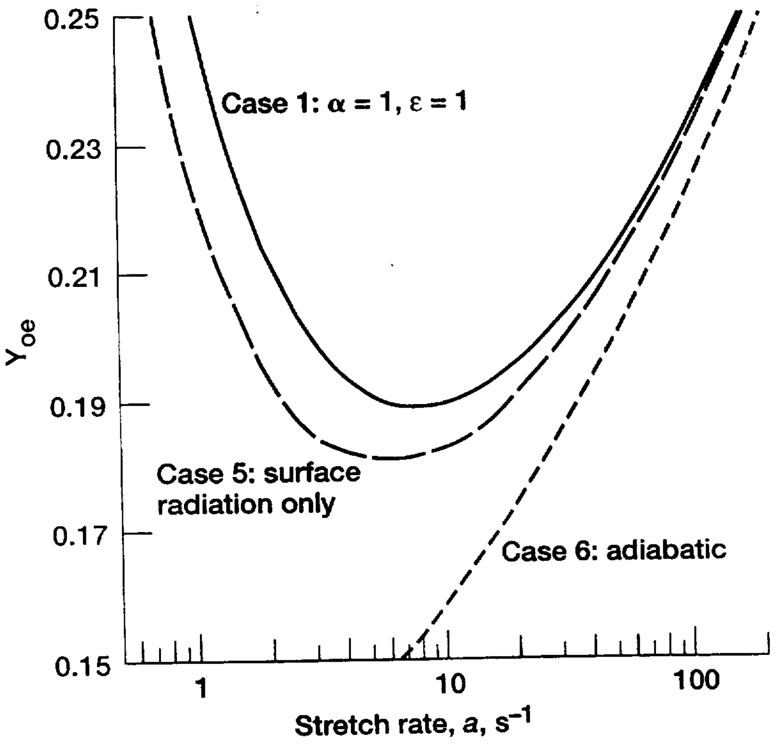

Figure A4-9: Flammability map: ambient oxygen mass fraction vs. stretch rate.

9.0 References

Aghalayam, P.; Bui, P-A.; Vlachos, D. G. "The Role of Radical Wall Quenching in Flame Stability and Wall Heat Flux: Hydrogen-Air Mixtures," *Combustion Theory and Modeling*, **2** (1998) 515-530.

Aldrich Catalog (1994-95) (Ref. TP 202.A55).

Atreya A.; Agrawal, S. "Effect of Radiative Heat Loss on Diffusion Flames in Quiescent Microgravity Atmosphere," *Combustion and Flame*, **115** (1998) 372-382.

Bedir, H.; T'ien, J. S.; Lee, H. S. "Comparison of Different Radiation Treatments for One-dimensional Diffusion Flames," *Proceedings of the Eastern States Section Meeting of The Combustion Institute*, Hilton Head, SC, Dec. (1996).

Bedir, H. "Gas-Phase Radiative Effects in Diffusion Flames," Ph.D. Thesis, Department of Mechanical and Aerospace Engineering, Case Western Reserve University, May 1998.

Bhattacharjee[1], S.; Altenkirch, R. A. in *Low-Gravity Fluid Dynamics and Transport Phenomena* (J.N. Koster and R.L. Sani, Eds.), AIAA, Washington DC (1990) 723.

Bhattacharjee[2], S; Altenkirch, R. A. "Radiation-Controlled, Opposed-Flow Flame Spread in a Microgravity Environment," *Twenty-third Symposium (International) on Combustion*, The Combustion Institute (1990) 1627-1633.

Bhattacharjee, S.; Altenkirch, R. A. "Experimental Results in Flame Spread Over Thin Condensed Fuels in a Quiescent, Microgravity Environment," *Twenty-fourth Symposium (International) on Combustion*, The Combustion Institute (1992) 1669-1676.

Bonne, U. "Radiative Extinguishment of Diffusion Flames at Zero Gravity," *Combustion and Flame*, **16** (1971) 147-159.

Brau, A.; Jonkman, R. M. "Classical Theory of Rotational Relaxation in Diatomic Gases," *The Journal of Chemical Physics*, **52** (1970) 477-484.

Bui-Pham, M.; Seshardri, K. "Comparison Between Experimental Measurements and Numerical Calculations of the Structure of Heptane-Air Diffusion Flames," *Proceedings of the Western States Section of the Combustion Institute*, Fall Meeting, paper 90-05 (1990).

Chao, B. H.; Law, C. K.; T'ien, J. S. "Structure and Extinction of Diffusion Flames with Flame Radiation," *Twenty-third Symposium (International) on Combustion*, The Combustion Institute, (1990) 523-531.

Chen, C. H.; Cheng, M. C. "Gas-Phase Radiative Effects on Downward Flame Spread in Low Gravity," *Combustion Science and Technology*, **97** (1994) 63-83.

Chen, C. H.; T'ien, J. S. "Diffusion Flame Stabilization at the Leading Edge of a Fuel Plate," *Combustion Science and Technology*, **50** (1986) 283 .

Chen, J. Y. "Reduced Reaction Mechanisms for Methanol-Air Diffusion Flames," *Proceedings of the Western States Section of the Combustion Institute*, Fall Meeting, paper 90-07 (1990).

Clegg, G. A.; Melia, T. P.; Tyson, A. "Thermodynamics of Polymerization of Heterocyclic Compounds I – The Heat Capacity, Entropy and Enthalpy of Trioxane," *Polymer*, **9 [2]** (1968) 75-79.

Daguse, T.; Crooenenbroek, J. C.; Rolon, J. C.; Darabina, N.; Soufiani, A. "Study of Radiative and Diffusive Effects on Laminar Counterflow H2/O2/N2 Diffusion Flames," *Combustion and Flame*, **106** (1996) 271-287.

De Ris, J. "Fire Radiation—A Review," *Seventeenth Symposium (International) on Combustion*, The Combustion Institute (1979) 1003.

Dietrich, D. L.; Ross, H. D.; Shu, Y.; Chang, P.; and T'ien, J. S., "Candle Flames in Non-Buoyant Atmospheres," *Combustion Science and Technology*, **156** (2000) 1-24.

Dixon-Lewis, G. "Structure of Laminar Flames," *Twenty-third Symposium (International) on Combustion*, The Combustion Institute (1990) 305.

Dixon-Lewis, G. et al. "Calculation of the Structure and Extinction Limit of a Methane-Air Counterflow Diffusion Flame in the Forward Stagnation Region of a Porous Cylinder," *Twentieth Symposium (International) on Combustion*, The Combustion Institute, (1984) 1893-1904.

Dorofeeva, O. V. "Ideal gas thermodynamic properties of oxygen Heterocyclic compounds. Part 2. Six-membered, seven-membered, and eight-membered rings," *Thermochim. Acta*, **200** (1992) 121-150.

Fernandes, N. E.; Park, Y. K.; Vlachos, D. G. "The Autothermal Behavior of Platinum Catalyzed Hydrogen Oxidation: Experiments and Modeling," *Combustion and Flame* **118** (1999) 164-178.

Frate, F. C.; Bedir, H.; Sung, C. J.; T'ien, J.S. "On Flammability Limits of Dry CO/O2 Opposed-Jet Diffusion Flames," *Twenty-Eighth Symposium (International) on Combustion*, The Combustion Institute (2000).

Foutch, D. W.; T'ien, J. S. "Extinction of a Stagnation-Point Diffusion Flame at Reduced Gravity," *AIAA Journal* **25**[7] (1987) 972.

Friedman, R. J.; Levy, J. B.; Rumbel, K. S. Atlantic Research Corp., AFOSR TN-59-173, AD NO 211-213 (1959) Atlantic Research Corp.

Glarborg, P.; Kee, R. J.; Grcar, J. F.; Miller, J. A. "PSR: A Fortran Program for Modeling Well-Stirred Reactors," *SAND86-8209*, Sandia National Laboratories (1986).

Godson, W. L. "The Evaluation of Infrared Radiative Fluxes Due to Atmospheric Water Vapor," *Quarterly Journal of the Royal Meteorological Society*, **79** (1953) 367-379.

Grayson, G.; Sacksteder, K. R.; Ferkul, P. V.; T'ien, J. S. "Flame Spreading Over a Thin Solid in Low-speed Concurrent Flow—Drop Tower Experimental Results and Comparison with Theory," *Microgravity Science and Technology*, **VII** [2] (1994) 187-196.

Grcar, H. F., "The Twopnt Program for Boundary Value Problems," Report *SAND91-8230*, Sandia National Laboratories (1992).

Gummalla[1], M.; Vlachos, D. G.; Delichatsios, M. A. "Bifurcations and Structure of Surface Interacting Methane-Air Diffusion Flames," submitted to *Combustion and Flame*.

Gummalla[2], M.; Bui, P. A.; Vlachos, D. G. "Nonlinear Dynamics of Surface Stabilized Premixed and Diffusion Flames: Current Trends and Future Directions," accepted to *Chem. Eng. Sci.*

Handbook of Thermoplastics (1997) (Ref. TP 1180.T5H36).

Hills, J.; Howard, C. J. "Rate Coefficient Temperature Dependence and Branching Ratio for the OH+ClO Reaction," *J. Chem. Phys.* **81** (1984) 4458.

Hippler, H.; Troe, J.; Willner, J. "Shock Wave Study of the Reaction HO2+HO2 → H2O2+O2: Confirmation of a Rate Constant Minimum Near 700 K," *Journal of Chemical Physics*, **93** (1990) 1755-1760.

Hirschfelder, J. O.; Curtiss, C. F.; Bird, R. B. *Molecular Theory of Gases and Liquids*. John Wiley and Sons, New York, N.Y. (1954).

Hochgreb, S. "An Experimental and Numerical Study on the Oxidation of Formaldehyde," Ph.D. Dissertation, Princeton University (1991).

Hochgreb, S. Personal communication with the author, Aug. (1999).

Hochgreb[1], S.; Dryer, F. L. "Decomposition of 1,3,5-Trioxane at 700-800 K," *J. Phys. Chem.*, **96** (1992) 295-297.

Hochgreb[2], S.; Dryer, F. L. "A Comprehensive Study on CH_2O Oxidation Kinetics," *Combustion and Flame*, **91** (1992) 257-284.

Hochgreb, S.; Yetter, R. A.; Dryer, F. L. "The Oxidation of CH_2O in the Intermediate Temperature Range (943-995 K)," *Twenty-third Symposium (International) on Combustion*, The Combustion Institute (1990) 171-177.

Irdam, E. A.; Kiefer, J. H. "The Decomposition of 1,3,5-Trioxane at Very High Temperatures," *Chemical Physics Letters*, **166** (1990) 491-499.

Jiang, C. B.; "A Model of Flame Spread Over a Thin Solid in Concurrent Flow with Flame Radiation," Ph.D. Thesis, Department of Mechanical and Aerospace Engineering, Case Western Reserve University, May (1995).

Kashiwagi, T; "Experimental Observation of Radiative Ignition Mechanisms" *Combustion and Flame*, **34** (1979) 231-244.

Kee, R. J.; Dixon-Lewis, G.; Warnatz, J.; Coltrin, M. E.; Miller, J. A. "TRAN: A FORTRAN Computer Code Package for the Evaluation of Gas-Phase, Multicomponent Transport Properties," SAND86-8246, Sandia National Laboratories (1986).

Kee, R. J.; Miller, J. A.; Evans, G. H. "A Computational Model of the Structure and Extinction of Strained, Opposed Flow, Premixed Methane-Air Flames," *Twenty-second Symposium (International) on Combustion*, The Combustion Institute (1988) 1479.

Kee, R. J.; Rupley, F. M.; Miller, J. A. "CHEMKIN II: A FORTRAN Chemical Kinetics Package for the Analysis of Gas-Phase Chemical Kinetics," SAND 89-8009, Sandia National Laboratories (1989).

Kee, R. J.; Grcar, J. F.; Smooke, M. D.; Miller, J. A.; Meeks, E. "PREMIX: A FORTRAN Program for Modeling Steady Laminar One-Dimensional Premixed Flames," *Reaction Design*, San Diego, CA (1998).

Kinoshita, C. M.; Pagni, P. J. "Stagnation–Point Combustion with Radiation," *Eighteenth Symposium (International) on Combustion*, The Combustion Institute (1981) 1415-1425.

Kirk-Othmer Encyclopedia of Chemical Technology, 2nd Edition (Ref. TP 9. E685).

Lay, T. H. et al. "Thermodynamic Parameters and Group Additivity Ring Corrections for Three- to Six-Membered Oxygen Heterocyclic Hydrocarbons," *J. Phys. Chem. A*, **101** (1997) 2471-2477.

Lee, S. T.; T'ien, J. S. "The Effect of Soot Radiation on the Combustion of Solid Fuels," *Journal of the Chinese Society of Mechanical Engineers*, **10** (1989) 243-253.

Lide, D. R., Ed., *CRC Handbook of Chemistry and Physics*, 76th Edition (1996).

Liñán, A. The Asymptotic Structure of Counterflow Diffusion Flames for Large Activation Energies. *Acta Astronautica*, **1** (1974) 1007-1039.

Liu, Y.; Rogg, R. "Modelling of Thermally Radiating Diffusion Flames with Detailed Chemistry and Transport," *Heat Transfer in Radiating and Combusting Systems* (M.G. Carvalles et al., Eds.), Springer-Verlag, New York (1991) 114-127.

Lutz, E.; Kee, R. J.; Miller, J. A. "SENKIN: A FORTRAN Program for Predicting Homogeneous Gas Phase Chemical Kinetics with Sensitivity Analysis," SAND87-8248, Sandia National Laboratories (1988).

Lutz, E.; Kee, R. J.; Grcar, J. F.; Rupley, F. M. "OPPDIF: A FORTRAN Program for Computing Opposed Flow Diffusion Flames," SAND 96-8243, Sandia National Laboratories (1996).

Maas, U.; Pope, S. B. "Simplifying Chemical Kinetics: Intrinsic Low-Dimensional Manifolds in Composition Space," *Combustion and Flame*, **88** (1992) 239-264.

Malkmus, W. "Random Lorentz Band Model with Exponential Tailed s-1 Line Intensity Distribution," *J. Opt. Soc. Am.*, **57** (1967) 323-329.

Maryott, A.; Acree, S. F. "Dipole Moment and Structure of Trioxane," *Journal of Research of the National Bureau of Standards*, RP1596 (1944).

Material Safety Data Sheet for Trioxane, Aldrich Chemical Co. (1989).

Mather, S.; Tondon, P. K.; Saxena, S. C. "Thermal Conductivity of Binary, Ternary and Quaternary Mixtures of Rare Gases," *Molecular Physics*, **12** (1967) 569-579.

Melia, T. P.; Bailey, D.; Tyson, A. "Thermodynamics of Addition Polymerization, I. The system trioxane-polyoxymethylene," *J. Appl.Chem.*, **17** (1967) 15-17.

Melius, C. F. et al. "Unimolecular Decomposition of 1,3,5-Trioxane: Comparison of Theory and Experiment," *Proceedings of the Eastern States Section of the Combustion Institute* (1990) 131-134.

Monchick, L.; Mason, E. A. "Transport Properties of Polar Gases," *Journal of Chemical Physics*, **35** (1961) 1676-1697.

National Institute of Standards Chemistry Web book: http://webbook.nist.gov/chemistry/

Negrelli, D. E.; Lloyd, J. R.; Novotny, J. L. "A Theoretical and Experimental Study of Radiation Convection Interaction in a Diffusion Flame," *Journal of Heat Transfer*, **99** (1977) 212-220.

Nishioka, M.; Law, C. K.; Takeno, T. "A Flame-Controlling Continuation Method for Generation S-Curve Responses with Detailed Chemistry," *Combustion and Flame*, **104** (1996) 328-342.

Oh, T. K.; Lee, S. K.; Chung, S. H. "Effect of Gas-Phase and Surface Radiation on the Structure and Extinction of Diffusion Flames Stabilized on a Condensed Fuel," *International Journal of Heat and Mass Transfer*, **37** (1994) 2893-2900.

Olson, S. L. "Buoyant Low Stretch Stagnation Point Diffusion Flames Over a Solid Fuel," Ph.D. Thesis, Case Western Reserve University, Cleveland, Ohio, May (1997).

Ozisik, M. N. *Radiative Transfer and Interactions with Conduction and Convection*, John Wiley and Sons (1973).

Park, Y. K.; Aghalayam, P.; Vlachos. D.G. "A Generalized Approach for Predicting Coverage Dependent Reaction Parameters of Complex Surface Reactions: Application to H2 Oxidation over Platinum," Submitted to *J. Phys. Chem.*

Parker, J. G. "Rotational and Vibrational Relaxation in Diatomic Gases," *The Physics of Fluids*, **2** (1959) 449-462.

Rhatigan, J. L.; Bedir, H.; T'ien, J. S. "Gas Phase Radiative Effects on the Burning and Extinction of a Solid Fuel," *Combustion and Flame*, **112** (1998) 231-241.

Ritter, E. R.; Bozelli, J. W. "Thermodynamic Property Estimation for Radicals and Molecules (THERM)," New Jersey Institute of Technology, March 16 (1987).

Roth, P.; Just, T. "Kinetics of the High Temperature, Low Concentration CH4 Oxidation Verified by H and O Atom Measurements," *Twentieth Symposium (International) on Combustion*, The Combustion Institute (1984) 807.

Rothman, L. S.; Gamache, R. R.; Tipping, R. H.; Rinsland, C. P.; Smith, M. A. H.; Benner, D. C.; Malathy Devi, V.; Flaud, J. M.; Camy-Peyret, C.; Perrin, A.; Goldman, A.; Massie, S. T.; Brown, L. R. "HITRAN molecular database," *J. Quant. Spec. Rad. Transfer*, **48** (1992) 469-507.

Seigel, R.; Howell, J. R. *Thermal Radiation Heat Transfer*, 2nd Ed., Hemisphere Publishing Corp. (1981).

Shih, H. Y.; Bedir, H.; T'ien, J. S.; Sung, C. J. "Computed Flammability Limits of Opposed-Jet H2/O2/CO2 Diffusion Flames at Low Pressure," *J. Propulsion and Power*, **15-6** (1999) 903-908.

Siddall, R. G. "Flux Methods for the Analysis of Radiant Heat Transfer," *Journal of the Institute of Fuel*, **47** (1974) 101-109.

Silbulkin, M.; Kulkarni, A. K.; Annamalai, K. "Burning on a Vertical Fuel Surface with Finite Chemical Reaction Rate," *Combustion and Flame*, **44** (1982) 187-199.

Silbulkin, M.; Kulkarni, A. K.; Annamalai, K. "Effects of Radiation on the Burning of Vertical Fuel Surfaces," *Eighteenth Symposium (International) on Combustion*, The Combustion Institute (1981) 611-617.

Smith, G. P.; Golden, D. M.; Frenklach, M.; Moriarty, N. W.; Eiteneer, B.; Goldenberg, M.; Bowman, C. T.; Hanson, R.; Soonho S.; Gardiner, W. C. Jr.; Lissianski, V; Qin, Z., http://www.me.berkeley.edu/gri_mech/

Sohn, C. H.; Kim, J. S.; Chung, S. H.; and Maruta, K. "Nonlinear Evolution of Diffusion Flame Oscillations Triggered by Radiative Heat Loss," *Combustion and Flame*, **123** (2000) 95-106.

Sohrab, S. H.; Williams, F. A. "Extinction of Diffusion Flames Adjacent to Flat Surfaces of Burning Polymers," *Journal of Polymer Science, Polymer Chemistry Edition*, **19** (1981) 2955-2976.

Soufiani, A.; Taine, J. "High Temperature Gas Radiative Property Parameters of Statistical Narrowband Model for H2O, CO2, and CO and Correlated k Model for H2O and CO2," *International Journal of Heat and Mass Transfer*, **40** (1997) 987.

Soufiani, A.; Taine, J. "Experimental and Theoretical Studies of Combined Radiative and Convective Transfer in CO_2 and H_2O Laminar Flows," *International Journal of Heat and Mass Transfer*, **32** (1989) 447-486.

Soufiani, A.; Hartman, J. M.; Taine, J. "Validity of Band Model Calculations for CO_2 and H_2O Applied to Radiative Properties and Conductive-Radiative Transfer," *J. Quant. Spec. Rad. Transfer*, **33** (1985) 243-257.

Spalding, D. B. "Proceedings of the Royal Society (London)," **A240** (1957) 83.

Sung, C. J.; Kistler, J. S; Nishioka, M.; Law, C. K. "Further Studies on Effects of Thermophoresis on Seeding Particles in LDV Measurements of Strained Flames," *Combustion and Flame*, **105** (1996) 189-201.

Sung, J., Personal communication with the author. Aug. (1999).

T'ien, C. L.; Lee, S. C. "Flame Radiation," *Prog. Energy Combust. Sci.*, **8** (1982) 41-59.

T'ien, J. S.; Bedir, H. "Radiative Extinction of Diffusion Flames – A Review," *Proceedings of the First Asia-Pacific Conference on Combustion*, Osaka, Japan, May (1997).

T'ien, J. S. "Diffusion Flame Extinction at Small Stretch Rates: The Mechanism of Radiative Loss," *Combustion and Flame*, **65** (1986) 31-34.

T'ien, J. S.; Singhal, S. N.; Harrold, D. P.; Prahl, J. M. "Combustion and Extinction in the Stagnation-Point Boundary Layer of a Condensed Fuel" *Combustion and Flame*, **33** (1978) 55-68.

The Merck Index, An Encyclopedia of Chemicals, Drugs, and Biologicals, 11th Edition (1989).

Timonen, R. S.; Ratajczak, E.; Gutman, D. "Kinetics of the Reactions of the Formyl Radical with Oxygen, Nitrogen Dioxide, Chlorine, and Bromine," *J Phys. Chem.*, **92** (1988) 651-655.

Timonen[1], R. S.; Ratajczak, E.; Gutman, D.; Wagner, A. F. "Kinetics of the Reaction between Formyl Radicals and Atomic Hydrogen," *J Phys. Chem.*, 91 (1987) 692-694.

Timonen[2], R. S.; Ratajczak, E.; Gutman, D.; Wagner, A. F. "The Addition and Dissociation Reaction H + CO ↔ HCO 2. Experimental Studies and Comparison with Theory," *J Phys. Chem.*, **91** (1987) 5325-5332.

Tsang, W.; Hampson, R. F. "Chemical Kinetic Data Base for Combustion Chemistry. Part 1. Methane and Related Compounds," *J Phys. Chem. Ref. Data* **15** (1986) 1087-1279.

Van Bommel, M. J.; Van Miltenburg, J. C.; Schuijff, A. "Heat-Capacity Measurements and Thermodynamic Functions of 1,3,5-Triazine and 1,3,5-Trioxane," *J. Chem. Thermodynamics*, **20** (1988) 397-403.

Vlachos, D. G.; Schmidt, L. D.; Aris, R. "Ignition and Extinction of Flames Near Surfaces: Combustion of H2 in Air," *Combustion and Flame* **95** (1993) 313.

Vlachos, D. G.; Schmidt, L. D.; Aris, R. "Ignition and Extinction of Flames Near Surfaces: Combustion of CH4 in Air," *AI ChE Journal* **40** (1994) 1005.

Walker, J. F.; Carlisle, P. J. "Trioxane," *Chemical and Engineering News*, **21** (1943) 1250-1251.

Warnatz, J., *Ber. Bunsenges. Phys. Chem.*, **82** (1978) 834-841.

Yetter, R. A.; Dryer, F. L. "A Comprehensive Reaction Mechanism for Carbon Monoxide/Hydrogen/Oxygen Kinetics," *Combustion Science and Technology*, **79** (1991) 97-128.

REPORT DOCUMENTATION PAGE	Form Approved OMB No. 0704-0188

1. AGENCY USE ONLY *(Leave Blank)*	2. REPORT DATE June 2001	3. REPORT TYPE AND DATES COVERED NASA Technical Paper

4. TITLE AND SUBTITLE Effects of Gas-Phase Radiation and Detailed Kinetics on the Burning and Extinction of a Solid Fuel	5. FUNDING NUMBERS
6. AUTHOR(S) Jennifer L. Rhatigan, Ph.D.	
7. PERFORMING ORGANIZATION NAME(S) AND ADDRESS(ES) Lyndon B. Johnson Space Center Houston, Texas 77058	8. PERFORMING ORGANIZATION REPORT NUMBERS S-879
9. SPONSORING/MONITORING AGENCY NAME(S) AND ADDRESS(ES) National Aeronautics and Space Administration Washington, DC 20546-0001	10. SPONSORING/MONITORING AGENCY REPORT NUMBER TP-2001-210770

11. SUPPLEMENTARY NOTES

12a. DISTRIBUTION/AVAILABILITY STATEMENT Available from the NASA Center for AeroSpace Information (CASI) 7121 Standard Hanover, MD 21076-1320 Subject Category: 28	12b. DISTRIBUTION CODE

13. ABSTRACT *(Maximum 200 words)*

This is the first attempt to analyze both radiation and detailed kinetics on the burning and extinction of a solid fuel in a stagnation-point diffusion flame. We present a detailed and comparatively accurate computational model of a solid fuel flame along with a quantitative study of the kinetics mechanism, radiation interactions, and the extinction limits of the flame.

A detailed kinetics model for the burning of solid trioxane (a trimer of formaldehyde) is coupled with a narrowband radiation model, with carbon dioxide, carbon monoxide, and water vapor as the gas-phase participating media. The solution of the solid trioxane diffusion flame over the flammable regime is presented in some detail, as this is the first solution of a heterogeneous trioxane flame. We identify high-temperature and low-temperature reaction paths for the heterogeneous trioxane flame.

We then compare the adiabatic solution to solutions that include surface radiation only and gas-phase and surface radiation using a black surface model. The analysis includes discussion of detailed flame chemistry over the flammable regime and, in particular, at the low stretch extinction limit. We emphasize the low stretch regime of the radiatively participating flame, since this is the region representative of microgravity flames. When only surface radiation is included, two extinction limits exist (the blow-off limit, and the low stretch radiative limit), and the burning rate and maximum flame temperatures are lower, as expected. With the inclusion of surface and gas-phase radiation, results show that, while flame temperatures are lower, the burning rate of the trioxane diffusion flame may actually increase at low stretch rate due to radiative feedback from the flame to the surface.

14. SUBJECT TERMS fuel, solid fuel, diffusion flame, extinction, gas-phase radiation, kinetics, surface radiation	15. NUMBER OF PAGES 155	16. PRICE CODE

17. SECURITY CLASSIFICATION OF REPORT Unclassified	18. SECURITY CLASSIFICATION OF THIS PAGE Unclassified	19. SECURITY CLASSIFICATION OF ABSTRACT Unclassified	20. LIMITATION OF ABSTRACT Unlimited

Standard Form 298 (Rev Feb 89) (MS Word Mar 97)
Prescribed by ANSI Std. 239-18
298-102

NSN 7540-01-280-5500